Approximate $\mathrm{N^3LO}$ Parton Distribution Functions

In the pursuit of theoretical uncertainties…

Jamie Wythen McGowan

A dissertation submitted in partial fulfillment

of the requirements for the degree of

Doctor of Philosophy

of

University College London.

Department of Physics & Astronomy

University College London

March 30, 2023

Declaration

This thesis is the result of my own work, except where explicit reference is made to the work of others, and has not been submitted for another qualification to this or any other university.

Parts of this work have been published or are due to be published in the following articles:

1. Approximate N^3LO Parton Distribution Functions with Theoretical Uncertainties: MSHT20aN^3LO PDFs, J. McGowan, T. Cridge, L. Harland-Lang and R. Thorne, Eur. Phys. J. C 83, 185 (2023), 2207.04739 [hep-ph]

2. Phenomenology of the antimatter asymmetry and its impact on parton distribution functions, T. Cridge, L. Harland-Lang, J. McGowan and R. Thorne, In preparation [hep-ph]

3. Phenomenology of $7 + 8$ TeV dijet final states from the LHC and their impact on parton distribution functions, T. Cridge, L. Harland-Lang, J. McGowan and R. Thorne, In preparation [hep-ph]

Jamie McGowan

Abstract

This thesis presents the first global analysis of parton distribution functions (PDFs) at approximate N^{3}LO in the strong coupling constant α_s, extending beyond the current highest NNLO achieved in PDF fits. To achieve this, a general formalism for the inclusion of theoretical uncertainties from missing higher orders (MHOs) in a PDF fit is established. By using the currently available knowledge surrounding the next highest order (N^{3}LO) in α_s, consistent, justifiable and explainable approximate N^{3}LO (aN^{3}LO) PDFs are constructed, including estimates for missing higher order uncertainties (MHOUs). Specifically, N^{3}LO approximations for splitting functions, transition matrix elements, coefficient functions and K-factors for multiple processes are introduced. Crucially, these are constrained to be consistent with the wide range of already available information about N^{3}LO to match the complete result at this order as accurately as possible. Using this approach, this thesis includes results from a fully consistent approximate N^{3}LO global fit within the MSHT framework. This relies on an expansion of the Hessian procedure used in previous MSHT fits to allow for sources of theoretical uncertainties. These are included as nuisance parameters in a global fit, controlled by knowledge and intuition based prior distributions. The differences between these aN^{3}LO

PDFs and the standard NNLO MSHT20 PDF set are investigated, as well as the impact of using aN^{3}LO PDFs on the LHC production of a Higgs boson at this order. Alongside this, guidelines are provided on how these PDFs should be be used in phenomenological investigations. Finally, the effect of fitting to recent high-x datasets currently not included as standard in the MSHT20 global fit is discussed, with a focus on aN^{3}LO PDFs at high-x.

Impact Statement

The work presented in this thesis is concerned with extending our accuracy and understanding of the fundamental structure of the proton.

The precision of data from the Large Hadron Collider (LHC) is now at a point where developing a more accurate and in-depth theory of the proton is unavoidable. The plethora of final states observed at the LHC (and future iterations of hadron colliders) provides a conveyor belt of particles, some of which we know well and others that lie waiting to be discovered. Therefore, to be able to fully saturate the capabilities of particle colliders, one must look to extend our theoretical descriptions to new levels.

The doctoral work discussed in this thesis is concerned with an essential ingredient in mathematically describing particle collisions involving a hadron in the initial state, such as a proton. Specifically, this work contributes towards extending the accuracy of parton distribution functions (PDFs) which describe the internal sub-structure of a proton (i.e. quarks and gluons). An increase in the accuracy and theoretical understanding of PDFs will allow physicists to be able to make more precise, robust and reliable predictions about the behaviour of matter when collided together at current experiments, for example at the LHC, and also future collider experiments.

The particle physics community has a track record of developing innovative new technologies that have multiple applications outside of the field. The contributions made here are directly concerned with theoretical descriptions that inform the planning of future particle physics experiments and therefore are a driving factor in pushing the wider community to develop these novel technologies.

Acknowledgements

Over the past 4 years, the work that is (not so briefly) summarised in this thesis has tested me beyond my expectations. Throughout this journey, I have been incredibly humbled by the guidance and support I have received from my colleagues, family and friends. Therefore, there are many people who deserve thanks for helping me in many different ways!

Firstly, I would like to thank my supervisor, Robert Thorne, for your unfaltering belief and support throughout the duration of my PhD. Your foresight and experience as a researcher has been an inspiration for me and something I will remember, and aspire to, in my own career. I don't believe anyone could wish for a more understanding, relatable and kind supervisor, therefore I will be forever grateful to have been given the opportunity to work with you on this fascinating area of research.

Further to this, I would like to extend a very special thanks to Tom and Lucian for your clear comments and insightful perspectives on this work. Those several hours worth of conversations between the four of us helped immensely in pushing this work to the level it is at today.

Mum and Dad, there is not a lot of words that can describe the level of gratitude I have for you both. Even though we have not been able to see each other as much as we would like over the past few years, you have always been there and you have always

encouraged me to aim as high as possible, inside and outside academia. Therefore this PhD is as much mine as it is yours – even though Mum will probably have that very confused look on her face when she reads the title!

To all my friends, you have been a constant source of escapism that has been, and will continue to be, very special in my life. While there are many of you I would love to name, I would like to thank Dom, Elliot, Luke, Michalis, Ollie, Ryan and Tom (ordered alphabetically to avoid any favouritism) for providing countless hours of laughter, entertainment and chaos. The fact that we can meet up after months of not seeing each other, and continue as if no time has passed, is incredible. So thank you boys, for continually supplying the best weekends of the year!

During the course of this PhD work, the world was plunged into a pandemic, therefore I would be remiss of me not to extend my appreciation for Chris and Hilary McCloskey. There are not many people who can say that they enjoyed living in lockdown with their "in-laws" for 9 months, but I can! I truly cannot thank you enough for your hospitality, understanding and selflessness during this time.

Last, but by no means least, Hannah, for being with me every step of the way in this PhD, for your limitless encouragement, patience, support and understanding (not to mention the well-timed tough love). I am eternally grateful to have you in my life.

Contents

Chapter 1.

Introduction

The Standard Model of Particle Physics is one of the most precise theories in modern science. The Standard Model has withstood decades of onslaught from the world's best experimental measurements by adapting and evolving to explain ever more mysteries inside the infinitely large, minute realm of particles. However, despite the theory's unprecedented success, we also know that the Standard Model is at least incomplete and at most, fundamentally incorrect. Its failures in explaining phenomena such as baryon asymmetry, dark energy/matter and neutrino oscillations are what motivate us to push the precision of experimental measurements used to test the Standard Model to new depths.

In recent years, the level of precision achieved at the Large Hadron Collider (LHC) has reached far beyond what was once thought possible. This has initiated a new era of high precision phenomenology that has pushed the need for a robust understanding of theoretical uncertainty to new levels. A primary focus of the precision phenomenology program at the LHC is to investigate and provide insight into the internal structure

of the proton. The theoretical description of this internal structure is formulated with parton distribution functions (PDFs). PDFs are non-perturbative quantities which, at present, cannot be derived from first principles and are therefore determined from a global QCD analysis of experimental data. PDFs and their uncertainties are essential ingredients for precision measurements involving hadronic initial states. Therefore improving the determination of PDFs, their uncertainties and our overall understanding of the internal structure of the proton is heavily motivated by the high impact potential for fundamental discoveries e.g. the origin of mass and spin or the properties of cosmic neutrinos. Furthermore with current and future experiments pushing measurements to the point where any small deviation from SM predictions may signal new physics, a robust understanding of all sources of PDF uncertainties is essential. PDF uncertainties arise from; experimental uncertainties (propagated from the fact that PDFs are determined from experimental data that are characterised by both statistical and systematic uncertainties), the fitting methodology (such as from the specific chosen form of parameterisations of PDFs) and also theoretical uncertainties which will be a primary focus of this thesis.

Due to the perturbative nature of calculations in Quantum Chromodynamics (QCD), with respect to the strong coupling constant α_s, a leading theoretical uncertainty arises from the truncation of perturbative expansions [1, 2]. The current state of the art for PDFs is next-to-next-to leading order (NNLO) [3–8]. However, these PDF sets do not generally include theoretical uncertainties arising from the truncation of perturbative calculations that enter the fit. The consideration of these so-called Missing Higher Order Uncertainties (MHOUs), and how to estimate them, is the topic of much discussion among groups involved in fitting parton distribution functions (PDFs) [9–13].

More recently, a method of utilising a scale variation approach to estimating these uncertainties has been included in an NLO PDF fit [9]. This approach is based upon the fact that to all orders, a physical calculation must not depend on any unphysical scales introduced into calculations. Therefore varying the factorisation and renormalisation scales is, in principle, a first attempt at estimating the level of theory uncertainty from missing higher orders (MHOs). Motivated by the renormalisation group invariance of physical observables, this method is theoretically grounded to all orders. However, the method of scale variations has been shown to be less than ideal in practice [10, 14]. An obvious difficulty is the arbitrary nature in the chosen range of the scale variation, as well as the choice of central scale. Expanding on this further, even if a universal treatment of scale variations was agreed upon, these variations are unable to predict the effect of various classes of logarithms (e.g. small-x, mass threshold and leading large-x contributions) present at higher orders. As an example, studies of fits including small-x resummation have recently been done [15, 16], showing significant PDF changes. Since it is these contributions that are often the most dominant at higher orders, this is an especially concerning pitfall in the use of scale variations to estimate MHOUs. Rather more subtle are the challenges encountered when considering and accounting for correlations between fit and predictions using PDFs [10, 12]. These aspects are considered further in Chapter 5, alongside a brief description of structure function results with scale variations using MSHT20 PDFs. The rest of this thesis will then focus on an alternative method to the above based on parameterising the missing higher orders with a set of nuisance parameters, using the available (albeit incomplete) current knowledge [17, 18].

In this thesis, the inclusion of approximate $\mathrm{N^3LO}$ ($\mathrm{aN^3LO}$) components into a global PDF fit will be described within the MSHT20 framework. In particular, we first consider approximations to the $\mathrm{N^3LO}$ structure functions and DGLAP evolution of

the PDFs, including the relevant heavy flavour transition matrix elements. We make use of all available knowledge to constrain an approximate parameterisation of the N^{3}LO theory, including the calculated Mellin moments, low-x logarithmic behaviour and full results where they exist. For the case of hadronic observables (where less N^{3}LO information is available), we include approximate N^{3}LO K-factors which are guided by the size of known NLO and NNLO corrections. Based on the uncertainty in our knowledge of each N^{3}LO function, we obtain a theoretical confidence level (C.L.) constrained by a prior. The corresponding theoretical uncertainties are therefore regulated by our theoretical understanding (or lack thereof). Applying the above procedure, we have performed a full global fit at approximate N^{3}LO, with a corresponding theoretical uncertainty (from MHOs) included within a nuisance parameter framework. At present we assume that the majority of this uncertainty is due to the missing information at N^{3}LO, but that some is associated with orders even beyond this, most obviously further effects due to small-x resummation. We will discover that, indeed, the results support this interpretation. As will be discussed, adopting this procedure allows the correlations and sources of uncertainties to be easily controlled. The preferred form of the aN^{3}LO corrections is determined from the fit quality to data, subject to theoretical constraints from the known information about higher orders. This study is the first of its kind and has been submitted to a journal for publication, however all text and figures (unless stated otherwise) within this thesis have been written/produced by the author.

The outline of this thesis is as follows. Chapters 2 to 4 lay the foundations for the work undertaken in this thesis by providing a general overview of the Standard Model, describing the relevant aspects of Deep Inelastic Scattering (DIS) theory and finally assessing the current landscape of modern PDF sets, with a particular focus on MSHT20. Building on these discussions, in Chapter 5 we breifly explore a scale varia-

tion approach to theoretical uncertainties and subsequently present a formalism for the inclusion of these uncertainties via nuisance parameters in a PDF fit. In Chapter 6 we describe the structure functions up to N^{3}LO and their role in QCD calculations. In Chapter's 7, 8 and 9 we present our approximations for the N^{3}LO splitting functions, transistion matrix elements and coefficient functions, while in Chapter 10 we present the K-factors at aN^{3}LO. In Chapter 11 we present the MSHT aN^{3}LO PDFs with theoretical uncertainties and analyse the implications of the approximations in terms of a full MSHT global fit. Chapter 12 contains examples of using these aN^{3}LO PDFs in predictions up to N^{3}LO. In addition, Chapter 13 provides an analysis of aN^{3}LO PDFs with currently available dijet LHC data, in contrast to inclusive jet data in the standard MSHT20 aN^{3}LO set and explores the effect of SeaQuest data [19] at high-x. Finally in Chapter 14 recommendations for how to best utilise these PDFs will be presented, and the work presented in this thesis is summarised in Chapter 15.

Chapter 2.

The Standard Model

The Standard Model of Particle Physics (SM) is an evolving theory which describes the universe from its fundamental constituents. Over the course of the 20th century, significant advances were made in the formulation of the SM which have elicited a wealth of discoveries. From JJ Thompson's discovery of the electron at the turn of the 20th century [20], the timeline of the particle physics developed with Rutherford's early atomic model around a decade later [21], shortly followed by Bohr's improved model [22] which led to the development of Quantum Mechanics by some of the greatest minds of the century. With the next 50 years seeing a boom in particle physics experiments fuelling the further development of the SM, by the 1970's the modern description of QCD was presented [23].

The particles outlined in Fig. 2.1 summarise the modern day picture of the SM and are mathematically described by Quantum Field Theory (QFT) which in many ways forms the backbone of the SM. The general idea of QFT (i.e. describing quantum fields) can be achieved via a path integral formalism of Lagrangian mechanics and the

$$
\begin{aligned}
\text{Quarks}: &\quad \begin{pmatrix} u \\ d \end{pmatrix} \quad \begin{pmatrix} c \\ s \end{pmatrix} \quad \begin{pmatrix} t \\ b \end{pmatrix} \\
\text{Leptons}: &\quad \begin{pmatrix} e \\ \nu_e \end{pmatrix} \quad \begin{pmatrix} \mu \\ \nu_\mu \end{pmatrix} \quad \begin{pmatrix} \tau \\ \nu_\tau \end{pmatrix} \\
\text{Vector Bosons}: &\quad \gamma,\ W^{\pm},\ Z^0,\ g \\
\text{Scalar Bosons}: &\quad H
\end{aligned}
$$

Figure 2.1.: Summary of constituents which make up the Standard Model (SM). The top two lines contain the three generations of fermionic matter present in the SM arranged into doublets. Note that the list of antifermions is not listed here, these are denoted by $\bar{f}$ for all quarks and neutrinos and by an opposite charge in the case of the electron, muon and tau leptons. The bottom two lines display the bosonic matter contained within the SM which facilitate the interactions and dynamics between particles.

canonical quantisation of Hamiltonian mechanics. More specifically, one can describe the scattering amplitude as

$$
{}_{\text{final}}\langle \phi_b | \phi_a \rangle_{\text{initial}} = \langle \phi_b | \hat{\mathcal{S}} | \phi_a \rangle \tag{2.1}
$$

where $|\phi_a\rangle$ and $|\phi_b\rangle$ are the observed initial and final states of the system and $\hat{\mathcal{S}}$ is a scattering operator which enables the transition from $|\phi_a\rangle$ to $|\phi_b\rangle$. The form of this scattering operator (also called a Dyson-Wick operator) and the states it acts on then depend on the Lagrangian density $\mathcal{L}$ of the system. In particular, in the case where we define the states and operators as evolving via the non-interacting Hamiltonian density $\mathcal{H}_0$ (directly proportional to the non-interacting part of the Lagrangian density $\mathcal{L}_0$), (2.1) can be shown to be,

$$
\langle \phi_b | \hat{\mathcal{S}} | \phi_a \rangle = \langle \phi_b | T \left[\exp\left(-i \int d^4x : \mathcal{H}_I : \right) \right] | \phi_a \rangle, \tag{2.2}
$$

where $T[\dots]$ ensures the proper time ordering[1] of states demanded by the Dyson-Wick expansion, $:\cdots:$ defines the normal ordering convention[2] and $\mathcal{H}_I$ is the interacting Hamiltonian density. The above expression is true in the so-called 'interaction picture' which essentially assumes that we have free fields (evolving with $\mathcal{H}_0$) involved in the occasional interaction assuming $\mathcal{H}_{\text{int}}$ is small.

From (2.2), the relevant Feynman rules can be constructed via the use of Green's functions. The essential ingredient for this mathematical description of nature is the Lagrangian density $\mathcal{L}$. This is where the physics of the SM resides.

An extensive analysis of $\mathcal{L}_{\text{SM}}$ is beyond the scope of this thesis, however we are able to uncover some of the general features of the relevant interactions to this work by considering the free fermionic action describing a spin-$\frac{1}{2}$ particle via a spinor field ψ:

$$S_\psi = \int d^4x \bar{\psi}(i\gamma^\mu \partial_\mu - m)\psi. \tag{2.3}$$

The SM is built on the principle of gauge symmetries, whereby the action of a system is invariant under particular phase transformations. It is trivial to see that under a global phase transformation (assuming a global U(1) type symmetry) $\psi \to e^{i\alpha}\psi$ ($\bar{\psi} \to \bar{\psi}e^{-i\alpha}$), the action S_ψ is unchanged. However when we consider a local U(1)

[1] In very simple terms, the proper time ordering ensures that we account for the ambiguity of integration variables when evolving over time. For example, if we evolve with two integration variables t_1 and t_2, one must consider the case of t_1 or t_2 being the later time and therefore define a time ordered product.

[2] Normal ordering ensures that any terms that are identically 0 due to the contractions of annihilation operators acting on the vacuum are ignored.

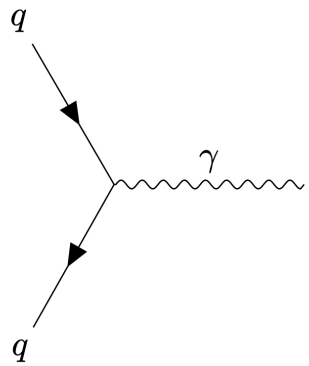

Figure 2.2.: The leading order vertex in QED which represents the electromagnetic coupling of the fermion and photon fields.

transformation (where $\alpha \rightarrow \alpha(x)$) S_ψ is no longer invariant:

$$S'_\psi = \int d^4x \bar{\psi} e^{-i\alpha(x)} (i\gamma^\mu \partial_\mu - m) e^{i\alpha(x)} \psi \tag{2.4}$$

$$= \int d^4x \{\bar{\psi}(i\gamma^\mu \partial_\mu - m)\psi - \bar{\psi}\gamma^\mu \psi \partial_\mu \alpha(x)\} \tag{2.5}$$

$$= S - \int d^4x \bar{\psi}\gamma^\mu \psi \partial_\mu \alpha(x) \neq S_\psi. \tag{2.6}$$

The problematic term here is the derivative which therefore requires modification to demand invariance. Considering a redefinition $\partial_\mu \rightarrow D_\mu = \partial_\mu + igA_\mu$ where A_μ is a vector field added to allow for gauge invariance, one can show that S_ψ is locally phase invariant under the condition that $A_\mu \rightarrow A_\mu + \partial_\mu \alpha(x)/g$. However, before we adapt the action S_ψ we must also consider any other potential terms which are allowed by the local gauge symmetry. By considering the commutator of the covariant derivative D_μ one can show that,

$$[D_\mu, D_\nu] = ig(\partial_\mu A_\nu - \partial_\nu A_\mu) = igF_{\mu\nu}. \tag{2.7}$$

where $F_{\mu\nu}$ is a field strength tensor and is also an invariant quantity.

By constructing a Lorentz-invariant quantity from $F_{\mu\nu}$, we are able to rewrite our action as:

$$S_{\psi}^{QED} = \int d^4x \left(\bar{\psi}(i\gamma^{\mu}\partial_{\mu} - m)\psi - \frac{1}{4}F_{\mu\nu}F^{\mu\nu} - g\bar{\psi}\gamma^{\mu}A_{\mu}\psi \right) \tag{2.8}$$

which defines the action for quantum electrodynamics where this mathematically required vector field A_{μ} is labeled a gauge boson and can be interpreted as the photon. From left to right in (2.8) we have the kinematic term of the fermion, the dynamics of the electromagnetic field (i.e. Mawell's equations) and an interaction term which results in diagrams such as that shown in Fig. 2.2.

Extending this same procedure to non-abelian gauge symmetries, such as the SU(3) symmetry which describes QCD, one must consider the generators of the group more carefully. In this case, our original local gauge transformation becomes more generally $\psi \to e^{i\sum_i^N \alpha_i T_i}\psi$ where T_i are the set of generators corresponding to the particular gauge symmetry ($N = 3^2 - 1 = 8$ generators for SU(3)).

Demanding local gauge invariance once again results in the redefinition:

$$D_{\mu} = \partial_{\mu} + igA_{\mu}^{i}T^{i} \tag{2.9}$$

under the condition that,

$$A_{\mu}^{i} \to A_{\mu}^{i} + \partial_{\mu}\alpha^{i} - gf^{ijk}A_{\mu}^{j}\alpha^{k} \tag{2.10}$$

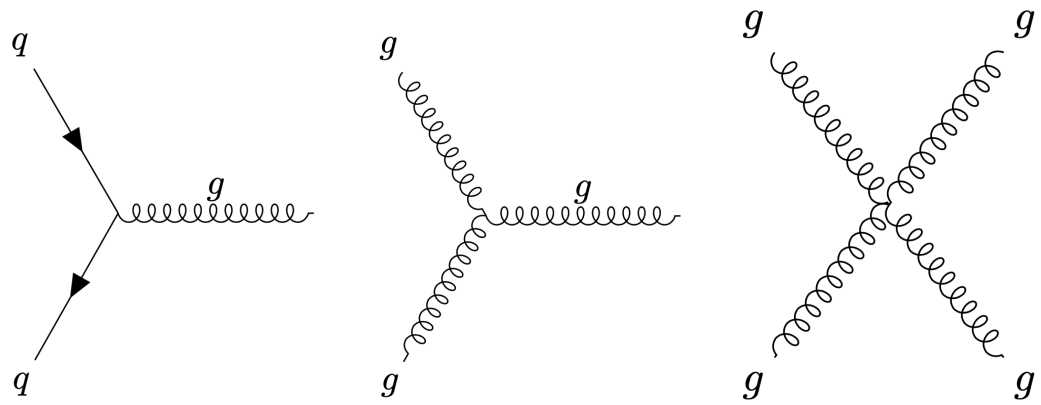

Figure 2.3.: The leading order diagrams for the allowed strong force couplings in QCD. Left is the diagram displaying the coupling of the gluonic and fermionic fields, whereas the middle and right diagrams represent the three and four point self-interactions that define the gluonic field strength.

where f^{ijk} are the structure constants for SU(3) defined by $[T_i, T_j] = if_{ijk}T_k$. Finally, following the same procedure as for the abelian QED case one can find that,

$$[D_\mu, D_\nu] = ig\left(\partial_\mu A^i_\nu T^i - \partial_\nu A^i_\mu T^i - gf^{ijk}A^j_\mu A^k_\nu T^i\right) = igG^i_{\mu\nu}T^i \tag{2.11}$$

where this new field strength tensor allows for three and four point interactions between the vector fields A^i_μ when constructing the Lorentz invariant quantity $G^i_{\mu\nu}G^{\mu\nu}_i$. These interactions are represented in the centre and right diagrams of Fig. 2.3.

Using these ingredients one can construct the QCD gauge invariant action S^{QCD}_ψ as,

$$S^{QCD}_\psi = \int d^4x \left(\bar{\psi}(i\gamma^\mu\partial_\mu - m)\psi - \frac{1}{4}G^i_{\mu\nu}G^{\mu\nu}_i - g\bar{\psi}T^i\gamma^\mu A^i_\mu\psi\right) \tag{2.12}$$

where similar to the QED case, from left to right we have the kinematics of the fermion field, the QCD field strength and an interaction term between the fermionic and gluonic fields (represented in the left diagram of Fig. 2.3).

In the context of SU(3), these vector fields/gauge bosons are interpreted as the set of allowed 8 variations of gluons (for each allowed combination of colour charge). Furthermore, the three and four point self-interactions of these gluons are what give rise to the asymptotic nature of the strong force and are ultimately the foundation of why QCD predictions are currently unable to be calculated from first principles.

At this point in the discussion we have provided a general overview of the procedures involved in deriving the form of the fermionic content of the SM Lagrangian by demanding gauge invariance under U(1) and SU(3) which describe QED and QCD respectively. In performing these exercises, we saw the introduction of the photon (A_μ) and a set of gluons (A^i_μ) to facilitate the local gauge invariances as gauge bosons. However, to complete our discussion of fermionic interactions within the SM we must also consider the third force which enters the SM, namely the eletroweak force (described by $\mathrm{SU}(2) \otimes \mathrm{U}(1)$). For a more in-depth discussion the reader is referred to the following references [24–26]. Following the familiar form of gauge transformations, a fermion field transforms as,

$$\psi \to \left(e^{-i\tau_k \omega_k(x)} + e^{-iY\alpha(x)} \right) \psi \tag{2.13}$$

where τ_k (a set of 2×2 matrices) and Y (a constant) are the generators of SU(2) and U(1) respectively. Following convention, we will define the covariant derivative with two new vector fields,

$$D^{\mathrm{EW}}_\mu = \partial_\mu - ig\tau^k W^k_\mu(x) - ig' Y B_\mu(x) \tag{2.14}$$

$$W^i_\mu \to W^i_\mu + \partial_\mu \omega^i - g\epsilon^{ijk} W^j_\mu \omega^k \tag{2.15}$$

$$B_\mu \to B_\mu + \partial_\mu \alpha \tag{2.16}$$

where W_k^μ and B^μ are the gauge fields corresponding to the SU(2) and U(1) groups respectively and ϵ^{ijk} are the structure constants for SU(2) defined by $[\tau_i, \tau_j] = i\epsilon_{ijk}\tau_k$[3]. The EW Lagrangian density is then:

$$\mathcal{L}_{\text{EW}} = \bar{\psi}(i\gamma^\mu D_\mu^{\text{EW}} - m)\psi - \frac{1}{4}W_{\mu\nu}^k W_k^{\mu\nu} - \frac{1}{4}B_{\mu\nu}B^{\mu\nu} \tag{2.17}$$

Summing up (2.8), (2.12) and (2.17) we can construct the Lagrangian density for a fermion field ψ which interacts with the three forces described by the SM.

So far we have neglected any gauge boson mass terms of the form $m^2\ A_\mu A^\mu$ in writing the Lagrangian densities. The reason for this is that terms of this form break the local gauge invariance required and contradict experimental observations. In order to allow for these terms to exist mathematically, we must consider the presence of a scalar field ϕ (namely, the Higgs field) which has gauge invariant transformations under $\text{SU}(2) \times \text{U}(1)$. In its vacuum state, this field can be described by a conventional choice of phase (the unitary gauge) as:

$$\langle \phi \rangle = \frac{1}{\sqrt{2}} \begin{pmatrix} 0 \\ v \end{pmatrix} \tag{2.18}$$

[3] ϵ^{ijk} is the Levi-Civita symbol.

where v is the vacuum expectation value of the Higgs field. From here we can introduce excitations $h(x)$ about the minimum of the vacuum,

$$\langle \phi \rangle = \frac{1}{\sqrt{2}} \begin{pmatrix} 0 \\ v + h(x) \end{pmatrix}. \tag{2.19}$$

Expanding the kinetic term for this field under the EW covariant derivative $\left| D_\mu^{\mathrm{EW}} \phi \right|^2$, one is able to naturally uncover interactions of the gauge boson fields with the vacuum state of the Higgs field. The gauge boson mass terms then arise from $\left| D_\mu^{\mathrm{EW}} \phi \right|^2$ evaluated at the vacuum expectation value:

$$\mathcal{L}_{\mathrm{Higgs}} = \frac{1}{2}\partial^\mu h\, \partial_\mu h + \frac{1}{4}(v+h)^2(g'^{\,2} B_\mu B^\mu + g^2 W_\mu^k W^{\mu,k} - 2g' g B_\mu W^{\mu,3}) \\ - \frac{1}{8}\lambda(h^2 + 2vh)^2 \tag{2.20}$$

where we can further interpret the mass eigenstates of the vector bosons as:

$$W_\mu^\pm = \frac{1}{\sqrt{2}}(W_\mu^1 \mp i W_\mu^2) \qquad \text{with mass} \quad m_W = g\frac{v}{2} \tag{2.21}$$

$$Z_\mu = \frac{1}{\sqrt{g^2 + g'^2}}(g W_\mu^3 - g' B_\mu) \qquad \text{with mass} \quad m_Z = \sqrt{g^2 + g'^2}\frac{v}{2} \tag{2.22}$$

$$A_\mu = \frac{1}{\sqrt{g^2 + g'^2}}(g' W_\mu^3 + g B_\mu) \qquad \text{with mass} \quad m_A = 0. \tag{2.23}$$

With these redefinitions, the covariant derivative becomes,

$$D_\mu = \partial_\mu - i\frac{g}{\sqrt{2}}(W_\mu^+ T^+ + W_\mu^- T^-) - \frac{i}{\sqrt{g^2 + g'^2}} Z_\mu (g^2 T^3 - g'^2 Y) \\ - i\frac{g g'}{\sqrt{g^2 + g'^2}} A_\mu (T^3 + Y) \tag{2.24}$$

where the electromagnetic interaction is defined by the electric charge $e = gg'/\sqrt{g^2 + g'^2}$ and the quantum number $Q = T^3 + Y$, where $Q = -1$ for the electron.

Essentially by introducing a scalar field and choosing a vacuum expectation value, we are able to spontaneously break the electroweak gauge symmetry and uncover gauge invariant mass terms for the vector bosons. Furthermore, the extra terms added onto (2.20) from the excitation $h(x)$ then describe interactions of the Higgs field with itself i.e. $HH \to HH$, the mass of the Higgs boson $m_h = \sqrt{\lambda}v$ and the interactions with vector bosons i.e. $ZZ \to H$, $ZZ \to HH$, $W^+W^- \to H$ or $W^+W^- \to HH$.

With the mass of the gauge bosons reconciled, in general we also gain terms of the form $g_H\bar{\psi}\psi\phi$ which can resolve the invariance of fermion masses. However, before we tackle terms involving fermions we must discuss the chirality of the $\mathrm{SU}(2) \otimes \mathrm{U}(1)$ gauge group. For the purposes of this thesis, the upshot of this is that the weak force only couples to fields with a particular projection value of the spin onto the momentum unit vector. This property is called handedness with the left and right handed states corresponding to the two possible projections i.e. against or with the direction of momentum. Weak interactions violate parity invariance meaning that left and right handed particles are treated differently and therefore belong to different representations of the $\mathrm{SU}(2)_L$ group. Due to this, Leptons and Quarks transform as a left-handed weak doublet and right-handed weak iso-singlet representations. If we restrict our discussion to the electron e and a massless neutrino ν_e, we can build these representations as:

$$\psi_L = \begin{pmatrix} \nu_e \\ \\ e_L \end{pmatrix} \qquad \psi_R = e_R \tag{2.25}$$

where the subscripts denote the left (L) and right (R) handedness of the particles. The covariant derivative displayed in (2.14) under these representations then becomes:

$$D_\mu^{\mathrm{EW}}\psi_L(x) = \left(\partial_\mu - ig\tau_k W_\mu^k(x) - ig'YB_\mu(x)\right)\psi_L(x) \tag{2.26}$$

$$D_\mu^{\mathrm{EW}}\psi_R(x) = \left(\partial_\mu - ig'YB_\mu(x)\right)\psi_R(x) \tag{2.27}$$

Since the left and right handed particles have this behaviour, in order to recover a mass term in the Lagrangian, we must consider a gauge invariant interaction with the Higgs field as,

$$\mathcal{L}_{e,\phi} = -\sqrt{2}\lambda_e\left[\bar{\psi}_L(x)\phi(x)\psi_R(x) + \bar{\psi}_R(x)\phi^\dagger(x)\psi_L(x)\right] \tag{2.28}$$

$$= -\lambda_e(v+h(x))\left[\bar{e}_L(x)e_R(x) + \bar{e}_R(x)e_L(x)\right] = -\lambda_e(v+h(x))e\bar{e} \tag{2.29}$$

where as before, an interaction of the electron with the vacuum expectation value reveals a mass term with $m_e = \lambda_e v$, as well as an interaction with the Higgs field.

Extending this treatment to the quark representations, we have the left and right handed quarks as:

$$\psi_L^1 = \begin{pmatrix} u \\ d \end{pmatrix}_L \qquad \psi_L^2 = \begin{pmatrix} c \\ s \end{pmatrix}_L \qquad \psi_L^3 = \begin{pmatrix} t \\ b \end{pmatrix}_L \tag{2.30}$$

$$\psi_R^{1+} = u_R \qquad \psi_R^{2+} = c_R \qquad \psi_R^{3+} = t_R \tag{2.31}$$

$$\psi_R^{1-} = d_R \qquad \psi_R^{2-} = s_R \qquad \psi_R^{3-} = b_R \tag{2.32}$$

where all 3 families of quark representations have an identical treatment but with different masses. Analogous to (2.28) we can also then write,

$$\mathcal{L}_{quark,\phi} = -\sqrt{2}\sum_{i,j}^{N=3}\Big[\bar{\psi}_L^i \eta_{ij}^- \phi \psi_R^{j,-} + \bar{\psi}_L^i \eta_{ij}^+ \phi^c \psi_R^{j,+} + \bar{\psi}_R^{j,-} \eta_{ji}^{*-} \phi^c \psi_L^i + \bar{\psi}_R^{j,+} \eta_{ji}^{*+} \phi \psi_L^i\Big] \quad (2.33)$$

where $\phi^c = i\sigma_2\phi^\dagger$ and η_{ij} describes the mixing of flavour states i.e. across quark generations into mass eigenstates. Using (2.18), we are able to define the mass matrices $\vec{m}^{\pm} = v\vec{\eta}^{\pm}$ which can be diagonalised by bi-unitary transformations of the flavour eigenstates. It is this mixing of weak interaction states which yields the Cabibbo-Kobayashi-Maskawa (CKM) matrix [27,28]. Note that a similar derivation can be done for the leptons when considering neutrinos as massive particles which gives rise to the Pontecorvo-Maki-Nakagawa-Sakata (PMNS) matrix [29,30].

Thus far this overview has revealed general features of the SM which will form the foundation of the theory that is relevant to this thesis. Specifically, this work is primarily concerned with the quark content of the SM and their corresponding couplings to gauge bosons facilitating the weak nuclear force ($W^{\pm}$, Z) and strong force (g). In particular for Deep Inelastic Scattering (DIS), discussed in Chapter 3, the QCD couplings of the quarks and gluons coming from the definitions of (2.9) and (2.11) give rise to the splitting functions. From these vertices one can build a picture of how higher order diagrams i.e. next-to-leading order (NLO), next-to-next-to-leading order (NNLO) in the strong coupling constant α_s can be built up. These diagrams are of particular importance, as one of the main goals of this thesis is to parameterise and estimate the effects from unknown higher orders in QCD perturbation theory.

Finally, to conclude this chapter we will revisit the colour self-interactions discovered in the form of $G^{\mu\nu}$ (see (2.11)). As mentioned, the purely gluonic interactions give rise to an extra term in the QCD potential which facilitates the *confinement* and *asymptotic freedom* properties of the strong force. To help understand this, we can write a toy equation as

$$V(r) \propto \frac{\alpha}{r} + kr \qquad \text{with} \quad r > 0, \tag{2.34}$$

where r is the separation distance between two strongly interacting partons (i.e. quarks and gluons). Without self-interactions we recover a force much like that found for QED in (2.7) whereby the potential falls off as described by the first term in (2.34). However when self-interactions are considered, the second term in (2.34) must be taken into account. This extra term with $k > 0$ can be physically interpreted as demanding an infinite amount of energy to separate two strongly interacting partons, a phenomenon termed *confinement*. On the other side of the spectrum, at very short distances (high energies), (2.34) becomes more Coulomb-like ($\propto 1/r$). However, at these high energies, the colour charge is suppressed ($\alpha \ll 1$) and the quarks become 'free', which gives rise to *asymptotic freedom*.

Interpreting this behaviour in terms of energy i.e. short distances $\rightarrow$ high-Q^2 and long distances $\rightarrow$ low-Q^2, one can also gain some understanding as to how logarithmic divergences can occur in QCD in the ultra-violet (UV) and infra-red (IR) regimes. For example, when considering higher order integrals of the form $\propto \int_0^\infty dQ^2 1/Q^2 \rightarrow \infty$ without any regularisation of the high energy (UV) limit. Conversely if we consider a radiative correction to a cross section (as will be done in Chapter 3 in the case of a quark emitting a gluon), these higher order corrections include terms of the form $\propto d\kappa^2 1/\kappa^2$ where κ can be interpreted as a tranverse momentum scale, which diverge

as $\kappa \to 0$. Since the limit of $\kappa \to 0$ is in the low energy domain, these are termed IR divergences (or equivalently collinear/soft divergences due to the collinear/soft nature of the emission).

Renormalisation is a common procedure to regularise the UV divergences in the SM which involves regulating the theory by introducing a non-physical scale termed a renormalisation scale μ_R. As this variable is non-physical, observables such as cross sections or structure functions (discussed in Chapter 3) are forbidden to depend on this scale[4]. Within the procedure of renormalisation, parameters of the SM such as the gauge couplings inherit a scale dependence governed by the renormalisation group equation (RGE). In terms of the strong coupling constant α_s, this can be written as:

$$Q^2 \frac{\partial \alpha_s}{\partial Q^2} = \beta(\alpha_s) \tag{2.35}$$

where $\beta(\alpha_s)$ is a perturbatively calculable quantity currently known up to N^{3}LO in α_s. After renormalisation, one can show that for an SU(3) gauge coupling,

$$\beta(\alpha_s) = -2\left(11 - \frac{2}{3}n_f\right)\frac{\alpha_s^2}{4\pi} \tag{2.36}$$

where for $n_f < 16$, $\beta(\alpha_s) < 0$, which without any regularisation from massive gauge bosons, leads to the properties of confinement and asymptotic freedom described above. Specifically, $\alpha_s \to \infty$ as $Q^2 \to 0$ and $\alpha_s \to 0$ as $Q^2 \to \infty$ yielding a decoupling of the quarks and gluons at high-Q^2.

Looking closely at the low-Q^2 regime, we observe that our perturbation order parameter α_s becomes large and therefore leads to the breakdown of perturbative QCD. As discussed earlier, the magnitude of energy needed to dissociate strongly coupled

[4] In practice there is a varying level of scale dependence left over in all physical observables due to the truncation of perturbative calculations in QCD.

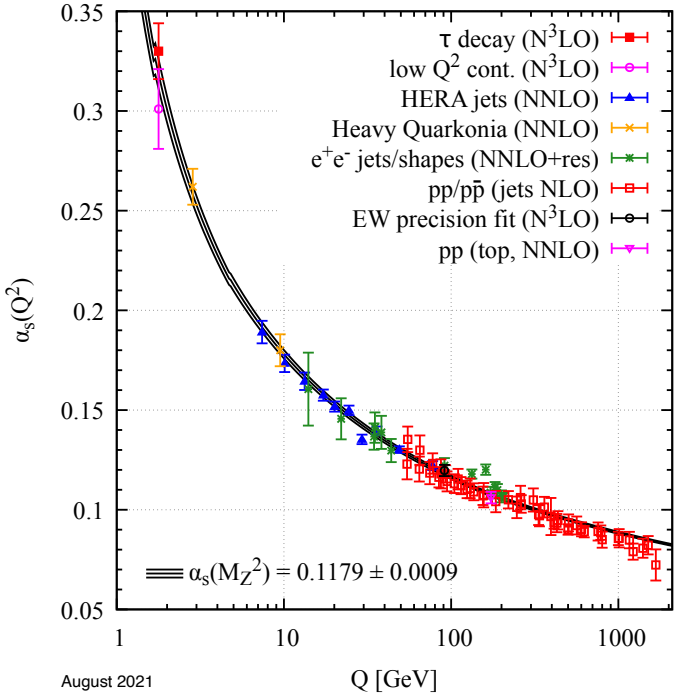

Figure 2.4.: A summary of experimental extractions of the strong coupling constant (α_s) as a function of energy [31].

partons at these long distances becomes so large that the energy of the incoming lepton in DIS acts to spawn more coloured particles which then combine into stable hadronic states (*hadronisation*). Note that for QED and electroweak couplings we find that $\beta > 0$ which means at low energy scales $\alpha \ll 1$ and perturbation theory can be used without concern.

There are many different experiments which contribute to the world average of α_s. The determinations from different experiments are extracted at different values of Q^2 and therefore experimentally describe asymptotic freedom and confinement phenomena (at high and low Q^2) as in Fig. 2.4. It is these results and the theoretical prescriptions described above that emphasize the need for phenomenological models of hadrons.

In the next chapter, we focus on reviewing the theory of hadrons from a perspective that will link together results from experiments and the fundamental theory discussed in this chapter. We will begin our journey with a broad theoretical picture of deep inelastic scattering (DIS) processes and move forward by motivating the necessity for parton distribution functions (PDFs).

Chapter 3.

Deep Inelastic Scattering

The theory of hadronic matter such as protons and neutrons involves the notion that these particles are not fundamental. In other words, hadrons are composite particles which are constructed by combinations of quarks and gluons (as discussed in Chapter 2). This concept naturally led to the influx of collision experiments in particle physics as an attempt to break these hadrons apart and glimpse inside. To this day, Deep Inelastic Scattering (DIS) experiments have remained one of the most powerful tests of perturbative QCD. These processes are discussed within this chapter and involve the inelastic collision of a lepton probe with a hadron (most commonly an electron-proton collision) at such high energies that perturbative QCD is valid.

3.1. The Parton Model

To paint a clearer picture of how QCD interactions are dealt with, we consider the case of deep inelastic lepton-proton scattering mediated by the exchange of a virtual

photon γ:

$$e(p_1) + H(K) \rightarrow e(p_2) + X \tag{3.1}$$

where H and X are the initial and final state protons respectively and the differential cross section can be written as,

$$\frac{d^3\sigma}{d^3p_2} = \frac{1}{4E_1M}\,\frac{1}{(2\pi)^3 2E_2}\sum_X (2\pi)^4\,\delta^4(q + K - p_X)\,\frac{1}{2}\overline{\sum}|\mathcal{M}|^2. \tag{3.2}$$

Using the usual Feynman rules, we can calculate the matrix element of the amplitude as,

$$i\mathcal{M} = (ie)^2\bar{u}(p_2)\gamma^\mu u(p_1)i\frac{-g_{\mu\nu}}{q^2}\langle X|J_h^\nu|H(K)\rangle, \tag{3.3}$$

where J_h^ν is the hadronic current that transforms H into X, e is the coupling strength of the leptonic current and q is the 4-momentum transfer carried by the γ probe. Summing and averaging over spins and applying appropriate trace theorems we arrive at,

$$\sum_{e^-spins}|\mathcal{M}|^2 = \frac{e^4}{(q^2)^2}L_{\mu\nu}\langle H(K)|J_h^\mu|X\rangle\langle X|J_h^\nu|H(K)\rangle \tag{3.4}$$

where $L_{\mu\nu}$ is the leptonic tensor given by:

$$L_{\mu\nu} = 4(p_{1,\mu}p_{2,\nu} + p_{1,\nu}p_{2,\mu} - g_{\mu\nu}p_1 \cdot p_2). \tag{3.5}$$

Further to this, combining (3.2) and (3.4) we are able to collect all hadronic terms into a hadronic tensor,

$$W_H^{\mu\nu} = \frac{1}{4\pi}\sum_X (2\pi)^4 \delta^4(q + K - p_X)\langle H(K)|J_h^\mu|X\rangle\langle X|J_h^\nu|H(K)\rangle. \tag{3.6}$$

When factoring the cross section in this way one can observe that $L_{\mu\nu}$ describes a clean leptonic signal, while $W_H^{\mu\nu}$ encapsulates the more complicated electromagnetic interaction with the proton $H(K)$.

Analysis of the Lorentz structure of $W_H^{\mu\nu}$ allows us to write a general form[1]:

$$W_H^{\mu\nu} = \left(-g^{\mu\nu} + \frac{q^\mu q^\nu}{q^2}\right) W_1 + \left(K^\mu - \frac{K\cdot q}{q^2}q^\mu\right)\left(K^\nu - \frac{K\cdot q}{q^2}q^\nu\right) W_2, \tag{3.7}$$

where all the necessary Lorentz invariance is accounted for in the pre-factors of $W_{1,2}$ which are completely general functions describing the structure of the hadron. Furthermore, performing the contraction of $L_{\mu\nu}W_H^{\mu\nu}$ we obtain,

$$L_{\mu\nu}W_H^{\mu\nu} = 4Q^2 W_1 + 2m_H^2(4E_1E_2 - Q^2)W_2, \tag{3.8}$$

where $Q^2 = -q^2$, m_H is the hadron mass and $E_{1,2}$ are the incoming and outgoing lepton energies. At this point it is useful to define the quantities:

$$\nu = K\cdot q, \qquad x = \frac{Q^2}{2\nu}, \qquad y = \frac{\nu}{K\cdot p_1} \tag{3.9}$$

[1] The true general form consists of 6 terms with different Lorentz pre-factors, however all but two can be left out of this equation due to parity invariance, symmetry considerations and current conservation at the vertex demanding $q_\mu W^{\mu\nu} = q_\nu W^{\mu\nu} = 0$.

where in the hadronic rest frame ν is a measure of the energy transfer, x is the fraction of the proton momentum carried by the parton involved in the collision and y is a measure of the inelasticity (i.e. the fractional energy lost by the leptonic probe).

Rewriting (3.8) in terms of the variables x, y and ν reveals

$$L_{\mu\nu}W_H^{\mu\nu} = 8E_1M\left(xyW_1 + \frac{1-y}{y}\nu W_2\right)\left[1+\mathcal{O}\left(\frac{M^2}{Q^2}\right)\right]. \tag{3.10}$$

Moving forward, one is able to incorporate this result into (3.2) and write

$$\frac{d^2\sigma}{dxdy} = \frac{4\pi\alpha^2}{Q^2}2ME_1\left(xy^2\,F_1(x,Q^2) + (1-y)\,F_2(x,Q^2)\right)\left[1+\mathcal{O}\left(\frac{M^2}{Q^2}\right)\right] \tag{3.11}$$

where $F_1(x,Q^2) = W_1(x,Q^2)$ and $F_2(x,Q^2) = \nu W_2(x,Q^2)$ are structure functions which describe the structure of the proton as 'seen' by the virtual photon.

3.2. Electron-quark Scattering

In an attempt to provide some insight into the interpretation of these structure functions, we can consider the case of electron-positron annihilation, whereby the differential cross section reads as,

$$\frac{d\sigma}{dQ^2} = \frac{1}{16\pi\hat{s}^2}\,2e_q^2e^4\,\frac{\hat{t}^2+\hat{u}^2}{\hat{s}^2} \tag{3.12}$$

The above cross section is related to $e^-q \to e^-q$ scattering by a crossing symmetry. Therefore by redefining the Mandelstam variables in (3.12), one can show

$$\frac{d\sigma}{d\hat{t}} = \frac{1}{16\pi\hat{t}^2}\,2e_q^2e^4\,\frac{\hat{s}^2+\hat{u}^2}{\hat{t}^2} \tag{3.13}$$

where $\hat{s} = (p_1 + \xi K)^2 = 2\xi p_1 K = \xi Q^2/xy$, $\hat{t} = (p_1 - p_2)^2 = q^2 = -Q^2$, $\hat{u} = (\xi K - p_2)^2 = \hat{s}(y-1)$ and ξ is the proportion of proton momentum K carried by the incoming parton. Writing (3.13) in terms of x and y we can write,

$$\frac{d\sigma}{dy} = \frac{2\pi e_q^2}{Q^4}\alpha^2\, 2m_H E_1 x \left[1 + (1-y)^2\right] \tag{3.14}$$

where $\alpha = e^2/4\pi$. Finally, $x = \xi$ must be true in order to ensure the outgoing quark is on-shell[2]. This allows (3.14) to be rewritten as

$$\frac{d^2\sigma}{dxdy} = \frac{4\pi\alpha^2}{Q^4}\, 2m_H E_1 \left[xy^2 + 2x\,(1-y)\right] \frac{1}{2} e_q^2 \delta(x-\xi) \tag{3.15}$$

where comparing with (3.11) one can observe,

$$\begin{aligned} F_1(x, Q^2) &= \frac{1}{2} e_q^2 \delta(x-\xi), \\ F_2(x, Q^2) &= x\, e_q^2 \delta(x-\xi), \end{aligned} \tag{3.16}$$

which in turn defines the *Callan-Gross relation* as $F_2 = 2xF_1$[3] [32].

The result in (3.16) can be interpreted as the structure functions providing information about a single constituent quark at $x = \xi$. Furthermore, since the structure functions contain a distribution across all momentum fractions of a quark constituent, we can further generalise (3.16) to sum over all quarks weighted by the probability distribution of each quark constituent:

$$F_2(x, Q^2) = 2x\, F_1(x, Q^2) = \sum_{q,\bar{q}} \int_0^1 d\xi q(\xi) x\, e_q^2 \delta(x-\xi) = \sum_{q,\bar{q}} e_q^2 x q(x) \tag{3.17}$$

[2] Assuming a massless quark, $p_2^2 = (p_1 + q)^2 = q^2 + 2p_1 \cdot q = -2p_1 \cdot q(x - \xi) = 0$.
[3] This relation also confirms the spin-1/2 nature of partons.

where $q(x)$ are the parton distribution functions (PDFs) which describe the probability of probing a particular constituent of the target proton.

Additionally the PDFs are subject to extra constraints with regards to the conservation of momenta and flavour,

$$\int_0^1 dx \sum_i x f_i(x, Q^2) = 1, \tag{3.18}$$

$$\int_0^1 dx u_V(x, Q^2) = 2 \qquad \int_0^1 dx d_V(x, Q^2) = 1. \tag{3.19}$$

The constraint in (3.18) demands that the momentum of all quarks and antiquarks found inside the proton adds up to the total momentum of the proton, whereas (3.19) demands the conservation of quark flavour number for the proton[4].

3.3. The Improved Parton Model

In the previous section, the form of (3.17) mathematically defines the naive parton model shown in Fig. 3.1. We observe the structure function describing a parton fluctuating out of the proton with momentum fraction x before being involved in the collision (described by (3.11) and depicted in Fig 3.1). In the lowest order description (i.e. with an idealised point-like interaction) described by (3.17), the structure function is fully characterised by the PDFs. However, as we dive deeper into this model, one can realise that this idealised point-like interaction is a highly inaccurate representation of a particle collision. To improve this 'naive' parton model, one can introduce the

[4]Note that for a neutron these constraints are flipped i.e. $\int_0^1 dx d_V = 2$ and $\int_0^1 dx u_V = 1$.

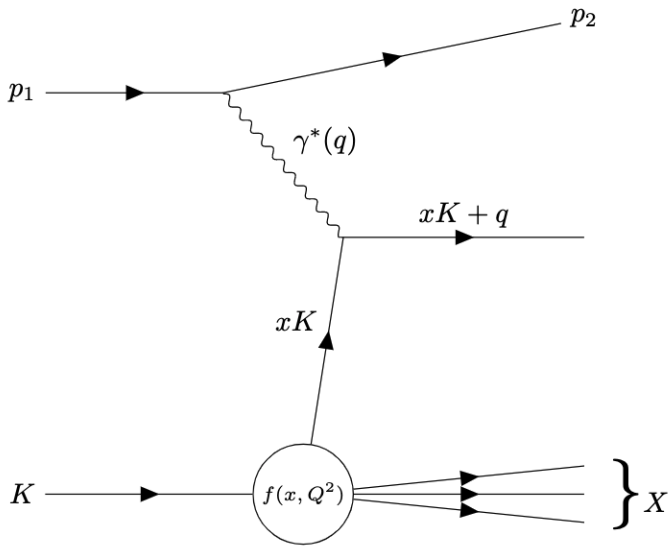

Figure 3.1.: DIS naive parton model. A single parton fluctuates out of the proton with momentum fraction x of the total proton momentum K, while the other partons are considered 'spectators'. This parton is then involved in a hard interaction with a virtual photon.

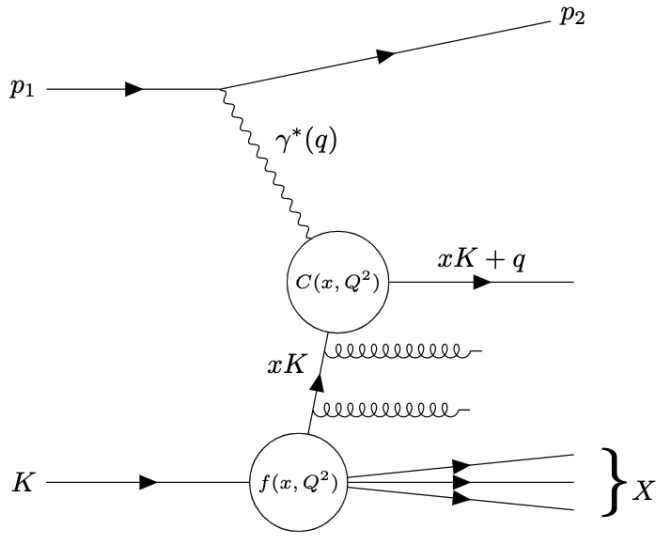

Figure 3.2.: DIS improved parton model.

possibility of QCD interactions at the interaction vertex that are present at higher orders. By generalising Fig 3.1 in this way, we transition to the 'improved' parton model, as depicted in Fig. 3.2.

In this new interpretation, a parton fluctuates out of the proton with probability $f(x, Q^2)$, evolves up to the hard interaction vertex with some non-zero splitting probability and is subsequently involved in a process dependent collision defined at all orders by a coefficient function $C(x, Q^2)$. The separation of these ingredients is performed using the *factorisation theorem* [33] which allows for the PDFs to absorb the non-perturbative regime below some defined factorisation scale μ_f and for the inclusion of perturbatively calculable splitting kernels $P(x)$ to describe the evolution. Similarly to the renormalisation scale μ_r, introduced to regularise UV divergences in calculations, μ_f is able to regularise the collinear IR divergences which occur at timescales longer than $\mathcal{O}(1/\Lambda_{QCD})$[5].

If we consider the case of a quark emitting a gluon before the interaction point in Fig. 3.1 one can show that,

$$\frac{F_2(x, Q^2)}{x} = \sum_{i=\{q,\bar{q}\}} e_i^2 \int_x^1 \frac{dy}{y} f_i(y) \left\{ \delta(1 - \frac{x}{y}) + \frac{\alpha_s}{4\pi} P\left(\frac{x}{y}\right) \ln \frac{Q^2}{\kappa^2} + \dots \right\} \tag{3.20}$$

where κ is a lower cutoff scale which regularises the collinear divergences as $\kappa \to 0$ and $P(x)$ is the splitting function describing the probability for gluon emission. By

[5] The 'hard' scattering physics is defined at timescales $\mathcal{O}(1/Q)$, due to this we assume a large separation between the 'hard' and 'soft' physics.

introducing an unphysical factorisation scale μ_f we can rewrite the above as:

$$\frac{F_2(x,Q^2)}{x} = \sum_{i=\{q,\bar{q}\}} e_i^2 \int_x^1 \frac{dy}{y} f_i(y) \left\{ \delta(1-\frac{x}{y}) + \frac{\alpha_s}{4\pi} P\left(\frac{x}{y}\right) \ln \frac{Q^2}{\mu_f^2} + \frac{\alpha_s}{4\pi} P\left(\frac{x}{y}\right) \ln \frac{\mu_f^2}{\kappa^2} + \dots \right\} \quad (3.21)$$

where the second term in (3.20) has been factored into a calculable and singular part (containing the IR divergence $\kappa \to 0$). Since the bare PDF is not analytically calculable we are able to absorb these divergences into the definition of the PDF:

$$f_i(x,\mu_f^2) = f_i(x) + \frac{\alpha_s}{4\pi} \int_x^1 \frac{dy}{y} f_i(y) P\left(\frac{x}{y}\right) \ln \frac{\mu_f^2}{\kappa^2} \quad (3.22)$$

where this new renormalised PDF has a dependence on the unphysical scale μ_f which was introduced to factor out the collinear divergences. A rather subtle byproduct of this definition is the ability to define a gluon PDF through the different types of potential parton splittings that $P(x)$ can define i.e. $P_{ij}(x)$ where $i,j \in \{q,\bar{q},g\}$. For example from the bare quark PDF, one can define the emission of a gluon, however we must also account for this emitted gluon to be subsequently probed by the hard collision. Therefore at $\mathcal{O}(\alpha_s)$ one is able to define a renormalised gluon PDF.

Combining all this together we are able to write,

$$\frac{F_2(x,Q^2)}{x} = \sum_{i=\{q,\bar{q}\}} e_i^2 \int_x^1 \frac{dy}{y} f_i(y,\mu_f^2) \left\{ \delta(1-\frac{x}{y}) + \frac{\alpha_s}{4\pi} P\left(\frac{x}{y}\right) \ln \frac{Q^2}{\mu_f^2} + \dots \right\} \quad (3.23)$$

where following from the RGE we demand that any dependence on μ_f be cancelled to all orders in perturbation theory. From (3.23) one is able to observe that by the factorisation theorem described above, the PDFs no longer need to be defined at the scale of a particular process Q^2. The significance of separating any process dependent

calculation from the definition of the PDFs is that parton distributions measured in various different processes can be related. This universality is what enables PDF fitting groups to be able to fit to a variety of different datasets that constrain different regions of (x, Q^2), resulting in extremely accurate descriptions of the protons internal structure.

In order to complete our factorised picture of the structure function in (3.23), we must also allow for the dynamics of the high-Q^2 hard process physics to be factored out in terms of a coefficient function.

$$F_2(x, Q^2) = \sum_{i=q,\bar{q},g} C_i(x, Q^2) \otimes f_i(x, Q^2) + \mathcal{O}\left(\Lambda^2/Q^2\right) \tag{3.24}$$

where $\mu_f^2 = Q^2$ and $f_i(x, Q^2)$ is the renormalised PDF from (3.22). Fig. 3.2 displays this factorisation of process-independent ($f(x, Q^2)$) and process-dependent ($C(x, Q^2)$) parts which further demonstrates the universality of PDFs. For example, in a collision such as the LHC the PDFs can be inserted into the cross section calculation as,

$$\sigma_{pp'\to X} = \sum_{i,j\in\{q,\bar{q},g\}} \int dx_p dx_{p'} f_i(x_p, Q^2) f_j(x_{p'}, Q^2) \hat{\sigma}_{pp'\to X} + \mathcal{O}\left(\Lambda^2/Q^2\right) \tag{3.25}$$

where $\hat{\sigma}_{pp'\to X}$ contains the process dependent theory and the PDFs $f_i(x, Q^2)$ are universally determined and inserted here.

3.4. Dokshitzer-Gribov-Lipatov-Alterelli-Parisi (DGLAP)

As mentioned in the interpretation of renormalised PDFs, the universality of PDFs is based upon the fact that PDFs can be evolved to a different scale to which that they are extracted. In a global fit, data points will be extracted at various different energy scales depending on what is experimentally accessible and the energy where different processes occur. Due to this, we must also require a method to evolve the PDFs in Q^2. Conveniently in the previous section, we have already derived a description of renormalised PDFs which now incorporate a scale dependence governed by the renormalisation group equation (since this scale is fictitious and must vanish when considering observable quantities). The PDF evolution is therefore achieved via the Dokshitzer-Gribov-Lipatov-Alterelli-Parisi (DGLAP) equation [34–36],

$$\mu_f^2 \frac{\partial f_i(x,\mu_f^2)}{\partial \mu_f^2} = \sum_{i,j\in\{q,\bar{q},g\}} \frac{\alpha_s(\mu_r^2)}{4\pi} \int_x^1 \frac{dz}{z} P_{ij}\left(\frac{x}{z}\right) f_j(z,\mu_f^2). \tag{3.26}$$

As discussed above, the DGLAP equation is a direct consequence of the renormalisation of soft divergences into the definition of PDFs in (3.22), where μ_f is chosen at some arbitrarily low scale and μ_r is similarly chosen at a much higher scale to cut off UV divergences in the hard cross section and coupling constants.

Notice that in (3.26) we have an upgraded splitting function P_{ij} which includes the sum over multiple parton flavours. This new notation now incorporates potential splittings between all partons including the gluon and it is clear that (3.26) is actually a set of coupled differential equations where the potential splittings of the quark PDFs bring about changes in the gluon and vice versa.

The set of QCD splitting functions discussed here are perturbatively calculable quantities currently known up to NNLO, and later parameterised up to approximate N^{3}LO in Chapter 7. However at leading order in α_s, the individual splitting kernels that facilitate the convolutions in (3.26) are

$$P_{qq} = C_F \left[\frac{1+x^2}{(1-x)_+} + \frac{3}{2}\,\delta(1-x) \right], \tag{3.27}$$

$$P_{qg} = T_R \left[x^2 + (1-x)^2 \right], \tag{3.28}$$

$$P_{gq} = C_F \left[\frac{1+(1-x)^2}{x} \right], \tag{3.29}$$

$$P_{gg} = 2\,C_A \left[\frac{x}{(1-x)_+} + \frac{1-x}{x} + x\,(1-x) \right] + \left(\frac{11}{6}\,C_A - \frac{4}{6}\,T_F \right) \delta(1-x), \tag{3.30}$$

where $C_F = 4/3$, $C_A = 3$, $T_F = n_f\,T_R$, $T_R = 1/2$ and n_f is the number of light quarks kinematically allowed to exist[6].

Tracking back to global PDF fits, the standard procedure is to parameterise initial state PDFs at some low value of Q^2 (as will be discussed in Chapter 4) and subsequently evolve these using the DGLAP equation up (or down – although this is not likely given the low initial scale) to the scale of the process being fit to. There is some ambiguity in how this scale is chosen for certain observables, however a general rule is to choose an

[6]The matching of descriptions across the quark mass thresholds i.e. $n_f \to n_f + 1$ as $Q^2 > m_q^2$, will be discussed in the next section.

appropriate kinematic quantity, for example in DIS fits $\mu_f^2 = \mu_r^2 = Q^2$ is the typical choice.

The application of the DGLAP procedure therefore allows us to truly unlock the full constraining power in global PDF fits and ultimately gives rise to sets of precisely determined universal PDFs which can be used in the particle physics community. The details of these sets are further discussed in Chapter 4.

3.5. General Mass Variable Flavour Number Scheme (GM-VFNS)

In this section we will outline the procedure taken for heavy flavour production in DIS when the heavy quark mass m_h is treated as a hard scale. We begin by fixing the number of light quark flavours (n_f) and expressing all light quark PDFs (and the gluon PDF) in the same manner as discussed above while absorbing the description of heavy quark partons into a Fixed Flavour Number Scheme (FFNS) coefficient function. Setting $\mu_r^2 = \mu_f^2 = Q^2$ and rewriting (3.24) in this way gives,

$$F_2(x,Q^2) = \sum_{\alpha\in\{H,q\}} \sum_{i\in\{q,\bar{q},g\}} C_{\alpha,i}^{\mathrm{FF},\,n_f}(x,Q^2,Q^2/m_H^2) \otimes f_i^{n_f}(x,Q^2) + \mathcal{O}\left(\Lambda^2/m_H^2\right) \quad (3.31)$$

where we have made the dependence on the heavy quark mass scale explicit in the FFNS coefficient function.

By the factorisation theorem, the description in (3.31) must be equivalent to the scenario where the quark mass is a soft scale and is therefore absorbed into the

description of PDFs i.e. there are $n_f + 1$ PDFs, now including a heavy quark PDF.

$$F_2(x,Q^2) = \sum_{\alpha\in\{H,q\}} \sum_{j\in\{H,q,\bar{q},g\}} C_{\alpha,j}^{\text{ZM},\, n_f+1}(x,Q^2) \otimes f_j^{n_f+1}(x,Q^2,Q^2/m_H^2) + \mathcal{O}\left(\Lambda^2/m_H^2\right) \tag{3.32}$$

This narrative is valid in the region that $Q^2 \gg m_h^2$, where the mass of the heavy quark becomes negligible (or more robustly $Q^2 \to \infty$). If one relaxes this constraint on the coefficient function, still describing $n_f + 1$ flavours, one can define the General Mass Variable Flavour Number Scheme (GM-VFNS) in exactly the same way as (3.32) but with $C_{\alpha,j}^{\text{ZM},\, n_f+1} \to C_{\alpha,j}^{\text{VF},\, n_f+1}$. This new description is valid across all Q^2 and in the limit that $Q^2 \to \infty$, must be identical to the ZM-VFNS coefficient function.

Considering (3.31) and (3.32) (in either the ZM-VFNS or GM-VFNS format), there is one extra parton flavour to parameterise in the latter. Applying the factorisation theorem again, one can describe a perturbatively calculable heavy quark via the introduction of transition matrix elements [37, 38] which absorb logarithms in Q^2/m_H^2 as[7]

$$f_j^{n_f+1}(x,Q^2,Q^2/m_H^2) = A_{ji}(Q^2/m_H^2) \otimes f_i^{n_f}(x,Q^2). \tag{3.33}$$

Ignoring higher twist corrections and equating (3.31) and (3.32) (also with (3.33)) one can find the relation:

$$C_{\alpha,i}^{\text{FF},\, n_f}(x,Q^2,Q^2/m_H^2) = C_{\alpha,j}^{\text{VF},\, n_f+1}(x,Q^2) \otimes A_{ji}(Q^2/m_H^2) + \mathcal{O}\left(\Lambda^2/m_H^2\right) \tag{3.34}$$

[7] Strictly speaking, a new scale $\tilde{\mu}$ is introduced into the transition matrix elements from the factorisation theorem, much like how μ_f was introduced for the PDFs. However since the scale at which evolution begins can be chosen to be exactly $\tilde{\mu}^2 = m_H^2$, the matching condition between subsequent flavours reduces to a perturbative calculation in α_s with no logarithms in $(\tilde{\mu}^2/m_H^2)$.

It is the above equation that allows for new expressions to be defined for the coefficient functions. The coefficient functions described by the GM-VFNS procedure allow for the inclusion of smooth interpolations across heavy quark mass thresholds and hold true in the asymptotic limits at each order in perturbation theory. In Chapter 9, the description of the GM-VFNS coefficient functions will be extended beyond the currently known NNLO to include approximate N^3LO effects and later be included into a global PDF fit.

Chapter 4.

Parton Distribution Functions

The QCD parton model presented in Chapter 3 depends heavily on the inclusion of PDFs into structure function calculations. As discussed in Chapter 3, PDFs are non-perturbative quantities that (at present) cannot be derived from first principles[1] and are therefore fit to experimental data.

4.1. Background

In the late 1960's and early 1970's simple models of PDFs were developed [39] by employing limited experimental data, combined with multiple theory considerations. However, as more experimental data became available, the idea of fitting PDFs to a global collection of data emerged. By 1982 PDF fits had become sophisticated enough to be able to determine the shape of the gluon [40, 41] and the foundations were well

[1] See [**?**] for a recent review of Lattice QCD which has potential for shedding light in this area. Or more likely, being able to supplement the current data-driven approach with theoretical lattice determinations for particular quantities in the least constrained (x, Q^2) regions.

established for the first LO PDF fits in 1984 [42, 43]. Due to the universality of PDFs, over the next decade PDF fits enjoyed a wealth of data by adopting the *global* QCD analysis strategy [44] along with an increase in theoretical understanding, with NLO fits becoming the state-of-the-art in 1988 [44–48].

In 1992 the field of PDF fits saw its most influential experiment turn on, the HERA collider at DESY. HERA allowed for an extensive analysis of previously inaccessible regions in (x, Q^2) by colliding 920 GeV protons with $\simeq$ 27.5 GeV electrons in DIS experiments. In 1994 this data was included in the release of the MRS(A) [49] and CTEQ3 [50] PDFs which were then further updated with more precise data from HERA and the Tevatron as and when these became available.

Since this time PDF sets have become more robust by incorporating: PDF uncertainties [51–58], the treatment of heavy flavours [59–61] (see Chapter 3), NNLO theory [62–66] and a wide range of advancements in fitting procedures [67–70] along with a continuously increasing amount of data from global experiments. One source of data which has become progressively more influential in recent years is the LHC, with many LHC datasets now included as standard in modern PDF sets [3, 4, 6, 71]. As we will discuss in this thesis, several high precision datasets from the LHC are extremely important in constraining PDFs especially when considering higher orders than NNLO.

4.2. PDF Determination

In an ideal world one would hope to write down an analytic expression which could describe the Bjorken x dependence of PDFs, whilst also being consistent with the Q^2 evolution predicted from perturbative QCD. However as discussed in previous

MSHT20 Global fit Datasets	
BCDMS μp F_2 [72]	CDF II W asym. [73]
BCDMS μd F_2 [72]	DØ II $W \to \nu e$ asym. [74]
NMC μp F_2 [75]	DØ II $p\bar{p}$ incl. jets [76]
NMC μd F_2 [75]	ATLAS W^+, W^-, Z [77]
SLAC ep F_2 [78,79]	CMS W asym. $p_T > 35$ GeV [80]
SLAC ed F_2 [78,79]	CMS W asym. $p_T > 25, 30$ GeV [81]
E665 μd F_2 [82]	LHCb $Z \to e^+e^-$ [83]
E665 μp F_2 [82]	LHCb W asym. $p_T > 20$ GeV [84]
NuTeV νN F_2 [85]	CMS $Z \to e^+e^-$ [86]
NuTeV νN xF_3 [85]	ATLAS High-mass Drell-Yan [87]
NMC $\mu n/\mu p$ [88]	Tevatron, ATLAS, CMS $\sigma_{t\bar{t}}$ [89–101]
E866 / NuSea pp DY [102]	CMS double diff. Drell-Yan [103]
E866 / NuSea pd/pp DY [104]	LHCb 2015 W, Z [105,106]
HERA ep F_2^{charm} [107]	LHCb 8 TeV $Z \to ee$ [108]
NMC/BCDMS/SLAC/HERA F_L [72,75,79,110–112]	CMS 8 TeV W [109]
	ATLAS 7 TeV jets [113]
CCFR $\nu N \to \mu\mu X$ [114]	CMS 7 TeV $W + c$ [115]
NuTeV $\nu N \to \mu\mu X$ [114]	ATLAS 7 TeV high prec. W, Z [116]
CHORUS νN F_2 [117]	CMS 7 TeV jets [118]
CHORUS νN xF_3 [117]	DØ W asym. [119]
HERA e^+p CC [120]	ATLAS 8 TeV Z p_T [121]
HERA e^-p CC [120]	CMS 8 TeV jets [122]
HERA e^+p NC 820 GeV [120]	ATLAS 8 TeV sing. diff. $t\bar{t}$ [123]
HERA e^-p NC 460 GeV [120]	ATLAS 8 TeV sing. diff. $t\bar{t}$ dilep. [124]
HERA e^+p NC 920 GeV [120]	ATLAS 8 TeV High-mass DY [125]
HERA e^-p NC 575 GeV [120]	ATLAS 8 TeV W + jets [126]
HERA e^-p NC 920 GeV [120]	CMS 8 TeV double diff. $t\bar{t}$ [127]
CDF II $p\bar{p}$ incl. jets [128]	ATLAS 8 TeV W [129]
DØ II Z rap. [130]	CMS 2.76 TeV jet [131]
CDF II Z rap. [132]	CMS 8 TeV sing. diff. $t\bar{t}$ [133]
DØ II $W \to \nu\mu$ asym. [134]	ATLAS 8 TeV double diff. Z [135]

Table 4.1.: Exhaustive list of all datasets included in the MSHT20 standard global fit [3]. The fit results presented in this thesis will be obtained from a fit to all these data unless stated otherwise.

chapters, this is not possible due to the non-perturbative nature of QCD in certain areas of (x, Q^2). In lieu of this idealised theoretical description, modern PDF determination involves assuming an initial parameterisation at some Q_0^2 starting scale and fitting this parameterisation to data. Where as a general rule the value of Q_0^2 should be large enough such that $\alpha_s(Q_0^2)$ remains small enough to preserve the validity of perturbative QCD.

Once these initial parameterisations are chosen, the DGLAP equations (discussed in Chapter 3) are used to evolve the PDFs to different Q^2 values, where the PDFs are convoluted with relevant coefficient functions for each process and used to make theoretical predictions for physical quantities such as structure functions. The results for these physical quantities are then used to fit to experimental data sets to obtain an overall global χ^2 result. An exhaustive list of those included in the current MSHT20 fit is included in Table 4.1.

By calculating the gradients of the χ^2 with respect to the PDF parameters, one is able to adjust the parameters of the fit in order to minimise the global χ^2 value. In order to achieve a final result, this process is iterated with the PDF parameters being altered in the direction of a smaller global χ^2 at each step. The resultant PDF parameterisations are usually provided on computationally efficient (x, Q^2) LHAPDF [136] grids. These grids can be utilised in theoretical calculations to obtain the value of PDFs at any point in (x, Q^2) via interpolation, without the need for any further explicit evolution in Q^2.

The choice of the initial parameterisation naturally represents a model uncertainty in PDF extraction which as we will see, is also sensitive to the exact forms of any aN^{3}LO parameterisation. Although this sensitivity is washed out as the PDFs are evolved to $Q^2 > Q_0^2$, remnants and indirect effects will likely remain. There are several different groups which use variations of the general formalism above extracted with different input parameterisations and methodological choices. The work presented in this thesis is done within the MSHT20 framework which is summarised in the following section.

4.3. MSHT20 Framework

The latest major update from the Mass Scheme Hessian Tolerance (MSHT) collaboration, the MSHT20 PDF set [3], supersedes the previous MMHT14 set [68]. An extended parameterisation is introduced with this update, particularly for the $\bar{d}/\bar{u}$ and strange quark, along with more eigenvector sets to accommodate the extra parameters. The MSHT20 global fit also includes a variety of LHC data, final HERA and Tevatron data and a variety of other datasets summarised in Table 4.1, with almost all included QCD cross sections inserted at NNLO. In particular, all LHC jet data, Z p_T distribution data and top quark cross sections are included with theoretical calculations at NNLO precision [137–139]. In addition to this, electroweak corrections are included wherever possible/required, although these will not be discussed in this thesis.

The MSHT20 framework is built upon parameterising a set of PDFs for all x at an input scale $Q_0^2 = 1\ \text{GeV}^2$ and evolving these input PDFs across a range of Q^2 using the DGLAP evolution equations from Chapter 3. The DIS heavy flavour sector is obtained using the general mass variable flavour scheme based on the TR scheme [60, 140, 141] as described in Chapter 3.

The general form of these input distributions are:

$$xf(x, Q_0^2 = 1\ \text{GeV}^2) = A(1-x)^{\eta} x^{\delta} \left(1 + \sum_{i=1}^{n} a_i T_i^{\text{Ch}}(y(x))\right) \tag{4.1}$$

where T_i^{Ch} are the Chebyshev polynomials in y, with $y = 1 - 2\sqrt{x}$. The latest update to the MSHT framework in [3] uses $n = 6$ in general, with slight variations in the parameterisations for the gluon and the strangeness asymmetry. For completeness

these are:

$$u_V(x,Q_0^2) = A_u(1-x)^{\eta_u}x^{\delta_u}\left(1+\sum_{i=1}^{6}a_{u,i}T_i(y(x))\right) \tag{4.2a}$$

$$d_V(x,Q_0^2) = A_d(1-x)^{\eta_d}x^{\delta_d}\left(1+\sum_{i=1}^{6}a_{d,i}T_i(y(x))\right) \tag{4.2b}$$

$$S(x,Q_0^2) = A_S(1-x)^{\eta_S}x^{\delta_S}\left(1+\sum_{i=1}^{6}a_{S,i}T_i(y(x))\right) \tag{4.2c}$$

$$s_+(x,Q_0^2) = A_{s+}(1-x)^{\eta_{s+}}x^{\delta_{s+}}\left(1+\sum_{i=1}^{6}a_{s_+,i}T_i(y(x))\right) \tag{4.2d}$$

$$s_-(x,Q_0^2) = A_{s-}(1-x)^{\eta_{s-}}\left(1-\frac{x_0}{x}\right)x^{\delta_{s-}} \tag{4.2e}$$

$$(\bar{d}/\bar{u})(x,Q_0^2) = A_\rho(1-x)^{\eta_\rho}\left(1+\sum_{i=1}^{6}a_{\rho,i}T_i(y(x))\right) \tag{4.2f}$$

$$g(x,Q_0^2) = A_g(1-x)^{\eta_g}x^{\delta_g}\left(1+\sum_{i=1}^{4}a_{g,i}T_i(y(x))\right) - A_{g-}(1-x)^{\eta_{g-}}x^{\delta_{g-}} \tag{4.2g}$$

Here we see the familiar form outlined in (4.1) with a couple of exceptions due to the lack of constraining power from data. The parameters A_i, η_i, δ_i, $a_{i,j}$ are left free and determined from a mixture of constraints such as $\bar{d}/\bar{u} \to$ constant as $x \to 0$, the sum rules in (3.19) and (3.18) and most importantly, the fit quality to data. Additionally, the form of the gluon PDF parameterisation includes an extra term which allows extra freedom to the gluon at low-x and is included to improve the fit quality to small-x data [142]. In total, the MSHT20 analysis includes 52 parton parameters contained within (4.2).

With the parameterisation above and the inclusion of new LHC data in the MSHT20 analysis, an increase in the strange quark between $x = 0.001 - 0.3$ is reported compared to the previous iteration. Also due to the inclusion of precision jet data, the high-x gluon exhibits a slight decrease which will be investigated further in Chapter 13 in the

context of aN^{3}LO. As will be seen, the initial parameterisation of the gluon is heavily sensitive to the N^{3}LO effects discussed in this thesis.

Considering the strong coupling constant, the MSHT20 NNLO PDFs prefer a value of $\alpha_s(M_Z^2) = 0.1174 \pm 0.0013$ [143] where in general, jet data prefer a slightly lower value of α_s and the W, Z data prefer it slightly higher. MSHT20 also incorporates the charm and bottom pole masses as $m_c = 1.4$ GeV and $m_b = 4.75$ GeV respectively.

The fitting procedure in the MSHT global fit follows a Hessian method whereby the global minimisation statistic χ^2 is assumed to be quadratic about its minimum. This global minimum is found using the Levenburg-Marquardt method [144, 145] by finding local gradients with respect to the PDF parameters and iteratively moving towards the global minimum. Defining the set of n parameters as $\{a_1, \ldots, a_n\}$ one can write:

$$\chi^2 - \chi_0^2 = \sum_{i,j=1}^{n} (a_i - a_i^0) H_{ij} (a_j - a_j^0) \tag{4.3}$$

where any quantities denoted by 0 are related to the true minima of χ^2 and the Hessian matrix H_{ij} is described by:

$$H_{ij} = \frac{1}{2} \sum_n \frac{\partial^2 \chi_0^2}{\partial a_i \partial a_j} \tag{4.4}$$

Since in general, a derivative of an observable $F(\{a_i\})$ with respect to each PDF parameter a_i is not easily ascertainable, standard linear error propagation is not preferred. Instead the Hessian matrix is diagonalised to obtain eigenvectors and eigenvalues which represent orthogonal linear combinations of the parameters a_i. These eigenvec-

tors are defined by

$$C\,\mathbf{v}_k = \lambda_k \mathbf{v}_k \tag{4.5}$$

where λ_k and $\mathbf{v}_k$ are a set of eigenvalues and eigenvectors and $C = H^{-1}$ is the covariance matrix.

Along with the central MSHT20 NNLO PDF value, the standard NNLO set includes 64 Hessian error PDFs for positive/negative eigenvector directions (i.e. 32 eigenvectors), where pairs of eigenvector sets $S_k^{\pm}$ can be used to span the χ^2 hypersphere. The size of the PDF uncertainties described by the error set e.g. for a 68% confidence level (C.L.) are determined using a dynamical tolerance procedure which adapts the size of $\Delta\chi^2$ in accordance with the fit, rather than being set by some other means (i.e. by hand in an idealised setting). The dynamical tolerance procedure is described in detail in Section 6 of [64], where it was deduced that to accommodate a multitude of data sets in conflict with one another when being included into a global fit, one typically requires an elevated tolerance (i.e. $T > 1$) to produce an adequate level of variation in the fit for a 68% confidence interval and therefore more reliable error estimates. The dynamical tolerance procedure follows from assuming that each χ^2_n for the n^{th} dataset follows a χ^2 distribution with N degrees of freedom (N data points),

$$P_N(\chi^2) = \frac{(\chi^2)^{N/2-1}\, e^{-\chi^2/2}}{2^{N/2}\Gamma(N/2)} \tag{4.6}$$

$$\int_0^{\xi_{68}} d\chi^2 P_N(\chi^2) = \text{erf}(1/\sqrt{2}). \tag{4.7}$$

Starting from the central fit (i.e. at the global minimum χ^2_0), one is able to move along each eigenvector direction ($\pm e_k$) by adjusting the relevant parameters via,

$$a_i = a_i^0 \pm t\, e_{k,i} \tag{4.8}$$

where $e_{k,i}$ is the i^{th} value of the k^{th} eigenvector, a_i^0 are the best fit parameters and t is the tolerance factor to scan across (nominally chosen to be from $t = 1, \ldots, 6$). Once a new minima is found for each value of t, one can plot the change in χ^2_n for each data set n and assess its difference from the global minimum $\chi^2_{n,0}$. Note that due to the interplay between datasets, the minima for each of the individual data sets will most likely not line up with the global fit minimum. Therefore it is possible for χ^2_n to be smaller than $\chi^2_{n,0}$ at some value of $t \neq 0$.

The most probable value for the χ^2 distribution in (4.6) is $\xi_{50} \simeq N$ for a dataset with N data points. As discussed, since the value of $\chi^2_{n,0}$ may be far away from ξ_{50} at the global minimum χ^2_0 (and potentially be outside the 68% confidence interval), it is necessary to rescale $\chi^2_{n,0}$ before defining the 68% C.L. region as,

$$\chi^2_n < \left(\frac{\chi^2_{n,0}}{\xi_{50}}\right) \xi_{68} \tag{4.9}$$

which essentially states that we wish a tolerance value to be chosen as the highest value possible without χ^2_n exceeding the 68% C.L. for each dataset n.

By scanning across values of t in all eigenvector directions, one is able to characterise a data set with its χ^2_n values for each chosen t and its 68% C.L. limit obtained from (4.7). Finally, for each of the eigenvector directions, we choose the value of t at the point where (4.9) is minimally violated for a single dataset and define the final tolerance values as $T = \sqrt{\Delta\chi^2_{\text{global}}}$ at this value of t.

Following from the above, uncertainties on a quantity $F(\{a_i\})$ may be calculated with symmetric errors as,

$$\Delta F = \frac{1}{2}\sqrt{\sum_{k=1}^{n}\left(F(S_k^+) - F(S_k^-)\right)^2} \tag{4.10}$$

or with asymmetric errors by

$$(\Delta F)_+ = \frac{1}{2}\sqrt{\sum_{k=1}^{n}\left(\max\left[F(S_k^+) - F(S_0), F(S_k^-) - F(S_0), 0\right]\right)^2} \tag{4.11}$$

$$(\Delta F)_- = \frac{1}{2}\sqrt{\sum_{k=1}^{n}\left(\max\left[F(S_0) - F(S_k^+), F(S_0) - F(S_k^-), 0\right]\right)^2} \tag{4.12}$$

where S_0 is the central PDF set.

In this thesis, the MSHT20 fitting procedure will be expanded from the description above to include 20 extra N^{3}LO parameters which will parameterise the effects at higher orders in perturbative QCD discussed in Chapter 3. The details of how this expansion is achieved will be examined in detail in Chapter 5.

The later chapters included in this thesis present a selection of theory calculations pertaining to the evolution of initial scale PDFs and the different processes included in the MSHT20 global fit, all of which are extended to approximate N^{3}LO. The quantities discussed are primarily involved in various convolutions initially described in Chapter 3 and explicitly extended to N^{3}LO in Chapter 6. Inside the MSHT20 analysis, Gaussian-Legendre Quadrature is the integration procedure which takes the PDFs, defined on 96 logarithmically spaced points in x_i, and facilitates the convolutions by

computing a weighted sum to approximate an integral as

$$\int dx f(x) \simeq \sum_{i=1}^{96} w_i f(x_i). \tag{4.13}$$

Similarly, when performing the DGLAP evolution described in Chapter 3, the evolution is performed using the same procedure but in Q^2 (also on a logarithmic scale containing 96 points).

When combining these two variables, we naturally have an (x, Q^2) grid description where the PDFs have been numerically calculated at 96 points in both directions. For the PDF central value and for each eigenvector direction, these grids are distributed and made available under the LHAPDF [136] configuration. All modern PDF sets are distributed in this way and therefore LHAPDF provides a consistent and convenient format to use multiple different types of PDFs, without the need for bespoke software for each PDF set.

4.4. Other Modern PDF Sets

In this section we briefly describe the other PDF sets which are included in the latest PDF4LHC21 combination [8], namely the CT18 [4] and NNPDF3.1 [5] PDF sets where in the latter case these PDFs are now superseded by a more up-to-date NNPDF4.0 set [6].

4.4.1. CT18

The latest release of general-purpose PDFs from the CTEQ-TEA (CT) collaboration are the CT18 PDFs [4]. The CT18 NNLO fit includes a total of 3681 data points from 39 experiments including LHC 7 and 8 TeV data, HERA I+II combined data and other default sets included in the previous CT14 release [65]. The approach of the CT18 collaboration is to prioritise including all data points in each dataset in order to provide as wide a kinematic coverage as possible. In performing such an inclusive fit, the CT18 analysis is able to utilise the full constraining power of each dataset and additionally identify regions of disagreement within the data.

The standard procedure for CT is to employ the SACOT-χ heavy quark scheme at NNLO [146] with charm and bottom pole masses of $m_c = 1.3$ GeV and $m_b = 4.75$ GeV respectively. Furthermore, the x-dependence of the CT18 PDFs is parameterised by Bernstein polynomials combined by the customary x^{α} and $(1-x)^{\beta}$ small and large-x factors in order to control the overall parameterisation in these limits. For each parton flavour the CT collaboration include 5-8 independent fitting parameters except for the strangeness PDF which has 4. Additionally, the included parameters are such that the PDFs at large-x are always non-negative to avoid the potential for negative differential cross sections), while a handful of other parameters are constrained by sum rules. The final form of these PDFs is based on 29 parameters and along with the central PDFs, includes 58 Hessian error PDF sets for positive/negative eigenvector directions (i.e. 29 eigenvectors).

The parameterisation is subsequently fit via the minimisation of a global log-likelihood function which quantifies the agreement of the form of the PDFs with the data. Considerations regarding the quality of this global fit are manifested in the overall size of the PDF uncertainties. By investigating the global χ^2 landscape, the CT

collaboration are then able to examine the consistency of fits through enhanced values of χ^2 in regions of (x, Q^2) (a benefit of fitting to the entire kinematic range available for each dataset). Further to this, the size of the uncertainties provided with the CT18 PDFs not only reflects the quality of the fit but is carefully decided based on a detailed analysis of the spread of alternative PDF solutions (with varying functional forms). Therefore the PDF uncertainty reported encapsulates an estimation for the uncertainty on methodological choices made in the parameterisation.

CT18 PDFs are available in a selection of formats (full details can be found in [4]), for example the CT18Z PDFs includes the ATLAS 7 TeV W/Z data [116] which was left out of the main CT18 release due to tensions with other datasets. The CT18Z set therefore exhibit an elevated strangeness at $x = 0.02 - 0.1$ from CT18 and an enhanced small-x gluon, where the latter is a result of choosing an x-dependent factorisation scale which mimics the small-x resummation effects particularly relevant for the combined HERA data. The CT collaboration also includes two other PDF sets which include only the ATLAS 7 TeV W/Z data [116] and only the x-dependent factorisation scale, intended as intermediaries between the standard CT18 set and CT18Z described above.

4.4.2. NNPDF

The final global PDF set included in the PDF4LHC21 combination are the NNPDF3.1 PDFs [5] (now superseded by the NNPDF4.0 set [147]). As with MSHT and CT, the NNPDF analysis incorporates many new LHC measurements alongside the combined HERA measurements. As with the other PDF groups, NNLO in α_s is standard for almost all theoretical predictions included in the NNPDF fit. In an extensive determination of the strong coupling constant, the NNPDF collaboration reported a value of

$\alpha_s(M_Z) = 0.1185 \pm 0.0017$ including all experimental, methodological and theoretical uncertainties (via scale variations) [148]. In the NNPDF analysis, the charm and bottom pole masses are $m_c = 1.51$ GeV and $m_b = 4.92$ GeV respectively.

Of particular interest to the work in this thesis are two studies performed by the NNPDF collaboration in relation to small-x resummation [15] and theoretical uncertainty estimates [9]. The former study involved the supplementation of fixed order NLO and NNLO PDFs with NLO + small-x NLL and NNLO + small-x NLL in the DIS structure functions, similar to the additions made in this thesis work. It was observed that the HERA inclusive and charm data displayed a marked improvement in their corresponding χ^2's. The second study is related to the incorporation of MHOU's via scale variations, in which a general procedure for the inclusion of such uncertainties into PDF determinations at NLO was presented and extensively studied to assess the potential impact of higher order uncertainties.

The general fitting strategy employed by NNPDF involves converting experimental data into an ensemble of artificial Monte Carlo (MC) replicas. The data replicas are constructed via Gaussian distributions around each data point, characterised by the corresponding experimental uncertainty. The law of large numbers then ensures that given enough replicas, the generated pseudo data will encompass all experimental information. Each initial state PDF (including the charm PDF) is then modelled via a Neural Network (NN) multiplied by small and large x factors:

$$x f_k(x, Q_0^2;\, \boldsymbol{\theta}) = A_k\, x^{1-\alpha_k}(1-x)^{\beta_k}\mathrm{NN}_k(x;\, \boldsymbol{\theta}) \tag{4.14}$$

where k denotes the element of the flavour/evolution PDF basis (more information in [147]). With this procedure, combined with the DGLAP evolution and the MC

generated pseudo data described above, the NNPDF collaboration perform a global fit using a validation set to prevent overfitting the NN's via an early stopping technique.

In contrast to the Hessian based approaches discussed above, the PDF uncertainties in the NNPDF analysis are found via a MC based approach by fitting to all replica datasets. The PDF replicas are then used to define the uncertainty bands. However, it has been shown that MC and Hessian based approaches have a good degree of correspondence to one another [149–154] and therefore it is possible to sample a subset of MC PDF replicas from NNPDF to produce a Hessian set similar to the MSHT and CT sets (or vice versa). In the PDF4LHC21 combination MC replicas are created from all PDF sets (MSHT, CT and NNPDF) in order to achieve the final combination.

4.4.3. Comparison with MSHT20

As discussed above, the methodologies of all three PDF fitting groups entering the PDF4LHC21 combination differ significantly. For example, MSHT20 NNLO PDFs adopt a parameterisation including Chebyshev polynomials and have a final PDF ensemble based on 52 free parameters, compared to the CT collaboration who favour Bernstein polynomials and 29 free parameters and NNPDF who employ neural networks and have an order of magnitude higher number of free parameters in their final ensemble.

Other areas of methodology that differ between the groups are in the constraints applied to parameterisations of the PDFs. In the MSHT framework the only constraint employed is by the data (and required sum rules), allowing complete flexibility of the parameterisation as long as the data is fit to a good standard. This means that it is possible for the PDFs to take any shape in its final form (and indeed become negative).

This is in direct contrast to other groups discussed, where in the CT procedure the parameterisation is chosen such that the PDFs at large-x are non-negative and in NNPDF, a direct constraint is applied directly to the minimisation procedure in order to demand positivity of PDFs. Positive PDFs are desirable (but not required) because they alleviate some risks in predicting unphysical negative observable quantities. Having said this, negative observable quantities can still be predicted with positive PDFs depending on how these are computed with other quantities (i.e. hard cross sections) (see [155, 156] for an ongoing discussion).

Fig. 4.1 (taken from [8]) shows a direct comparison of the three PDF sets discussed above (albeit with NNPDF 3.1 instead of NNPDF 4.0) at $Q = 100$ GeV. In this comparison the charm and bottom pole masses are set to the MSHT20 choice of $m_c = 1.4$ GeV and $m_b = 4.75$ GeV respectively. Therefore in this comparison (and in the PDF4LHC21 combination) the MSHT20 NNLO set is the same as will be used extensively for the rest of this thesis. The CT18 and NNPDF3.1 sets are modified to this choice of the heavy quark pole masses and are termed CT18$'$ and NNPDF3.1$'$.

Although all three groups agree within uncertainties across most of the range of x values shown, some noteable features which have relevance to later chapters in this thesis can be observed. For instance in the gluon PDF, NNPDF3.1$'$ sees a reduction around $x \sim 0.2$ which is not seen by the other two groups. The large-x behaviour of the MSHT20 gluon at approximate N^{3}LO is discussed in detail in Chapter 13.

Further to this, due to the exclusion of the ATLAS 7 TeV high prec. W, Z [116] from the CT18 standard PDF set, a smaller strangeness central value is reported above $x \sim 10^{-3}$ when compared to MSHT20 and NNPDF3.1$'$ (although at even higher $x > 10^{-1}$, NNPDF3.1$'$ also prefer a further enhanced strange PDF than the other two groups).

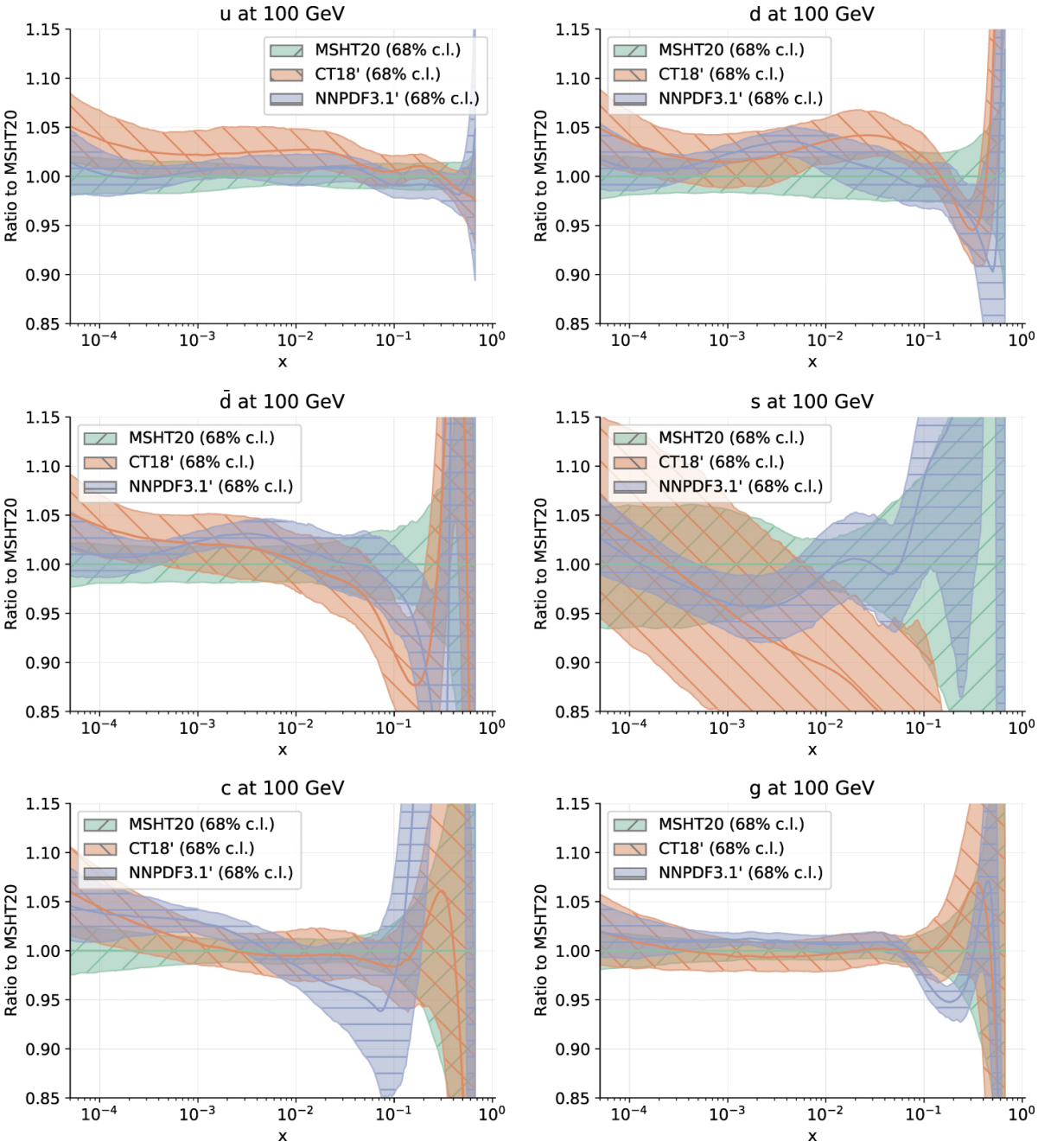

Figure 4.1.: Comparison of the CT18′, MSHT20, and NNPDF3.1′ global sets, normalised to the central value of MSHT20, as a function of x at $Q = 100$ GeV. The plots display the PDF results for the u, d, $\bar{d}$, s, c quarks and the gluon. In the cases of CT18′ and MSHT20 the results shown are displaying the Monte Carlo representations of the original Hessian sets where the error bands correspond to 68% CL uncertainties. Figure is copied from [8].

Finally, another expected prominent difference between NNPDF3.1′ and other PDF sets can be see within the charm PDF due to the fact that the charm is fitted within the NNPDF methodology, rather than perturbatively generated. The result of this is a marked enhancement in the shape of the charm at large-x which remains up to high-Q^2 along with larger uncertainties than MSHT20 and CT18′ in this region, due to the lack of constraining power (which originates from the gluon in the perturbative case).

Throughout the remainder of this thesis, the PDF comparisons will be solely shown within the MSHT20 ecosystem, predominantly building off the MSHT20 NNLO standard set introduced in this chapter. At various points reference will be made towards the differences between different groups PDF sets, however care must be taken in comparing theoretical predictions across misaligned orders in perturbation theory, therefore no direct quantitative comparisons of the aN^{3}LO PDFs presented here with will be made with NNLO sets from other PDF groups.

Chapter 5.

Theoretical Uncertainties

In the modern world of science, a measurement's uncertainty is equally important as the measurement itself. The concept of providing an experimental uncertainty is commonplace in many areas of physics, allowing scientists to quantify the degree of confidence on the accuracy of a measurement. However, dealing with uncertainties in theoretical predictions is, at present, a somewhat unfamiliar idea.

As we move into a new era of high precision measurements in high energy physics, accompanied by advanced fitting methodologies for PDF fits, PDF uncertainties have have reached a new level of accuracy. In more constrained regions, this PDF uncertainty can easily reach below the few-percent level where theoretical uncertainties can begin to have a substantial effect.

The concept of a theoretical uncertainty is much the same as an experimental uncertainty i.e. providing a degree of uncertainty on a prediction or model. One of the leading sources of theoretical uncertainty in QCD predictions is due to the truncation of perturbative calculations expanded up to some order in the strong coupling constant

α_s. These unknown higher orders in perturbative calculations are commonly written as $+ \mathcal{O}(\alpha_s^{n+1})$ at the end of a perturbative expansion known up to n, but how can one actually quantify this mysterious (and often ignored) term. These sources of uncertainty are commonly termed Missing Higher Order Uncertainties (MHOUs).

In this chapter we will briefly assess a method of estimating MHOUs via scale variations, then describe the mathematical procedures used in a novel approach to implement N^{3}LO approximations with theoretical uncertainties into a global PDF fit. These procedures are discussed in terms of the Hessian minimisation method employed by the MSHT fit and extended by theoretically grounded arguments to accommodate theoretical uncertainties.

5.1. Scale Variations

A widely adopted method of estimating the effect of missing higher orders in fixed order QCD calculations is by varying the factorisation and renormalisation scales (μ_f and μ_r) by some arbitrary factor – the conventional choice being a factor of 2 in either direction of the central scale for a given process. As discussed in Chapters 2 and 3, the dependence of a physical quantity on these intermediate scales must vanish as we move to an all order description. The result of this provides smooth estimates for MHOUs based on the principle of Renormalisation Group (RG) invariance.

RG invariance demands that a prediction to all orders is independent of any intermediate scale. For this reason, calculations of physical observables must only depend on the physical scale Q^2 and so the μ_r and μ_f dependencies must cancel out.

A general RG invariant function $C(\alpha_s(\mu^2), \frac{\mu^2}{Q^2})$ is required to obey,

$$\mu^2 \frac{d}{d\mu^2} C(\alpha_s(\mu^2), \frac{\mu^2}{Q^2}) = 0. \tag{5.1}$$

Let us also define two new variables for the convenience of this derivation as,

$$\xi = \ln \frac{Q^2}{\Lambda^2} \qquad\qquad \chi = \ln \frac{\mu^2}{Q^2}, \tag{5.2}$$

where this change of variables yields,

$$\frac{d}{d\mu^2} = \frac{1}{\mu^2} \frac{d}{d\chi}. \tag{5.3}$$

With (5.1) in a simpler form, we can expand this equation out using the chain rule as follows,

$$\begin{aligned} \frac{d}{d\chi} C(\alpha_s(\xi+\chi),\chi) &= \frac{d}{d\chi}\alpha_s(\xi+\chi) \frac{\partial}{\partial \alpha_s} C(\alpha_s(\xi+\chi),\chi)\Big|_\chi + \frac{\partial}{\partial \chi} C(\alpha_s(\xi+\chi),\chi)\Big|_{\alpha_s} \\ &= \frac{d}{d\xi}\alpha_s(\xi+\chi) \frac{\partial}{\partial \alpha_s} C(\alpha_s(\xi+\chi),\chi)\Big|_\chi + \frac{\partial}{\partial \chi} C(\alpha_s(\xi+\chi),\chi)\Big|_{\alpha_s} \\ &= \frac{\partial}{\partial \xi} C(\alpha_s(\xi+\chi),\chi)\Big|_\chi + \frac{\partial}{\partial \chi} C(\alpha_s(\xi+\chi),\chi)\Big|_{\alpha_s} = 0 \end{aligned} \tag{5.4}$$

The above reveals a new relationship between the partial derivatives of an RG invariant quantity with respect to our new variables. Taking our original quantity $C(\alpha_s(\xi+\chi),\chi)$ and performing a Taylor expansion around the point where $\mu^2 = Q^2$ or $\chi = 0$ reveals the following expression,

$$\begin{aligned} C(\alpha_s(\xi+\chi),\chi) = C(\alpha_s(\xi+\chi),0) + \chi \frac{\partial}{\partial \chi} C(\alpha_s(\xi+\chi),0)\Big|_{\alpha_s} \\ + \frac{1}{2}\chi^2 \frac{\partial^2}{\partial \chi^2} C(\alpha_s(\xi+\chi),0)\Big|_{\alpha_s} + \dots \end{aligned} \tag{5.5}$$

where using (5.4) one can state,

$$C(\alpha_s(\xi+\chi),\chi) = C(\alpha_s(\xi+\chi),0) - \chi\frac{\partial}{\partial\xi}C(\alpha_s(\xi+\chi),0)\Big|_{\alpha_s} + \frac{1}{2}\chi^2\frac{\partial^2}{\partial\xi^2}C(\alpha_s(\xi+\chi),0)\Big|_{\alpha_s} + \dots. \tag{5.6}$$

In general, (5.6) displays how any RG invariant quantity can be described in terms of a Taylor expansion. Reminding ourselves of the dependence of α_s on μ^2 (or equivalently t) we can relate the above back to the running coupling of QCD using,

$$\mu^2\frac{d}{d\mu^2}\alpha_s(\mu^2) = \frac{d}{d\xi}\alpha_s(t) = \beta(\alpha_s(\xi)), \tag{5.7}$$

$$\frac{d}{d\xi}C(\alpha_s(\xi),0) = \frac{d\alpha_s}{d\xi}\frac{\partial}{\partial\alpha_s}C(\alpha_s(\xi),0) = \beta(\alpha_s(\xi))\frac{\partial}{\partial\alpha_s}C(\alpha_s(\xi),0) = \mathcal{O}(\alpha_s) \tag{5.8}$$

where the final equality is stated noting that $\beta(\alpha_s) = \mathcal{O}\left(\alpha_s^2\right)$. Subsequently, with each derivative of C with respect to ξ, we gain an extra power of α_s due to the chain rule. Tracking back to the expression in (5.6) and bearing in mind that the expression $C(\alpha_s,\chi)$ is also expanded in powers of α_s, one can match the two sides of this equation order by order as,

$$C^{(0)}(\alpha_s(\xi+\chi),\chi) = C^{(0)}(\alpha_s(\xi+\chi),0), \tag{5.9a}$$

$$C^{(1)}(\alpha_s(\xi+\chi),\chi) = C^{(1)}(\alpha_s(\xi+\chi),0) - \chi\frac{\partial}{\partial\xi}C^{(0)}(\alpha_s(\xi+\chi),0), \tag{5.9b}$$

$$C^{(2)}(\alpha_s(\xi+\chi),\chi) = C^{(2)}(\alpha_s(\xi+\chi),0) - \chi\frac{\partial}{\partial\xi}C^{(1)}(\alpha_s(\xi+\chi),0) + \frac{1}{2}\chi^2\frac{\partial^2}{\partial\xi^2}C^{(0)}(\alpha_s(\xi+\chi),0). \tag{5.9c}$$

Finally, the expressions for the theory uncertainties can be found by subtracting off the central values $C^{(n)}(\alpha_s(\xi), 0)$ at each order n.

The form of the expressions in (5.9) reveal that at each increasing order, the leading uncertainty from the order below is subtracted off by the term linear in χ in each case (and the subleading uncertainties by the terms multiplying each subsequent power of χ^n). This therefore ensures that the predicted MHOUs are reduced at each order as we would expect from a valid perturbation theory. However, another prominent feature one may notice is the dependence of the uncertainty predicted on the chosen variation manifested in χ. As we will discuss, the lack of any universal truth guiding a sensible choice of variation represents a significant shortcoming in the scale variation approach to estimating MHOUs.

As previously discussed in Chapter 3, structure functions are physical quantities calculated from hadronic processes which by definition, are RG invariant. Isolating the coefficient function from (3.24) and following a derivation similar to the one described above for a general quantity, the renormalisation scale dependence present in the perturbative expansion of the coefficient function can be found as,

$$C(\alpha_s(Q^2)) = c^{(0)} + \alpha_s(Q^2)c^{(1)} + \alpha_s^2(Q^2)\left\{c^{(2)} - \beta_0 c^{(1)} \ln\left(\frac{\mu_r^2}{Q^2}\right)\right\} + \dots . \tag{5.10}$$

The above expression describes the origin of the dependence of a structure function on the renormalisation scale, however we must also consider the same procedure with the scale dependence in PDFs.

The PDFs evolve according to the splitting functions, which are calculated to a finite order in a perturbative expansion. This truncation therefore gives rise to another

source of MHOU in structure function calculations through the DGLAP equation,

$$\mu_f^2 \frac{d}{d\mu_f^2} f(x, \mu_f^2) = P(x, \alpha_s(\mu_f^2)) \otimes f(x, \mu_f^2). \tag{5.11}$$

where the scale μ_f is the factorisation scale. In order to provide a cleaner space for the following derivation, we will opt to work in Mellin space via the application of a Mellin transform (see [157, 158] for more details). In Mellin space, convolutions mutate into simple multiplications and therefore (5.11) can be written in Mellin space as,

$$\mu^2 \frac{d}{d\mu^2} f(\mu^2) = \gamma(\alpha_s(\mu^2)) f(\mu^2), \tag{5.12}$$

where $\gamma(\alpha_s(\mu^2))$ is now the anomalous dimension defined as the Mellin transform of the x-space splitting functions. Solving the above expression and defining an initial scale PDF f_0 which is fitted to the data one can show,

$$f(\mu^2) = \exp\left(\int_{\mu_0^2}^{\mu^2} \frac{d\mu'^2}{\mu'^2} \gamma(\alpha_s(\mu'^2)) \right) f_0, \tag{5.13}$$

where we are permitted to ignore the lower limit of μ_0^2 and absorb this into the fitting procedure of f_0.

Adopting the change of variables outlined in (5.2), the expression for $f(\mu^2)$ can be rewritten as,

$$\begin{aligned} f(\alpha_s(\xi+\chi),\chi) &= \exp\left(\int^{\xi+\chi} d\xi^{'}\gamma(\alpha_s(\xi^{'}),\chi)\right) f_0 \\ &= \exp\left(\left[\int^{\xi+\chi} d\xi^{'}\gamma(\alpha_s(\xi^{'}),0)\right] - \chi\gamma(\alpha_s(\xi+\chi),0)\right. \\ &\qquad \left. + \frac{1}{2}\chi^2\frac{d}{d\xi}\gamma(\alpha_s(\xi+\chi),0) + \dots\right) f_0 \\ &= \left[1 - \chi\gamma(\xi+\chi) + \frac{1}{2}\chi^2\left(\gamma^2(\xi+\chi)\right.\right. \\ &\qquad \left.\left. + \frac{d}{d\xi}\gamma(\xi+\chi)\right) + \dots\right] f(\xi+\chi,0) \end{aligned} \tag{5.14}$$

where $f(\xi+\chi,0) = \exp\left(\int^{\xi+\chi} d\xi^{'}\gamma(\alpha_s(\xi^{'}),0)\right) f_0$ is the initial central PDF, f_0 is the PDF parameterised in x at a fixed initial scale Q_0^2 and the factorisation scale dependence is defined explicitly outside of the PDF definition.

The two ingredients (5.10) and (5.14) are input into the definition of the structure function via a convolution (see (3.24)) to achieve the full scale dependence of the physical quantity at a specified order in perturbation theory. However in performing this convolution, the individual scale dependencies are tangled up which leads to issues regarding correlations between scales and also the presence of complicated convolutions (some of which are provided analytically in Appendix A). In the next section we investigate the effects of scale variations (as described above) on the $F_2(x,Q^2)$ structure functions using the MMHT14 PDF set.

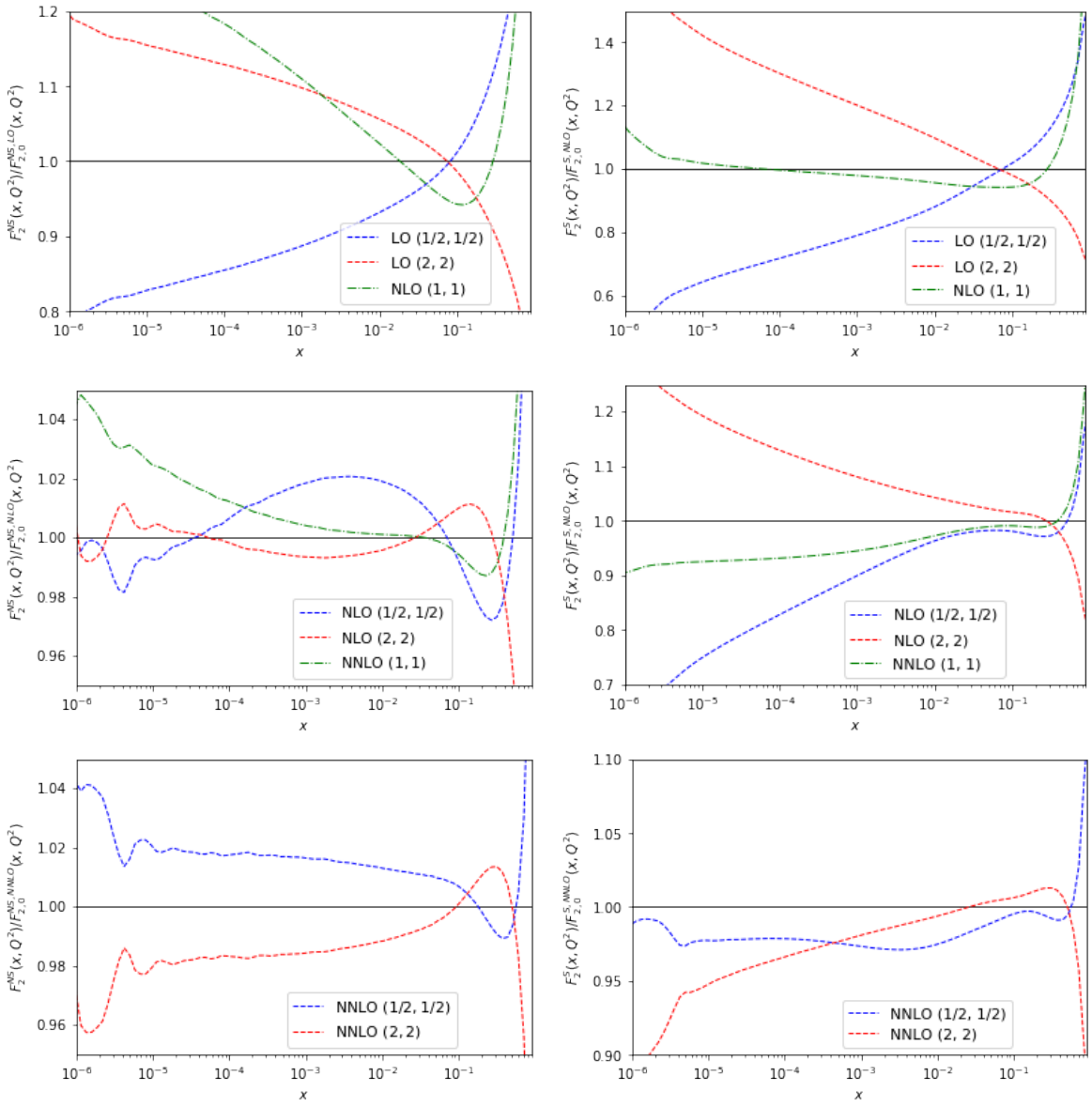

Figure 5.1.: Ratio of scale variations found from the non-singlet (left) and singlet (right) F_2 structure functions at LO (top), NLO (middle) and NNLO (bottom) in α_s. The notation (a_{μ_f}, a_{μ_r}) is used to label the results, where $a_{\mu_{f/r}}$ are the factors that multiply the central scale as $\mu_{f/r} = a_{\mu_{f/r}} Q$. All plots are displayed as a ratio to the central scale.

5.1.1. Structure Functions with Scale Variations

In this less than extensive study, a 3-point convention $(a_{\mu_f}, a_{\mu_r}) = (1,1)$, $(1/2,1/2)$, $(2,2)$ has been adopted from [9] where $a_{\mu_{f/r}}$ are the factors which multiply the central energy scale Q. Although the above choice of variation is employed here, we also note that due to the arbitrary nature of scale variations, any choice is equally as valid. Fig. 5.1 displays a selection of results from a study done with MMHT14 NLO and NNLO PDFs [68] as input to non-singlet (left) and singlet (right) $F_2(x, Q^2)$ structure functions. In all plots, the ratio to the central structure function prediction with $(a_{\mu_f}, a_{\mu_r}) = (1,1)$ at the current order is shown (NLO - above, NNLO - below).

Moving down the individual plots shown in Fig. 5.1 for non-singlet and singlet structure function quantities, one can appreciate the reduction in the scale variation between orders. For example in the non-singlet results (left set of plots), most of the uncertainty from LO is cancelled by the NLO, with the LO variation around $10\% - 15\%$ being reduced to around $1\% - 3\%$ at NLO. Similarly at NNLO, the resultant perturbative expansion is more precise across the range of all valid x values. This trend follows the expectation that estimates of MHOUs across subsequent orders are reduced, as predicted from the RG equation discussed in the previous section.

As a sanity check, the central values of the next highest order prediction are plotted where available in Fig. 5.1. In general there is good agreement between the predictions at LO and NLO with scale variations and the next highest order central value, with any notable disagreements occurring in the non-singlet case only where $F_2^{\mathrm{NS}} \to 0$.

Considering the bottom set of plots, it is apparent that the scale variations of the NNLO singlet structure function become a lot smaller than those at NLO and no longer surround the NNLO central value for a substantial region in x. As mentioned, the

procedure of scale variation employed here is far from extensive, however this result does highlight one of the potential shortcomings in using scale variations. Specifically, the estimations of MHOUs are not guaranteed to lie above and below the central value meaning a particular prediction may require additional processing of uncertainties to ascertain a final MHOU.

We also must question the method of scale variations as a whole at this point. The completely arbitrary choice of scale is a problem that has no natural solution and has potential to predict highly inaccurate MHOUs. More examples of this behaviour can be seen in a study by NNPDF [147] where a more extensive scale variation procedure is used. Therefore while the theoretical procedures outlined in the previous section provide an intuitive way of understanding how higher order effects can reduce the dependence of a physical quantity on various scale choices, in practice it can be argued that scale variations are not a good proxy for estimating MHOUs.

Complications also arise when considering correlations of scale variations between fit and prediction [10, 12]. It has been shown that if scale variation is used to estimate a MHOU on a PDF, then keeping this treatment consistent from the fit to prediction, can lead to an overestimation of theoretical uncertainty. Whereas if scale variation is only used at the time of fitting/prediction then it cannot account for the full extent of MHOUs.

5.2. Hessian Method with Nuisance Parameters

More recently a different method of estimating theoretical uncertainties has been proposed [17, 18] whereby all the uncertainties are estimated via nuisance parameters. This method lends itself more competently to dealing with correlations between

uncertainties. For example, the nuisance parameter for a splitting function can be estimated independently from any coefficient nuisance parameter and so allows for far greater control of the correlations of uncertainties. Although this method does still contain some level of arbitrariness in the estimation of nuisance parameters, we are now permitted to use our intuition and understanding to tackle this issue rather than relying on any potential mechanical inaccuracies from scale variations.

At present, not all the ingredients necessary for full N^{3}LO theory predictions are known, where there is missing information the N^{3}LO theory predictions will therefore include additional theoretical nuisance parameters, allowing their variation via an additional degree of freedom in specific theoretical pieces. These theoretical nuisance parameters will be constrained via an additional χ^2 penalty in the global fit and will accommodate a level of uncertainty for each added approximate N^{3}LO ingredient (more information on how these prior variations are decided is included in Section's 6.2, 6.3 and 10.1). From this point, the fitting procedure remains similar to previous MSHT fits with a number of extra theory nuisance parameters which are treated in the same manner as experimental nuisance parameters inherent in PDF fits i.e. they can be fit to the data via an expanded Hessian matrix. The remainder of this chapter and this thesis will be discussing the implementation and results from including this procedure in a global PDF fit.

Following the notation and description from [12], in the Hessian prescription, the Bayesian probability can be written as

$$P(T|D) \propto \exp\left(-\frac{1}{2}(T-D)^T H_0 (T-D)\right) \tag{5.15}$$

where H_0 is the Hessian matrix and $T = \{T_i\}$ is the set of theoretical predictions fit to N experimental data points $D = \{D_i\}$ with $i = 1, \ldots, N$. Note that in the above we

assume that $P(T)$ and $P(D)$ follow the same Gaussian prior about the same unknown true theory i.e. $P(T|D) = P(D|T)$. In this section we explicitly show the adaptation of this equation to accommodate extra theoretical parameters (with penalties) into the total χ^2 and Hessian matrices.

To adapt this equation to include a single extra theory parameter, we can make the transformation $T \rightarrow T + tu = T'$, where t is the chosen central value of the theory parameter considered and u is some non-zero vector such that uu^T is the theory covariance matrix for t. In defining this new theoretical prescription T', we are making the general assumption that the underlying theory is now not necessarily identical to our initial NNLO theory[1] T.

We now seek to include a nuisance parameter θ, centered around t, to allow the fit to control this extra theory addition. Demanding that when $\theta = t$, T' remains unaffected with the theory addition unaltered from its central value t leads to the expression,

$$T' + (\theta - t)u = T + tu + (\theta - t)u. \tag{5.16}$$

To maintain clarity in this derivation, we will absorb the central value t into the nuisance parameter via a redefinition $\theta' = \theta - t$, where θ' is interpreted as the shift from the central value and therefore centered around 0. To constrain θ' within the fitting procedure, we must also define a prior probability distribution $P(\theta')$ centered

[1] For the aN^{3}LO prescription defined in this paper this is indeed the case, although for any extra theory parameters that do not inherently change the theory from T, this transformation still holds in the case that $t = 0$.

around 0 and characterised by some standard deviation $\sigma_{\theta'}$,

$$P(\theta') = \frac{1}{\sqrt{2\pi}\sigma_{\theta'}} \exp(-\theta'^{\,2}/2\sigma_{\theta'}^2). \tag{5.17}$$

Throughout this paper, we refer to the chosen variation of theory predictions in the language of the standard deviation $\sigma_{\theta'}$ presented here. A caveat to this however is that technically speaking, this standard deviation is chosen with a level of arbitrariness based on general assumptions and known information about the theory (we will show how this is done in more detail in Section's 6.2, 6.3 and 10.1). Although this definition of $\sigma_{\theta'}$ lacks the full extent of statistical meaning of a true standard deviation, the same is also true for scale variations as well as various experimental systematic uncertainties, which are often not strictly Gaussian. Furthermore, a more robust statistical meaning is recovered for the constraints on various theoretical parameters after a fit is performed, where we become less sensitive to a prior. Using this information and making the redefinition $u \to u/\sigma_{\theta'}$ (in order to normalise the covariance matrix), we can update Equation (5.15) to be

$$P(T|D\theta) \propto \exp\left(-\frac{1}{2}(T + tu + \frac{(\theta - t)}{\sigma_{\theta'}}u - D)^T H_0 (T + tu + \frac{(\theta - t)}{\sigma_{\theta'}}u - D)\right) \tag{5.18}$$

$$P(T'|D\theta') \propto \exp\left(-\frac{1}{2}(T' + \frac{\theta'}{\sigma_{\theta'}}u - D)^T H_0 (T' + \frac{\theta'}{\sigma_{\theta'}}u - D)\right) \tag{5.19}$$

From here, Bayes theorem tells us

$$P(T'|D\theta')P(\theta'|D) = P(\theta'|T'D)P(T'|D) \tag{5.20}$$

where our nuisance parameter θ' is assumed to be independent of the data i.e. $P(\theta'|D) = P(\theta')$. Integrating over θ' gives

$$P(T'|D) = \underbrace{\int d\theta' P(\theta'|T'D)}_{=1} P(T'|D) = \int d\theta' P(T'|D\theta')P(\theta'). \tag{5.21}$$

Combining Equations (5.17), (5.19) and (5.21) it is possible to show that,

$$P(T'|D) \propto \int d\theta' \exp\left(-\frac{1}{2}\left[(T' + \frac{\theta'}{\sigma_{\theta'}}u - D)^T H_0 (T' + \frac{\theta'}{\sigma_{\theta'}}u - D) + \theta'^2/\sigma^2_{\theta'}\right]\right). \tag{5.22}$$

To make progress with this equation we consider the exponent and refactor terms in powers of θ',

$$\left(u^T H_0 u + 1\right)\frac{\theta'^2}{\sigma^2_{\theta'}} + 2u^T H_0 (T' - D)\frac{\theta'}{\sigma_{\theta'}} + (T' - D)^T H_0 (T' - D). \tag{5.23}$$

Defining $M^{-1} = \frac{1}{\sigma^2_{\theta'}}\left(u^T H_0 u + 1\right)$ one can complete the square by taking the first two terms in (5.23) as $M^{-1}\left[\theta'^2 + \frac{2}{\sigma_{\theta'}} M u^T H_0 (T' - D)\theta'\right]$ and subsequently arriving at,

$$M^{-1}\left[\theta' + \frac{1}{\sigma_{\theta'}} M u^T H_0 (T' - D)\right]^2 - \frac{1}{\sigma^2_{\theta'}} M \left(u^T H_0 (T' - D)\right)^2 + (T' - D)^T H_0 (T' - D). \tag{5.24}$$

In Equation (5.24), we are able to simplify the first term by defining,

$$\bar{\theta}'(T, D) = \frac{1}{\sigma_{\theta'}} M u^T H_0 (D - T'). \tag{5.25}$$

Expanding the second term leaves us with,

$$\left(u^T H_0 (T' - D)\right)^2 = (T' - D)^T H_0 u u^T H_0 (T' - D) \tag{5.26}$$

The second and third term in Equation (5.24) can then be combined to give,

$$(T' - D)^T \left(H_0 - \frac{1}{\sigma_{\theta'}^2} M H_0 u u^T H_0 \right) (T' - D). \tag{5.27}$$

Further to this we note that the following is true:

$$\begin{aligned}(H_0^{-1} + uu^T)\left(H_0 - \frac{1}{\sigma_{\theta'}^2} M H_0 u u^T H_0 \right) &= 1 + uu^T H_0 - \frac{1}{\sigma_{\theta'}^2} M u u^T H_0 - \frac{1}{\sigma_{\theta'}^2} M u u^T H_0 u u^T H_0 \\ &= 1 + uu^T H_0 - \frac{1}{\sigma_{\theta'}^2} M u u^T H_0 - \frac{1}{\sigma_{\theta'}^2} M u (\sigma_{\theta'}^2 M^{-1} - 1) u^T H_0 = 1. \end{aligned} \tag{5.28}$$

Using Equation (5.28) we are finally able to rewrite Equation (5.22) as,

$$P(T'|D) \propto \int d\theta' \exp\left(-\frac{1}{2} M^{-1} (\theta' - \overline{\theta}')^2 - \frac{1}{2} (T' - D)^T (H_0^{-1} + uu^T)^{-1} (T' - D) \right). \tag{5.29}$$

At this point we can make a choice whether to redefine our Hessian matrix as $H = (H_0^{-1} + uu^T)^{-1}$, or keep the contributions completely separate. By redefining the Hessian we can include correlations between the standard set of MSHT parameters included in H_0 and the new theoretical parameter θ' contained within uu^T during the diagonalisation procedure discussed in Chapter 4. However, by doing so we lose information about the specific contributions to the total uncertainty i.e. one cannot then decorrelate the theoretical and standard PDF uncertainties a posteriori. Whereas for the decorrelated choice, although we sacrifice knowledge related to the correlations between the separate sources of uncertainty, the sources can be treated completely

separably. This is beneficial when attempting to decorrelate sources of uncertainty from fit to prediction – a shortcoming of the scale variation approach outlined in the previous section.

Interpreting Equation (5.29) as in Equation (5.15) we can write down the two χ^2 contributions,

$$\chi^2_1 = (T' - D)^T (H_0^{-1} + uu^T)^{-1} (T' - D) = (T' - D)^T H (T' - D), \tag{5.30}$$

$$\chi^2_2 = M^{-1} (\theta' - \overline{\theta}')^2. \tag{5.31}$$

Where χ^2_1 is the contribution from the fitting procedure, χ^2_2 is the posterior penalty contribution applied when the theory addition strays too far from its fitted central value and M is the posterior error matrix for this contribution. The form of these central values and their corresponding uncertainties are discussed for each aN^{3}LO function in Chapter's 7 to 9.

5.2.1. Multiple Theory Parameters

To accommodate multiple sources of MHOUs from the various perturbative expansions discussed in Chapter 3, the discussion in the previous section must be extended to multiple theory nuisance parameters.

In the case of multiple $N_{\theta'}$ theory parameters, Equation (5.19) becomes

$$P(T'|D\theta') \propto \exp\left(-\frac{1}{2} \sum_{i,j}^{N_{\text{pts}}} \left(T'_i + \sum_{\alpha=1}^{N_{\theta'}} \frac{\theta'_\alpha}{\sigma_{\theta'_\alpha}} u_{\alpha,i} - D_i \right) H^0_{ij} \left(T'_j + \sum_{\beta=1}^{N_{\theta'}} \frac{\theta'_\beta}{\sigma_{\theta'_\beta}} u_{\beta,j} - D_j \right) \right) \tag{5.32}$$

where we have explicitly included the sum over the number of data points N_{pts} in the matrix calculation for completeness.

The prior probability for all N^{3}LO nuisance parameters also becomes

$$P(\theta') = \prod_{\alpha=1}^{N_{\theta'}} \frac{1}{\sqrt{2\pi}\sigma_{\theta'_\alpha}} \exp(-{\theta'_\alpha}^2/2\sigma^2_{\theta'_\alpha}). \tag{5.33}$$

Constructing $P(T'|D)$ using Bayes theorem as before, results in the expression,

$$P(T'|D) \propto \int d^{N_{\theta'}}\theta' \exp\left(-\frac{1}{2}\left[\sum_{i,j}^{N_{\text{pts}}} \left(T'_i + \sum_{\alpha=1}^{N_{\theta'}} \frac{\theta'_\alpha}{\sigma_{\theta'_\alpha}} u_{\alpha,i} - D_i \right) H^0_{ij} \times \right.\right.$$
$$\left.\left. \times \left(T'_j + \sum_{\beta=1}^{N_{\theta'}} \frac{\theta'_\beta}{\sigma_{\theta'_\beta}} u_{\beta,j} - D_j \right) + \sum_{\alpha,\beta}^{N_{\theta'}} \frac{\theta'_\alpha}{\sigma_{\theta'_\alpha}} \frac{\theta'_\beta}{\sigma_{\theta'_\beta}} \delta_{\alpha\beta} \right] \right). \tag{5.34}$$

Following the same procedure as laid out in the previous section, defining $M^{-1}_{\alpha\beta} = (\delta_{\alpha\beta} + u_{\alpha,i} H^0_{ij} u_{\beta,j})/\sigma_{\theta'_\alpha}\sigma_{\theta'_\beta}$ and completing the square leaves us with,

$$(T'_i - D'_i)H^0_{ij}(T'_j - D'_j) + \sum_{\alpha,\beta}^{N_{\theta'}} M^{-1}_{\alpha\beta} \left[\left(\theta'_\alpha + \sum_{i,j}^{N_{\text{pts}}} \sum_{\delta=1}^{N_{\theta'}} \frac{1}{\sigma_{\theta'_\alpha}} M_{\alpha\delta} u_{\delta,i} H^0_{ij}(T'_j - D_j) \right)^2 \right.$$
$$\left. - \left(\sum_{i,j}^{N_{\text{pts}}} \sum_{\delta=1}^{N_{\theta'}} \frac{1}{\sigma_{\theta'_\alpha}} M_{\alpha\delta} u_{\delta,i} H^0_{ij}(T'_j - D_j) \right)^2 \right], \tag{5.35}$$

where the summation over the β index in $M^{-1}_{\alpha\beta}$ is implicit in the squared terms of the squared bracket expressions.

As in the previous section for a single parameter, we can define,

$$\overline{\theta}'_\alpha(T', D) = \sum_{i,j}^{N_{\text{pts}}} \sum_{\delta=1}^{N_{\theta'}} \frac{1}{\sigma_{\theta'_\alpha}} M_{\alpha\delta} u_{\delta,i} H^0_{ij} (D_j - T'_j) \tag{5.36}$$

$$H_{ij} = \left(\left(H^0_{ij} \right)^{-1} + \sum_{\alpha=1}^{N_{\theta'}} u_{\alpha,i} u_{\alpha,j} \right)^{-1} \tag{5.37}$$

which leads to the final expression for $P(T|D)$,

$$P(T'|D) \propto \int d^{N_{\theta'}}\theta' \exp\left(-\frac{1}{2} \left[\sum_{\alpha,\beta}^{N_{\theta'}} \left(\theta'_\alpha - \overline{\theta}'_\alpha \right) M^{-1}_{\alpha\beta} \left(\theta'_\beta - \overline{\theta}'_\beta \right) + \sum_{i,j}^{N_{\text{pts}}} \left(T'_i - D_i \right) H_{ij} \left(T'_j - D_j \right) \right] \right). \tag{5.38}$$

5.2.2. Decorrelated parameters

In the treatment above we investigated the case of correlated parameters whereby the Hessian matrix was redefined in Equation (5.37). In performing this redefinition we sacrifice information contained within $u_{\alpha,i}u_{\alpha,j}$ in order to gain information about the correlations between the original PDF parameters making up H^0_{ij} and any new N^{3}LO nuisance parameters. In this case, we can perform a fit to find H_{ij} but one is unable to separate this Hessian matrix into individual contributions.

As will be discussed in later chapters, the K-factors we include in the N^{3}LO additions are somewhat more separate from other N^{3}LO parameters considered. The

reason for this is that not only are they concerned with the cross section data directly, they are also included for processes separate from inclusive DIS[2].

Thinking in terms of the process dependent and process independent contributions to the DIS picture in Fig. 3.2 (or any other non-DIS process), the factorisation theorem naturally separates these two ingredients. Therefore this decorrelation can be understood and justified based on the argument that PDFs are universal and consequently should not depend on the hard processes.

Hence, we have some justification to include the aN^{3}LO K-factor's nuisance parameters as completely decorrelated from other PDF parameters (including other N^{3}LO theory parameters). Of course, this procedure ignores some inevitable correlations between non-DIS processes and the DGLAP evolution, however the dominant constraint on the aN^{3}LO splitting functions arises from small-x DIS data, therefore this approximation is assumed to be valid. The form of these aN^{3}LO splitting functions will be discussed in detail in Chapter 7. To perform the decorrelation we can rewrite Equation (5.37) as,

$$\left(\left(H_{ij}^{0}\right)^{-1}+\sum_{\alpha=1}^{N_{\theta'}}u_{\alpha,i}u_{\alpha,j}+\sum_{p=1}^{N_p}\sum_{\delta=1}^{N_{\theta_K}}u_{\delta,i}^{p}u_{\delta,j}^{p}\right)^{-1}=\left(H_{ij}^{-1}+\sum_{p=1}^{N_p}K_{ij,p}^{-1}\right)^{-1}=H'_{ij} \quad (5.39)$$

where $N_{\theta'} \rightarrow N_{\theta'}+N_{\theta_K}$, $K_{ij,p}$ defines the extra decorrelated contributions from the N^{3}LO K-factor's parameters, stemming from N_p processes; H_{ij} is the Hessian matrix including correlations with parameters associated with N^{3}LO structure function theory; and H'_{ij} is the fully correlated Hessian matrix. It is therefore possible to construct these matrices separately and perform the normal Hessian eigenvector analysis (de-

[2]It is true that we may still expect some indirect correlation with the parameters controlling the N^{3}LO splitting functions, which are universal across all processes. However, as we will show, these correlations are small and can be ignored.

scribed in Chapter 4) on each matrix in turn. In doing this, we maintain a high level of flexibility in our description by assuming the sets of parameters (contained in H_{ij}^{-1} and $K_{ij,p}$) to be suitably orthogonal.

Chapter 6.

Approximating N^{3}LO

With the general procedure for estimating MHOUs explained in the previous chapter, we must now turn our attention to where the leading MHO's reside. Since a complete theory is known up to NNLO for the neutral current structure function we consider in this work, we require the extension of the perturbative ingredients discussed in Chapter 3 to N^{3}LO.

This chapter will describe the extension of the DIS $F_2(x, Q^2)$ structure function to N^{3}LO in α_s and summarise the known and unknown information at this order. Following this, two methods of approximation will be presented which are used in Chapter's 7, 8 and 9 in order to estimate the various N^{3}LO functions.

6.1. Extension of DIS to N^{3}LO

The general form of a structure function $F(x, Q^2)$ is a convolution between the PDFs $f_i(x, Q^2)$ and some defined process dependent coefficient function $C(x, \alpha_s(Q^2))$,

$$F(x, Q^2) = \sum_{i=q,\bar{q},g} \left[C_i(\alpha_s(Q^2)) \otimes f_i(Q^2) \right](x) \tag{6.1}$$

where we have the sum over all partons i and implicitly set the factorisation and renormalisation scales as $\mu_f^2 = \mu_r^2 = Q^2$, a choice that will be used throughout this thesis for DIS scales. We also note that the relevant charge weightings are implicit in the definition of the coefficient function for each parton.

In Equation (6.1), the perturbative and non-perturbative regimes are separated out into coefficient functions C_i and PDFs f_i respectively. Since these coefficient functions are perturbative quantities, they are an important aspect to consider when transitioning to N^{3}LO.

The PDFs $f_i(x, Q^2)$ in Equation (6.1) are non-perturbative quantities. However, their evolution in Q^2 is perturbatively calculable. In a PDF fit, the PDFs are parameterised at a chosen starting scale Q_0^2, which is in general different to the scale Q^2 at which an observable (such as $F(x, Q^2)$) is calculated. It is therefore important that we are able to accurately evolve the PDFs from Q_0^2 to the required Q^2 to ensure a fully consistent and physical calculation. To permit this evolution, we introduce the standard factorisation scale μ_f.

The flavour singlet distribution is defined as,

$$\Sigma(x,\mu_f^2) = \sum_{i=1}^{n_f}\left[q_i(x,\mu_f^2) + \overline{q}_i(x,\mu_f^2)\right], \tag{6.2}$$

where $q_i(x,\mu_f^2)$ and $\overline{q}_i(x,\mu_f^2)$ are the quark and anti-quark distributions respectively, as a function of Bjorken x and the factorisation scale μ_f^2. The summation in Equation (6.2) runs over all flavours of (anti-)quarks i up to the number of available flavours n_f.

This singlet distribution is inherently coupled to the gluon density. Because of this, we must consider the gluon carefully when describing the evolution of the flavour singlet distribution with the energy scale μ_f. The Dokshitzer-Gribov-Lipatov-Altarelli-Parisi (DGLAP) [34] equations that govern this evolution are:

$$\frac{d\boldsymbol{f}}{d\ln\mu_f^2} \equiv \frac{d}{d\ln\mu_f^2}\begin{pmatrix}\Sigma\\ g\end{pmatrix} = \begin{pmatrix}P_{qq} & n_f P_{qg}\\ P_{gq} & P_{gg}\end{pmatrix} \otimes \begin{pmatrix}\Sigma\\ g\end{pmatrix} \equiv \boldsymbol{P}\otimes\boldsymbol{f} \tag{6.3}$$

where $P_{ij} : i,j \in q,g$ are the splitting functions and the factorisation scale μ_f is allowing the required evolution up to the physical scale Q^2. The matrix of splitting functions $\boldsymbol{P}$ appropriately couples the singlet and gluon distribution by means of a convolution in the momentum fraction x. We note here that $P_{qq} \equiv P_{q\to gq}$ is decomposed into non-singlet (NS) and a pure-singlet (PS) parts defined by,

$$P_{qq}(x) = P_{\rm NS}^{+}(x) + P_{\rm PS}(x), \tag{6.4}$$

where the P_{NS}^{+} is a non-singlet distribution splitting function which has been calculated approximately to four loops in [159][1]. The non-singlet part of P_{qq} dominates at large-x

[1] In this discussion, we only consider the P_{NS}^{+} non-singlet distribution as this is the distribution which contributes to the singlet evolution. Other non-singlet distributions are briefly discussed in Chapter 7

but as $x \to 0$, this contribution is highly suppressed due to the relevant QCD sum rules. On the other hand, due to the involvement of the gluon in the pure-singlet splitting function (as described above), this contribution grows towards small-x and therefore begins to dominate.

Turning to the splitting function matrix, each element can be expanded perturbatively as a function of α_s up to N^{3}LO as,

$$\boldsymbol{P}(x, \alpha_s) = \alpha_s \boldsymbol{P}^{(0)}(x) + \alpha_s^2 \boldsymbol{P}^{(1)}(x) + \alpha_s^3 \boldsymbol{P}^{(2)}(x) + \alpha_s^4 \boldsymbol{P}^{(3)}(x) + \dots , \tag{6.5}$$

where we have omitted the scale argument of $\alpha_s(\mu_r^2 = \mu_f^2) \equiv \alpha_s$ for brevity and $\boldsymbol{P}^{(0)}$, $\boldsymbol{P}^{(1)}$, $\boldsymbol{P}^{(2)}$ are known [34, 62, 63, 160–163]. $\boldsymbol{P}^{(3)}$ are the four-loop quantities which we approximate in Chapter 7 using information from [159, 164–172].

Considering Equation (6.1), $\Sigma(Q^2)$ and $g(Q^2)$ are the singlet and gluon PDFs respectively, evolved to the required Q^2 energy of the process via Equation (6.3). For more information on the relevant formulae used in this convolution, the reader is referred to [173].

Thus far, we have limited our discussion to only light quark flavours. However, as we move through the full range of Q^2 values, the number of partons which are kinematically accessible increases. More specifically, as we pass over the charm and bottom mass thresholds (where $Q^2 = m_{c,b}^2$) we must account for the heavy quark PDFs and their corresponding contributions.

To deal with the heavy quark contributions to the total structure function, whilst remaining consistent with the light quark picture described above, we consider

$$f_\alpha^{n_f+1}(x, Q^2) = \left[A_{\alpha i}(Q^2/m_h^2) \otimes f_i^{n_f}(Q^2) \right](x), \tag{6.6}$$

where we have an implied summation over partons i and $A_{\alpha i}$ are the heavy flavour transition matrix elements [37, 38] which explicitly depend on the heavy flavour mass threshold m_h, where these contributions are activated[2]. We also denote the PDFs as $f_i^{n_f}$ and $f_i^{n_f+1}$ to indicate whether the PDF has been evolved with only light flavours (n_f) or also with heavy flavours ($n_f + 1$). In this work we only consider contributions at heavy flavour threshold i.e. where $Q^2 = m_h^2$. We then define the PDFs:

$$f_q^{n_f+1}(x, Q^2) = \left[A_{qq,H}(Q^2/m_h^2) \otimes f_q^{n_f}(Q^2) + A_{qg,H}(Q^2/m_h^2) \otimes f_g^{n_f}(Q^2)\right](x) \quad (6.7a)$$

$$f_g^{n_f+1}(x, Q^2) = \left[A_{gq,H}(Q^2/m_h^2) \otimes f_q^{n_f}(Q^2) + A_{gg,H}(Q^2/m_h^2) \otimes f_g^{n_f}(Q^2)\right](x) \quad (6.7b)$$

$$f_H^{n_f+1}(x, Q^2) = \left[A_{Hq}(Q^2/m_h^2) \otimes f_q^{n_f}(Q^2) + A_{Hg}(Q^2/m_h^2) \otimes f_g^{n_f}(Q^2)\right](x) \quad (6.7c)$$

where we have an implicit summation over light flavours of q and a generalised theoretical description to involve heavy flavour contributions[3]. Equation (6.7a) and Equation (6.7b) are the light flavour quark and gluon PDFs defined earlier, modified to include contributions mediated by heavy flavour loops. Whereas in Equation (6.7c) we describe the heavy flavour PDF, perturbatively calculated from the light quark and gluon PDFs.

By considering the number of vertices (and hence orders of α_s) required for each of these transition matrix elements to contribute to their relevant 'output' partons, we are immediately able to show:

[2] The indices here run as $\alpha \in \{H, q, g\}$ and $i \in \{q, g\}$, since n_f is the number of light flavours.

[3] Note that the notation $A_{\alpha i,H}$ is exactly equivalent to $A_{\alpha i}$. When H is not present in the final state of matrix element interactions, we opt for the $A_{\alpha i,H}$ notation. This is to remind the reader that these elements are considering only those interactions involving a heavy quark.

$$
\begin{aligned}
A_{qq,H} &= \delta(1-x) \; + \; \mathcal{O}(\alpha_s^2) & \qquad A_{gg,H} &= \delta(1-x) \; + \; \mathcal{O}(\alpha_s) \\
A_{qg,H} &= \mathcal{O}(\alpha_s^2) & \qquad A_{Hq} &= \mathcal{O}(\alpha_s^2) \\
A_{gq,H} &= \mathcal{O}(\alpha_s^2) & \qquad A_{Hg} &= \mathcal{O}(\alpha_s)
\end{aligned} \tag{6.8}
$$

where $A_{qq,H}$ and $A_{gg,H}$ include LO δ-functions to ensure this description is consistent with the light quark picture discussed earlier. It is therefore the A_{Hg} transition matrix element which provides our lowest order contribution to the heavy flavour sector (i.e. $g \to H\overline{H}$).

The insertion of scale independent contributions to $A_{\alpha i}$ introduce unwanted discontinuities at NNLO into the PDF evolution. In order to ensure the required smoothness and validity of the structure functions across (x, Q^2), these discontinuities must be accounted for elsewhere in the structure function picture. Equating the coefficient functions above the mass threshold m_h^2 (describing the total number of flavours including heavy flavour quarks) and those below this threshold, discontinuities are able to be absorbed by a suitable redefinition of the coefficient functions. This procedure provides the foundation for the description of different number schemes.

There are two number schemes which are preferred at different points in the Q^2 range. Towards $Q^2 \leq m_h^2$ we adopt the Fixed Flavour Number Scheme (FFNS). Towards $\frac{Q^2}{m_h^2} \to \infty$, the heavy contributions can be considered massless and therefore the Zero Mass Variable Flavour Number Scheme (ZM-VFNS) is assumed. In order to join the FFNS and ZM-VFNS schemes seamlessly together, we ultimately wish to describe the General Mass Variable Number Scheme (GM-VFNS) [59] (which is valid across all Q^2). This scheme can then account for discontinuities from transition matrix elements and re-establish a smooth description of the structure functions.

In [60] an ambiguity in the definition of the GM-VFNS scheme was pointed out (namely the freedom to swap $\mathcal{O}(m_h^2/Q^2)$ terms without violating the definition of the GM-VFNS). We note here that since [64], MSHT PDFs have employed the TR scheme to define the distribution of $\mathcal{O}(m_h^2/Q^2)$ terms, the specific details of which are found in [60, 140, 141]. The general method to relate the FFNS and GM-VFNS number schemes is to compare the prediction for a result e.g. the F_2 structure function in the FFNS scheme:

$$\begin{aligned} F_2(x,Q^2) &= F_{2,q}(x,Q^2) \; + \; F_{2,H}(x,Q^2) \\ &= C_{q,i}^{\text{FF},\,n_f} \otimes f_i^{n_f}(Q^2) + C_{H,i}^{\text{FF},\,n_f} \otimes f_k^{n_f}(Q^2) \\ &= C_{q,q}^{\text{FF},\,n_f} \otimes f_q^{n_f}(Q^2) + C_{q,g}^{\text{FF},\,n_f} \otimes f_g^{n_f}(Q^2) \\ &+ C_{H,q}^{\text{FF},\,n_f} \otimes f_q^{n_f}(Q^2) + C_{H,g}^{\text{FF},\,n_f} \otimes f_g^{n_f}(Q^2) \end{aligned} \tag{6.9}$$

and the GM-VFNS scheme,

$$\begin{aligned} F_2(x,Q^2) = \sum_{\alpha\in\{H,q,g\}} \Big(& C_{q,\alpha}^{\text{VF},\,n_f+1} \otimes A_{\alpha i}(Q^2/m_h^2) \otimes f_i^{n_f}(Q^2) \\ & + C_{H,\alpha}^{\text{VF},\,n_f+1} \otimes A_{\alpha i}(Q^2/m_h^2) \otimes f_i^{n_f}(Q^2) \Big) , \end{aligned} \tag{6.10}$$

where $F_{2,q}$ and $F_{2,H}$ are the light and heavy flavour structure functions respectively[4]. C^{FF,n_f} and C^{VF,n_f+1} are the FFNS (known up to NLO [174, 175] with some information at NNLO [176–178] including high-Q^2 transition matrix elements at $\mathcal{O}(\alpha_s^3)$ [178–183]) and GM-VFNS coefficient functions respectively, and $A_{\alpha i}(Q^2/m_h^2)$ are the transition matrix elements. We note that the above also applies to other structure functions and for clarity, in the following we consider the light and heavy structure functions separately.

[4]The extra contribution from $F_{2,H}$ allows for the possibility of final state heavy flavours.

6.1.1. $F_{2,q}$

Expanding the first term in Equation (6.10) in terms of the transition matrix elements results in,

$$\begin{aligned} F_{2,q}(x,Q^2) = C_{q,H}^{\mathrm{VF},\,n_f+1} \otimes \left[A_{Hq}(Q^2/m_h^2) \otimes f_q^{n_f}(Q^2) + A_{Hg}(Q^2/m_h^2) \otimes f_g^{n_f}(Q^2) \right] \\ + C_{q,q}^{\mathrm{VF},\,n_f+1} \otimes \left[A_{qq,H}(Q^2/m_h^2) \otimes f_q^{n_f}(Q^2) + A_{qg,H}(Q^2/m_h^2) \otimes f_g^{n_f}(Q^2) \right] \\ + C_{q,g}^{\mathrm{VF},\,n_f+1} \otimes \left[A_{gq,H}(Q^2/m_h^2) \otimes f_q^{n_f}(Q^2) + A_{gg,H}(Q^2/m_h^2) \otimes f_g^{n_f}(Q^2) \right], \end{aligned} \tag{6.11}$$

which is valid at all orders. The first term in Equation (6.11) is the contribution to the light quark structure function from heavy quark PDFs (since the term contained within square brackets is exactly our definition in Equation (6.7c)). Due to this, the coefficient function $C_{q,H}$ describes the transition of a heavy quark to a light quark via a gluon and is therefore forbidden to exist below NNLO. The second and third terms here are the purely light quark and gluon contributions, with extra corrections from heavy quark at higher orders.

Using the definitions in Equation (6.8) we can obtain an equation for $F_{2,q}(x, Q^2)$ up to $\mathcal{O}(\alpha_s^3)$ as,

$$
\begin{aligned}
F_{2,q}(x,Q^2) = {} & C_{q,q}^{\mathrm{VF},\,(0)} \otimes f_q(Q^2) + \frac{\alpha_s}{4\pi}\left\{C_{q,q,\,n_f+1}^{\mathrm{VF},\,(1)} \otimes f_q(Q^2) + C_{q,g,\,n_f+1}^{\mathrm{VF},\,(1)} \otimes f_g(Q^2)\right\} \\
& + \left(\frac{\alpha_s}{4\pi}\right)^2 \left\{\left[C_{q,q,\,n_f+1}^{\mathrm{VF},\,(2)} + C_{q,q}^{\mathrm{VF},\,(0)} \otimes A_{qq,H}^{(2)}\right] \otimes f_q(Q^2) + \left[C_{q,g,\,n_f+1}^{\mathrm{VF},\,(2)}\right. \right. \\
& \left. \left. + C_{q,g,\,n_f+1}^{\mathrm{VF},\,(1)} \otimes A_{gg,H}^{(1)} + C_{q,q}^{\mathrm{VF},\,(0)} \otimes A_{qg,H}^{(2)}\right] \otimes f_g(Q^2)\right\} \\
& + \left(\frac{\alpha_s}{4\pi}\right)^3 \left\{\left[C_{q,q,\,n_f+1}^{\mathrm{VF},\,(3)} + C_{q,q,\,n_f+1}^{\mathrm{VF},\,(1)} \otimes A_{qq,H}^{(2)} + C_{q,g,\,n_f+1}^{\mathrm{VF},\,(1)} \otimes A_{gq,H}^{(2)}\right.\right. \\
& \left. + C_{q,q}^{\mathrm{VF},\,(0)} \otimes A_{qq,H}^{(3)}\right] \otimes f_q(Q^2) \\
& + \left[C_{q,g,\,n_f+1}^{\mathrm{VF},\,(3)} + C_{q,g,\,n_f+1}^{\mathrm{VF},\,(1)} \otimes A_{gg,H}^{(2)} + C_{q,q,\,n_f+1}^{\mathrm{VF},\,(1)} \otimes A_{qg,H}^{(2)}\right. \\
& \left. + C_{q,g,\,n_f+1}^{\mathrm{VF},\,(2)} \otimes A_{gg,H}^{(1)} + C_{q,q}^{\mathrm{VF},\,(0)} \otimes A_{qg,H}^{(3)}\right] \otimes f_g(Q^2) \\
& \left. + C_{q,H}^{\mathrm{VF},\,(2)} \otimes A_{Hg}^{(1)} \otimes f_g(Q^2)\right\} + \mathcal{O}(\alpha_s^4) \qquad (6.12)
\end{aligned}
$$

where $C_{q,q}^{\mathrm{VF},\,(0)} = \delta(1-x)$ up to charge weighting. Equation (6.12) defines the light quark structure function to N^{3}LO including heavy flavour corrections[5].

6.1.2. $F_{2,H}$

Moving to the heavy quark structure function in Equation (6.9), as above the second term in Equation (6.10) can be expanded in terms of the transition matrix elements to

[5] We also note that $\alpha_s^{n_f+1} \neq \alpha_s^{n_f}$ and account for this, but omit in expressions such as Equation (6.12) for simplicity

obtain,

$$\begin{aligned} F_{2,H}(x,Q^2) = C_{H,H}^{\mathrm{VF},\,n_f+1} \otimes \left[A_{Hq}(Q^2/m_h^2) \otimes f_q^{n_f}(Q^2) + A_{Hg}(Q^2/m_h^2) \otimes f_g^{n_f}(Q^2) \right] \\ + C_{H,q}^{\mathrm{VF},\,n_f+1} \otimes \left[A_{qq,H}(Q^2/m_h^2) \otimes f_q^{n_f}(Q^2) + A_{qg,H}(Q^2/m_h^2) \otimes f_g^{n_f}(Q^2) \right] \\ + C_{H,g}^{\mathrm{VF},\,n_f+1} \otimes \left[A_{gq,H}(Q^2/m_h^2) \otimes f_q^{n_f}(Q^2) + A_{gg,H}(Q^2/m_h^2) \otimes f_g^{n_f}(Q^2) \right], \end{aligned} \tag{6.13}$$

which is valid at all orders. Similar to Equation (6.11), we have a contribution from the heavy flavour quarks, the light quarks and the gluon respectively. However in this case, due to the required gluon intermediary, the coefficient functions associated with the light quark flavours and gluon are forbidden to exist below NNLO. Considering the $C_{H,H}$ function, we are able to choose this to be identically the ZM-VFNS light quark coefficient function $C_{q,q}$ up to kinematical suppression factors, since at $Q^2 \to \infty$ these functions must be equivalent [59, 141, 184].

The full heavy flavour structure function then reads as,

$$
\begin{aligned}
F_{2,H}(x,Q^2) = \frac{\alpha_s}{4\pi}\left[C_{H,g}^{\mathrm{VF},\,(1)} + C_{H,H}^{\mathrm{VF},\,(0)} \otimes A_{Hg}^{(1)}\right] \otimes f_g(Q^2) \\
+ \left(\frac{\alpha_s}{4\pi}\right)^2 \Bigg\{ \left[C_{H,q}^{\mathrm{VF},\,(2)} + C_{H,H}^{\mathrm{VF},\,(0)} \otimes A_{Hq}^{(2)}\right] \otimes f_q(Q^2) \\
+ \left[C_{H,g}^{\mathrm{VF},\,(2)} + C_{H,g}^{\mathrm{VF},\,(1)} \otimes A_{gg,H}^{(1)} + C_{H,H}^{\mathrm{VF},\,(1)} \otimes A_{Hg}^{(1)} + C_{H,H}^{\mathrm{VF},\,(0)} \otimes A_{Hg}^{(2)}\right] \otimes f_g(Q^2) \Bigg\} \\
+ \left(\frac{\alpha_s}{4\pi}\right)^3 \Bigg\{ \left[C_{H,q}^{\mathrm{VF},\,(3)} + C_{H,g}^{\mathrm{VF},\,(1)} \otimes A_{gq,H}^{(2)} \right. \\
\left. + C_{H,H}^{\mathrm{VF},\,(1)} \otimes A_{Hq}^{(2)} + C_{H,H}^{\mathrm{VF},\,(0)} \otimes A_{Hq}^{(3)}\right] \otimes f_q(Q^2) \\
+ \left[C_{H,g}^{\mathrm{VF},\,(3)} + C_{H,g}^{\mathrm{VF},\,(2)} \otimes A_{gg,H}^{(1)} + C_{H,g}^{\mathrm{VF},\,(1)} \otimes A_{gg,H}^{(2)} + C_{H,H}^{\mathrm{VF},\,(2)} \otimes A_{Hg}^{(1)} \right. \\
\left. + C_{H,H}^{\mathrm{VF},\,(1)} \otimes A_{Hg}^{(2)} + C_{H,H}^{\mathrm{VF},\,(0)} \otimes A_{Hg}^{(3)}\right] \otimes f_g(Q^2) \Bigg\}
\end{aligned}
\tag{6.14}
$$

where combining Equation (6.12) and Equation (6.14), one can obtain the full structure function $F_2(x,Q^2)$. Equating the FFNS expansion from Equation (6.9) to the above expressions in the GM-VFNS setting, one can find relationships between the two pictures. In Chapter 9 we use this equivalence to enable the derivation of the GM-VFNS functions at N^{3}LO.

To summarise, we have identified the leading theoretical ingredients entering the structure functions and detailed how these affect the PDFs. As we will discuss further, when pushing these equations to N^{3}LO, there is already some knowledge available. For example, the N^{3}LO ZM-VFNS coefficient functions are known precisely for $n_f = 3$ from [185], as are a handful of Mellin moments [159, 171, 172, 179] and leading small and large-x terms [164–170, 178, 180–182] associated with the splitting functions and transition matrix elements at N^{3}LO. Using this information, we approximate these

functions to N^{3}LO and incorporate the results into the first approximate N^{3}LO global PDF fit.

6.2. Approximation Framework: Discrete Moments

As discussed in Chapter 3 and more specifically in Sect. 6.1, there exists sets of splitting functions and transition matrix elements which, along with the coefficient functions, are primary sources of MHOUs.

In order to estimate the sources of MHOUs from N^{3}LO splitting functions and transition matrix elements, and ultimately include them into the multi-parameter framework described in Chapter 5, one must acquire some approximation at N^{3}LO. Here we summarise how using available sets of discrete Mellin moments for each function, along with any already calculated exact leading terms, can guide N^{3}LO estimations.

To perform the parameterisation of the unknown N^{3}LO quantities, we follow a similar estimation procedure as in [186, 187] following the form,

$$F(x) = \sum_{i=1}^{N_m} A_i f_i(x) + f_e(x). \tag{6.15}$$

In Equation (6.15), N_m is the number of available moments, A_i are calculable coefficients, $f_i(x)$ are functions chosen based on our intuition and theoretical understanding of the full function, and $f_e(x)$ encapsulates all the currently known leading exact contributions at either large or small-x. To describe this, consider a toy situation where we are given four data points described by some unknown degree 6 polynomial. Along with this information, we are told the dominant term at large-x is described by $2x^6$.

In this case, one may wish to attempt to approximate this function by means of a set of 4 simultaneous equations formed from Equation (6.15) equated to each of the four data points (or constraints). The result of this is then a unique solution for each chosen set of functions $\{f_i(x)\}$. However, a byproduct of this is that for each $\{f_i(x)\}$, one lacks any means to control the uncertainty in these approximate solutions. In order to allow a controllable level of uncertainty into this approximation, one must introduce an extra degree of freedom. This degree of freedom will be introduced through an unknown coefficient $a \equiv A_{N_m+1}$, which for convenience, will be absorbed into the definition of $f_e(x) \to f_e(x,a)$. In this toy example one is then able to choose to define the functions $f_i(x)$ as,

$$\begin{aligned} f_1(x) &= x^4, \\ f_2(x) &= x^3 \\ f_3(x) &= x^2 \\ f_4(x) &= 1 \quad \text{or} \quad x, \\ f_e(x,a) &= 2x^6 + ax^5, \end{aligned} \tag{6.16}$$

where we have prioritised approximating the large-x behaviour more precisely than the small-x behaviour i.e. the small-x behaviour contains an inherent functional uncertainty from the ambiguity in the choice of functions for $f_4(x)$. This could easily be adapted and even reversed depending on which region of x we are most sensitive to. Using these functions, one is then able to assemble a set of potential approximations to the overall polynomial, each uniquely defined by a set of functions and corresponding coefficients $\{A_i, a, f_i\}$.

As mentioned, for the N^{3}LO additions considered in this framework we use the available calculated moments as constraints for the corresponding simultaneous equa-

tions. In the case of the N^{3}LO QCD splitting functions, from recent results considering the four-loop splitting functions with the Balitsky-Fadin-Kuraev-Lipatov (BFKL) equation [170], the small-x leading logarithm (LL) is known exactly for all P_{ij}. Similarly for the N^{3}LO transition matrix elements, there is a mixture of small and large-x exact behaviours already known [180–183]. A summary of all the known and used ingredients for all N^{3}LO approximations is provided in Appendix C. The details of these known quantities will be discussed in detail in Chapter 7 and Chapter 8. We also mention here that towards the small-x regime, the leading terms present in the splitting functions and transition matrix elements exhibit the relations,

$$F_{gg}(x \to 0) \simeq \frac{C_A}{C_F} F_{gq}(x \to 0), \tag{6.17a}$$

$$F_{qq}(x \to 0) \simeq \frac{C_F}{C_A} F_{qg}(x \to 0), \tag{6.17b}$$

where $F_{ij} \in \{P_{ij}, A_{ij,H}\}$ and C_A, C_F are the usual QCD constants. Although Equation (6.17) are exact at leading order, it is known that as we expand to higher orders, these will break down due to the effect of large sub-leading logarithms. Due to this, we do not demand this relation as a constraint in our approximations. Instead we discuss the validity of Equation (6.17) in comparison with the aN^{3}LO functions.

Following from [186,187], we must choose a set of candidate functions for each $f_i(x)$. Our convention is to assign these functions such that at large-x, $f_1(x)$ is dominant, while at small-x, $f_{N_m}(x)$ is dominant. With $f_i(x)\ \forall i \in \{2, \ldots, N_m - 1\}$, dominating in the region between. This ensures enough scope to cover the full kinematic range of x with the goal of achieving a full picture of the entire function, not just in one specific region of x. The sets of functions assigned to each $f_i(x)$ are determined for each N^{3}LO function based on knowledge from lower orders and our intuition about what to expect at N^{3}LO.

Analogous to our toy polynomial example, we allow the inclusion of an unknown next-to-leading small-x logarithm (NLL) term (NNLL in the P_{gg} case) into the f_e function of our parameterisation. The coefficient of this NLL (NNLL) term is then controlled by a variational parameter a. This parameter uniquely defines the solution to the sets of simultaneous equations considered i.e. for each set of functions $f_i(x)$ there exists a unique solution for every possible choice of a. The final step to consider in this approximation is how to choose the prior allowed variation of a in a sensible way for each N^{3}LO approximation. To do this, we consider the criteria outlined below:

Criteria 1: At very small-x ($x < 10^{-5}$), we require the asymptote of f_e to be contained within the uncertainty band of the N^{3}LO approximation i.e. the full function cannot be in a large tension with the small-x description.

Criteria 2: At large-x ($x > 10^{-2}$) the N^{3}LO contribution should have relatively little effect. More specifically, we do not expect as large of a divergence as we do at small-x. Due to this, we require that the trend of the N^{3}LO approximation follow the general trend of the NNLO function at large-x.

The allowed variation in a gives us an uncertainty which, at its foundations, is chosen via a conservative estimate based on all the available prior knowledge about the function and lower orders being considered. To determine a full predicted uncertainty for the function and allow for a computationally efficient fixed functional form, the variation of a can absorb the uncertainty from the ambiguity in the choice of functions $f_i(x)$ (essentially expanding the allowed range of a). Since the functions are approximations themselves, increasing the allowed variation of a to encapsulate

the total uncertainty predicted by the initial treatment described above is a valid simplification.

A worked example following this procedure is provided for the $P_{qg}^{(3)}$ and $A_{Hg}^{(3)}$ functions in Chapter's 7 and 8 respectively.

6.3. Approximation Framework: Continuous Information

In the previous section we described the approximation framework employed for functions with discrete Mellin moment information, combined with any available exact information. For the N^{3}LO coefficient function approximations, we have access to a somewhat richer vein of information than the discrete moments discussed for the framework in Section 6.2. More specifically, approximations of the FFNS coefficient functions at N^{3}LO are known for the heavy quark contributions to the heavy flavour structure function $F_{2,H}(x, Q^2)$ at $Q^2 < m_{c,b}^2$ [176–178] (discussed further in Chapter 6). These approximations include the exact LL and mass threshold contributions, with an approximated NLL term (the details of this are described in Chapter 9). Furthermore, the N^{3}LO ZM-VFNS coefficient functions are known exactly [185]. Both of these contributions can then be combined with the transition matrix element approximations to define the GM-VFNS functions in the $Q^2 \leq m_c^2, m_b^2$ and $Q^2 \to \infty$ regimes (as introduced in Chapter 3 and extended to N^{3}LO in Chapter 6). Due to this, we base our approximations for the $C_{H,\{q,g\}}^{(3)}$ functions on the known continuous information in the low and high-Q^2 regimes.

To achieve a reliable approximation for $C^{(3)}_{H,\{q,g\}}$, we first fit a regression model with a large number of functions in (x, Q^2) space made available to the model (in order to reduce the level of functional bias in the parameterisation). This produces an unstable result at the extremes of the parameterisation (large-x and low-Q^2). However, it provides a basis for manually choosing a stable parameterisation to move between the two known regimes (low-Q^2 and high-Q^2).

Using the regression model predictions as a qualitative guide, we choose a stable and smooth interpolation between the two Q^2 regimes (low-Q^2 and high-Q^2) as given in Equation (6.18). This interpolation is observed to mirror the expected behaviour observed from lower orders, the regression model qualitative prediction having been calculated independently of lower orders and the best fit quality to data. By definition, we also ensure an exact cancellation between the coefficient functions and the transition matrix elements at the mass threshold energies as demanded by the theoretical description in Chapter 3 and more specifically in Chapter 6.

For the contributions to the heavy flavour structure function $F_{2,H}$ the final interpolations in the FFNS regime are defined as,

$$C^{\text{FF, (3)}}_{H,\,\{q,g\}} = \begin{cases} C^{\text{FF, (3)}}_{H,\,\{q,g\},\,\text{low-}Q^2}(x, Q^2 = m_h^2)\; e^{0.3\;(1-Q^2/m_h^2)} \\ \qquad\qquad + C^{\text{FF, (3)}}_{H,\,\{q,g\}}(x, Q^2 \to \infty)\left(1 - e^{0.3\;(1-Q^2/m_h^2)}\right) & \text{, if } Q^2 \geq m_h^2, \\ \\ C^{\text{FF, (3)}}_{H,\,\{q,g\},\,\text{low-}Q^2}(x, Q^2) & \text{, if } Q^2 < m_h^2. \end{cases} \tag{6.18}$$

where $C^{\text{FF, (3)}}_{H,\,\{q,g\},\,\text{low-}Q^2}$ are the already calculated approximate heavy flavour FFNS coefficient functions at $Q^2 \leq m_h^2$, and $C^{\text{FF, (3)}}_{H,\,\{q,g\}}(Q^2 \to \infty)$ is the limit at high-Q^2 found

from the known ZM-VFNS coefficient functions and relevant subtraction terms. Both of these limits will be discussed in detail on a case-by-case basis in Chapter 9.

For the heavy flavour contributions to $F_{2,q}$, we have no information about the low-Q^2 N^{3}LO FFNS coefficient functions. In this case, we use intuition from lower orders to provide a soft (lightly weighted) low-Q^2 target for our regression model in (x, Q^2). The chosen expected low-Q^2 behaviour is again discussed on a case-by-case basis in Chapter 9 for the relevant coefficient functions. However, since the overall contribution is very small from these functions, the exact form of these functions is not phenomenologically important at present. Further to this, our understanding from lower orders is that these functions have a weak dependence on Q^2 and so the form of the low-Q^2 description is even less important. As with the $C^{(3)}_{H,\,\{q,g\}}$ coefficient functions, the regression results provide an initial qualitative guide which exhibits instabilities in the extremes of (x, Q^2). We therefore employ a similar technique as before to ensure a smooth extrapolation across all (x, Q^2) into the unknown behaviour at low-Q^2. For these functions, the ansatz used is given as,

$$C^{\text{FF},\,(3)}_{q,\,\{q,g\}} = \begin{cases} C^{\text{FF, NS},\,(3)}_{q,\,q}(x, Q^2 \to \infty)\left(1 + e^{-0.5\,(Q^2/m_h^2)-3.5}\right), \\ C^{\text{FF, PS},\,(3)}_{q,\,q}(x, Q^2 \to \infty)\left(1 - e^{-0.25\,(Q^2/m_h^2)-0.3}\right), \\ C^{\text{FF},\,(3)}_{q,\,g}(x, Q^2 \to \infty)\left(1 - e^{-0.05\,(Q^2/m_h^2)+0.35}\right), \end{cases} \tag{6.19}$$

where $C^{\text{FF},\,(3)}_{q,\{q,g\}}(x, Q^2 \to \infty)$ is the known limit at high-Q^2.

Chapter 7.

N^{3}LO Splitting Functions

Splitting functions at N^{3}LO allow us to more accurately describe the evolution of the PDFs. These functions are estimated here and the resulting approximations are included within the framework described in Chapter 6. In all singlet cases we set $n_f = 4$ before constructing our approximations and ignore any corrections to this from any further change in the number of flavours[1]. In the non-singlet case, we calculate the approximate parts of $P_{qq}^{\mathrm{NS},\,(3)}$ with $n_f = 4$ however, there is a relatively large amount of information about the n_f-dependence included from [159]. Therefore in the final result we choose to allow the leading n_f-dependence to remain for the non-singlet splitting function.

[1] An exception to this are the cases of P_{qg} and P_{qq}^{PS} where we have already defined $P_{qg} \equiv n_f P_{qg}$ and $P_{qq}^{\mathrm{PS}} \equiv n_f P_{qq}^{\mathrm{PS}}$. Therefore the leading n_f dependence is already taken into account.

7.1. 4-loop Approximations

$P_{qg}^{(3)}$

We begin by considering the four-loop quark-gluon splitting function. Here we provide a more detailed explanation of the method described in Section 6.2 which will then be applied to the remaining splitting functions considered in this section. Four even-integer moments are known for $P_{qg}^{(3)}(n_f = 4)$ from [171,172], along with the LL small-x term from [164].

The functions we make available for the P_{qg} analysis are,

$$\begin{aligned}
f_1(x) &= \frac{1}{x} \quad \text{or} \quad \ln^4 x \quad \text{or} \quad \ln^3 x \quad \text{or} \quad \ln^2 x, \\
f_2(x) &= \ln x, \\
f_3(x) &= 1 \quad \text{or} \quad x \quad \text{or} \quad x^2, \\
f_4(x) &= \ln^4(1-x) \quad \text{or} \quad \ln^3(1-x) \quad \text{or} \quad \ln^2(1-x) \quad \text{or} \quad \ln(1-x), \\
f_e(x,\rho_{qg}) &= \frac{C_A^3}{3\pi^4}\left(\frac{82}{81} + 2\zeta_3\right)\frac{1}{2}\frac{\ln^2 1/x}{x} + \rho_{qg}\,\frac{\ln 1/x}{x},
\end{aligned} \tag{7.1}$$

where ρ_{qg} is the variational parameter. This is varied between $-2.5 < \rho_{qg} < -0.9$, which has been chosen to satisfy the criteria described in Section 6.2. The set of functions in Equation (7.1) is chosen from the analysis of lower orders. Specifically, following the pattern of functions from lower orders, it can be shown that at this order we expect the most dominant large-x term to be $\ln^4(1-x)$ and $\ln^4 x$ to be the highest power of $\ln x$ at small-x.

Fig. 7.1 displays an example of the variation found from the different choices of functions that encapsulate the chosen range of ρ_{qg}. We also show the upper (A) and

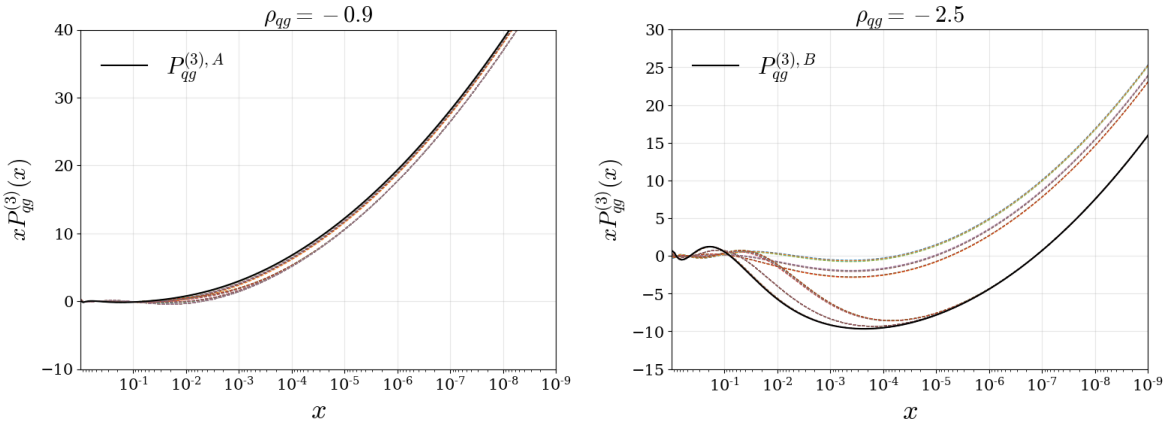

Figure 7.1.: Combinations of functions with an added variational factor (ρ_{qg}) controlling the NLL term. Combinations of functions at the upper (left) and lower (right) bounds of the variation are shown. The solid lines indicate the upper and lower bounds for this function chosen from the relevant criteria. The coloured lines show the candidate functions from each combination of functional forms in (7.1).

lower (B) bounds (at small-x) for the entire uncertainty (solid line) combining the variation in the functions and in the variation of ρ_{qg}. The upper ($P_{qg}^{(3),A}$) and lower ($P_{qg}^{(3),B}$) bounds are given by,

$$P_{qg}^{(3),A} = 5.5219\,\frac{1}{x} + 10.401\,\ln x - 6.5373\,x^2 + 0.0036299\,\ln^4(1-x) + \frac{C_A^3}{3\pi^4}\left(\frac{82}{81} + 2\zeta_3\right)\frac{1}{2}\frac{\ln^2 1/x}{x} - 1.7\,\frac{\ln 1/x}{x}, \quad (7.2)$$

$$P_{qg}^{(3),B} = 12.582\,\ln^2 x + 5.3065\,\ln x + 1.7957\,x^2 - 0.0041296\,\ln^4(1-x) + \frac{C_A^3}{3\pi^4}\left(\frac{82}{81} + 2\zeta_3\right)\frac{1}{2}\frac{\ln^2 1/x}{x} - 2.5\,\frac{\ln 1/x}{x}. \quad (7.3)$$

Using this information, a fixed functional form is chosen to be,

$$P_{qg}^{(3)} = A_1 \ln^2 x + A_2 \ln x + A_3 x^2 + A_4 \ln^4(1-x) + \frac{C_A^3}{3\pi^4}\left(\frac{82}{81} + 2\zeta_3\right)\frac{1}{2}\frac{\ln^2 1/x}{x} + \rho_{qg}\frac{\ln 1/x}{x} \quad (7.4)$$

and ρ_{qg} is allowed to vary as $-2.5 < \rho_{qg} < -0.8$. This fixed functional form identically matches with the lower bound $P_{qg}^{(3),B}$ and the expansion of the variation of ρ_{qg} enables (to within $\sim 1\%$) the absorption of the small-x upper bound uncertainty (predicted from $P_{qg}^{(3),A}$) into the variation. In other areas of x there are larger deviations from the upper bound ($\sim 10\%$) when using this convenient fixed functional form. However, in these regions the function is already relatively small, therefore any larger percentage deviations are negligible. Also since the heuristic choice of variation found earlier is intended as a guide, we are not bound by any solid constraints to precisely reconstruct it with our subsequent choice of fixed functional form. Therefore it is entirely justified to be able to slightly adapt the shape of the variation in less dominant regions.

$P_{qq}^{\mathrm{NS},\,(3)}$

As discussed in Chapter 3, the quark-quark splitting function is comprised of a pure-singlet and non-singlet contribution. We approximate each part independently, although the final quark-quark singlet function will be almost completely dominated by the pure-singlet, except at very high-x.

The four-loop non-singlet splitting function has been the subject of relatively extensive research and is known exactly for a number of regimes. For example in [159], some important exact contributions to the four-loop non-singlet splitting functions are presented, along with 8 even-integer moments for each of the $+$ and $-$ distributions [159].

In this discussion we are exclusively approximating the non-singlet +-distribution, as this is the part that contributes to the full singlet quark-quark splitting function. The other relevant non-singlet distributions $P_{\text{NS}}^{(3),\,-}$ and $P_{\text{NS}}^{(3),\,\text{sea}}$ (described in [62]), are set to the central values predicted from [159] since any variation in these functions are negligible. All presently known information is used in this approximation, with results similar to that seen in [159] but with our own choice of functions.

$$f_1(x) = \frac{1}{(1-x)_+}, \qquad f_2(x) = (1-x)\,\ln(1-x), \qquad f_3(x) = (1-x)\,\ln^2(1-x),$$
$$f_4(x) = (1-x)\,\ln^3(1-x), \quad f_5(x) = 1, \quad f_6(x) = x, \quad f_7(x) = x^2, \quad f_8(x) = \ln^2 x,$$

$$\begin{aligned} f_e(x,\rho_{qq}^{\text{NS}}) &= C_F n_c^3 P_{\text{L},0}^{(3)}(x) + C_F n_c^2 n_f P_{\text{L},1}^{(3)}(x) + P_{Ln_f}^{(3)+}(x) + \rho_{qq}^{\text{NS}}\,\ln^3 x \\ &\quad - 55.876\,\ln^4 x - 2.8313\,\ln^5 x - 0.14883\,\ln^6 x - 2601.7 - 2118.9\,\ln(1-x) \\ &\quad + n_f\left(4.6584\,\ln^4 x + 0.2798\,\ln^5 x + 312.16 + 337.93\,\ln(1-x)\right) \end{aligned} \tag{7.5}$$

where the functions $C_F n_c^3 P_{\text{L},0}^{(3)}(x) + C_F n_c^2 n_f P_{\text{L},1}^{(3)}(x)$ and $P_{Ln_f}^{(3)+}(x)$ can be found in Equation (4.11) and Equation (4.14) respectively within [159], and ρ_{qq}^{NS} is our variational parameter. Note that the ansatz from Equation (6.15) has been extended to include 8 pairs of functions and coefficients, to accommodate 8 known moments. Within the $f_e(x,\rho_{qq}^{\text{NS}})$ part of Equation (7.5), we have chosen to vary the coefficient of the most divergent unknown small-x term ($\ln^3 x$) with the variation across $0 < \rho_{qq}^{\text{NS}} < 0.014$. Due to the high level of information and larger number of functions allowed to be included, we ignore any functional uncertainty and explicitly define each function. Therefore the only variation needed to be considered as an uncertainty stems from the variation of ρ_{qq}^{NS}.

The resulting approximation is then,

$$P_{\rm NS}^{(3),\,+} = A_1\,\frac{1}{(1-x)_+} + A_2\,(1-x)\,\ln(1-x) + A_3\,(1-x)\,\ln^2(1-x) + A_4\,(1-x)\,\ln^3(1-x) + A_5 + A_6\,x + A_7\,x^2 + A_8\,\ln^2 x + f_e(x,\rho_{qq}^{\rm NS}), \quad (7.6)$$

where no alterations are made to the allowed range of $0 < \rho_{qq}^{\rm NS} < 0.014$.

$P_{qq}^{\rm PS,\,(3)}$

We now restrict our analysis to focus on approximating the pure-singlet part of $P_{qq}^{(3)}$, thereby providing a more accurate set of functions with a focus on the small-x regime. To ensure the $P_{qq}^{\rm PS,\,(3)}$ function does not interfere with the large-x regime (where the non-singlet description dominates) the ansatz from Equation (6.15) is adapted to be:

$$P_{ij}^{(3)}(x) = \Big\{A_1 f_1(x) + A_2 f_2(x) + A_3 f_3(x) + A_4 f_4(x)\Big\}(1-x) + f_e(x,\rho_{qq}^{\rm PS}). \quad (7.7)$$

This modified parameterisation guarantees that any instabilities in the pure singlet approximation will not wash out the non-singlet behaviour at large-x.

Using four available even-integer moments for $n_f = 4$ [171, 172] and the exact small-x information [164], the chosen set of functions for this approximation is,

$$\begin{aligned}
f_1(x) &= \frac{1}{x} && \text{or} \quad \ln^4 x, \\
f_2(x) &= \ln^3 x && \text{or} \quad \ln^2 x && \text{or} \quad \ln x, \\
f_3(x) &= 1 && \text{or} \quad x && \text{or} \quad x^2, \\
f_4(x) &= \ln^4(1-x) && \text{or} \quad \ln^3(1-x) && \text{or} \quad \ln^2(1-x) \quad \text{or} \quad \ln(1-x), \\
f_e(x, \rho_{qq}^{\rm PS}) &= \frac{C_A^2 C_F}{3\pi^4}\left(\frac{82}{81} + 2\zeta_3\right)\frac{1}{2}\frac{\ln^2 1/x}{x} + \rho_{qq}^{\rm PS}\,\frac{\ln 1/x}{x}, && && && (7.8)
\end{aligned}$$

where $\rho_{qq}^{\rm PS}$ is varied as $-0.7 < \rho_{qq}^{\rm PS} < 0$. For the variation produced from stable combinations of these functions, we coincidentally end up with the same functional form for both the upper $P_{\rm PS}^{(3),\,A}$ and lower $P_{\rm PS}^{(3),\,B}$ bounds. Therefore trivially, the fixed functional form is defined as:

$$\begin{aligned}
P_{\rm PS}^{(3)} = \left\{A_1\,\frac{1}{x} + A_2\,\ln^2 x + A_3\,x^2 + A_4\,\ln^2(1-x)\right\}(1-x) + \\
\frac{C_A^2 C_F}{3\pi^4}\left(\frac{82}{81} + 2\zeta_3\right)\frac{1}{2}\frac{\ln^2 1/x}{x} + \rho_{qq}^{\rm PS}\,\frac{\ln 1/x}{x}(1-x) \quad (7.9)
\end{aligned}$$

where the variation of $\rho_{qq}^{\rm PS}$ is unchanged and the entire predicted variation is encapsulated in this form.

$P_{gq}^{(3)}$

As with the previous singlet splitting functions, four even-integer moments for $n_f = 4$ are known [171, 172] along with the LL small-x information [165–167]. The set of

functions we make available for the combinations in our approximation are stated as,

$$\begin{aligned} f_1(x) &= \frac{\ln 1/x}{x} \quad \text{or} \quad \frac{1}{x}, \\ f_2(x) &= \ln^3 x, \\ f_3(x) &= x \quad \text{or} \quad x^2, \\ f_4(x) &= \ln^4(1-x) \quad \text{or} \quad \ln^3(1-x) \quad \text{or} \quad \ln^2(1-x) \quad \text{or} \quad \ln(1-x), \\ f_e(x,\rho_{gq}) &= \frac{C_A^3 C_F}{3\pi^4}\zeta_3 \frac{\ln^3 1/x}{x} + \rho_{gq}\,\frac{\ln^2 1/x}{x}, \end{aligned} \tag{7.10}$$

where ρ_{gq} is set as $\rho_{gq} = -1.8$. In this case, the variation from the choice of functions is large enough to satisfy the criteria in Section 6.2 and encapsulate a sensible $\pm 1\sigma$ variation without including any further variation in ρ_{gq}. Similarly to previous approximations, for stable variations we estimate this variation with the fixed functional form,

$$P_{gq}^{(3)} = A_1\,\frac{\ln 1/x}{x} + A_2\,\ln^3 x + A_3\,x + A_4\,\ln(1-x) + \frac{C_A^3 C_F}{3\pi^4}\zeta_3\frac{\ln^3 1/x}{x} + \rho_{gq}\,\frac{\ln^2 1/x}{x} \tag{7.11}$$

where the allowed range of ρ_{gq} is expanded to $-1.8 < \rho_{gq} < -1.5$ to approximate the variation from the choice of functions. As with the $P_{qg}^{(3)}$ fixed functional form, this new range recovers a variation which is within $\sim 1\%$ of the original, in the dominant areas of x.

$P_{gg}^{(3)}$

Finally we move to the approximation of the gluon-gluon splitting function, where four available even-integer moments for $P_{gg}^{(3)}(n_f = 4)$ are known from [171, 172]. The

list of functions (including the known small-x LL and NLL terms from [165–169]) used for the approximation is,

$$\begin{aligned}
f_1(x) &= \frac{1}{x} \quad \text{or} \quad \ln^3 x \quad \text{or} \quad \ln^2 x, \\
f_2(x) &= \ln x, \\
f_3(x) &= 1 \quad \text{or} \quad x \quad \text{or} \quad x^2, \\
f_4(x) &= \frac{1}{(1-x)_+} \quad \text{or} \quad \ln^2(1-x) \quad \text{or} \quad \ln(1-x),
\end{aligned}$$

$$\begin{aligned}
f_e(x,\rho_{gg}) \;=\; & \frac{C_A^4}{3\pi^4}\zeta_3\frac{\ln^3 1/x}{x} + \frac{1}{\pi^4}\left[C_A^4\left(-\frac{1205}{162}+\frac{67}{36}\zeta_2+\frac{1}{4}\zeta_2^2-\frac{11}{2}\zeta_3\right)\right. \\
& + n_f C_A^3\left(-\frac{233}{162}+\frac{13}{36}\zeta_2-\frac{1}{3}\zeta_3\right) \\
& \left. + n_f C_A^2 C_F\left(\frac{617}{243}-\frac{13}{18}\zeta_2+\frac{2}{3}\zeta_3\right)\right]\frac{1}{2}\frac{\ln^2 1/x}{x} \;+\; \rho_{gg}\,\frac{\ln 1/x}{x}, \qquad (7.12)
\end{aligned}$$

where ρ_{gg} is varied as $-5 < \rho_{gg} < 15$ and $n_f = 4$. The fixed functional form is then chosen to be,

$$\begin{aligned}
P_{gg}^{(3)} = {} & A_1\,\ln^2 x + A_2\,\ln x + A_3\,x^2 + A_4\,\ln^2(1-x) + \frac{C_A^4}{3\pi^4}\zeta_3\frac{\ln^3 1/x}{x} \\
& + \frac{1}{\pi^4}\left[C_A^4\left(-\frac{1205}{162}+\frac{67}{36}\zeta_2+\frac{1}{4}\zeta_2^2-\frac{11}{2}\zeta_3\right) + n_f C_A^3\left(-\frac{233}{162}+\frac{13}{36}\zeta_2-\frac{1}{3}\zeta_3\right)\right. \\
& \left. + n_f C_A^2 C_F\left(\frac{617}{243}-\frac{13}{18}\zeta_2+\frac{2}{3}\zeta_3\right)\right]\frac{1}{2}\frac{\ln^2 1/x}{x} \;+\; \rho_{gg}\,\frac{\ln 1/x}{x}, \quad (n_f = 4) \qquad (7.13)
\end{aligned}$$

where we maintain the variation of ρ_{gg} from above, as the fixed functional form manages to encapsulate the variation predicted, without any extra allowed ρ_{gg} variation.

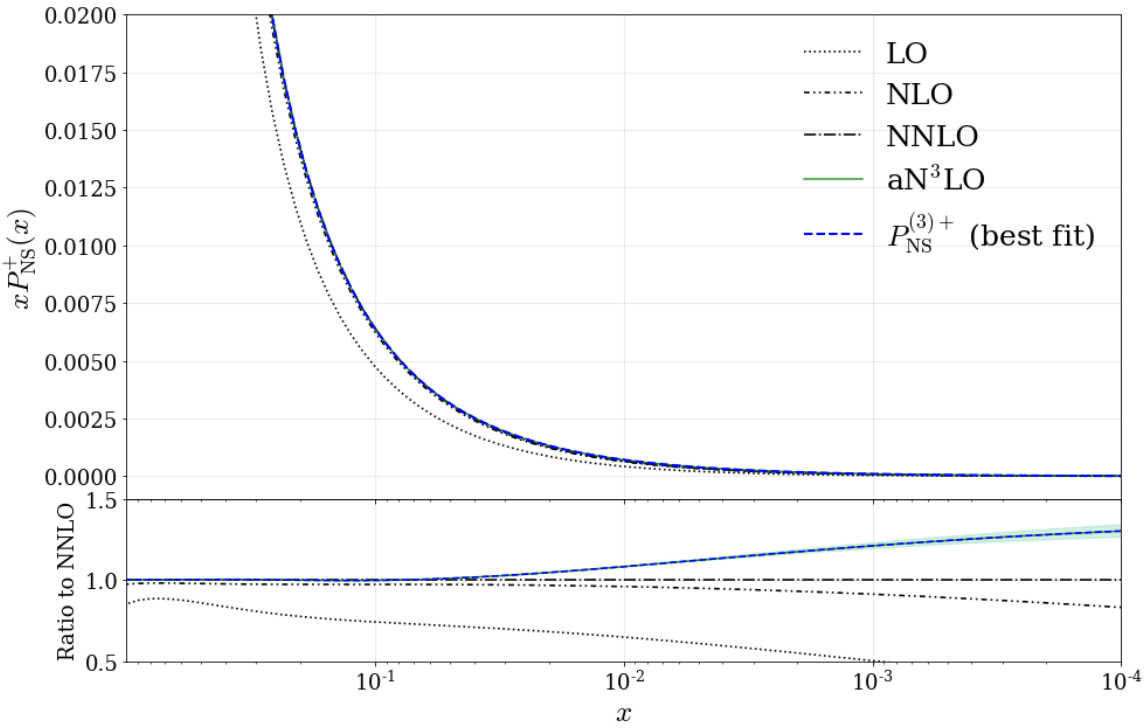

Figure 7.2.: Perturbative expansion up to aN^{3}LO for the non-singlet splitting function $P_{qq}^{\rm NS,+}$ including any corresponding allowed $\pm 1\sigma$ variation (shaded green region). The best fit value (blue dashed line) displays the prediction for this function determined from a global PDF fit.

7.2. Predicted aN^{3}LO Splitting Functions

Fig.'s 7.2, 7.3 and 7.4 show the perturbative expansions for each splitting function up to approximate N^{3}LO. Included with these expansions are the predicted variations ($\pm 1\sigma$) from Section 7.1 (shown in green) and the aN^{3}LO best fits (shown in blue – discussed further in Chapter 11). As a general feature, we observe that the singlet N^{3}LO approximations are much more divergent than lower orders due to the presence of higher order logarithms at small-x, further highlighting the need for an understanding of MHOUs which is not reliant on the NNLO central value.

Considering the non-singlet case shown in Fig. 7.2, we see a very close agreement at large-x between $P_{qq}^{\rm NS}$ expanded to NNLO and aN^{3}LO. This is a general feature of

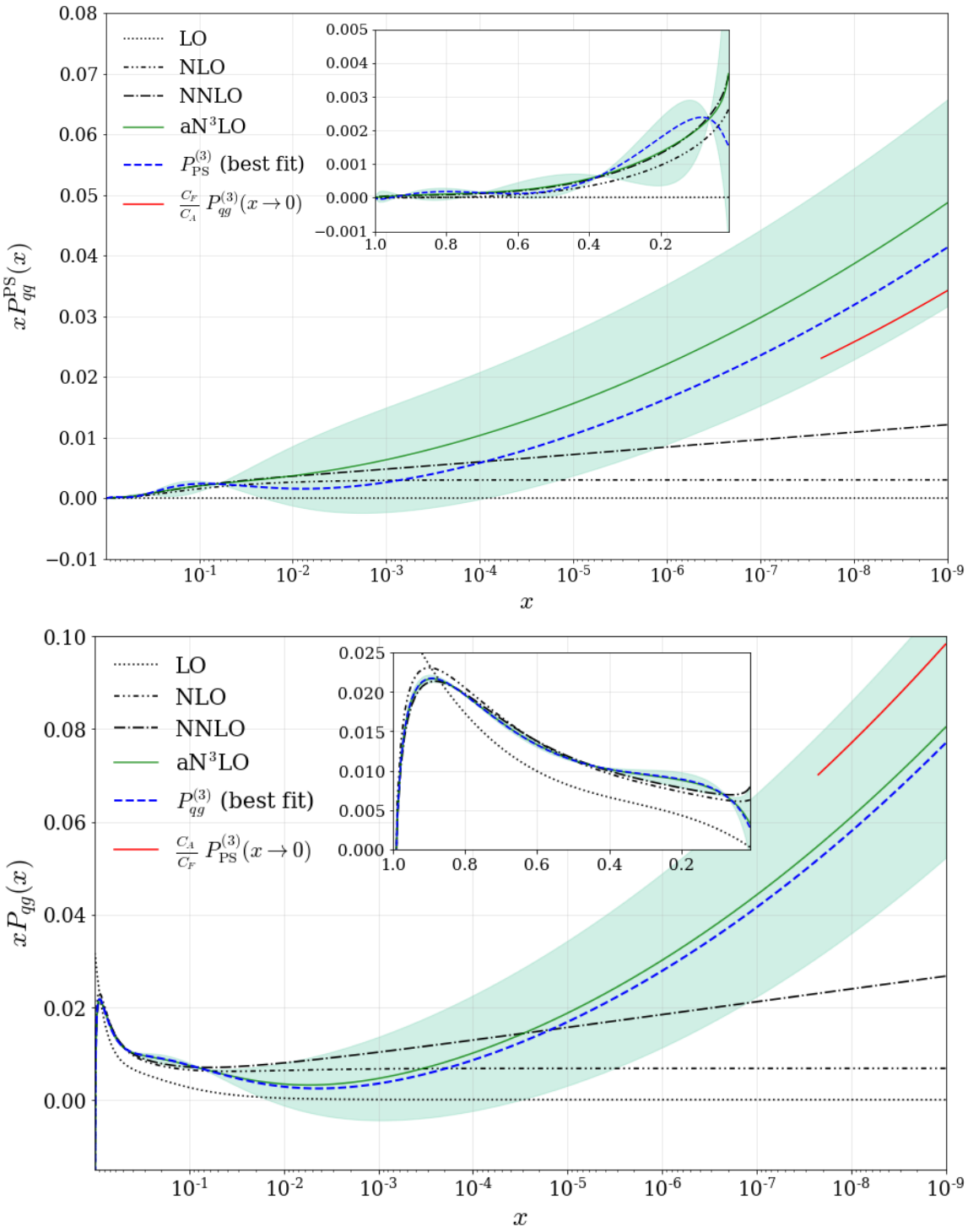

Figure 7.3.: Perturbative expansions up to aN^{3}LO for the quark singlet splitting functions $P_{qq}^{\rm PS}$ (top) and P_{qg} (bottom) including any corresponding allowed $\pm 1\sigma$ variation (shaded green region). The best fit values (blue dashed line) display the predictions for each function determined from a global PDF fit.

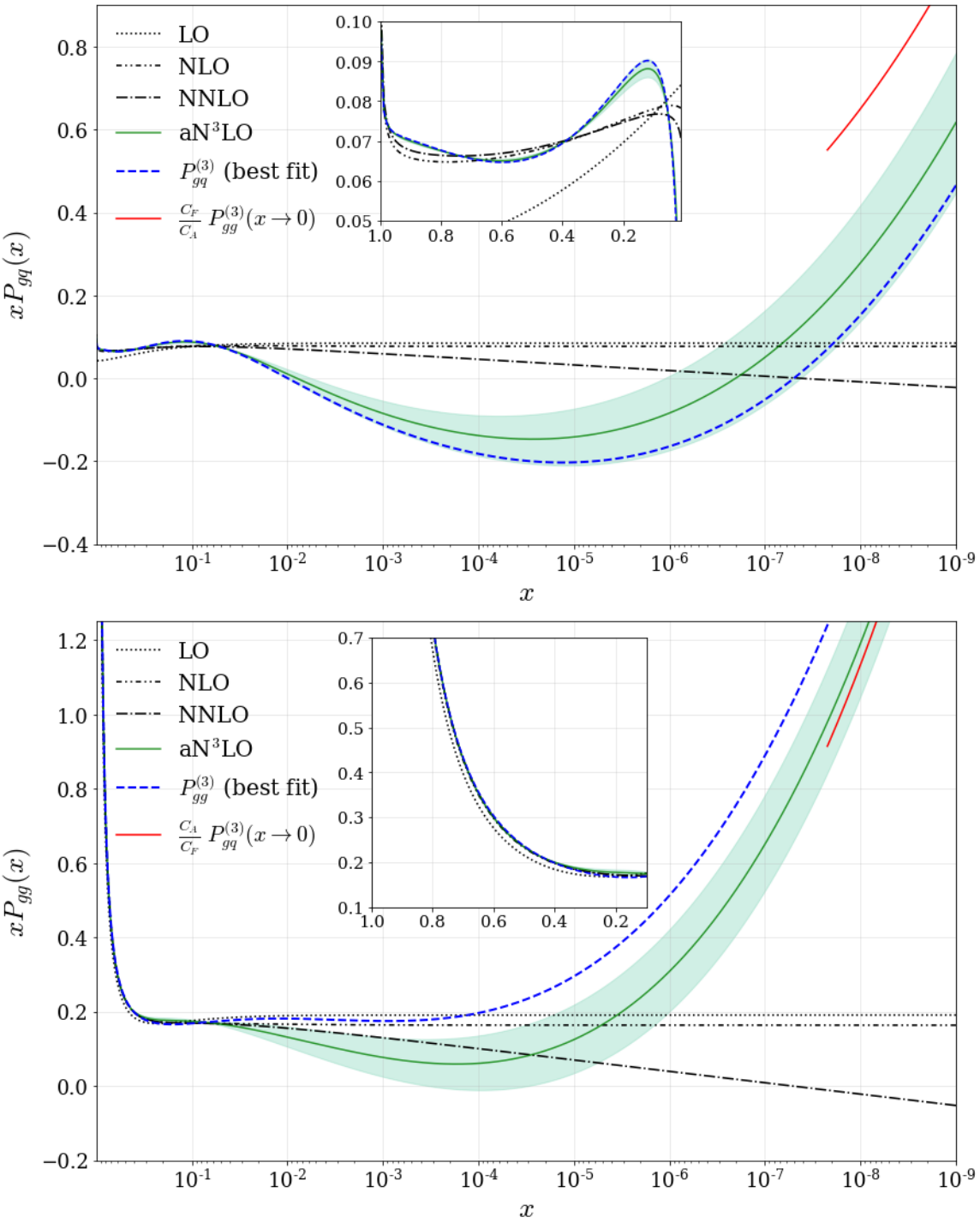

Figure 7.4.: Perturbative expansions for the gluon splitting functions P_{gq} (top) and P_{gg} (bottom) including any corresponding allowed $\pm 1\sigma$ variation (shaded green region). The best fit value (blue dashed line) displays the prediction for this function determined from a global PDF fit.

the non-singlet distribution, since by design, this distribution is largely unaffected by small-x contributions. The ratio plot in Fig. 7.2 provides clearer evidence for this, since it is only towards small-x (where the non-singlet distribution tends towards 0) that any noticeable difference between NNLO and aN^{3}LO can be seen.

The contributions to $P_{qq}^{\rm PS}$, P_{qg}, P_{gq} and P_{gg} shown in Fig.'s 7.3 and 7.4 respectively, display a much richer description at aN^{3}LO. In all cases, the divergent terms (with $x \to 0$) present in the approximations have a large effect from intermediate-x ($\sim 10^{-2}$) down to very small-x values. The asymptotic relationships (red line) Equation (6.17) defined using the best fit values of the aN^{3}LO expansions (i.e. comparable to the blue dashed line) are also shown in Fig.'s 7.3 and 7.4. As discussed earlier, these relations are violated by large sub-leading small-x terms and are therefore provided here as a qualitative comparison. Furthermore, we also observe a close resemblance to the N^{3}LO asymptotic results in Fig. 4 of [170]. Specifically for quark evolution, we show that the data prefers a similar form ($P_{qq}^{\rm PS}$ and P_{qg}) to the resummed splitting function results in [170] whereas for gluon evolution, this agreement is less prominent.

Superimposed onto these variations in Fig.'s 7.3 and 7.4 are the best fit values for the splitting functions, as predicted from a global fit of the full MSHT approximate N^{3}LO PDFs. The full fit results will be discussed in more detail in Chapter 11, however we note here that the fit produces relatively good agreement with the prior allowed variations for each of the splitting functions. For all functions except for P_{gg}, the best fit results lie within their $\pm 1\sigma$ variation range. This result implies that constraints from the data included in the global fit are in good agreement with the penalties describing quark evolution (i.e. $P_{\rm PS}$ and P_{qg} in Fig. 7.3). For the gluon evolution in Fig. 7.4 we observe a small level of tension with the data pushing towards a slightly harder small-x gluon than preferred by the penalty constraints for P_{gg}. An important

caveat to these best fit results is that the data included in the fit is sensitive to all orders in α_s. Therefore by proxy, the best fit predictions are also sensitive to corrections at all orders. This will certainly be a driving factor for any violations away from the expected N^{3}LO behaviour. However, since the ultimate goal of this investigation is to provide a theoretical uncertainty, the violation from higher orders is manifested into the defined penalties and therefore accounted for in the fit as a source of MHOU.

Finally, an important feature that can be seen across all these splitting function plots are points of zero aN^{3}LO uncertainty in the high-x regions. The regions where these points occur are where the moments are constraining the chosen fixed functional forms very tightly. In particular, for N_m moments (constraints) in Equation (6.15), we are left with $N_m - 1$ points of zero uncertainty predicted from our approximations. As stated, these points are dependent on the choice of our fixed functional form and are therefore regions where the uncertainty has been underestimated when compared to the functional uncertainty which the fixed form approximates. To provide a more complete estimate of the uncertainty in these areas, it would be necessary to smooth the uncertainty band out across these regions (or take into account several fixed functional forms). However, this shortcoming only occurs towards large-x, where the uncertainty is naturally smaller across these functions. Therefore if the uncertainty was smoothed, the effect would be negligible for the MHOUs this work aims to include in a PDF global fit. Further to this, these functions are ingredients in the DGLAP convolution where any smaller details are washed out by more dominant features inside convolutions with PDFs. For these reasons, we opt for computational efficiency and leave these points as shown.

	Moment	LO	NLO	NNLO	N^{3}LO
$P_{qq}^{\rm PS}$	$N=2$	-0.056588	-0.06362642	-0.06395712	-0.06412109
	$N=4$	-0.11104	-0.1261481	-0.12804822	-0.12835549
	$N=6$	-0.14329	-0.16188618	-0.16433013	-0.16470246
	$N=8$	-0.166448	-0.18751366	-0.19033329	-0.19074888
P_{qg}	$N=2$	0.042442	0.05008496	0.04991043	0.04983007
	$N=4$	0.023342	0.02203438	0.02110201	0.02112623
	$N=6$	0.016674	0.01387744	0.01311037	0.01316929
	$N=8$	0.013086	0.00979920	0.00919186	0.00927006
P_{gq}	$N=2$	0.056588	0.06362642	0.06395712	0.06412109
	$N=4$	0.015562	0.01903295	0.0195455	0.01965547
	$N=6$	0.008892	0.0112073	0.01158133	0.0116615
	$N=8$	0.006232	0.00801547	0.00831037	0.0083761
P_{gg}	$N=2$	-0.042442	-0.05008496	-0.04991043	-0.04983007
	$N=4$	-0.242978	-0.26161441	-0.26280015	-0.26326763
	$N=6$	-0.32551	-0.35114066	-0.35335022	-0.35384552
	$N=8$	-0.38091	-0.41151668	-0.41447721	-0.41495604

Table 7.1.: Numerical moments of singlet and gluon splitting function moments up to N^{3}LO for $\alpha_s = 0.2$ and $n_f = 4$.

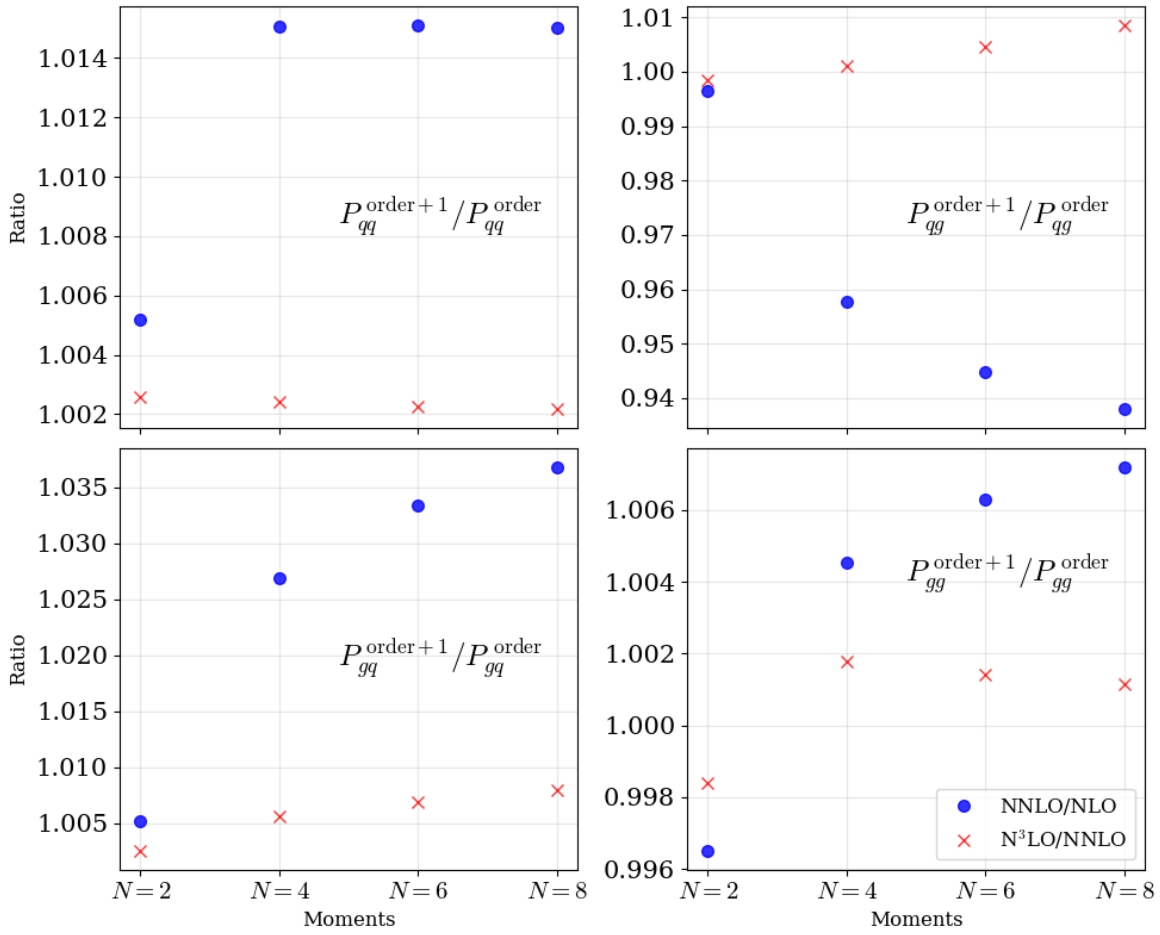

Figure 7.5.: The low-integer numerical Mellin moments of relevant singlet splitting functions (excluding $P_{qq}^{\text{NS},+}$) as a ratio between orders. In all cases the expected perturbative convergence is demonstrated.

Moment Analysis

Tracking back to the moments found for the splitting functions [171, 172] (shown in Table 7.1 and as a ratio in Fig. 7.5), we are able to identify the expected convergence in the perturbative expansions up to N^{3}LO. Fig. 7.5 illustrates the relative size of the NNLO and N^{3}LO contributions to the low even-integer moments.

Until recently (at the time of writing), there were only 3 moments available for the functions P_{gq} and P_{gg} approximated here. However, in [172] an extra moment

was published for these two gluon splitting functions. This extra information led to our predictions at small-x being more in line with the resummation results in [170] mentioned earlier. This is an example of how extra information can be added as and when it is available to update any approximations and utilise our full knowledge of the next highest order. By adopting this procedure, we immediately benefit from a slightly increased precision (with a relevant theoretical uncertainty) instead of having to delay the inclusion of higher order theory (for potentially decades) until a complete analytical calculation of the next order in α_s is known.

7.3. Numerical Results

We now consider the DGLAP evolution equations for the singlet and gluon shown in Equation (6.3). We expand this equation to α_s^4 and investigate the effects of the variation in the N^{3}LO contributions.

For the purposes of this analysis, the approximate functions (7.14), taken from [63], are used as sample distributions at an energy scale of $\mu_f^2 \simeq 30$ GeV^2, a scale chosen due to its relevance to DIS processes included in the MSHT global fit.

$$x\Sigma(x, \mu_f^2 = 30\ \text{GeV}^2) = 0.6\, x^{-0.3}(1-x)^{3.5}(1+5x^{0.8}) \tag{7.14a}$$

$$xg(x, \mu_f^2 = 30\ \text{GeV}^2) = 1.6\, x^{-0.3}(1-x)^{4.5}(1-0.6x^{0.3}) \tag{7.14b}$$

The expressions above are order independent and so provide a robust means to isolate the effects arising from higher orders in the splitting functions. For convenience we

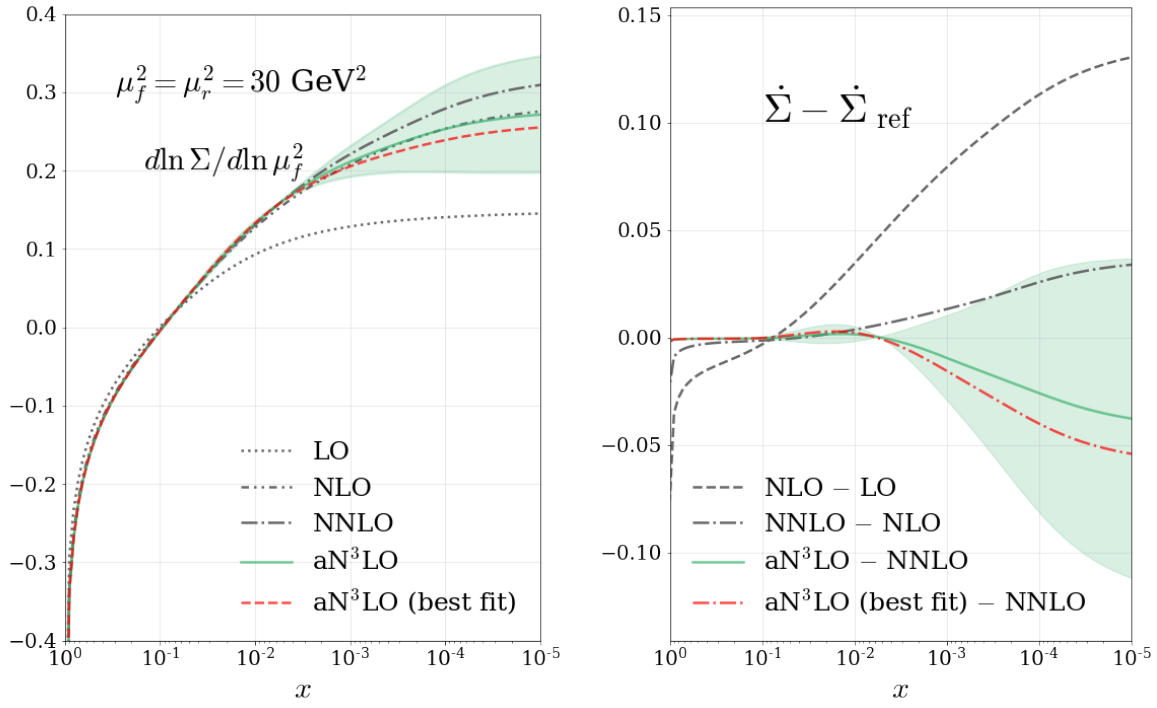

Figure 7.6.: The flavour singlet quark distribution evolution equation Equation (6.3) shown for orders up to the approximate N^{3}LO (left). The relative shift between subsequent orders of the flavour singlet evolution (right) where $\dot{\Sigma} = d\ln\Sigma/d\ln\mu_f^2$.

also assume

$$\alpha_s(\mu_r^2 = \mu_f^2 = 30\,\text{GeV}^2) \simeq 0.2. \tag{7.15}$$

where μ_r and μ_f are the renormalisation and factorisation scales respectively.

Singlet Evolution

Fig. 7.6 demonstrates the result of including the respective N^{3}LO expansions from Section 7.1 in an analysis of the evolution equation. Towards small-x this variation increases due to the larger uncertainty in the P_{qq}^{PS} and P_{qg} splitting functions at aN^{3}LO. On the right of Fig. 7.6, the difference plot displays the respective shifts from the previ-

ous order and demonstrates how this shift changes up to N^{3}LO. These results predict a reduction in the evolution of the singlet towards small-x from NNLO. Inspecting Fig. 7.3, we can see that this reduction is stemming from the contribution of the gluon with the P_{qg} function at 4-loops, which is the dominant contribution to the evolution. Towards larger x values ($10^{-2} < x < 10^{-1}$) we see a fractional increase in the quark evolution, also following the shape of the P_{qg} function. These results can therefore give some indication as to how we expect our gluon PDF to behave at N^{3}LO; since the structure functions are directly related to the quarks (through LO), the singlet evolution should remain fairly constant. Therefore we can expect that the fit will prefer a slightly harder gluon at small-x and a softer gluon between $10^{-2} < x < 10^{-1}$ relative to NNLO.

Fig. 7.6 displays a good level of agreement between the allowed N^{3}LO shift and the evolution at NLO and NNLO (within $\pm 1\sigma$ variation bands from theoretical uncertainties). Also shown in Fig. 7.6 is the evolution prediction using the best fit results for $P_{qq}^{(3)}$ and $P_{qg}^{(3)}$ (red dashed). This prediction tends to follow slightly below the center of the 1σ uncertainty band, where the data has balanced the two variations and is more in line with the NLO evolution than NNLO due to a negative contribution below 10^{-2}. Considering the magnitude of shifts from each order, the predicted shift from NNLO to aN^{3}LO is slightly larger than that from NLO to NNLO, contradicting what may be expected from perturbation theory. However, we remind the reader that these best fit results are, to some degree, sensitive to all orders in perturbation theory through the data constraint. Due to this, the resultant best fit can be thought of as an approximate asymptote to all orders. Interpreting the approximation in this way, restores our faith in perturbation theory and becomes an entirely plausible estimation of the missing higher orders.

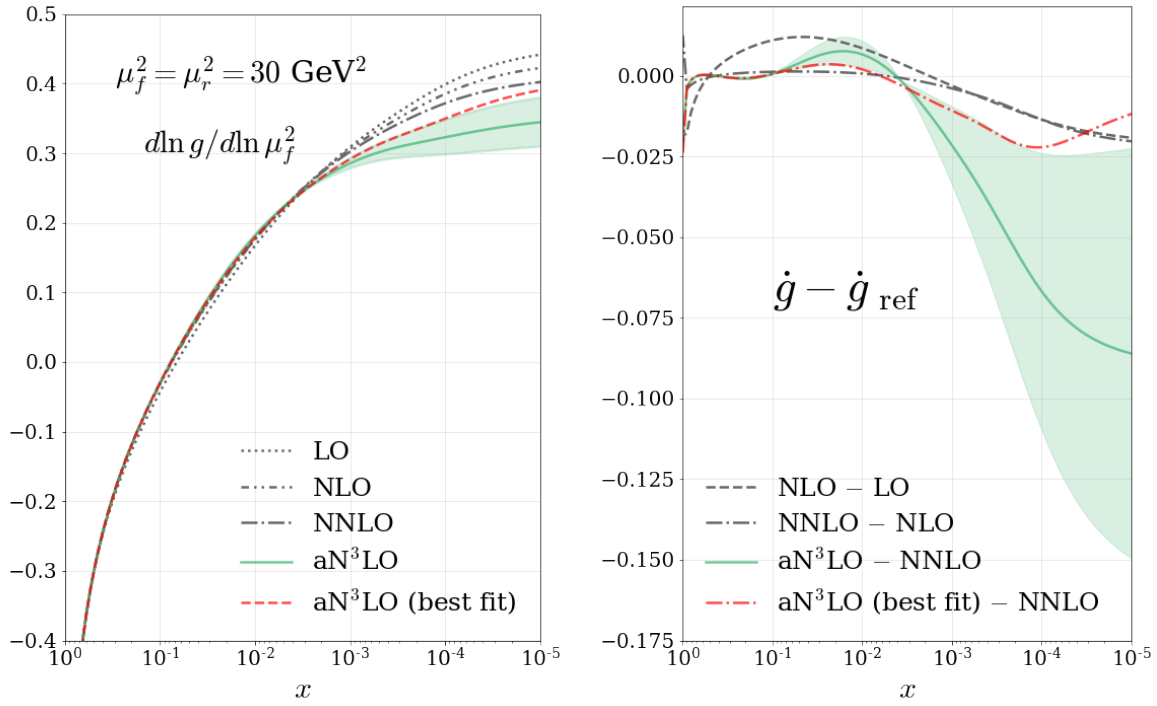

Figure 7.7.: The gluon distribution evolution equation Equation (6.3) shown for orders up to the approximate N^{3}LO (left). The relative shift between subsequent orders of the gluon evolution (right) where $\dot{g} = d\ln g/d\ln \mu_f^2$.

Fig. 7.6 also exhibits an example of how the points of zero uncertainty (discussed in Section 7.1) can affect the evolution predictions. We can see that at most the uncertainty is being underestimated by $< 1\%$ and therefore, for the reasons discussed earlier, we do not consider these regions further here.

Gluon Evolution

Fig. 7.7 displays the result of including the aN^{3}LO splitting function contributions into the gluon evolution equation. As with the singlet evolution case, this extra contribution is currently inducing a notable variation at N^{3}LO. The general trend at small-x is a reduction in the value of the evolution equation due to the N^{3}LO prediction for P_{gg}.

On the right hand side of Fig. 7.7 we observe the respective shifts from lower orders and how this shift changes up to N^{3}LO.

In the gluon evolution, there is a large variation coming from the uncertainty in the $P_{gg}^{(3)}$ function. Therefore when $P_{gg}^{(3)}$ is convoluted with the gluon PDF at small-x, one could expect a potentially large shift from NNLO. The best fit gluon evolution prediction in Fig. 7.7 is produced by utilising the best fit results for $P_{gq}^{(3)}$ and $P_{gg}^{(3)}$ functions (red dashed). In this prediction we see that the fit prefers a reduction in the evolution from NNLO, which is contained within the $\pm 1\sigma$ band until around $x \lesssim 10^{-4}$. Since at low-Q^2, the quark and gluon are comparable at small-x, this reduction is likely driven from the form of P_{gq} in Fig. 7.4. Combining this with the smaller gluon PDF at low-Q^2 therefore acts to slow the gluon evolution despite P_{gg} increasing. Furthermore, the best fit is seemingly more in line with the perturbative expectation of the evolution than the chosen variation[2]. Since this variation is chosen from the known information about the perturbative expansions, this is a manifestation of how the framework we present here can capture the relevant sources of theoretical uncertainty (and account for these via a penalty in a PDF fit). This is encouraging, as even with the large amount of freedom for this gluon evolution, it seems that the data is constraining and balancing the two contributions from the splitting functions in a sensible fashion. As discussed in the singlet evolution case, the relative shift from NNLO to N^{3}LO is slightly larger than one might hope for when dealing with a perturbative expansion. However, since this best fit is impacted to all orders from the experimental data (up to the leading logarithms at N^{3}LO i.e. even higher orders involve more divergent logarithms which are missed in this theoretical description),

[2]Due to the presence of more divergent higher order logarithms at this level, it is not certain or by any means guaranteed that the shift at N^{3}LO will follow the same trend outlined from lower orders.

we can interpret this shift as an approximate all order shift and once again restore its validity in perturbation theory.

As with the singlet case above, negligible points of non-zero uncertainty are displayed in Fig. 7.7. For the reasons discussed in the singlet case and in Section 7.1, these are not an area of concern at the current level of desired uncertainty and are therefore not considered further.

Chapter 8.

N^{3}LO Transition Matrix Elements

Heavy flavour transition matrix elements, A_{ij}, as described in Chapter 3, are exact quantities that describe the transition of all PDFs with n_f active flavours into a scheme with $n_f + 1$ active flavours. Due to discontinuous nature of A_{ij} at the heavy flavour mass thresholds, they are also present in the coefficient functions to ensure an exact cancellation of this discontinuity in physical quantities. This combination then preserves the smooth nature of the structure function, as demanded by the renormalisation group flows.

The general expansion of the heavy-quark transition matrix elements in powers of α_s reads,

$$A_{ij} = \delta_{ij} + \sum_{\ell=1}^{\infty} \alpha_s^{\ell} A_{ij}^{(\ell)} = \delta_{ij} + \sum_{\ell=1}^{\infty} \alpha_s^{\ell} \sum_{k=0}^{\ell} L_{\mu}^{k} a_{ij}^{(\ell,k)}, \tag{8.1}$$

where at each order the terms proportional to powers of $\mathrm{L}_{\mu} = \ln(m_h^2/\mu^2)$ are determined by lower order transition matrix elements and splitting functions. Therefore the focus only needs to be on the $a_{ij}^{(\ell,0)}$ expressions, as the rest are not only known [37,38],

but are guaranteed not to contribute at mass thresholds due to the presence of L_μ. These μ-independent terms can be decomposed in powers of n_f as

$$a_{ij}^{(3,0)} = a_{ij}^{(3,0),\,0} + n_f a_{ij}^{(3,0),\,1} \tag{8.2}$$

where a number of the n_f-dependent and independent terms are known exactly. The n_f parts are however sub-leading and so as a first approximation, are set to zero in this work. In keeping with the framework set out in Section 6.2, we will make use of the available known information (even-integer Mellin moments [179] and leading small and large-x behaviour [178, 180–183, 188]) about the heavy flavour transition matrix elements to approximate the μ-independent contributions $a_{ij}^{(3,0)}$. As discussed above, we make the choice to completely ignore any terms that do not contribute at mass threshold since not only are these sub-leading but can also be ignored by explicitly setting $\mu^2 = m_h^2$.

8.1. 3-loop Approximations

A_{Hg}

The $A_{Hg}^{(3)}$ function is still under calculation at the time of writing. Currently the first five even-integer moments are known for the $\overline{\text{MS}}$ scheme $A_{Hg}^{(3)}$ [179], along with the leading small-x terms [178].

The n_f-dependent contribution to the 3-loop unrenormalised A_{Hg} transition matrix element has also been approximated in [178], while all other contributions to $A_{Hg}^{(3)}(n_f = 0)$ were already known. For this approximation we work in the $\overline{\text{MS}}$ scheme using the

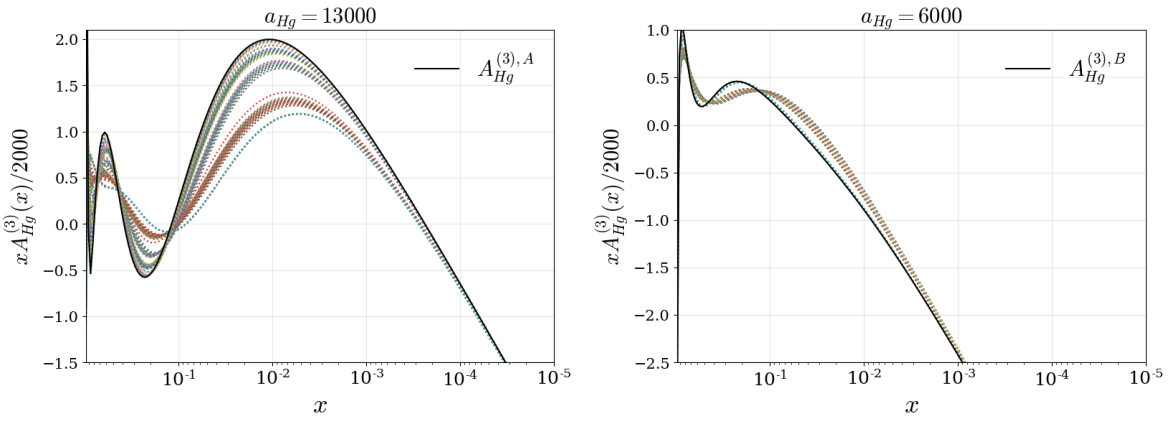

Figure 8.1.: Combinations of functions with an added variational factor (a_{Hg}) controlling the NLL term. Combinations of functions at the upper (left) and lower (right) bounds of the variation are shown. The solid lines indicate the upper and lower bounds for this function chosen from the relevant criteria.

framework set out in Section 6.2. We then approximate the function using the set of functions,

$$\begin{aligned}
f_{1,2}(x) &= \ln^5(1-x) \quad \text{or} \quad \ln^4(1-x) \quad \text{or} \quad \ln^3(1-x) \quad \text{or} \quad \ln^2(1-x) \\
&\quad \text{or} \quad \ln(1-x), \\
f_{3,4}(x) &= 2-x \quad \text{or} \quad 1 \quad \text{or} \quad x \quad \text{or} \quad x^2, \\
f_5(x) &= \ln x \quad \text{or} \quad \ln^2 x, \\
f_e(x, a_{Hg}) &= \left(224\,\zeta_3 - \frac{41984}{27} - 160\,\frac{\pi^2}{6}\right)\frac{\ln 1/x}{x} + a_{Hg}\,\frac{1}{x}
\end{aligned} \tag{8.3}$$

where a_{Hg} is varied as $6000 < a_{Hg} < 13000$. This variation is chosen from the criteria outlined in Section 6.2 and is comparable to that chosen in [178]. Fig. 8.1 displays the approximation of the $\overline{\text{MS}}$ $A_{Hg}^{(3)}$ with the variation from different combinations of functions in Equation (8.3) at the chosen limits of a_{Hg}. Comparing with Fig. 3 in [178], we see a slightly larger range of allowed variation. A small proportion of this difference can be accounted for by the difference in renormalisation schemes, with the majority of this change being from the differences in the criteria from Section 6.2. The

upper ($A_{Hg}^{(3),A}$) and lower ($A_{Hg}^{(3),B}$) bounds in the small-x region (shown in Fig. 8.1) are given by,

$$A_{Hg}^{(3),A} = 44.1703\ \ln^5(1-x) + 268.024\ \ln^4(1-x) + 45271.0\ x - 68401.4\ x^2 + 36029.8\ \ln x + \left(224\ \zeta_3 - \frac{41984}{27} - 160\ \frac{\pi^2}{6}\right) \frac{\ln 1/x}{x} + 12000\ \frac{1}{x} \quad (8.4)$$

$$A_{Hg}^{(3),B} = -18.9493\ \ln^5(1-x) - 138.763\ \ln^4(1-x) - 31692.1\ x + 33282.3\ x^2 - 3088.75\ \ln^2 x + \left(224\ \zeta_3 - \frac{41984}{27} - 160\ \frac{\pi^2}{6}\right) \frac{\ln 1/x}{x} + 6000\ \frac{1}{x} \quad (8.5)$$

Using this information, we then choose the fixed functional form,

$$A_{Hg}^{(3)} = A_1\ \ln^5(1-x) + A_2\ \ln^4(1-x) + A_3\ x + A_4\ x^2 + A_5\ \ln x + \left(224\ \zeta_3 - \frac{41984}{27} - 160\ \frac{\pi^2}{6}\right) \frac{\ln 1/x}{x} + a_{Hg}\ \frac{1}{x} \quad (8.6)$$

where the variation of a_{Hg} remains unchanged as it already encapsulates the predicted variation to within the $\sim 1\%$ level.

A_{Hq}^{PS}

The A_{Hq}^{PS} transition matrix element has been calculated exactly in [181]. Here we attempt to qualitatively reproduce this result via an efficient parameterisation to an appropriate precision.

Using the expressions for the small and large-x limits [181] and the known first six even-integer moments converted into $\overline{\mathrm{MS}}$ [179], we provide a user-friendly approxi-

mation as,

$$
\begin{aligned}
A_{Hq}^{\mathrm{PS},\,(3)} = \; & (1-x)^2\Big\{ -152.523\;\ln^3(1-x) - 107.241\;\ln^2(1-x)\Big\} \\
& - 4986.09\;x + 582.421\;x^2 - 1393.50\;x\ln^2 x - 4609.79\;x\ln x \\
& - 688.396\;\frac{\ln 1/x}{x} + (1-x)\;3812.90\;\frac{1}{x} + 1.6\;\ln^5 x - 20.3457\;\ln^4 x \\
& + 165.115\;\ln^3 x - 604.636\;\ln^2 x + 3525.00\;\ln x \\
& + (1-x)\Big\{0.246914\ln^4(1-x) - 4.44444\ln^3(1-x) - 2.28231\ln^2(1-x) \\
& - 357.427\ln(1-x) + 116.478\Big\} \qquad (8.7)
\end{aligned}
$$

where the first two lines have been approximated and the last four lines are the exact leading small and large-x terms. We note here that the approximated part of this parameterisation is in a much less important region of x than the exact parts, therefore any small differences in the approximated part from the exact function are unimportant.

$A_{qq,H}^{\mathrm{NS}}$

Moving to the non-singlet $A_{qq,H}^{\mathrm{NS}}$ function, we attempt to parameterise the work from [180, 188]. Specifically, we make use of the known even integer moments up to $N = 14$ [179], converted into the $\overline{\mathrm{MS}}$ scheme, with the even moments corresponding to the (+) non-singlet distribution.

As for $A_{Hg}^{(3)}$, the approximation is performed using the set of functions,

$$\begin{aligned} f_1(x) &= \ln x, \quad f_2(x) = \ln^2 x, \\ f_{3,4}(x) &= 1 \text{ or } x \text{ or } x^2 \text{ or } \ln(1-x), \\ f_5(x) &= 1/x, \quad f_6(x) = \ln^3(1-x), \quad f_7(x) = \ln^2(1-x), \\ f_e(x, a_{qq,H}^{\rm NS}) &= a_{qq,H}^{\rm NS} \ln^3 x \end{aligned} \tag{8.8}$$

where $a_{qq,H}^{\rm NS}$ is varied as $-90 < a_{qq,H}^{\rm NS} < -37$. To contain this variation in a fixed functional form we employ:

$$A_{qq,H}^{{\rm NS},\,(3)\,+} = A_1 \frac{1}{(1-x)_+} + A_2 \ln^3(1-x) + A_3 \ln^2(1-x) + A_4 \ln(1-x) + A_5 + A_6\, x + A_7 \ln^2 x + a_{qq,H}^{\rm NS} \ln^3 x \tag{8.9}$$

where the variation of $a_{qq,H}^{\rm NS}$ is unchanged.

$A_{gq,H}$

The 3-loop $A_{gq,H}$ function has been calculated exactly in [182]. As with the $A_{Hq}^{\rm PS}$ function above, we attempt to provide a simple and computationally efficient approximation to this exact form. To do this, we use the known even-integer moments (converted to the $\overline{\rm MS}$ scheme) and small and large-x information from [179, 182]. Gathering a fixed set of functions $f_i(x)$ and omitting any variational parameter $a_{gq,H}$, due to the higher amount of information available, the resulting approximation to the $\overline{\rm MS}$

$A^{(3)}_{gq,H}$ is:

$$\begin{aligned} A^{(3)}_{gq,H} = &-237.172\ \ln^3(1-x) - 201.497\ \ln^2(1-x) + 7247.70\ \ln(1-x) + 39967.3\ x^2 \\ &- 22017.7 - 28459.1\ \ln x - 14511.5\ \ln^2 x \\ &+ 341.543\ \frac{\ln 1/x}{x} + 1814.73\ \frac{1}{x} - \frac{580}{243}\ \ln^4(1-x) - \frac{17624}{729}\ \ln^3(1-x) \\ &- 135.699\ \ln^2(1-x) \end{aligned} \tag{8.10}$$

where the first two lines have been approximated and the last two lines are the exact small and large-x limits.

$A_{gg,H}$

Work is ongoing for the 3-loop contribution to $A_{gg,H}$ [189, 190]. Due to this, the entire approximation of $A^{(3)}_{gg,H}$ presented here is based on the first 5 even-integer Mellin moments [179]. To reduce the wild behaviour of this approximation from only using the Mellin moment information (converted into the $\overline{\text{MS}}$ scheme), we introduce a second mild constraint in the form of the relations in Equation (6.17). These relations are closely followed by the gluon-gluon functions up to NNLO, but there is no guarantee that this behaviour will continue at N^{3}LO. This constraint is given as,

$$A_{gg,H}(x \to 0) \simeq \frac{C_A}{C_F} A_{gq,H}(x \to 0). \tag{8.11}$$

It can be expected that even though this relation may not be followed exactly, it should not stray too far from this general 'rule of thumb'. Due to this a generous contingency of $\pm 50\%$ is allowed when using this rule. Furthermore, to ensure this relation is only used as a guide, we allow the variation to move beyond this rule as long as

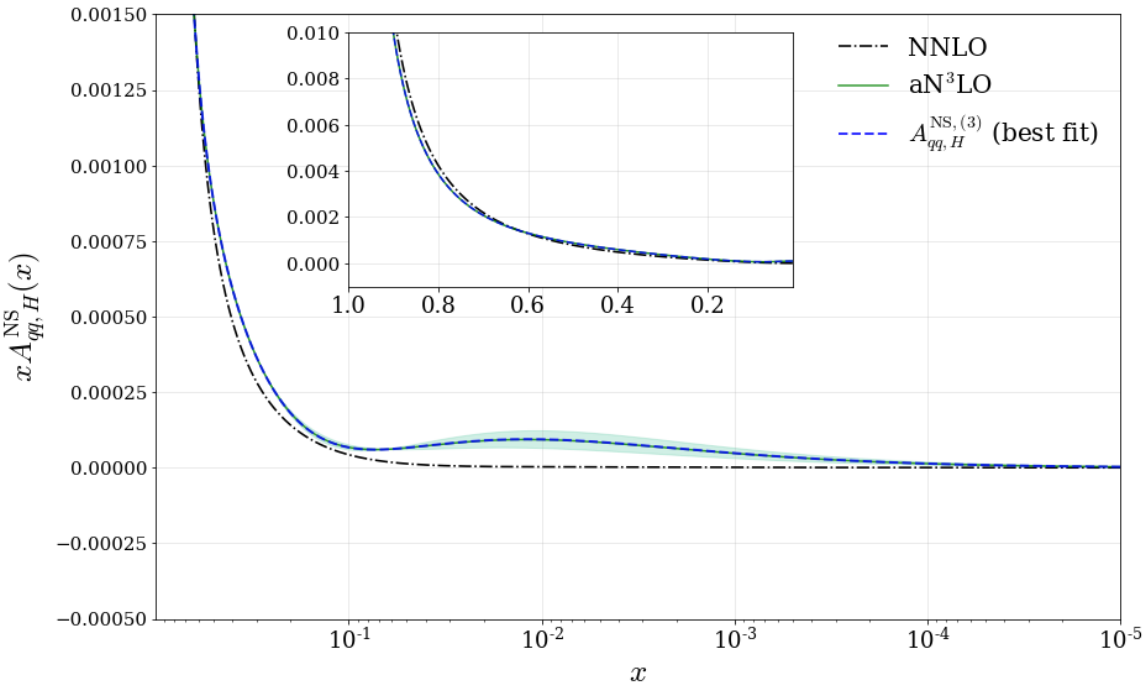

Figure 8.2.: Perturbative expansions for the transition matrix element $A_{qq,H}^{\mathrm{NS}}$ including any corresponding allowed $\pm 1\sigma$ variation (shaded green region). This function is shown at the mass threshold value of $\mu = m_h$. The best fit value (blue dashed line) displays the prediction for this function determined from a global PDF fit.

the criteria in Section 6.2 are still satisfied. As a result of this change in prescription and because the allowed variation is now on a much larger scale than that of any functional uncertainty, we choose a fixed functional form from the start and use the criteria described above to guide our choice of variation.

$$A_{gg,H}^{(3)} = A_1 \ln^2(1-x) + A_2 \ln(1-x) + A_3 x^2 + A_4 \ln x + A_5 x + a_{gg,H} \frac{\ln x}{x} \quad (8.12)$$

where $-2000 < a_{gg,H} < -700$.

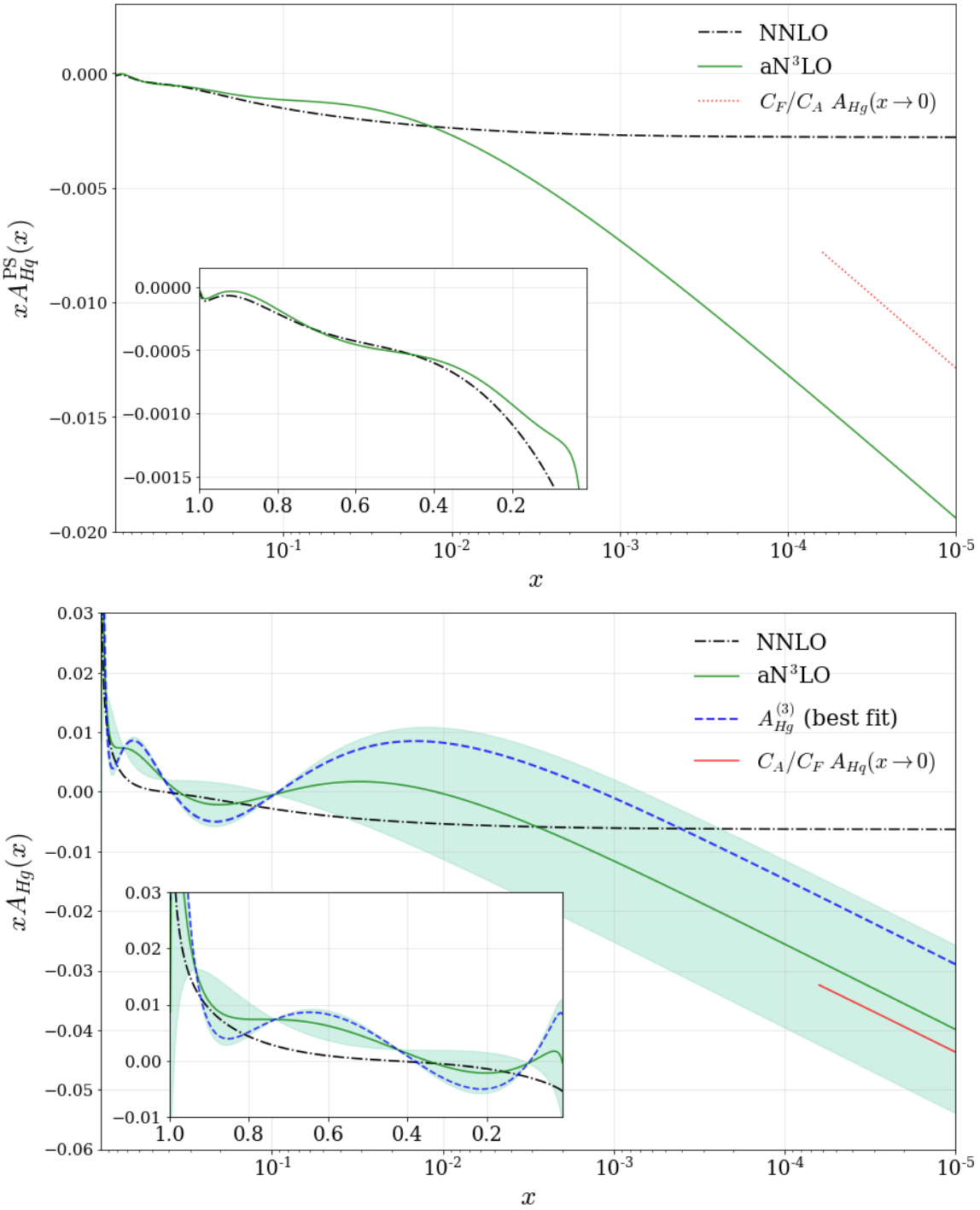

Figure 8.3.: Perturbative expansions for the transition matrix elements $A_{Hq}^{\rm PS}$ and A_{Hg} including any corresponding allowed $\pm 1\sigma$ variation (shaded green region). These functions are shown at the mass threshold value of $\mu = m_h$. The best fit values (blue dashed line) display the predictions for these functions determined from a global PDF fit.

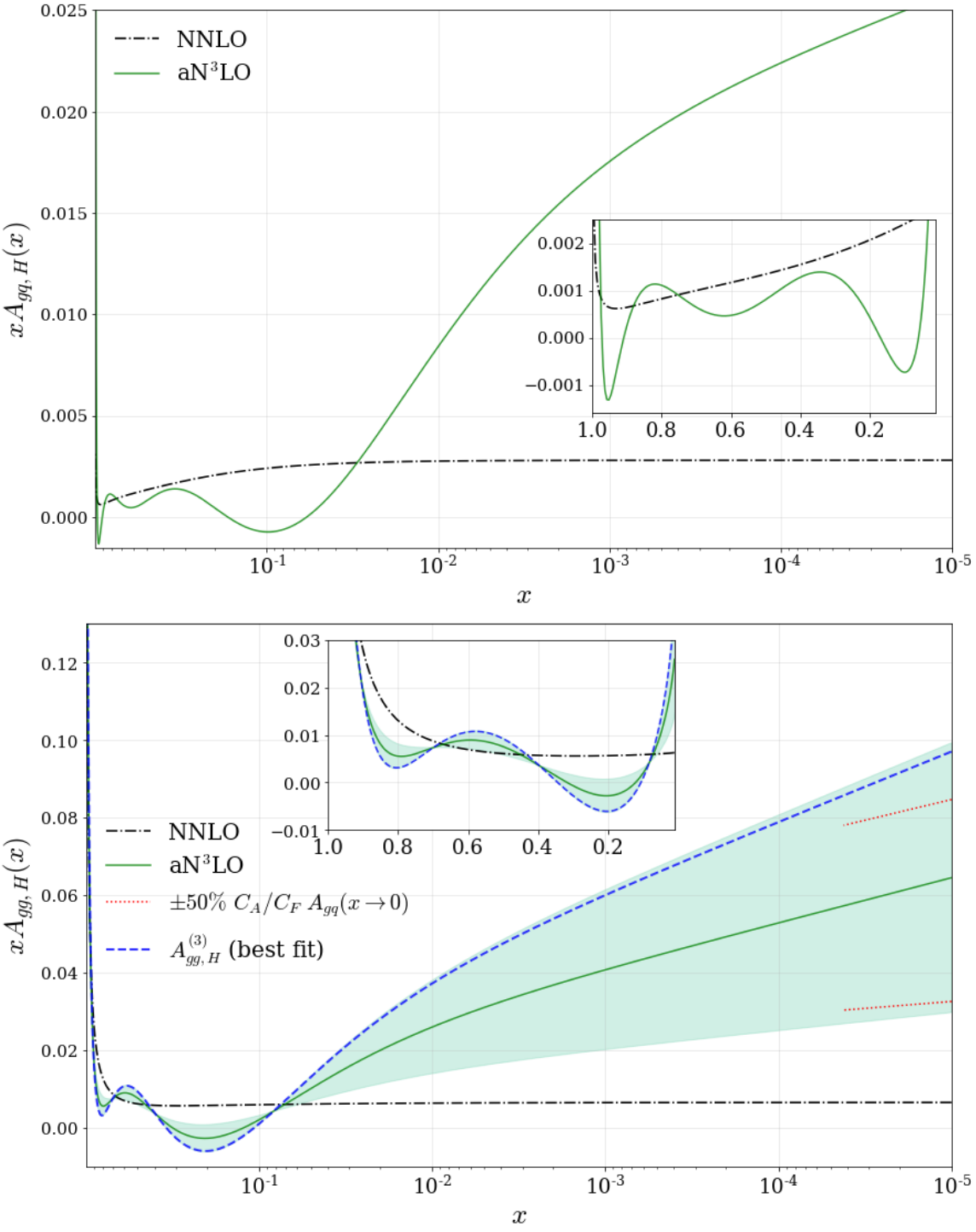

Figure 8.4.: Perturbative expansions for the transition matrix elements $A_{gq,H}$ and $A_{gg,H}$ including any corresponding allowed $\pm 1\sigma$ variation (shaded green region). These functions are shown at the mass threshold value of $\mu = m_h$. The best fit values (blue dashed line) display the predictions for these functions determined from a global PDF fit.

8.2. Predicted aN^{3}LO Transition Matrix Elements

Fig.'s 8.2, 8.3 and 8.4 show the perturbative expansions for each of the n_f-independent contributions to the transition matrix elements at the mass threshold value of $\mu = m_h$. Included with these expansions are the predicted variations ($\pm 1\sigma$) from Section 8.1 (shown in green) and the approximate N^{3}LO best fits (shown in blue - discussed further in Chapter 11).

$A_{qq,H}^{\rm NS}$ in Fig. 8.2 behaves as expected with little variation from NNLO until the magnitude of this function is very small. The approximations for the more dominant $A_{Hq}^{\rm PS}$ and A_{Hg} functions in Fig. 8.3 exhibit some slight sporadic behaviour towards large-x due to the increased logarithmic influence. However, since this is in a region where the magnitude of these functions become small, any instabilities will have a minimal effect on the overall result. The major feature prevalent across both these functions is the large deviation away from the NNLO behaviour, especially at small-x (and also mid-x for A_{Hg}).

Similarly for $A_{gq,H}$ in Fig. 8.4 (upper), we see some irregular behaviour towards large-x. As with $A_{Hq}^{\rm PS}$ and A_{Hg}, this behaviour is in a region where the magnitude of $A_{gq,H}$ is small. As discussed in Section 8.1, $A_{gq,H}^{(3)}$ is approximated without any variation due to the range of available information being large[1]. Due to this, and the fact that the region of potential instability (large-x) is highly suppressed, we can accept this function with negligible effect on any results. As more information becomes available about all these functions, it will be interesting to observe how the behaviour across x changes.

[1] Although an exact expression has been calculated for $A_{gq,H}^{(3)}$ [182], this function is not yet available in a computationally efficient format i.e. numerical grids.

The $A_{gg,H}$ function shown in Fig. 8.4 (lower) displays the $\pm 50\%$ bounds of violation we allow for the relation Equation (6.17). It follows that the allowed variation is conservative enough to include a generous violation of Equation (6.17) at N^{3}LO, with the prediction that the function is positive at small-x. This is an area where small-x information would clearly be very beneficial. With this information currently in progress, it will be very interesting to compare how well this variation captures the true small-x $A_{gg,H}$ behaviour.

The final best fit values shown in Fig.'s 8.2, 8.3 and 8.4 are determined from a global PDF fit with various datasets seen to be constraining these functions within the $\pm$ 1σ variations. As observed, we are able to show good agreement between the allowed variations and the best fit predictions. The perturbative expansion predicted for $A_{gg,H}$ is the least well constrained while also violating its expected relation with $A_{gq,H}$ more than one may originally expect. Since the small-x region in all cases changes dramatically at N^{3}LO, one potential explanation is that this function is compensating for an inaccuracy in another area of the theory. However, when comparing with the relationship between A_{Hg} and A_{Hq}^{PS}, Equation (6.17) also exhibits a significant violation at this order. This could suggest that for the N^{3}LO transition matrix elements, this relation may not be the best indicator of precision or consistency. Finally, we remember that the best fit in this case may be feeling a larger effect from higher orders, especially due to these functions only existing from NNLO. For example, in Chapter 7 we observed a high level of divergence introduced at 4-loops in the splitting functions. The best fit results shown here may therefore be sensitive to a similar level of divergence further along in their corresponding perturbative expansions.

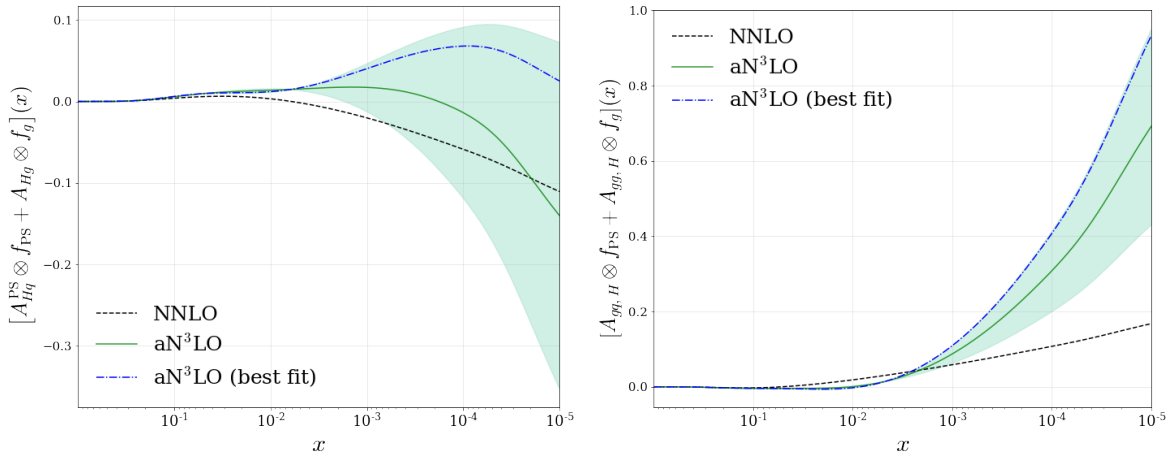

Figure 8.5.: Heavy flavour evolution contributions to the heavy quark ($H + \overline{H}$ (left)) and gluon (right) PDFs provided at $\mu \simeq 30$ GeV^2. These results include the $\mu = m_h$ contributions from $A_{Hq}^{\rm PS}$, A_{Hg}, $A_{gq,H}$ and $A_{gg,H}$ transition matrix elements up to aN^{3}LO.

As previously discussed, this lack of knowledge is contained within our choice of the predicted variations of these functions. Therefore this treatment only seeks to add to the predicted level of theoretical uncertainty from MHOs, as one expects.

8.3. Numerical Results

For these results, the same toy PDFs presented in Section 7.3 are employed which approximate the general order-independent PDF features at $Q^2 \simeq 30$ GeV^2. Note that due to the higher Q^2, these results are more representative of the b-quark. The left plot in Fig. 8.5 shows the result of including the N^{3}LO transition matrix element approximations we have determined into Equation (6.7c), which is describing the heavy quark distribution $(H + \overline{H})(x, Q^2 = m_h^2)$. The right plot in Fig. 8.5 is describing the heavy flavour contribution to the gluon at $(x, Q^2 = m_h^2)$ in Equation (6.7b) where the delta function describing the leading order contribution to $A_{gg,H}$ has been subtracted

out. The dominant contribution to the heavy quark (left plot) is stemming from the A_{Hg} function. Whereas the dominant contribution to the gluon (right plot) is from the $A_{gg,H}$ function. As one might expect, the predictions at N^{3}LO are more divergent at small-x, however it is also true that the general trend from NNLO is being followed across most values of x.

The best fit functions predicted from a global fit show the preferred aN^{3}LO contributions for both scenarios. The predicted behaviour from the global fit follows the results for the perturbative expansions in Section 8.2. For the $(H + \overline{H})(x, Q^2 = m_h^2)$ result (Fig. 8.5 left), the aN^{3}LO result is positive across a much wider range of x. Since this is a perturbatively calculated PDF, this is an encouraging result that could potentially eliminate some of the more unphysical shortcomings at NNLO without demanding positivity of the PDF a priori.

Chapter 9.

N^{3}LO Coefficient Functions

The final set of functions considered are the NC DIS coefficient functions which, when combined with the PDFs, form the structure functions discussed in Chapter 3.[1] We approximate the N^{3}LO heavy quark coefficient functions which accompany the heavy flavour transition matrix elements from Chapter 8 and also the N^{3}LO light quark coefficient functions. We note that our standard definition of the order of coefficient functions includes the longitudinal coefficient functions at order α_s at LO, at order α_s^2 at NLO etc. This means we already include order α_s^3 coefficient functions for the longitudinal coefficient functions at NNLO, whereas many groups only consider order α_s^2 at NNLO. Since little is known about longitudinal coefficient functions at order α_s^4,

[1] Charged current structure function data is limited to relatively high-x values compared to NC data and is either comparatively low statistics, high-Q^2 proton target data from HERA or nuclear target data (again often quite low statistics) on heavy nuclear targets. In both cases the effect of N^{3}LO corrections is small compared with uncertainties, especially when considering those involved with nuclear corrections. Also, heavy flavour contributions are less well known at high orders for CC structure functions. Hence, we do not include N^{3}LO for these processes, except dimuon data, which is particularly important for the poorly constrained strange quark, but which is a semi-inclusive DIS process, and for which we parameterise N^{3}LO corrections, as discussed in Chapter 10. An improvement would be necessary for more precise proton data, from the EIC for example.

and the data constraints from $F_L(x, Q^2)$ are very much less precise than from $F_2(x, Q^2)$, we simply remain at the precisely known order α_s^3 in this study.

9.1. Low-Q^2 N^{3}LO Heavy Flavour Coefficient Functions

As previously mentioned in Chapter 3, the standard MSHT theoretical description of NNLO structure functions includes approximations to the low-Q^2 FFNS coefficient functions $C^{(3),\mathrm{FF}}_{H,\{q,g\}}$ from [176–178]. Within these functions are the precisely known LL small-x terms and mass threshold information, along with an approximate NLL small-x term added into the MSHT fit. In the NNLO fit these approximate NLL parameters play a very small role due to not only being sub-leading, but also only affecting the FFNS scheme below the mass thresholds. At NNLO they are therefore heuristically set to a value that is theoretically justified and suits the NNLO best fit. At N^{3}LO these functions begin to directly affect the form of the full GM-VFNS scheme across all (x, Q^2). For this reason, these NLL parameters need to be considered as an independent source of theoretical uncertainty. In the aN^{3}LO fit, the NLL parameters are left free and included into the nuisance parameter framework set out in Chapter 5.

The standard NNLO MSHT fit contains terms of the form,

$$C^{(3),\,\mathrm{NLL}}_{H,i}(Q^2 \to 0) \propto -4\,\frac{1}{x} + c_i^{\mathrm{LL}}\,\frac{\ln 1/x}{x}, \qquad \left(c_g^{\mathrm{LL}} = \frac{C_F}{C_A}\,c_q^{\mathrm{LL}}\right), \tag{9.1}$$

where $i = q, g$ and c_i^{LL} is the precisely known leading small-x log coefficient. In the aN^{3}LO fit, the NLL coefficient is allowed to vary by $\pm 50\%$ ($\pm 1\sigma$ variation). This conservative range is chosen to enable the release of tension with the variational parameters associated with the N^{3}LO transition matrix elements. Here we stress that

this quantity is heuristically set even at NNLO, therefore our treatment is completely justified with the added benefit of now accounting for an uncertainty for this choice.

9.2. 3-loop Approximations

$C_{H,q}$

In this section the $C_{H,q}$ coefficient function is investigated. As discussed in Chapter 6, $C_{H,q}$ contributes to the heavy flavour structure function $F_{2,H}$. We begin by isolating this function from Equation (6.14) and relating the FFNS and GM-VFNS schemes at all orders from Equation (6.9) and Equation (6.13),

$$C_{H,q}^{\text{FF}} = \left[C_{H,H}^{\text{VF, NS}} + C_{H,H}^{\text{VF, PS}}\right] \otimes A_{Hq}^{\text{PS}} + C_{H,q}^{\text{VF}} \otimes \left[A_{qq,H}^{\text{NS}} + A_{qq,H}^{\text{PS}}\right] + C_{H,g}^{\text{VF}} \otimes A_{gq,H}. \quad (9.2)$$

Expanding this function we obtain:

$$\mathcal{O}(\alpha_s): \qquad C_{H,q}^{\text{FF, (1)}} = 0 \quad (9.3)$$

$$\mathcal{O}(\alpha_s^2): \qquad C_{H,q}^{\text{FF, (2)}} = C_{H,H}^{\text{VF, (0)}} \otimes A_{Hq}^{PS,\,(2)} + C_{H,q}^{\text{VF, (2)}} \otimes A_{qq,H}^{\text{NS, (0)}} \quad (9.4)$$

$$\mathcal{O}(\alpha_s^3): \qquad C_{H,q}^{\text{FF, (3)}} = C_{H,H}^{\text{VF, (1)}} \otimes A_{Hq}^{\text{PS, (2)}} + C_{H,H}^{\text{VF, (0)}} \otimes A_{Hq}^{\text{PS, (3)}} + C_{H,q}^{\text{VF, (3)}} \otimes A_{qq,H}^{\text{NS, (0)}} + C_{H,g}^{\text{VF, (1)}} \otimes A_{gq,H}^{(2)} \quad (9.5)$$

where we recall that $A_{qq,H}^{\text{NS, (0)}} = \delta(1-x)$.

NNLO

The first contribution from the heavy quarks appears at the $\mathcal{O}(\alpha_s^2)$ level. Fortunately there is a complete picture of this order [140] which provides some experience with the behaviour of these functions before moving into unknown territory. Fig. 9.1 shows the case for $C_{H,q}^{\text{VF, (2)}}$ converging onto $C_{H,q}^{\text{ZM, (2)}}$ at high-Q^2, as required by the definition of the GM-VFNS scheme outlined in Chapter 3.

From Fig. 9.1, immediately some intuition can be built up surrounding the form of these functions. It can be observed that the GM-VFNS function at low-Q^2 is consistently more positive than at high-Q^2. However, the values at low and high-Q^2 are of the same order of magnitude which provides evidence that the behaviour should not be substantially different across values of Q^2 when estimating our N^{3}LO quantities. Further to this, as $x \to 0$ the overall magnitude of $C_{H,q}^{(2)}$ becomes much larger, which is consistent with an inherently pure singlet quantity.

N^{3}LO

At $\mathcal{O}(\alpha_s^3)$ the N^{3}LO ZM-VFNS and low-Q^2 FFNS functions are known [176–178, 185] and parameterisations/approximations are available (up to the level of precision discussed in Section 9.1). Nevertheless, there is no direct information on how the full GM-VFNS function behaves at this order which is required for a full treatment of the heavy flavour coefficients. Using Equation (9.5) to estimate the N^{3}LO contribution, we have

$$C_{H,q}^{\text{VF, (3)}} = C_{H,q}^{\text{FF, (3)}} - C_{H,H}^{\text{VF, (1)}} \otimes A_{Hq}^{\text{PS, (2)}} - C_{H,g}^{\text{VF, (1)}} \otimes A_{gq,H}^{(2)} - A_{Hq}^{\text{PS, (3)}}. \tag{9.6}$$

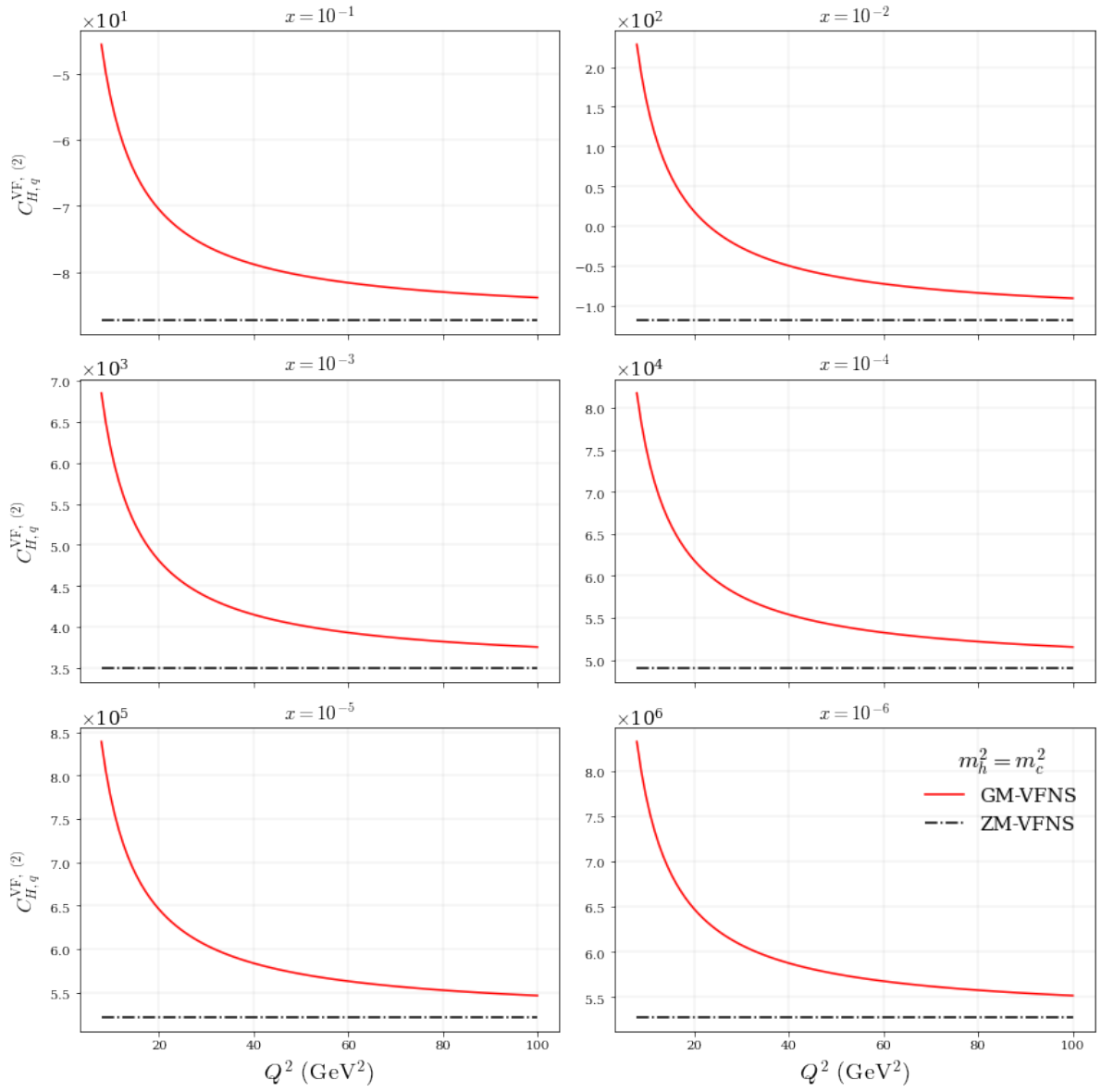

Figure 9.1.: The NNLO GM-VFNS function $C_{H,q}^{\mathrm{VF},\,(2)}$ compared with the NNLO ZM-VFNS function $C_{H,q}^{\mathrm{ZM},\,(2)}$ across a variety of x and Q^2 values. Mass threshold is set at the charm quark level ($m_h^2 = m_c^2 = 1.4\,\mathrm{GeV}^2$).

where $A_{Hq}^{\mathrm{PS},\,(3)}$ is the N^{3}LO transition matrix element approximated in Section 8.1.

It must be the case that the discontinuities introduced into the heavy flavour PDF from the transition matrix elements (at the threshold value of $Q^2 = m_h^2$) are cancelled exactly in the structure function. The cancellation of $A_{Hq}^{\mathrm{PS},\,(3)}$ is therefore guaranteed by its inclusion into the GM-VFNS coefficient function in Equation (9.6). Since in practice the transition matrix elements are convoluted with the PDFs separately to the coefficient functions, to ensure that this statement remains the case, the parameterisation will be performed in the FFNS number scheme. By doing this, we can explicitly switch to the GM-VFNS number scheme by including the subtraction term in Equation (9.6). This procedure then ensures that $A_{Hq}^{\mathrm{PS},\,(3)}$ is subtracted off exactly with no unphysical discontinuity.

Following the methodology set out in Section 6.3, the two regimes we wish to interpolate between are the approximate $C_{H,q}^{\mathrm{FF},\,(3)}(Q^2 \to 0)$ limit and

$$C_{H,q}^{\mathrm{FF},\,(3)}(Q^2 \to \infty) = C_{H,q}^{\mathrm{ZM},\,(3)} + C_{H,H}^{\mathrm{VF},\,(1)} \otimes A_{Hq}^{\mathrm{PS},\,(2)} + C_{H,g}^{\mathrm{VF},\,(1)} \otimes A_{gq,H}^{(2)} + A_{Hq}^{\mathrm{PS},\,(3)}, \quad (9.7)$$

where $C_{H,q}^{\mathrm{VF},\,(3)}$ is replaced with $C_{H,q}^{\mathrm{ZM},\,(3)}$ in the high-Q^2 limit. Equation (6.18) is then stable across all (x, Q^2), exactly cancelling any discontinuity that would violate the RG flow, whilst also demanding that the known FFNS approximation (for $Q^2 < m_h^2$) is followed[2].

[2]Since in practice the discontinuities from the transition matrix elements are added to PDFs regardless of what order coefficient function they are convoluted with, discontinuities of even higher order (e.g. α_s^4 and beyond) are also present in calculations. Because the order α_s^3 matrix elements are large these even higher order discontinuities are not insignificant. Therefore we add the same contributions to the unknown FFNS contributions below m_h^2 to impose continuity on structure functions. Such corrections are extremely small, except right at the transition point where they eliminate minor unphysical discontinuities.

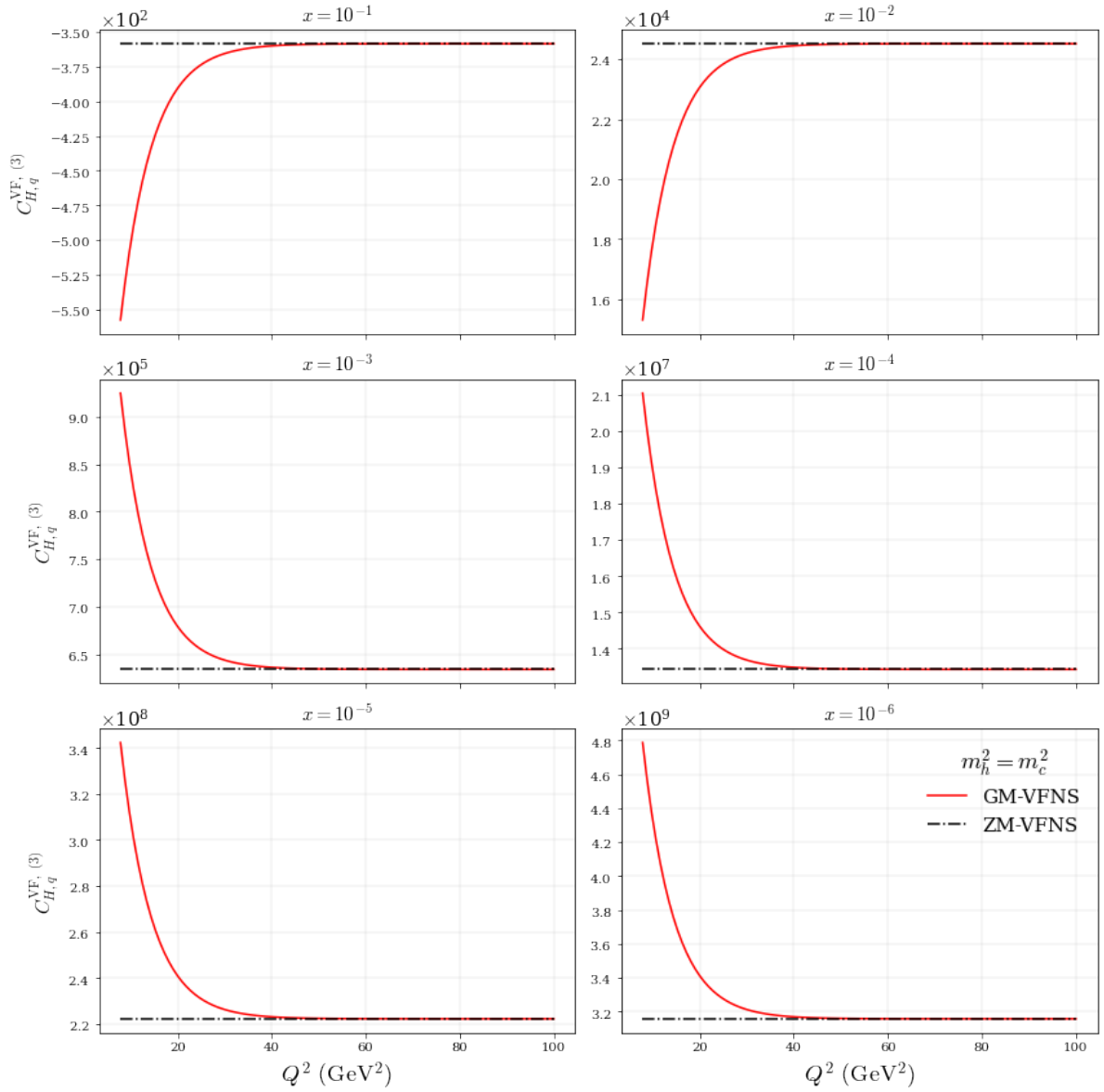

Figure 9.2.: N^{3}LO GM-VFNS function $C_{H,q}^{\mathrm{VF},\,(3)}$ compared with the N^{3}LO ZM-VFNS function $C_{H,q}^{\mathrm{ZM},\,(3)}$ across a variety of x and Q^2 values (shown without the variation from the low-Q^2 NLL term discussed in Section 9.1). $C_{H,q}^{\mathrm{VF},\,(3)}$ is parameterised via Equations (9.6), (9.7) and (6.18). Mass threshold is set at the charm quark level ($m_h^2 = m_c^2 = 1.4\,\mathrm{GeV}^2$).

Fig. 9.2 shows the result of estimating $C_{H,q}^{\mathrm{VF},\,(3)}$ using the above approximation for $C_{H,q}^{\mathrm{FF},\,(3)}$ and the relevant subtraction term from Equation (9.6). Note that this plot ignores any variation from the low-Q^2 NLL term discussed in Section 9.1, where this is fixed to its central value.

$C_{H,g}$

As with $C_{H,q}$, using Equation (6.9) and Equation (6.13) to isolate $C_{H,g}$ and relate the FFNS and GM-VFNS schemes,

$$C_{H,g}^{\mathrm{FF}} = C_{H,g}^{\mathrm{VF}} \otimes A_{gg,H} + C_{H,q}^{\mathrm{VF,\,PS}} \otimes A_{qg,H} + \left[C_{H,H}^{\mathrm{VF,\,NS}} + C_{H,H}^{\mathrm{VF,\,PS}}\right] \otimes A_{Hg} \tag{9.8}$$

$$\mathcal{O}(\alpha_s): \qquad C_{H,g}^{\mathrm{FF},\,(1)} = C_{H,g}^{\mathrm{VF},\,(1)} + C_{H,H}^{\mathrm{VF},\,(0)} \otimes A_{Hg}^{(1)} \tag{9.9}$$

$$\mathcal{O}(\alpha_s^2): \qquad C_{H,g}^{\mathrm{FF},\,(2)} = C_{H,g}^{\mathrm{VF},\,(2)} + C_{H,H}^{\mathrm{VF},\,(0)} \otimes A_{Hg}^{(2)} + C_{H,H}^{\mathrm{VF},\,(1)} \otimes A_{Hg}^{(1)} \tag{9.10}$$

$$\begin{aligned}\mathcal{O}(\alpha_s^3): \qquad C_{H,g}^{\mathrm{FF},\,(3)} = C_{H,g}^{\mathrm{VF},\,(3)} &+ C_{H,g}^{\mathrm{VF},\,(1)} \otimes A_{gg,H}^{(2)} + C_{H,H}^{\mathrm{VF,\,NS+PS},\,(2)} \otimes A_{Hg}^{(1)} \\ &+ C_{H,H}^{\mathrm{VF},\,(1)} \otimes A_{Hg}^{(2)} + C_{H,H}^{\mathrm{VF},\,(0)} \otimes A_{Hg}^{(3)}\end{aligned} \tag{9.11}$$

we uncover a NLO contribution to the heavy flavour structure function. This lower order contribution is a consequence of the gluon being able to directly probe the heavy flavour quarks, whereas a light quark must interact via a secondary interaction (hence the $C_{H,q}$ coefficient function beginning at NNLO).

NLO & NNLO

The NLO and NNLO contributions to $C_{H,g}$ are known exactly [140]. To build some experience and check our understanding, we can observe how the lower order GM-VFNS functions converge onto their ZM-VFNS counterparts in Fig. 9.3 and Fig. 9.4.

At NLO and NNLO the magnitude of the functions is generally higher in the low-Q^2 limit than at high-Q^2. In both cases, the function remains at the same order of magnitude across all Q^2. However, the relative change across Q^2 is smaller at NLO, and similar to that seen for $C_{H,q}^{(2)}$ at NNLO. Due to this, we can once again expect that although more of a scaling contribution at N^{3}LO may be present, it should not be too substantial across the range of Q^2.

N^{3}LO

As with the $C_{H,q}^{(3)}$ function at $\mathcal{O}(\alpha_s^3)$, the FFNS result at low-Q^2 is known (up to the level of precision discussed in Section 9.1), as well as the exact ZM-VFNS function at high-Q^2 [176–178, 185]. Considering the form of $C_{H,g}^{\text{VF, }(3)}$, there is an extra complication coming from the transition matrix element $A_{Hg}^{(3)}$. As discussed in Chapter 8, the $A_{Hg}^{(3)}$ function is not as well known as the $A_{Hq}^{(3)}$ function considered earlier and is accompanied by the variational parameter a_{Hg}. Since it is a requirement for $C_{H,g}^{(3)}$ to exactly cancel the PDF discontinuity introduced by $A_{Hg}^{(3)}$, this variation must be compensated for and included in the description,

$$C_{H,g}^{\text{VF, }(3)} = C_{H,g}^{\text{FF, }(3)} - C_{H,g}^{\text{VF, }(1)} \otimes A_{gg,H}^{(2)} - C_{H,H}^{\text{VF, NS+PS, }(2)} \otimes A_{Hg}^{(1)} - C_{H,H}^{\text{VF, }(1)} \otimes A_{Hg}^{(2)} - A_{Hg}^{(3)}. \quad (9.12)$$

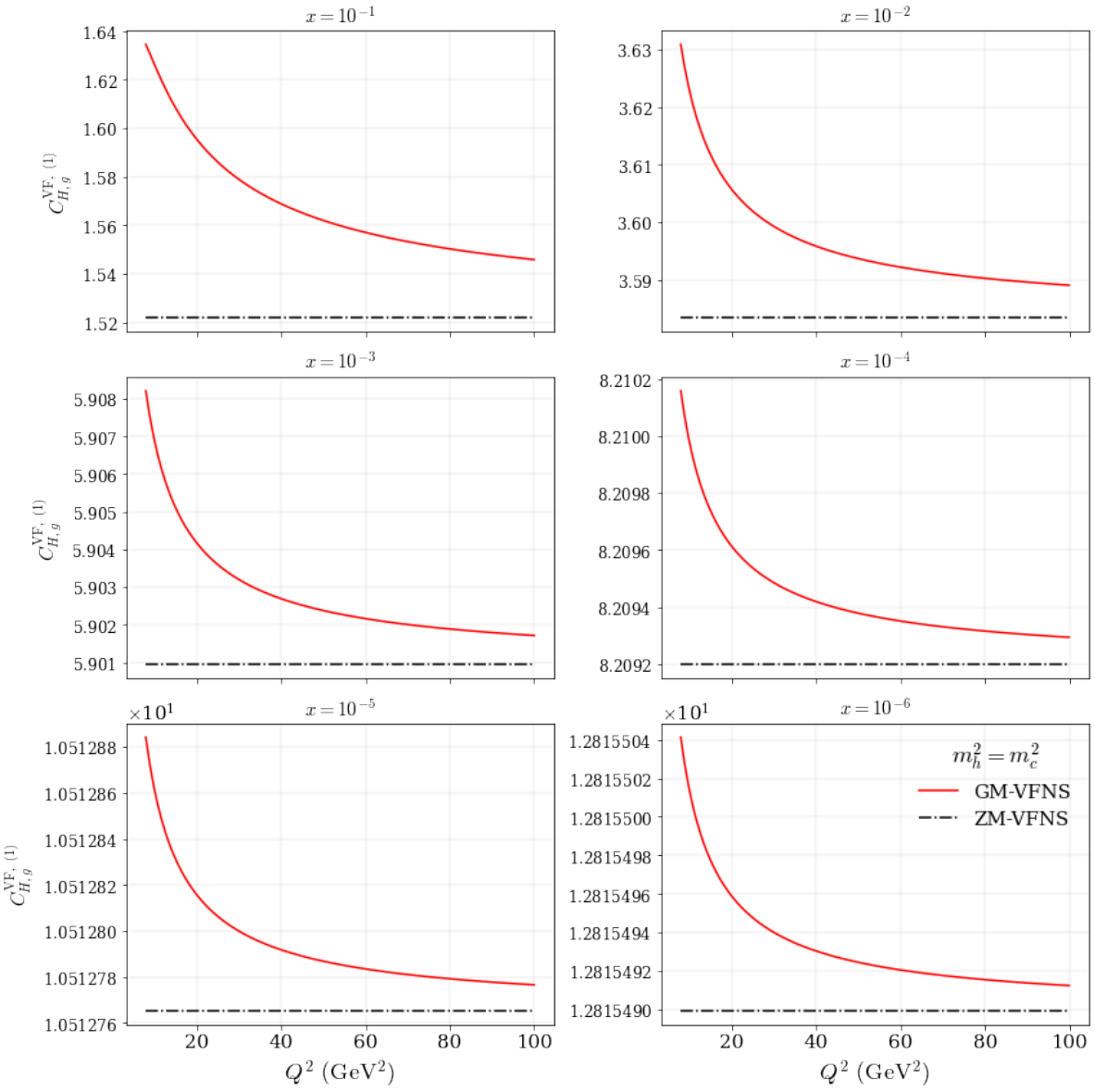

Figure 9.3.: The NLO GM-VFNS function $C_{H,g}^{\mathrm{VF},\,(1)}$ compared with the NLO ZM-VFNS function $C_{H,g}^{\mathrm{ZM},\,(1)}$ across a variety of x and Q^2 values. Mass threshold is set at the charm quark level ($m_h^2 = m_c^2 = 1.4\,\mathrm{GeV}^2$).

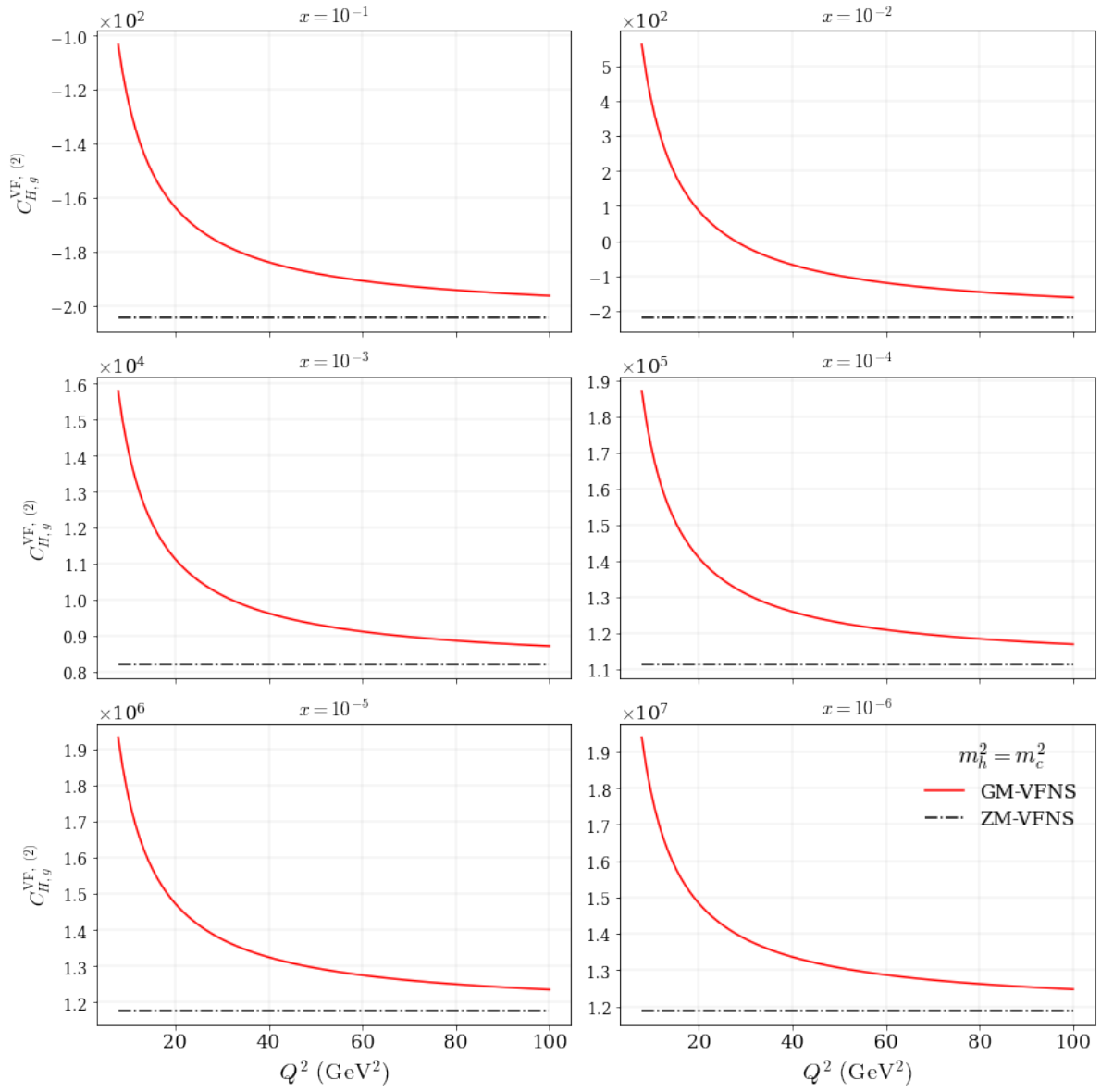

Figure 9.4.: The NNLO GM-VFNS function $C_{H,g}^{\mathrm{VF},\,(2)}$ compared with the NNLO ZM-VFNS function $C_{H,g}^{\mathrm{ZM},\,(2)}$ across a variety of x and Q^2 values. Mass threshold is set at the charm quark level ($m_h^2 = m_c^2 = 1.4\,\mathrm{GeV}^2$).

As in Section 9.2, transitioning to the FFNS number scheme ensures an exact cancellation via the subtraction term in Equation (9.12). Using the exact information for $C_{H,g}^{\text{FF, (3)}}(Q^2 \to 0)$ and the known high-Q^2 limit,

$$C_{H,g}^{\text{FF, (3)}}(Q^2 \to \infty) = C_{H,g}^{\text{ZM, (3)}} + C_{H,g}^{\text{VF, (1)}} \otimes A_{gg,H}^{(2)} + C_{H,H}^{\text{VF, NS+PS, (2)}} \otimes A_{Hg}^{(1)} + C_{H,H}^{\text{VF, (1)}} \otimes A_{Hg}^{(2)} + A_{Hg}^{(3)} \quad (9.13)$$

where $C_{H,g}^{\text{VF, (3)}}$ is replaced with $C_{H,g}^{\text{ZM, (3)}}$ in the high-Q^2 limit. Applying the framework set out in Equation (6.18), the resulting parameterisation is stable across all (x, Q^2). As $A_{Hg}^{(3)}$ and its variation is explicitly included in Equation (9.12) this ensures the continuity of the structure function with exact cancellations of discontinuities at mass thresholds.

Fig. 9.5 displays our approximation for the GM-VFNS coefficient function across a range of (x, Q^2) via a parameterisation for $C_{H,g}^{\text{FF, (3)}}$ and the relevant subtraction term in Equation (9.12). Fig. 9.5 also contains the uncertainty in this approximation stemming from $A_{Hg}^{(3)}$ (see Section 8.1). Note that Fig. 9.5 ignores any variation from the low-Q^2 NLL term discussed in Section 9.1, where this is fixed to its central value. The uncertainty shown in Fig. 9.5 is suppressed as we move to high-Q^2 owing to the required convergence of the GM-VFNS onto the corresponding ZM-VFNS gluon coefficient function at N^{3}LO.

Included in Fig. 9.5 is the best fit prediction for $C_{H,g}^{\text{VF, (3)}}$ (corresponding to the best fit of $A_{Hg}^{(3)}$ approximated in Chapter 8). Overall we see the resultant shape of $C_{H,g}^{(3)}$ is within our predicted range and follows a sensible shape that matches with the known high-Q^2 FFNS behaviour. Contrasting this with NNLO, the shape across the range of x values shown is less consistent. There is no guarantee that this should be the case, since we do not know how the perturbative nature of QCD will behave. However, we

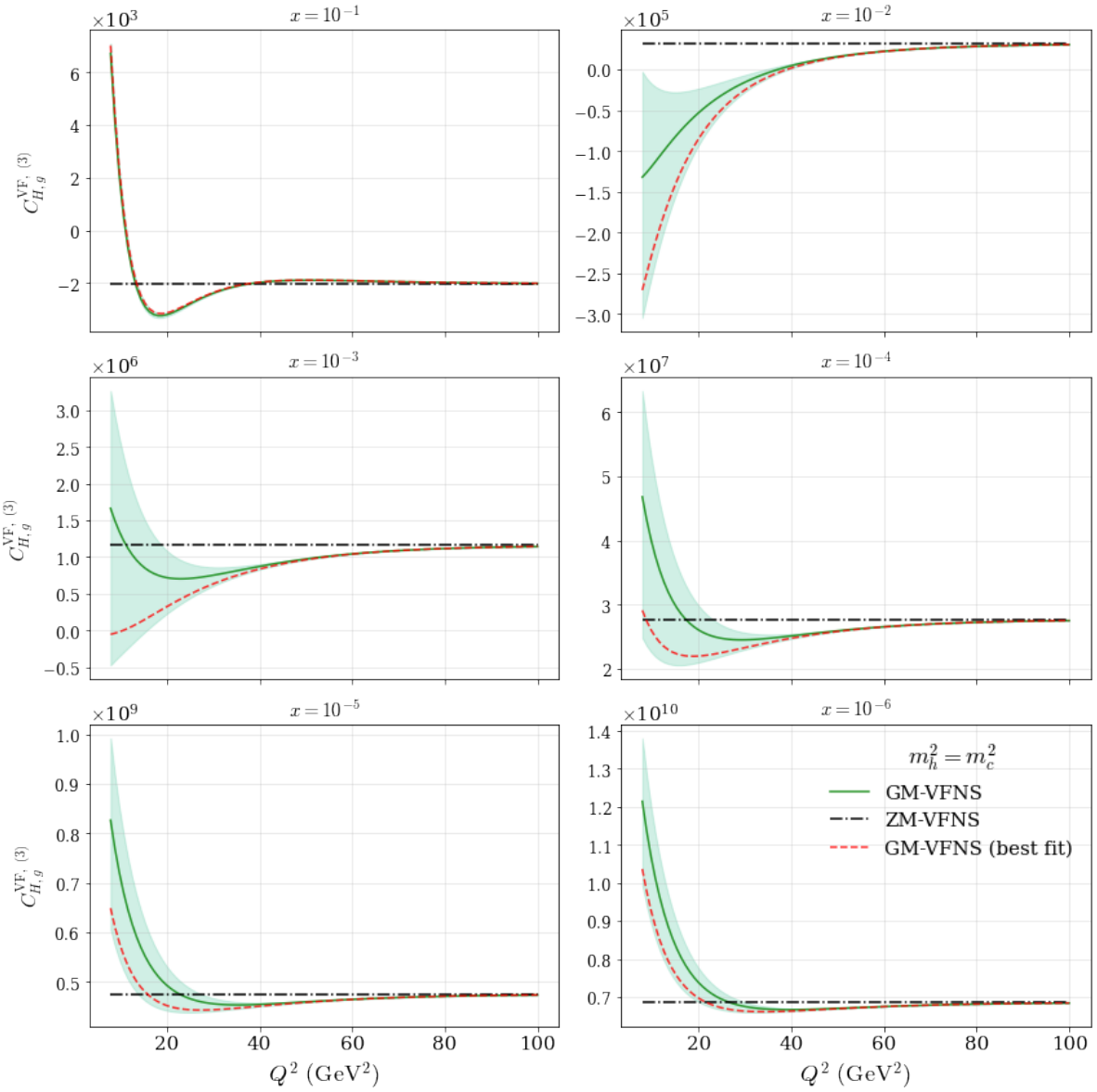

Figure 9.5.: The N^{3}LO GM-VFNS function $C_{H,g}^{\mathrm{VF},\,(3)}$ compared with the N^{3}LO ZM-VFNS function $C_{H,g}^{\mathrm{ZM},\,(3)}$ across a variety of x and Q^2 values (shown without the variation from the low-Q^2 NLL term discussed in Section 9.1). $C_{H,g}^{\mathrm{VF},\,(3)}$ is parameterised via Equations (9.12), (9.13) and (6.18). Mass threshold is set at the charm quark level ($m_h^2 = m_c^2 = 1.4\,\mathrm{GeV}^2$).

do maintain the relatively consistent order of magnitude across the evolution in Q^2, therefore the exact form of the shape across Q^2 will be less important in the resultant structure function picture.

$C^{\mathrm{NS}}_{q,q}$

The light quark coefficient functions involve small heavy flavour contributions at higher orders from heavy quarks produced away from the photon vertex. As discussed in Chapter 6 the low-Q^2 FFNS function in this case is unknown. However, since the heavy flavour contributions to the light quark structure function $F_{2,q}(x, Q^2)$ are very small, any choice of sensible variation in Q^2 has a near negligible effect on the overall structure function. Further to this, as is apparent from lower order examples, it can be expected that the light quark coefficient functions remain relatively constant across Q^2.

Using Equation (6.9) and Equation (6.11), the non-singlet coefficient function is stated as,

$$C^{\mathrm{FF,\ NS}}_{q,q} = A^{\mathrm{NS}}_{qq,H} \otimes C^{\mathrm{VF\ NS}}_{q,q}, \tag{9.14}$$

$$\mathcal{O}(\alpha_s^0): \quad C^{\mathrm{FF,\ (0)}}_{q,q,\ \mathrm{NS}} = C^{\mathrm{VF,\ (0)}}_{q,q,\ \mathrm{NS}} \tag{9.15a}$$

$$\mathcal{O}(\alpha_s^1): \quad C^{\mathrm{FF,\ (1)}}_{q,q,\ \mathrm{NS}} = C^{\mathrm{VF,\ (1)}}_{q,q,\ \mathrm{NS}} \tag{9.15b}$$

$$\mathcal{O}(\alpha_s^2): \quad C^{\mathrm{FF,\ (2)}}_{q,q,\ \mathrm{NS}} = C^{\mathrm{VF,\ (2)}}_{q,q,\ \mathrm{NS}} + A^{\mathrm{NS,\ (2)}}_{qq,H} \tag{9.15c}$$

$$\mathcal{O}(\alpha_s^3): \quad C^{\mathrm{FF,\ (3)}}_{q,q,\ \mathrm{NS}} = C^{\mathrm{VF,\ (3)}}_{q,q,\ \mathrm{NS}} + A^{\mathrm{NS,\ (3)}}_{qq,H} + C^{\mathrm{VF,\ (1)}}_{q,q,\ \mathrm{NS}} \otimes A^{\mathrm{NS,\ (2)}}_{qq,H}. \tag{9.15d}$$

From Equation (9.15) the FFNS contribution at LO and NLO is identical to the GM-VFNS and ZM-VFNS function at high-Q^2. Physically for heavy quarks to affect light quarks, a larger number of vertices than are allowed at LO and NLO must be present to enable interactions involving heavy quarks. We therefore begin our discussion at NNLO.

NNLO

At NNLO the functions included in Equation (9.15c) are known exactly [38, 186]. Assembling these together, we provide an example of how the GM-VFNS function converges to the familiar ZM-VFNS function for the light quark. By performing this exercise, expectations as to how $C^{\text{NS}}_{q,q}$ will behave at N^{3}LO can be constructed.

From Fig. 9.6 $C^{\text{VF, (2)}}_{q,q,\text{ NS}}$ quickly converges onto the ZM-VFNS function with the difference between the low and high-Q^2 being within 10% at large-x and within 0.01% at small-x. This weak scaling with Q^2 reinforces the statement that it is possible to approximate the N^{3}LO function relatively well without extensive low-Q^2 information.

N^{3}LO

Equation (9.15d) involves a mixture of functions known exactly (ZM-VFNS high-Q^2 limit [185]) and functions that are completely unknown ($C^{\text{FF, (3)}}_{q,q,\text{ NS}}$). This presents an issue as it is no longer possible to rely on $C^{FF,\text{ (3)}}_{q,q,\text{ NS}}$ to constrain the low-Q^2 limit. Nevertheless, by utilising the experience gained from NNLO, it is feasible to choose any sensible choice for the low-Q^2 limit. In practice, due to the observed weak scaling in Q^2, the exact form at low-Q^2 will not present any noticeable differences.

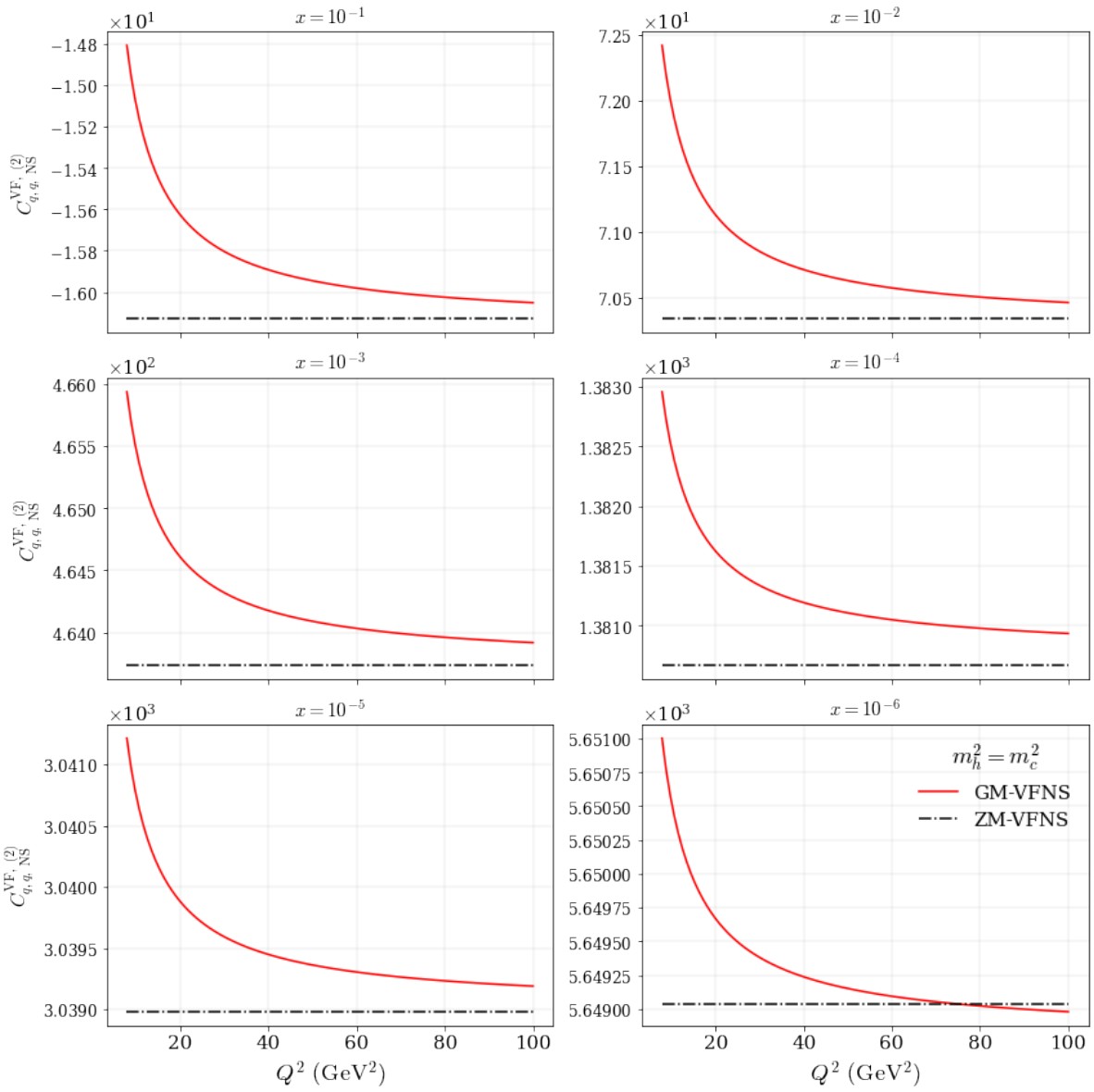

Figure 9.6.: The NNLO GM-VFNS function $C^{\mathrm{VF},\,(2)}_{q,q,\,\mathrm{NS}}$ compared with the NNLO ZM-VFNS function $C^{\mathrm{ZM},\,(2)}_{q,q,\,\mathrm{NS}}$ across a variety of x and Q^2 values. Mass threshold is set at the charm quark level ($m_h^2 = m_c^2 = 1.4\,\mathrm{GeV}^2$).

A naive choice for heuristically placing the $C^{\text{FF, (3)}}_{q,q,\text{ NS}}(Q^2 \to 0)$ function would be a constant value i.e. no scaling in Q^2. We propose to use the intuition from NNLO and the overall fit quality to give us potentially a more sensible and viable choice for the GM-VFNS approximation[3]. By inserting the high-Q^2 limit into the NS part of Equation (6.19), the result is a crude approximation to $C^{\text{FF, (3)}}_{q,q,\text{ NS}}(Q^2 \to 0)$. Combining this with Equation (9.15d), we obtain a GM-VFNS parameterisation which is relatively constant across Q^2 (similar to the NNLO behaviour) with any differences arising from the subtraction terms which are known.

Fig. 9.7 shows the result of this approximation for the full $C^{\text{VF, (3)}}_{q,q,\text{ NS}}$ function. We notice that the behaviour is similar to that of NNLO across all (x, Q^2) and appropriately larger in magnitude to account for the extra contributions obtained at N^{3}LO compared to NNLO. By definition, the parameterisation converges well to the ZM-VFNS scheme with the magnitude at high-Q^2 (ZM-VFNS regime) remaining similar to that at low-Q^2 for each specific value of x. This final point gives assurances that even if this low-Q^2 guess is not entirely representative of the actual N^{3}LO function, the effects of including this approximation are virtually negligible in a PDF fit. Also shown in Fig. 9.7 is the variation in the $C^{\text{VF, (3)}}_{q,q,\text{ NS}}$ function stemming solely from the $A^{\text{NS, (3)}}_{qq,H}$ function.

$C^{\text{PS}}_{q,q}$

To complete the light-quark GM-VFNS coefficient function picture the pure-singlet contribution from Equation (6.9) and Equation (6.11) is described by,

$$C^{\text{FF, PS}}_{q,q} = C^{\text{VF, PS}}_{q,q} \otimes A^{\text{PS}}_{qq,H} + C^{\text{VF}}_{q,g} \otimes A_{gq,H} + C^{\text{VF, PS}}_{q,H} \otimes A_{Hq} \tag{9.16}$$

[3]The differences in fit quality for sensible choices are $< 0.05\%$ compared to the overall χ^2 for the light quark NS coefficient function.

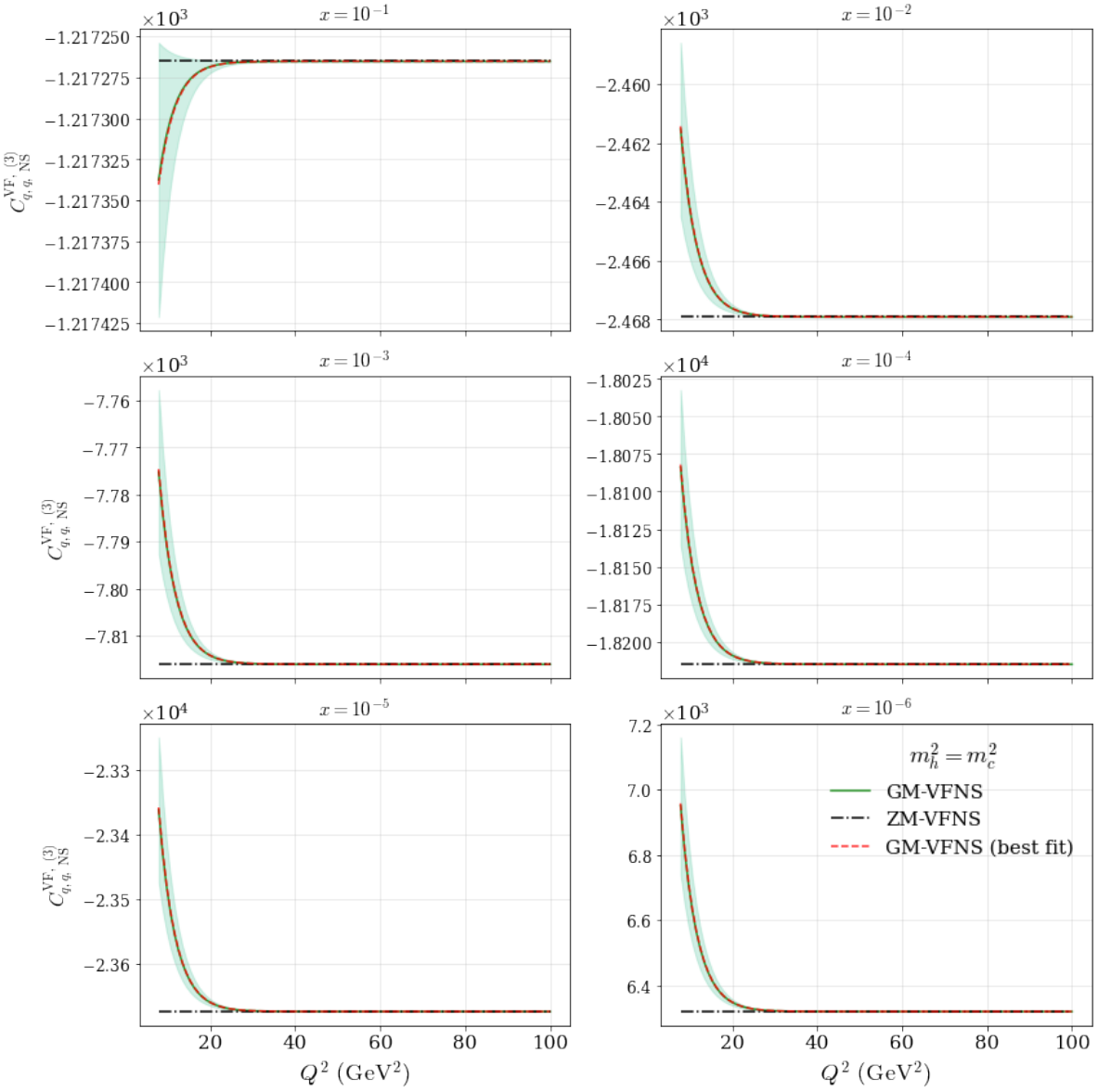

Figure 9.7.: The N^{3}LO GM-VFNS function $C^{\mathrm{VF},\,(3)}_{q,q,\,\mathrm{NS}}$ compared with the N^{3}LO ZM-VFNS function $C^{\mathrm{ZM},\,(3)}_{q,q,\,\mathrm{NS}}$ across a variety of x and Q^2 values. $C^{\mathrm{VF},\,(3)}_{q,q,\,\mathrm{NS}}$ is parameterised via Equations (9.15d) and (6.19). Mass threshold is set at the charm quark level ($m_h^2 = m_c^2 = 1.4\,\mathrm{GeV}^2$).

$$\mathcal{O}(\alpha_s^0): \qquad C_{q,q}^{\text{FF, PS, }(0)} = 0 \tag{9.17a}$$

$$\mathcal{O}(\alpha_s^1): \qquad C_{q,q}^{\text{FF, PS, }(1)} = 0 \tag{9.17b}$$

$$\mathcal{O}(\alpha_s^2): \qquad C_{q,q}^{\text{FF, PS, }(2)} = C_{q,q,\text{ PS}}^{\text{VF, }(2)} \tag{9.17c}$$

$$\mathcal{O}(\alpha_s^3): \qquad C_{q,q}^{\text{FF, PS, }(3)} = C_{q,q,\text{ PS}}^{\text{VF, }(3)} + C_{q,g}^{\text{VF, }(1)} \otimes A_{gq,H}^{(2)}. \tag{9.17d}$$

As with the non-singlet analysis the heavy flavour contributions to the pure-singlet appear at higher orders to allow for the possibility of heavy quark contributions. In the pure-singlet case, the heavy flavour contributions are pushed one order higher than the non-singlet due to the requirement for an extra intermediary gluon.

N^{3}LO

In the pure-singlet case, the FFNS function is non-existent up until N^{3}LO. Because of this, we choose to parameterise the pure-singlet with a weak constraint suppressing the FFNS function $C_{q,q}^{\text{FF, PS, }(3)}$ across all x for very low-Q^2. The reason for this is that the coefficient functions acquire more contributions as they exist through higher orders. If $C_{q,q}^{\text{FF, PS, }(3)}$ is beginning at this order, then one could expect the low-Q^2 form to be relatively small compared to the known ZM-VFNS function [185]. This is somewhat justified by the low-Q^2 kinematic restrictions for the singlet distribution which broadly manifest into a suppression at low-Q^2. We reiterate here that the low-Q^2 form of this function is still essentially around the same magnitude across all Q^2. Therefore, as with $C_{q,q}^{\text{FF, NS, }(3)}$, it will be virtually negligible in the overall structure function.

After constructing the approximation for $C_{q,q}^{\mathrm{FF,\,PS,\,(3)}}$ with Equation (6.19), Equation (9.17d) is used to approximate the GM-VFNS function. The exact form of Equation (9.17d) is chosen based on intuition and where the best fit quality can be achieved[4].

It can be seen from Fig. 9.8 that the overall magnitude of $C_{q,q,\,\mathrm{PS}}^{\mathrm{VF,\,(3)}}$ decreases substantially towards large-x as one would expect from a pure-singlet function. Inspecting the predicted values of $C_{q,q,\,\mathrm{PS}}^{\mathrm{VF,\,(3)}}$, we can confirm that the non-singlet function from Fig. 9.7 begins to dominate at large-x. Conversely towards small-x, $C_{q,q,\,\mathrm{PS}}^{\mathrm{VF,\,(3)}}$ is much larger than $C_{q,q,\,\mathrm{NS}}^{\mathrm{VF,\,(3)}}$, thereby preserving the familiar interplay between quark distributions. The suppression of the FFNS parameterisation towards low-Q^2 is also seen to give sensible results in terms of the expected percentage change in magnitude through the range of Q^2 values. Specifically we see $< 10\%$ difference in magnitude between low and high-Q^2. Since scale violating terms become more dominant at higher orders and we are essentially at leading order in terms of heavy flavour contributions, a high level of scaling with Q^2 is not expected at this order.

$C_{q,g}$

Finally the gluon-light quark coefficient function is constructed from Equation (6.9) and Equation (6.11) to be,

$$C_{q,g}^{\mathrm{FF}} = C_{q,q}^{\mathrm{VF}} \otimes A_{qg,H} \; + \; C_{q,g}^{\mathrm{VF}} \otimes A_{gg,H} + \; C_{q,H}^{\mathrm{VF,\,PS}} \otimes A_{Hg} \tag{9.18}$$

[4]The differences in fit quality for sensible choices are $< 0.1\%$ compared to the overall χ^2 for the light quark PS coefficient function.

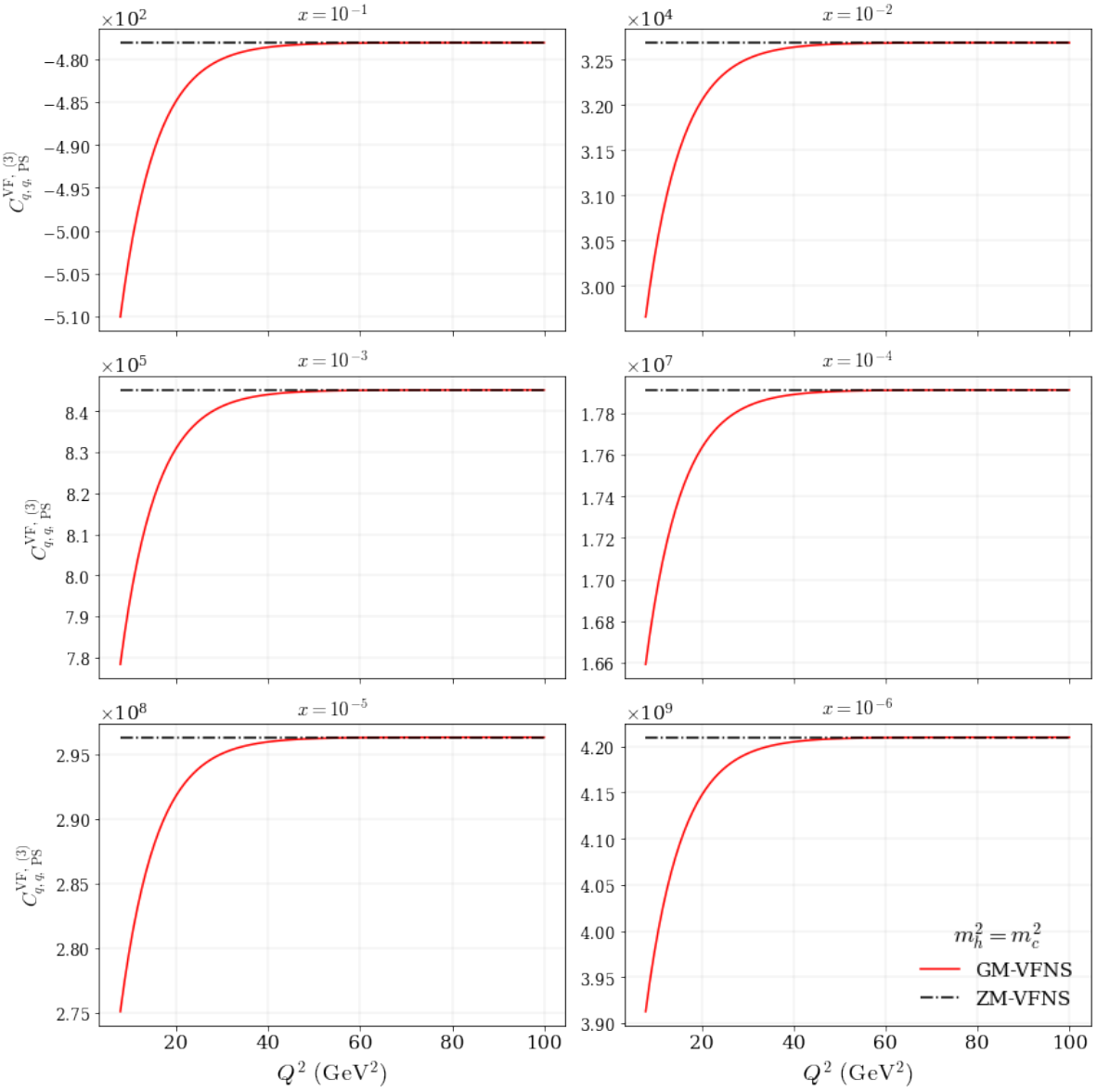

Figure 9.8.: The N^{3}LO GM-VFNS function $C^{\text{VF, (3)}}_{q,q,\text{ PS}}$ compared with the N^{3}LO ZM-VFNS function $C^{\text{ZM, (3)}}_{q,q,\text{ PS}}$ across a variety of x and Q^2 values. $C^{\text{VF, (3)}}_{q,q,\text{ PS}}$ is parameterised via Equations (9.17d) and (6.19). Mass threshold is set at the charm quark level ($m_h^2 = m_c^2 = 1.4\,\text{GeV}^2$).

$$\mathcal{O}(\alpha_s^0): \quad C_{q,g}^{\text{FF},(0)} = 0 \tag{9.19a}$$

$$\mathcal{O}(\alpha_s^1): \quad C_{q,g}^{\text{FF},(1)} = C_{q,g}^{\text{VF},(1)} \tag{9.19b}$$

$$\mathcal{O}(\alpha_s^2): \quad C_{q,g}^{\text{FF},(2)} = C_{q,g}^{\text{VF},(2)} + A_{qg,H}^{(2)} \tag{9.19c}$$

$$\mathcal{O}(\alpha_s^3): \quad C_{q,g}^{\text{FF},(3)} = C_{q,g}^{\text{VF},(3)} + A_{qg,H}^{(3)} + C_{qg}^{\text{VF},(1)} \otimes A_{gg,H}^{(2)} + C_{q,H,\text{PS}}^{\text{VF},(2)} \otimes A_{Hg}^{(1)}. \tag{9.19d}$$

For $C_{q,g}$, the FFNS function is non-existent up to NNLO, similar to $C_{q,q,\text{NS}}^{\text{FF},(3)}$. However, the $A_{qg,H}$ contribution at NNLO is sub-leading in n_f [38] and is therefore not considered here.

N^{3}LO

At N^{3}LO in Equation (9.19d), no information is available for the $C_{q,g}^{\text{FF},(3)}$ at low-Q^2. Whereas at high-Q^2 the ZM-VFNS function is known [185]. To construct the parameterisation, we apply the same method described for $C_{q,q,\text{PS}}^{\text{FF},(3)}$. Specifically, by applying a suppression to the FFNS parameterisation in the low-Q^2 limit. After constructing the parameterisation for $C_{q,g}^{\text{FF},(3)}$ with Equation (6.19), Equation (9.19d) is used to approximate the GM-VFNS function. Since there is no information in the low-Q^2 limit, the parameterisation in Equation (6.19) is chosen roughly based on how the fit prefers the evolution in Q^2 to behave.

Fig. 9.9 illustrates the GM-VFNS function in Equation (9.19d) with Equation (6.19) as $C_{q,g}^{\text{FF},(3)}$ across a range of x and Q^2. $C_{q,g}^{\text{VF},(3)}$ increases in magnitude when moving to smaller x and by definition converges onto the ZM-VFNS function. The convergence in this case is chosen to be less steep than for the light quark convergences due to some

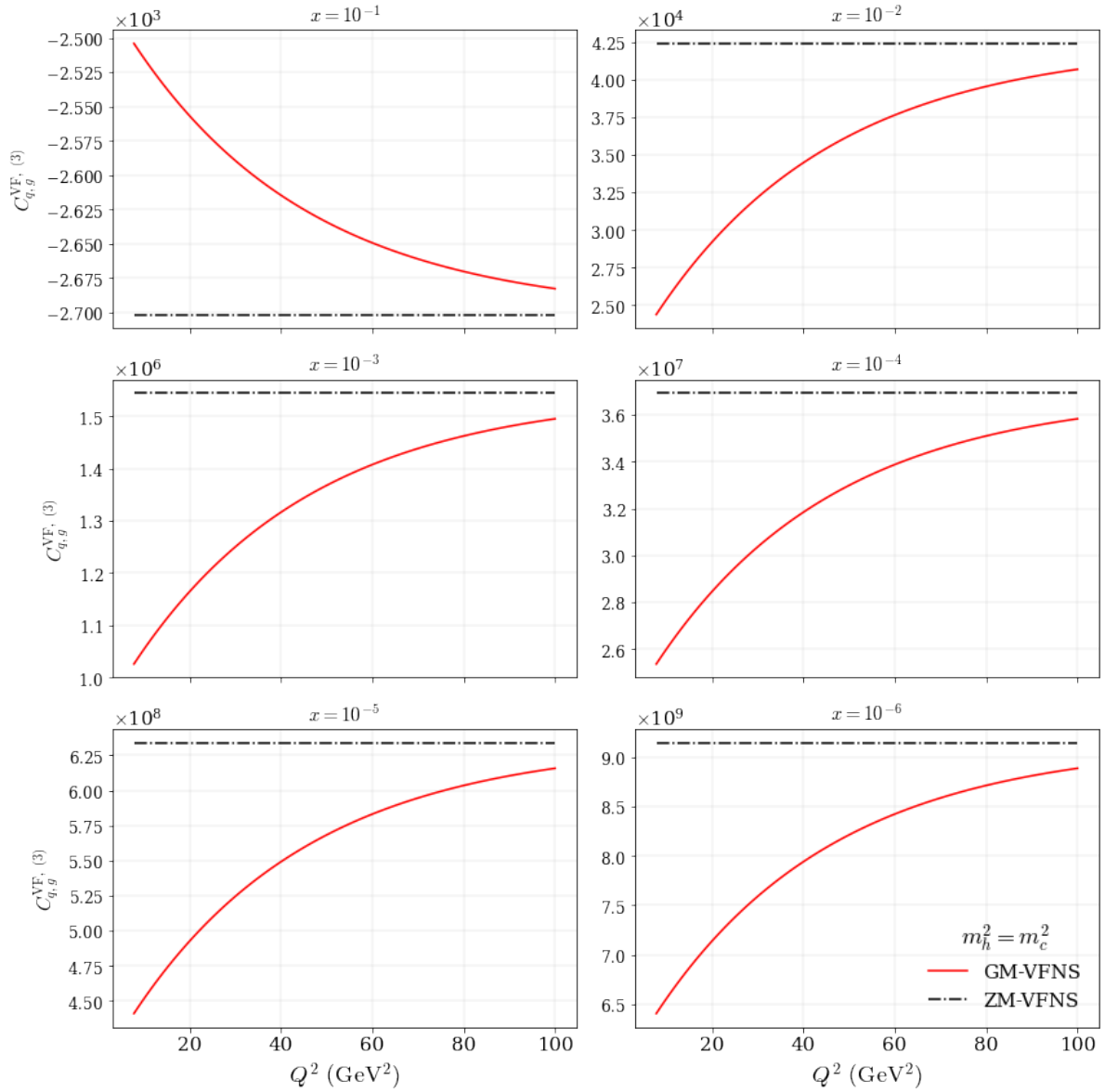

Figure 9.9.: The N^{3}LO GM-VFNS function $C_{q,g}^{\mathrm{VF},\,(3)}$ compared with the N^{3}LO ZM-VFNS function $C_{q,g}^{\mathrm{ZM},\,(3)}$ across a variety of x and Q^2 values. $C_{q,g}^{\mathrm{VF},\,(3)}$ is parameterised via Equations (9.19d) and (6.19). Mass threshold is set at the charm quark level ($m_h^2 = m_c^2 = 1.4\,\mathrm{GeV}^2$).

minor tensions in the fit[5]. The magnitude of $C_{q,g}^{\text{VF, (3)}}$ across the entire range of Q^2 is still relatively constant, although less flat than the behaviour predicted for $C_{q,q,\text{ PS/NS}}^{\text{VF, (3)}}$. However, considering Equation (9.19d), some justification for this behaviour can be offered. When comparing the contributions to the FFNS functions in the NS, PS and gluon cases (Equations (9.15d), (9.17d) and (9.19d) respectively), the A_{Hg} and $A_{gg,H}$ contributions involved in $C_{q,g}^{\text{FF}}$ are much larger than the contributions from $A_{gq,H}$, A_{Hq} and $A_{qq,H}^{\text{NS}}$. Therefore we can expect a larger difference across Q^2 for the $C_{q,g}^{\text{VF, (3)}}$ function. With this being said, the specific form at low-Q^2 is not very important in current PDF fits, only that the form is continuous and valid.

[5]The differences in fit quality for sensible choices of Equation (6.19) are $< 0.5\%$ compared to the overall χ^2 for the light quark gluon coefficient function.

Chapter 10.

N^{3}LO *K*-factors

Thus far the primary concern has been the N^{3}LO additions to the theoretical form of the DIS cross section. However, to complement these changes it is necessary to extend other cross section data to the same order. With these ingredients it is possible to maintain a consistent approximate N^{3}LO treatment across all datasets. At the time of writing, *K*-factors which provide exact transformations for each dataset up to NNLO are available[1]. Although there has been progress in N^{3}LO calculations for various processes including Drell-Yan (DY), approximate top production and Higgs processes [191–204], there is still missing information on how these *K*-factors behave above NNLO. In this section we investigate the effects of the *K*-factors for each dataset when extended to N^{3}LO. Five process categories are considered separately: Drell-Yan, Jets, p_T jets, $t\bar{t}$ production and Dimuon data. Inside each of these process categories we assume a perfect positive correlation between the behaviour of datasets i.e. all Drell-Yan *K*-factor shifts from NNLO are positively correlated. Clearly this treatment is a simplification, based on the expectation of a high degree of correlation between

[1] An exception to this is the CMS 7 TeV $W + c$ [115] dataset where *K*-factors are available only up to NLO.

datasets concerned with the same processes. In practice, the uncertainty introduced from including these *K*-factors is already relatively small compared to the other sources of MHOUs already discussed, therefore any correction to this is guaranteed to be small (this will be shown more clearly in Chapter 11).

10.1. Extension to aN^{3}LO

The extension to aN^{3}LO is parameterised with a mixture of the NLO and NNLO *K*-factors. This allows control of the magnitude and shape of the transformation from NNLO to aN^{3}LO, using the known shifts from lower orders.

The basic idea is presented as,

$$K^{\mathrm{N^3LO/LO}} = a_{\mathrm{NNLO}}\, K^{\mathrm{NNLO/LO}} + a_{\mathrm{NLO}}\, K^{\mathrm{NLO/LO}}, \tag{10.1}$$

where $K^{\mathrm{N^3LO/LO}}, K^{\mathrm{NNLO/LO}}$ and $K^{\mathrm{NLO/LO}}$ are the relevant *K*-factors with respect to the LO cross section, and $a_{\mathrm{N(N)LO}}$ are variational parameters controlling the mixture of NNLO and NLO *K*-factors included in the N^{3}LO *K*-factor approximation.[2] Hence we have 2 parameters for each of the five processes included in the fit, and now 20 theory nuisance parameters in total – 10 controlling aN^{3}LO *K*-factors, 5 controlling aN^{3}LO splitting functions and 5 controlling heavy flavour aN^{3}LO contributions.

To describe this formalism in terms of physical observables we consider the cross section,

$$\sigma = \sigma_0 + \sigma_1 + \sigma_2 + \cdots \equiv \sigma_{\mathrm{NNLO}} + \ldots, \tag{10.2}$$

[2]Where relevant, all *K*-factors are calculated with NNLO PDFs.

where there is an implicit order of α_s^{p+i} absorbed into the definition of σ_i beginning at the relevant LO for each process, i.e. $p = 0$ for DY.

$K^{\mathrm{NLO/LO}}$ is then the relative shift from σ_{LO} to σ_{NLO},

$$K^{\mathrm{NLO/LO}} = \frac{\sigma_0 + \sigma_1}{\sigma_0} = 1 + \frac{\sigma_1}{\sigma_0}. \tag{10.3}$$

Similarly for NNLO we have,

$$K^{\mathrm{NNLO/LO}} = \frac{\sigma_0 + \sigma_1 + \sigma_2}{\sigma_0} = 1 + \frac{\sigma_1}{\sigma_0} + \frac{\sigma_2}{\sigma_0}. \tag{10.4}$$

Moving to N^{3}LO, we write

$$\sigma = \sigma_0 + \sigma_1 + \sigma_2 + \sigma_3 + \cdots \equiv \sigma_{\mathrm{N^3LO}} + \ldots, \tag{10.5}$$

where $\sigma_3 = a_1\sigma_1 + a_2\sigma_2$ is some superposition of the two lower orders, with $(a_1, a_2) = (0, 0)$ reproducing the NNLO case.

Pushing forward with this approximation and using the definitions for $\sigma_{1,2}$ in terms of K-factors (Equations (10.3) and (10.4)) we have,

$$\sigma_{\mathrm{N^3LO}} = \sigma_{\mathrm{NNLO}} + a_1\sigma_1 + a_2\sigma_2 \tag{10.6}$$

$$= \sigma_{\mathrm{NNLO}} + a_1\sigma_0(K^{\mathrm{NLO/LO}} - 1) + a_2\sigma_0(K^{\mathrm{NNLO/LO}} - K^{\mathrm{NLO/LO}}) \tag{10.7}$$

since,

$$\sigma_1 = \sigma_0 \left(K^{\mathrm{NLO/LO}} - 1 \right) \tag{10.8}$$

$$\begin{aligned} \sigma_2 &= \sigma_0 \left(K^{\mathrm{NNLO/LO}} - \sigma_1 - \sigma_0 \right) \\ &= \sigma_0 \left(K^{\mathrm{NNLO/LO}} - K^{\mathrm{NLO/LO}} \right). \end{aligned} \tag{10.9}$$

From here one can obtain,

$$K^{\mathrm{NNLO/LO}} - K^{\mathrm{NLO/LO}} = \frac{\sigma_2}{\sigma_0} = \frac{\sigma_2 + \sigma_0}{\sigma_0} - 1 \approx \frac{\sigma_2 + \sigma_1 + \sigma_0}{\sigma_1 + \sigma_0} - 1 = K^{\mathrm{NNLO/NLO}} - 1, \tag{10.10}$$

assuming $\sigma_1 \ll \sigma_0$, which is in general true for a valid perturbative expansion. Using (10.10) $\sigma_{\mathrm{N^3LO}}$ can be expressed by,

$$\sigma_{\mathrm{N^3LO}} \simeq \sigma_{\mathrm{NNLO}} \left(1 + a_1 (K^{\mathrm{NLO/LO}} - 1) + a_2 (K^{\mathrm{NNLO/NLO}} - 1) \right), \tag{10.11}$$

where $\sigma_2 \ll \sigma_1 \ll \sigma_0$.

This defines the proposed approximated N^{3}LO cross section. It is given in terms of extra contributions from lower order shifts, which are controlled by variational parameters a_1 and a_2. It is also true that the contributions to N^{3}LO are expected to be suppressed by α_s/π in the NNLO case and $(\alpha_s/\pi)^2$ in the NLO case to account for the strengths of each contribution. Currently this is taken into account within the variational parameters a_1, a_2. However for the purpose of this description, it is more appropriate to explicitly redefine $a_1, a_2 = a_s^2 \hat{a}_1, a_s \hat{a}_2$ where $a_s = \mathcal{N} \alpha_s$ and $\mathcal{N}$ is some

normalisation factor. This then results in,

$$K^{\mathrm{N^3LO/LO}} = K^{\mathrm{NNLO/LO}}\left(1+\hat{a}_1\mathcal{N}^2\alpha_s^2(K^{\mathrm{NLO/LO}}-1)+\hat{a}_2\mathcal{N}\alpha_s(K^{\mathrm{NNLO/NLO}}-1)\right). \tag{10.12}$$

where the LO cross section σ_0 is cancelled and Equation (10.12) is written in terms of the K-factor shifts only. (10.12) also implicitly includes the correct order $\mathcal{O}(\alpha_s^3)$ in the parameterisation through (10.3) and (10.4). We can then choose $\mathcal{N}$ in order to set the approximate magnitude of our variational parameters $\hat{a}_1, \hat{a}_2$. Given $\alpha_s \sim 0.1$ for the processes considered, if we neglect $\mathcal{N}$ (i.e. choose $\mathcal{N} \sim 1$), then our order by order reduction in the magnitude of the K-factors would be $\sim 10\%$ for $\mathcal{O}(1)$ for variational parameters, however from previous orders we see that typically K-factors tend to be $30-40\%$ of the previous order, therefore we instead choose $\mathcal{N} \sim 3$. This then ensures the natural scale of variation allowed is also of this order with $\mathcal{O}(1)$ variational parameters describing the admixture of NLO and NNLO K-factors, with conservative penalties applied accordingly.

Reflecting on this, it is worth noting that these fitted K-factors will be sensitive to all orders, not just N^{3}LO. Considering these K-factors as approximating asymptotic behaviour to all orders in perturbation theory when assessing the stability of predictions, we can be less concerned with any somewhat large shifts from NNLO to aN^{3}LO, as we will specifically see in the case of Fig.'s 10.4 and 10.5. Finally, we remind the reader that at higher orders, new terms with more divergent leading logarithms appear which are missed by the current theoretical description. Due to this, the all-orders asymptotic description will still remain approximate up to the inclusion of more divergent leading logarithms in (x, Q^2) limits at even higher orders.

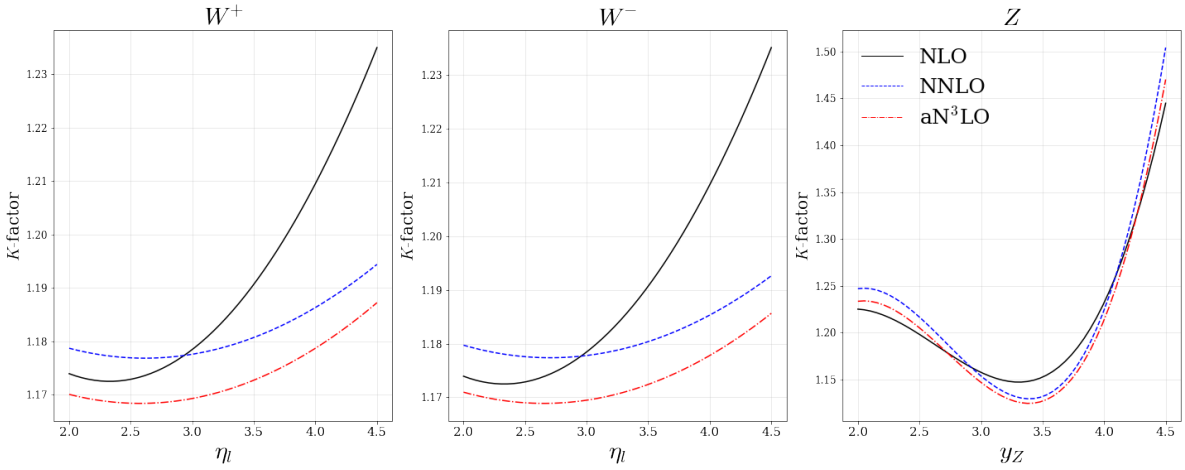

Figure 10.1.: *K*-factor expansion up to aN^{3}LO shown for the LHCb 2015 W, Z dataset [105,106]. The *K*-factors shown here are absolute i.e. all with respect to LO ($K^{\mathrm{N^mLO/LO}}\ \forall\ m \in \{1,2,3\}$).

10.2. Numerical Results

Using this formalism for the aN^{3}LO *K*-factors, we present the global fit results for each of the five process categories considered.

Drell-Yan Processes

For the Drell-Yan processes (all calculated at $\mu_{r,f} = m_{ll}/2$), a reduction of $\sim 1-2\%$ in the *K*-factor shift is predicted across most of the corresponding datasets at aN^{3}LO. This is in agreement with recent work [192]. An example of this reduction is shown in Fig. 10.1.

Conversely, Fig. 10.2 displays an example where the *K*-factor shift has much less of a contribution at N^{3}LO. This is a feature of the ATLAS datasets included in the fit due to the impact of chosen p_T cuts which reduce the sensitivity to higher orders.

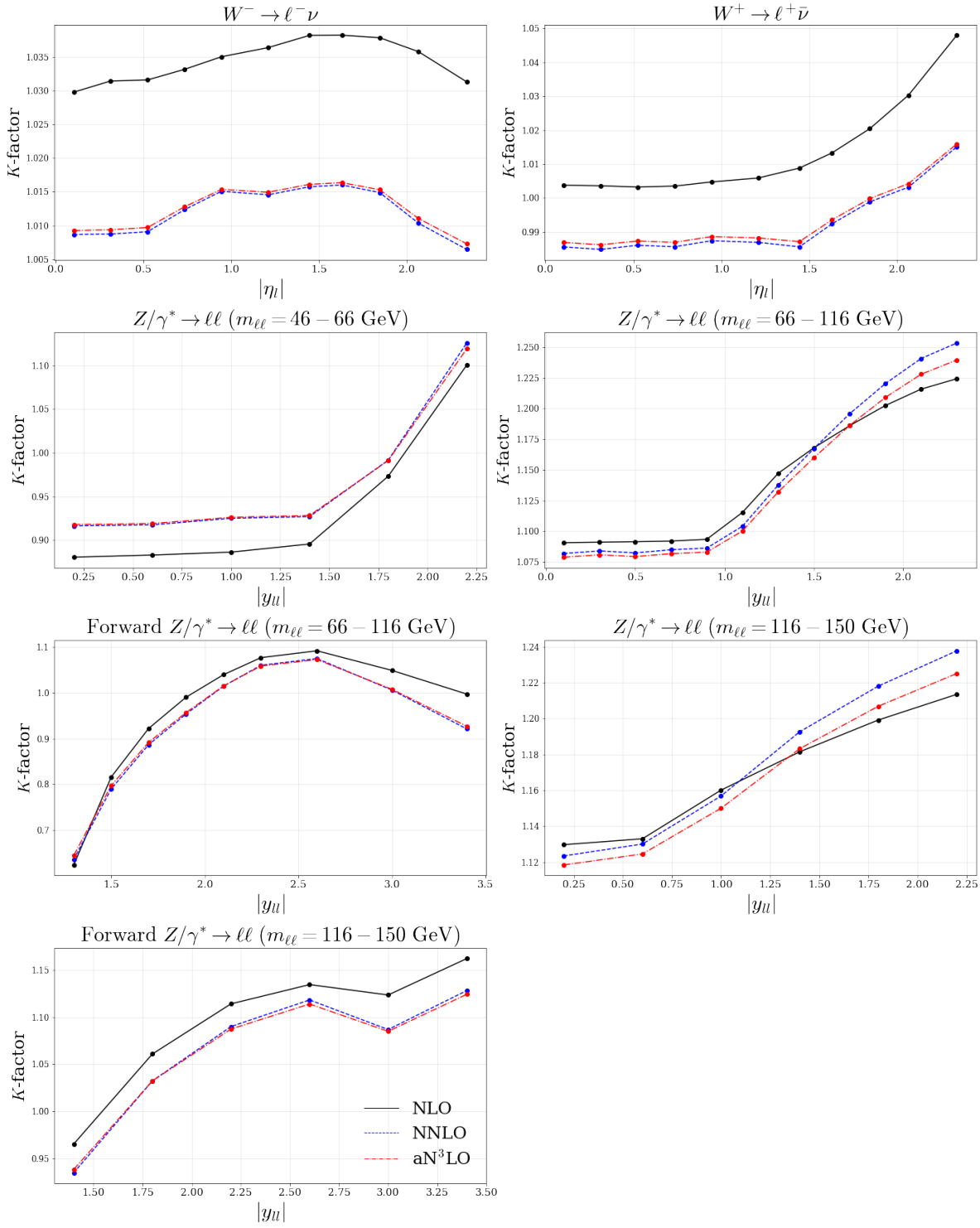

Figure 10.2.: *K*-factor expansion up to aN^{3}LO shown for the ATLAS 7 TeV high precision W, Z dataset [116]. The *K*-factors shown here are absolute i.e. all with respect to LO ($K^{\mathrm{N^mLO/LO}}\ \forall\ m \in \{1,2,3\}$).

DY Dataset	χ^2	$\Delta\chi^2$ from NNLO	$\Delta\chi^2$ from NNLO (NNLO K-factors)
E866 / NuSea pp DY [102]	209.2 / 184	-15.9	-11.0
E866 / NuSea pd/pp DY [104]	7.6 / 15	-2.7	-2.6
DØ II Z rap. [130]	16.8 / 28	$+0.5$	$+0.3$
CDF II Z rap. [132]	39.6 / 28	$+2.4$	$+1.6$
DØ II $W \to \nu\mu$ asym. [134]	16.8 / 10	-0.5	$+0.2$
CDF II W asym. [73]	19.9 / 13	$+0.9$	$+0.6$
DØ II $W \to \nu e$ asym. [74]	29.2 / 12	-4.7	-5.1
ATLAS W^+, W^-, Z [77]	30.0 / 30	$+0.1$	$+0.4$
CMS W asym. $p_T > 35$ GeV [80]	7.0 / 11	-0.8	-0.5
CMS W asym. $p_T > 25, 30$ GeV [81]	7.5 / 24	$+0.1$	$+0.0$
LHCb $Z \to e^+e^-$ [83]	20.6 / 9	-2.1	-1.7
LHCb W asym. $p_T > 20$ GeV [84]	12.9 / 10	$+0.5$	$+0.9$
CMS $Z \to e^+e^-$ [86]	17.3 / 35	-0.6	-0.6
ATLAS High-mass Drell-Yan [87]	18.5 / 13	-0.4	-1.2
CMS double diff. Drell-Yan [103]	137.1 / 132	-7.4	$+12.3$
LHCb 2015 W, Z [105, 106]	97.2 / 67	-2.2	-3.4
LHCb 8 TeV $Z \to ee$ [108]	27.1 / 17	$+0.9$	-0.1
CMS 8 TeV W [109]	12.0 / 22	-0.7	$+0.3$
ATLAS 7 TeV high prec. W, Z [116]	110.5 / 61	-6.2	-18.2
DØ W asym. [119]	8.6 / 14	-3.4	-2.5
ATLAS 8 TeV High-mass DY [125]	63.4 / 48	$+6.3$	$+2.8$
ATLAS 8 TeV W [129]	55.1 / 22	-2.3	-0.8
ATLAS 8 TeV double diff. Z [135]	80.8 / 59	-4.8	-2.4
Total	1044.8 / 864	-43.1	-30.5

Table 10.1.: Table showing the relevant DY datasets and how the individual χ^2 changes from NNLO by including the N^{3}LO treatment of K-factors, and theoretical N^{3}LO additions discussed earlier. The result with purely NNLO K-factors included for all data in the fit is also given.

Table 10.1 demonstrates that in most cases, the new fitted DY aN^{3}LO *K*-factors are producing a slightly better fit with a substantial cumulative effect. We remind the reader that we have included a total of 20 extra parameters into the fit (10 controlling aN^{3}LO *K*-factors, 5 controlling aN^{3}LO splitting functions and 5 controlling heavy flavour aN^{3}LO contributions). These extra 20 parameters are fit across all datasets and multiple processes, whereas the decrease here is for a subset of datasets corresponding to the DY processes included in a global fit. Therefore this decrease in χ^2 being comparable to the number of extra parameters, even when only considering the DY sets, is evidence that this extra N^{3}LO information is helping the fit perform better in general. This will be discussed further in Chapter 11 where a full global χ^2 breakdown is provided.

Across these datasets, the *K*-factors act to extend the description of these processes to approximate N^{3}LO. The result of including this procedure is a better fit in the DY regime while also relaxing tensions with other processes included in the fit. Comparing the $\Delta\chi^2$ results with and without aN^{3}LO *K*-factors, we can see the extent to which the *K*-factors and all other N^{3}LO additions are reducing the overall χ^2.

In some individual cases, the dataset χ^2 becomes slightly worse relative to NNLO (e.g. ATLAS 8 TeV High-mass DY [125]), whilst in a few others the χ^2 improvement upon addition of the aN^{3}LO splitting functions, transition matrix elements and coefficient function pieces is seen to deteriorate upon addition of the aN^{3}LO *K*-factors, e.g. such as for the ATLAS 7 TeV high prec. W, Z [116], which is observed to prefer N^{3}LO theory with NNLO *K*-factors. The addition of the aN^{3}LO *K*-factors do nonetheless result in a net reduction in χ^2 and for a large number of cases the aN^{3}LO *K*-factors allow for a slight reduction in the individual χ^2. The CMS double diff. Drell-Yan [103] shows a particularly large reduction when these are added on top of the aN^{3}LO theory,

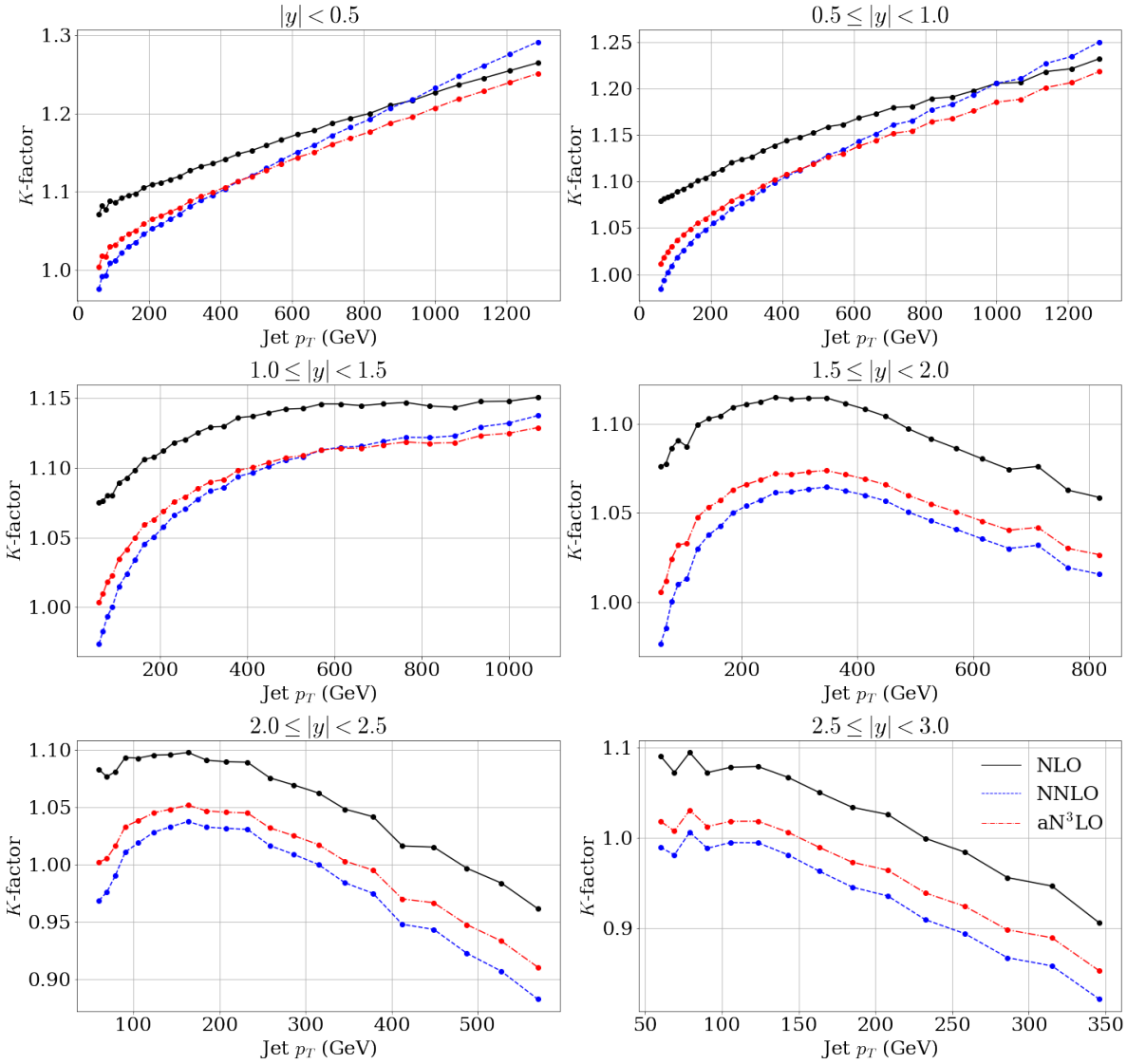

Figure 10.3.: *K*-factor expansion up to aN^{3}LO shown for the CMS 7 TeV jets dataset ($R = 0.7$) [118]. The *K*-factors shown here are absolute i.e. all with respect to LO ($K^{\mathrm{N^mLO/LO}}\ \forall\ m \in \{1,2,3\}$).

this is a dataset which shows some tension with the DIS N^{3}LO additions which is then eased by the addition of the aN^{3}LO *K*-factors

Jets Dataset	χ^2	$\Delta\chi^2$ from NNLO	$\Delta\chi^2$ from NNLO (NNLO *K*-factors)
CDF II $p\bar{p}$ incl. jets [128]	68.4 / 76	+8.0	+0.9
DØ II $p\bar{p}$ incl. jets [76]	113.6 / 110	−6.6	−3.6
ATLAS 7 TeV jets [113]	214.5 / 140	−7.1	+2.5
CMS 7 TeV jets [118]	189.8 / 158	+14.1	+13.9
CMS 8 TeV jets [122]	272.6 / 174	+11.3	+22.9
CMS 2.76 TeV jet [131]	113.9 / 81	+11.1	+13.3
Total	972.9 / 739	+30.8	+49.8

Table 10.2.: Table showing the relevant jet datasets and how the individual χ^2 changes from NNLO by including the N^{3}LO treatment of *K*-factors. The result with purely NNLO *K*-factors included for all data in the fit is also given.

Jet Production Processes

The jets processes (all calculated for $\mu_{r,f} = p_T^{jet}$) show a general increase in the *K*-factor shifts from NNLO as seen in Fig. 10.3, which displays the *K*-factor expansion up to aN^{3}LO for the CMS 7 TeV jets dataset [118]. It is apparent that there is a mild shift to N^{3}LO from the NNLO *K*-factor. This behaviour follows what one might expect for a perturbative expansion considering the forms of the NLO and NNLO functions.

A χ^2 summary of the Jets datasets is provided in Table 10.2. By combining the N^{3}LO structure function and DGLAP additions (Chapter's 7 to 9) with NNLO *K*-factors, the fit exhibits a substantial increase in the χ^2 from Jets data. Including aN^{3}LO *K*-factors acts to reduce some of this tension with around half the initial overall χ^2 increase still remaining. We note that in the case of the ATLAS 7 TeV jets [113], it is well known that there are issues in achieving a good fit quality across all rapidity bins (see [205] for a detailed study as well as [206] where the 8 TeV data are presented and the same issues observed). In [205, 206] the possibility of decorrelating some of the

systematic error sources where the degree of correlation is less well established, was considered and indeed in our study we follow such a procedure, as described in [3]. Alternatively, however, it might be that the issues in fit quality could at least part be due to deficiencies in theoretical predictions, such as MHOs. To assess this, we revert to the default ATLAS correlation scenario and repeat the global fit. We find that the χ^2 deteriorates by $+40.7$ points to 256.6, which is very close to the result found in a pure NNLO fit [3]. In other words, in our framework the impact of MHOUs does not resolve this issue.

The χ^2 results for datasets in Table 10.2 show evidence for some tensions with the N^{3}LO form of the high-x gluon. It is also apparent that the CMS data is in more tension than ATLAS datasets with N^{3}LO structure function and DGLAP theory. Therefore it will be interesting to see how this behaviour changes when considering this data as dijets in the global fit [207]. We do not consider the dijet data here, though this will be addressed in a future publication.

Z p_T & Vector Boson + Jets Processes

In the case of Z p_T & vector boson + jet processes (all calculated at $\mu_{r,f} = \sqrt{p_{T,ll}^2 + m_{ll}^2}$), the K-factor shift is almost completely dominated by the ATLAS 8 TeV Z p_T dataset [121] (due to the larger number of data points included in this dataset) shown in Fig. 10.4. The gluon is less directly constrained than the quarks in a global fit. Therefore it can be expected that the significant modifications at small-x will indirectly affect the high-x gluon, where these processes are most sensitive. Considering the jet production processes in Table 10.2, when performing separate PDF fits not including ATLAS 8 TeV Z p_T data [121], we find a reduction of $\Delta\chi^2 = -7.0$ in CMS 8 TeV jets data [122] eliminating most of the tension for this dataset (similar to MSHT20 NNLO results in

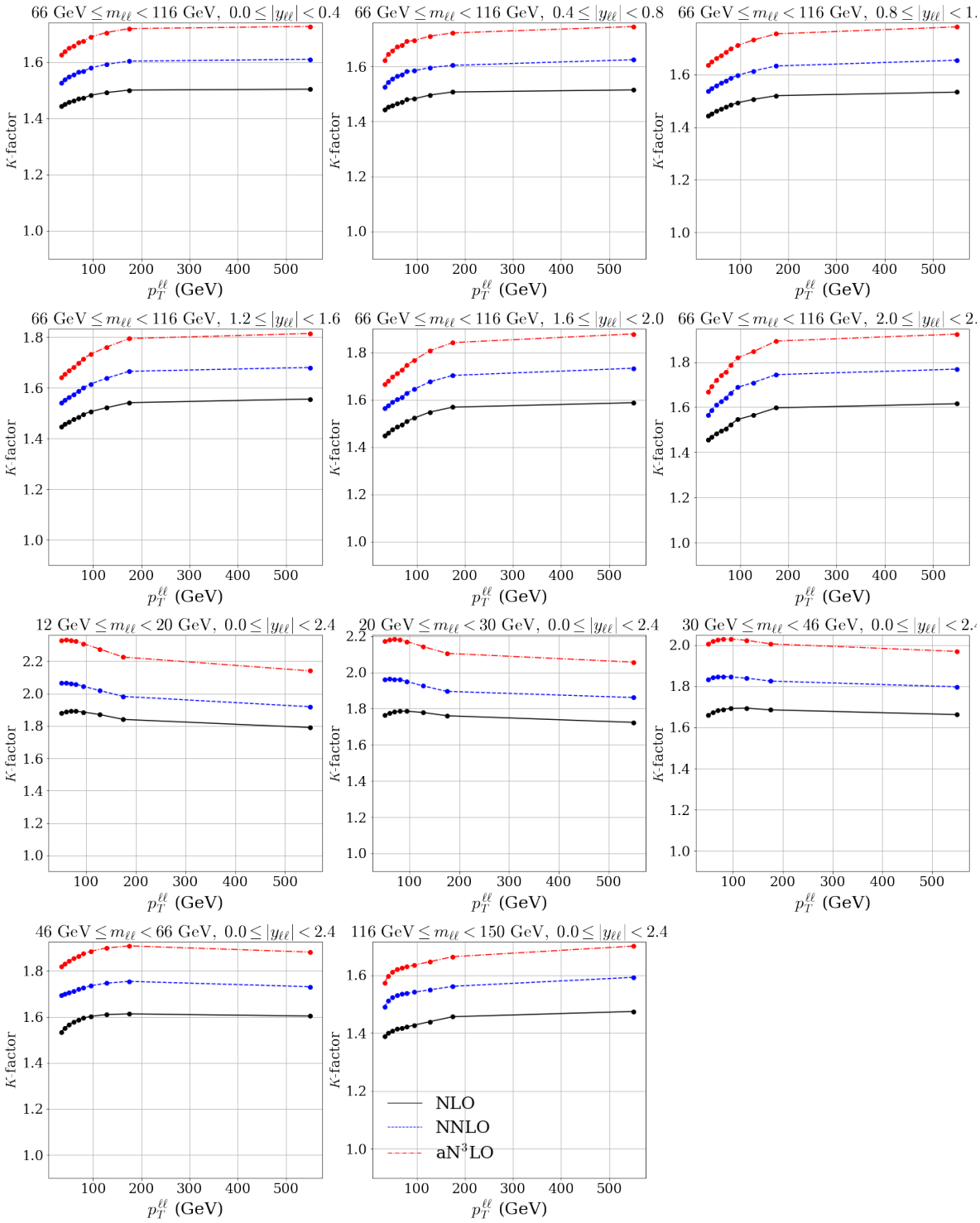

Figure 10.4.: *K*-factor expansion up to aN^{3}LO shown for the ATLAS 8 TeV Z p_T dataset [121]. The *K*-factors shown here are absolute i.e. all with respect to LO ($K^{\mathrm{N^mLO/LO}}\ \forall\ m \in \{1,2,3\}$).

p_T Jets Dataset	χ^2	$\Delta\chi^2$ from NNLO	$\Delta\chi^2$ from NNLO (NNLO *K*-factors)
CMS 7 TeV $W+c$ [115]	12.3 / 10	+3.7	+1.3
ATLAS 8 TeV Z p_T [121]	105.8 / 104	−82.7	−53.0
ATLAS 8 TeV W + jets [126]	19.1 / 30	+0.9	+0.3
Total	137.1 / 144	−78.1	−51.5

Table 10.3.: Table showing the relevant Z p_T & Vector Boson jet datasets and how the individual χ^2 changes from NNLO by including the N^{3}LO treatment of *K*-factors, and theoretical N^{3}LO additions discussed earlier. The result with purely NNLO *K*-factors included for all data in the fit is also given.

Table 16 of [3]). Further to this, when not including HERA and ATLAS 8 TeV Z p_T data we find a reduction of $\Delta\chi^2 = -26.4$ in CMS 8 TeV jet data [122] and $\Delta\chi^2 = -12.7$ in CMS 2.76 TeV jet data [131].

Although the overall magnitude of the *K*-factor in Fig. 10.4 may seem large, this new shift is contained within a 15% increase from NNLO (due to the NLO and NNLO *K*-factors also being significant). Moreover, not only does the size of this shift have some dependence on the central scale, but this shift may be more correctly interpreted as the preferred all-orders cross section rather than simply the pure N^{3}LO result.

The extent of the χ^2 reduction in the Z p_T datasets is shown in Table 10.3. Note that around $\sim$60% of the improvement to the ATLAS 8 TeV Z p_T [121] χ^2 is due to the extra N^{3}LO theory included in the DGLAP and DIS descriptions. It is also known the ATLAS 8 TeV Z p_T data [121] previously exhibited a significant level of tension with many datasets (including HERA data) at NNLO [3]. This was investigated by performing a global PDF fit with and without HERA data and comparing the individual χ^2's from each dataset. At NNLO it was found that the ATLAS 8 TeV Z p_T dataset [121] reduced by $\Delta\chi^2 = -39.2$ when fitting to all non-HERA data (see Table D.1). At N^{3}LO we show

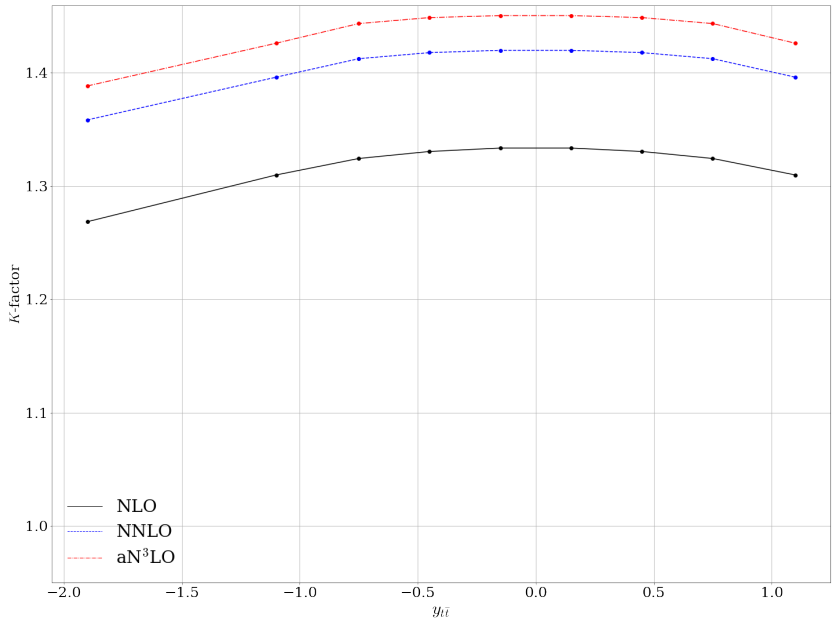

Figure 10.5.: *K*-factor expansion up to aN^{3}LO shown for the CMS 8 TeV single diff. $t\bar{t}$ dataset [133]. The *K*-factors shown here are absolute i.e. all with respect to LO ($K^{\mathrm{N^mLO/LO}}\ \forall\ m \in \{1,2,3\}$).

that the ATLAS 8 TeV Z p_T dataset [121] actually increased by $\Delta\chi^2 = +12.8$ when fitting to all non-HERA data (see Table D.2). This therefore completely eliminates this tension with the N^{3}LO additions and confirms the issue previously observed when attempting to fit the ATLAS 8 TeV Z p_T dataset [121] was concerned with MHOs. This is in contrast with the result observed for ATLAS 7 TeV jets [113] where the issues with fit quality were not alleviated by the inclusion of MHO information.

Finally we remind the reader that the CMS 7 TeV $W + c$ dataset [115] does not include a *K*-factor at NNLO. To overcome this, we tie the overall N^{3}LO *K*-factor shift to the NLO value ($K^{\mathrm{NNLO/NLO}} = 1$ in Equation (10.12)), therefore contributing as an overall normalisation effect.

Top Dataset	χ^2	$\Delta\chi^2$ from NNLO	$\Delta\chi^2$ from NNLO (NNLO *K*-factors)
Tevatron, ATLAS, CMS $\sigma_{t\bar{t}}$ [89–101]	14.2 / 17	−0.3	−0.7
ATLAS 8 TeV single diff. $t\bar{t}$ [123]	24.7 / 25	−0.9	−0.1
ATLAS 8 TeV single diff. $t\bar{t}$ dilep. [124]	2.1 / 5	−1.3	−0.8
CMS 8 TeV double diff. $t\bar{t}$ [127]	23.9 / 15	+1.4	+4.9
CMS 8 TeV single diff. $t\bar{t}$ [133]	8.4 / 9	−4.7	−5.5
Total	73.4 / 71	−5.9	−2.2

Table 10.4.: Table showing the relevant Top Quark datasets and how the individual χ^2 changes from NNLO by including the N^{3}LO treatment of *K*-factors, and theoretical N^{3}LO additions discussed earlier. The result with purely NNLO *K*-factors included for all data in the fit is also given.

Top Quark Processes

Moving to top quark processes, for the single differential datasets the scale choice for $\mu_{r,f}$ is $H_T/4$ with the exception of data differential in the average transverse momentum of the top or anti-top, p_T^t, $p_T^{\bar{t}}$, for which $m_T/2$ is used. For the double diff. dataset the scale choice is $H_T/4$ and for the inclusive top $\sigma_{t\bar{t}}$ a scale of m_t is chosen. Fig. 10.5 displays the *K*-factor shifts up to N^{3}LO for the CMS 8 TeV single diff. $t\bar{t}$ dataset [133], which shows the greatest reduction in its χ^2. A familiar perturbative pattern can be seen for this process's *K*-factors, with the shift at aN^{3}LO increasing by around 3–4% from NNLO. This is in agreement with a recent $\sim$3.5% predicted increase in the N^{3}LO $t\bar{t}$ production *K*-factor at 8 TeV in [194], whereby an approximate N^{3}LO cross section for $t\bar{t}$ production in proton-proton collisions has been calculated employing a resummation formalism [208–211].

The χ^2 results in Table 10.4 display a mildly better fit for top processes, with most datasets not feeling a large overall effect from the N^{3}LO additions. Comparing with

	NLO	NNLO	aN^{3}LO	aN^{3}LO (NNLO *K*-factors)
BR$(D \to \mu)$	0.095	0.088	0.080	0.079

Table 10.5.: Table displaying dimuon branching ratios (BRs) at NLO, NNLO, aN^{3}LO and aN^{3}LO with NNLO *K*-factors.

and without aN^{3}LO *K*-factors, we see a slightly better fit overall, with most of the reduction in overall χ^2 stemming from CMS 8 TeV double diff. $t\bar{t}$ data [127].

Semi-Inclusive DIS Dimuon Processes

The final set of results to consider in this Section are the aN^{3}LO *K*-factors associated with semi-inclusive DIS dimuon cross sections (with $\mu_{r,f}^2 = Q^2$). Although the dimuon is associated with the DIS process described from our approximate N^{3}LO structure function picture, it is a semi-inclusive DIS process. Therefore it is sensible to treat this process as entirely separate from DIS. The NNLO cross-sections used in this case are a general-mass variable flavour number scheme extension of the results in [212], as described in more detail in [3]. The *K*-factors shown in Fig. 10.6 (for the NuTeV $\nu N \to \mu\mu X$ data [114]) are somewhat similar to NNLO. The reason for this is mostly due to these datasets also including a branching ratio (BR$(D \to \mu)$) which absorbs any overall normalisation shifts. This behaviour is not a concern since in practice these two work in tandem and when combined together it makes no difference where the normalisation factors are absorbed into. Investigating the change in the BR's with the addition of N^{3}LO contributions in Table 10.5, the BR at N^{3}LO decreases substantially from NNLO, with little difference from the addition of aN^{3}LO *K*-factors. The predicted dimuon BR at aN^{3}LO is inside the allowed $\pm 1\sigma$ range of 0.092 ± 0.010.

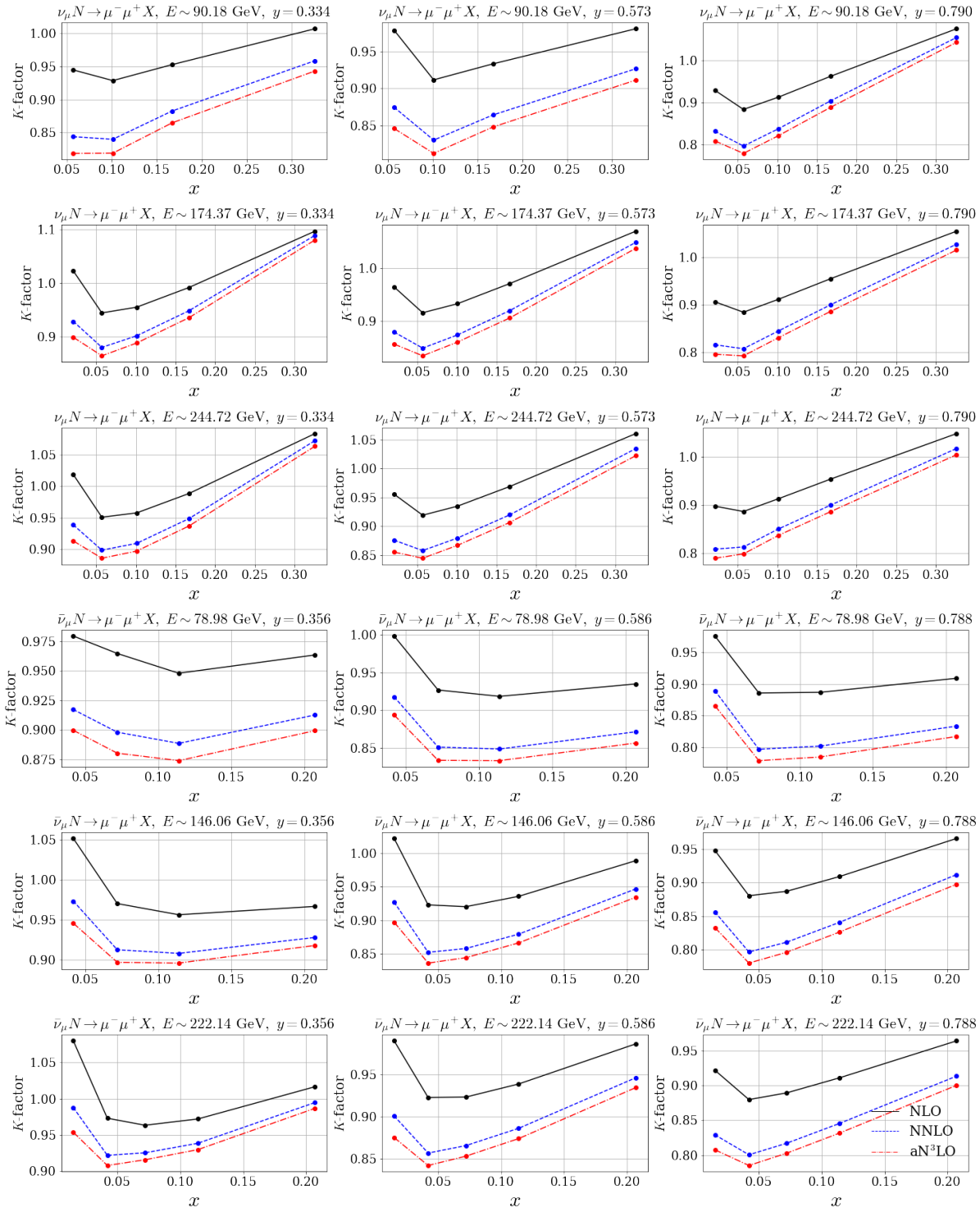

Figure 10.6.: K-factor expansion up to aN^{3}LO shown for the NuTeV $\nu N \to \mu\mu X$ dataset [114]. The K-factors shown here are absolute i.e. all with respect to LO ($K^{\mathrm{N^mLO/LO}}\ \forall\ m \in \{1,2,3\}$).

Dimuon Dataset	χ^2	$\Delta\chi^2$ from NNLO	$\Delta\chi^2$ from NNLO (NNLO *K*-factors)
CCFR $\nu N \to \mu\mu X$ [114]	69.2 / 86	+1.5	+2.9
NuTeV $\nu N \to \mu\mu X$ [114]	55.3 / 84	−3.1	−3.4
Total	124.6 / 170	−1.6	−0.5

Table 10.6.: Table showing the relevant Dimuon datasets and how the individual χ^2 changes from NNLO by including the N^{3}LO treatment of *K*-factors, and theoretical N^{3}LO additions discussed earlier. The result with purely NNLO *K*-factors included for all data in the fit is also given.

When performing a fit with the BR fixed at its central value (BR = 0.092), one is able to observe the effect of manually forcing the normalisation into the *K*-factor variation alone. The result of this is a worse global fit quality $\Delta\chi^2 = +11.2$, where +3.9 units arise from an increased penalty for the Dimuon *K*-factor description and +2.3 units from a slightly worse fit to the Dimuon datasets listed in Table 10.6. The rest of the observed increase in χ^2_{global} is dominated by a +4.1 increase in the ATLAS 7 TeV high prec. W, Z [116] data due to a smaller strange quark PDF (compensating the higher BR in dimuon datasets). Returning to consider the case of the *K*-factors and BR together, the predicted effect on dimuon datasets is very similar. However due to the errors accounting for a larger allowed shift in the BR relative to the *K*-factors, the fit favours moving the BR by a larger amount to reduce the penalty χ^2 contribution from *K*-factors which explains the results shown in Table 10.5.

Table 10.6 further confirms the expectation that the Dimuon datasets are not too sensitive to N^{3}LO additions. The results with and without a full treatment of aN^{3}LO *K*-factors are also similar in magnitude. It is therefore clear that the dimuon BR's are compensating for any indirect normalisation effects from the form of the PDFs in the full aN^{3}LO fit, as opposed to the aN^{3}LO *K*-factors.

Chapter 11.

MSHT20 Approximate N^{3}LO Global Analysis

With the inclusion of all N^{3}LO approximations discussed in earlier sections resulting in 20 extra free parameters from the NNLO MSHT20 fit, we now present the results for the first approximate N^{3}LO global PDF fit with theoretical uncertainties from MHOs. This includes the results for the best fit for the nuisance parameters describing the theoretical uncertainty. We remind the reader that these are parameterised specifically to represent the missing uncertainty at N^{3}LO, which is currently the dominant source of uncertainty due to missing higher orders. However, the fit will also be influenced, to a limited extent, by effects at even higher orders. Later in the Chapter we discuss this in more detail.

Dataset	N_{pts}	χ^2	$\Delta\chi^2$ from NNLO
BCDMS μp F_2 [72]	163	174.4	−5.8
BCDMS μd F_2 [72]	151	144.3	−1.7
NMC μp F_2 [75]	123	121.5	−2.6
NMC μd F_2 [75]	123	104.2	−8.4
SLAC ep F_2 [78,79]	37	31.6	−0.4
SLAC ed F_2 [78,79]	38	22.8	−0.2
E665 μd F_2 [82]	53	63.9	+4.2
E665 μp F_2 [82]	53	67.5	+2.9
NuTeV νN F_2 [85]	53	35.7	−2.6
NuTeV νN xF_3 [85]	42	34.8	+4.1
NMC $\mu n/\mu p$ [88]	148	131.6	+0.8
E866 / NuSea pp DY [102]	184	215.4	−9.7
E866 / NuSea pd/pp DY [104]	15	8.4	−2.0
HERA ep F_2^{charm} [107]	79	143.7	+11.4
NMC/BCDMS/SLAC/HERA F_L [72,75,79,110–112]	57	45.6	−22.9
CCFR $\nu N \to \mu\mu X$ [114]	86	68.3	+0.6
NuTeV $\nu N \to \mu\mu X$ [114]	84	56.7	−1.8
CHORUS νN F_2 [117]	42	29.2	−1.0
CHORUS νN xF_3 [117]	28	18.1	−0.3
HERA e^+p CC [120]	39	49.7	−2.3
HERA e^-p CC [120]	42	64.9	−5.3
HERA e^+p NC 820 GeV [120]	75	84.3	−5.6
HERA e^-p NC 460 GeV [120]	209	247.7	−0.6
HERA e^+p NC 920 GeV [120]	402	474.0	−38.7
HERA e^-p NC 575 GeV [120]	259	248.5	−14.5
HERA e^-p NC 920 GeV [120]	159	243.0	−1.4
CDF II $p\bar{p}$ incl. jets [128]	76	66.5	+6.1
DØ II Z rap. [130]	28	17.4	+1.0
CDF II Z rap. [132]	28	40.6	+3.4
DØ II $W \to \nu\mu$ asym. [134]	10	16.5	−0.8
CDF II W asym. [73]	13	18.2	−0.8

Table 11.1.: Full breakdown of χ^2 results for the aN^{3}LO PDF fit. The global fit includes the N^{3}LO treatment for transition matrix elements, coefficient functions, splitting functions and K-factor additions with their variational parameters determined by the fit.

Dataset	N_{pts}	χ^2	$\Delta\chi^2$ from NNLO
DØ II $W \to \nu e$ asym. [74]	12	30.7	−3.2
DØ II $p\bar{p}$ incl. jets [76]	110	113.3	−6.9
ATLAS W^+, W^-, Z [77]	30	30.0	+0.1
CMS W asym. $p_T > 35$ GeV [80]	11	6.7	−1.1
CMS W asym. $p_T > 25, 30$ GeV [81]	24	7.9	+0.5
LHCb $Z \to e^+e^-$ [83]	9	23.2	+0.5
LHCb W asym. $p_T > 20$ GeV [84]	10	12.6	+0.1
CMS $Z \to e^+e^-$ [86]	35	17.6	−0.4
ATLAS High-mass Drell-Yan [87]	13	18.4	−0.5
Tevatron, ATLAS, CMS $\sigma_{t\bar{t}}$ [89–101]	17	14.3	−0.2
CMS double diff. Drell-Yan [103]	132	133.2	−11.3
LHCb 2015 W, Z [105, 106]	67	103.2	+3.8
LHCb 8TeV $Z \to ee$ [108]	17	30.3	+4.1
CMS 8 TeV W [109]	22	11.5	−1.2
ATLAS 7 TeV jets [113]	140	215.9	−5.6
CMS 7 TeV $W + c$ [115]	10	10.8	+2.2
ATLAS 7 TeV high prec. W, Z [116]	61	119.3	+2.7
CMS 7 TeV jets [118]	158	186.8	+11.0
DØ W asym. [119]	14	12.2	+0.1
ATLAS 8 TeV Z p_T [121]	104	108.4	−80.0
CMS 8 TeV jets [122]	174	271.3	+10.0
ATLAS 8 TeV sing. diff. $t\bar{t}$ [123]	25	24.2	−1.4
ATLAS 8 TeV sing. diff. $t\bar{t}$ dilep. [124]	5	2.7	−0.7
ATLAS 8 TeV High-mass DY [125]	48	62.8	+5.7
ATLAS 8 TeV W + jets [126]	30	18.8	+0.7
CMS 8 TeV double diff. $t\bar{t}$ [127]	15	23.6	+1.0
ATLAS 8 TeV W [129]	22	53.0	−4.4
CMS 2.76 TeV jet [131]	81	109.8	+6.9
CMS 8 TeV sing. diff. $t\bar{t}$ [133]	9	10.3	−2.9
ATLAS 8 TeV double diff. Z [135]	59	80.4	−5.2

Table 11.1.: *(Continued)* Full breakdown of χ^2 results for the aN^{3}LO PDF fit. The global fit includes the N^{3}LO treatment for transition matrix elements, coefficient functions, splitting functions and K-factor additions with their variational parameters determined by the fit.

Low-Q^2 Coefficient			
$c_q^{\rm NLL} = -3.868$	0.004	$c_g^{\rm NLL} = -5.837$	0.844
Transition Matrix Elements			
$a_{Hg} = 12214.000$	0.601	$a_{qq,H}^{\rm NS} = -64.411$	0.001
$a_{gg,H} = -1951.600$	0.857		
Splitting Functions			
$\rho_{qq}^{NS} = 0.007$	0.000	$\rho_{gq} = -1.784$	0.802
$\rho_{qq}^{PS} = -0.501$	0.186	$\rho_{gg} = 19.245$	3.419
$\rho_{qg} = -1.754$	0.015		
K-factors			
$\mathrm{DY}_{\rm NLO} = -0.307$	0.094	$\mathrm{DY}_{\rm NNLO} = -0.230$	0.053
$\mathrm{Top}_{\rm NLO} = 0.041$	0.002	$\mathrm{Top}_{\rm NNLO} = 0.651$	0.424
$\mathrm{Jet}_{\rm NLO} = -0.300$	0.090	$\mathrm{Jet}_{\rm NNLO} = -0.691$	0.478
$p_T\mathrm{Jets}_{\rm NLO} = 0.583$	0.339	$p_T\mathrm{Jets}_{\rm NNLO} = -0.080$	0.006
$\mathrm{Dimuon}_{\rm NLO} = -0.444$	0.197	$\mathrm{Dimuon}_{\rm NNLO} = 0.922$	0.850
N^{3}LO Penalty Total	9.262 / 20	Average Penalty	0.463
		Total	4961.2 / 4363
		$\Delta\chi^2$ from NNLO	-160.1

Table 11.1.: *(Continued)* Full breakdown of χ^2 results for the aN^{3}LO PDF fit. The global fit includes the N^{3}LO treatment for transition matrix elements, coefficient functions, splitting functions and K-factor additions with their variational parameters determined by the fit.

11.1. χ^2 Breakdown

Table 11.1 shows the global χ^2 results for an aN^{3}LO best fit, inclusive of penalties associated with the new theory variational parameters (from Equation (5.31)). The theory parameters are labelled as: $A_{Hg}(a_{Hg})$, $A_{gg,H}(a_{gg,H})$, $A_{qq,H}^{\rm NS}(a_{qq,H}^{\rm NS})$ for the transition matrix elements; $P_{qq}^{\rm NS}(\rho_{qq}^{\rm NS})$, $P_{qq}^{\rm PS}(\rho_{qq}^{\rm PS})$, $P_{qg}(\rho_{qg})$, $P_{gq}(\rho_{gq})$ and $P_{gg}(\rho_{gg})$ for the splitting functions; and $c_q^{\rm NLL}$ and $c_g^{\rm NLL}$ correspond to the NLL parameters discussed in Section 9.1. These are supplemented by the 10 additional nuisance parameters for

the NLO and NNLO K-factors for the five process categories. These 20 additional parameters and their associated penalties are also shown in Table 11.1.

The extra N^{3}LO theory and level of freedom introduced has allowed the fit to achieve a total $\Delta\chi^2 = -160.1$ compared to MSHT20 NNLO total χ^2 (Table 7 from [3]). Comparing with lower order PDF fits, we find a smooth convergence in the fit quality which follows what one may expect from an increase in the accuracy of a perturbative expansion ($\chi^2/N_{\rm pts}$ = LO: 2.57, NLO: 1.33, NNLO: 1.17, N^{3}LO: 1.14). In part, this is due to the extra freedom in the K-factors, which will almost always act to reduce this χ^2 due to the minimisation procedure. However, even with this freedom, in most cases the N^{3}LO theory (non K-factor) contributions include large divergences from NNLO. With this in mind, we must conclude that the fit is preferring a description different from the current NNLO standard.

At NNLO (Table D.1), the tension between HERA and non-HERA datasets accounted for $\Delta\chi^2 = -61.6$ reduction in the overall fit quality when the former was removed, with the majority of this tension between HERA and ATLAS 8 TeV Z p_T [121] data. Whereas comparing fit results with and without HERA data at N^{3}LO, we find $\Delta\chi^2 = -48.0$. Although the overall difference is not too substantial we do report a substantial shift in the leading tensions, where most of the tension with HERA data is now residing with NMC F_2 [75] and CMS 8 TeV jets [122] data. Tensions with NMC F_2 [75] data are also seen to some extent at NNLO where we show a $\Delta\chi^2 = -20.6$ in a fit omitting HERA data (combining the NMC F_2 datasets shown in Table D.1). However at N^{3}LO, Table D.2 shows a $\Delta\chi^2 = -23.4$ reduction from NMC F_2 data in a fit omitting HERA data. Therefore whilst the N^{3}LO additions remove tensions with Z p_T data, it remains that the HERA data is preferring the high-x quarks to be lower than favoured by NMC data. This is suggestive of higher twist effects for NMC data

at low-Q^2 (as we observe a worse fit to low-Q^2 data). We also emphasise that when conducting a fit at NNLO with Z p_T data removed, an improvement of $\Delta\chi^2 = -41.3$ is observed in the rest of the data, whereas at N^{3}LO an improvement of $\Delta\chi^2 = -69.3$ is observed in all other datasets without removing Z p_T, therefore these results are not purely an effect of removing any Z p_T tension. Considering tensions with CMS 8 TeV jets [122] data, as discussed in Chapter 10, in general the jets datasets show tensions with the N^{3}LO description (especially for CMS 8 TeV jets [122]), therefore it will be interesting to observe how this picture evolves when considering this data in the form of dijets. Some of the above observations are also made in [15, 16] where studies of including small-x resummation results into a PDF fit have been reported.

Since a naturally richer description of the small-x regime is being included at N^{3}LO (again somewhat similar to similarly to studies in [15, 16]), which has a direct effect on the HERA datasets, the reduction of important tensions from NNLO is even further justification for the inclusion of the N^{3}LO theory. The extra N^{3}LO additions are allowing the large-x behaviour of the PDFs to be less dominated by data at small-x, while also producing a better fit quality at small-x (i.e. for HERA data).

Reflecting on the chosen prior distributions for each of the sources of N^{3}LO MHOUs, Table 11.1 confirms that no especially large penalties are being incurred in this new description. These results therefore demonstrate that the fit is succeeding in leveraging contributions (such as $P_{qq}^{(3)}$ and $P_{qg}^{(3)}$ in the quark evolution part of Equation (6.3)) to produce a better overall fit.

DIS Dataset	χ^2	$\Delta\chi^2$ from NNLO	$\Delta\chi^2$ from NNLO (NNLO K-factors)
BCDMS μp F_2 [72]	179.9 / 163	−0.3	−0.9
BCDMS μd F_2 [72]	143.1 / 151	−2.9	−1.2
NMC μp F_2 [75]	118.7 / 123	−5.3	−7.0
NMC μd F_2 [75]	106.2 / 123	−6.4	−10.0
SLAC ep F_2 [78,79]	32.0 / 37	+0.0	+0.6
SLAC ed F_2 [78,79]	21.9 / 38	−1.1	−1.4
E665 μp F_2 [82]	64.7 / 53	+5.1	+6.0
E665 μd F_2 [82]	67.5 / 53	+2.8	+3.1
NuTeV νN F_2 [85]	38.7 / 53	+0.5	+2.1
NuTeV νN xF_3 [85]	33.9 / 42	+3.2	+1.7
NMC $\mu n/\mu p$ [88]	128.5 / 148	−2.3	−2.9
HERA ep F_2^{charm} [107]	134.7 / 79	+2.4	+6.4
NMC/BCDMS/SLAC/HERA F_L [72,75,79,110–112]	45.5 / 57	−23.0	−23.2
CHORUS νN F_2 [117]	32.7 / 42	+2.6	+2.6
CHORUS νN xF_3 [117]	19.8 / 28	+1.3	+2.2
HERA e^+p CC [120]	51.8 / 39	−0.1	+0.3
HERA e^-p CC [120]	66.3 / 42	−3.8	−2.8
HERA e^+p NC 820 GeV [120]	83.8 / 75	−6.0	−5.9
HERA e^-p NC 460 GeV [120]	247.4 / 209	−0.9	−0.7
HERA e^+p NC 920 GeV [120]	476.7 / 402	−36.0	−32.9
HERA e^-p NC 575 GeV [120]	248.0 / 259	−15.0	−14.5
HERA e^-p NC 920 GeV [120]	243.3 / 159	−1.0	−0.9
Total	2585.2 / 2375	−86.4	−79.3

Table 11.2.: Table showing the relevant DIS datasets and how the individual χ^2 changes from NNLO by including the N^{3}LO contributions to the structure function $F_2(x, Q^2)$. The result within purely NNLO K-factors included for all data in the fit is also given.

DIS Processes

To complement the discussions in Chapter 10, we isolate the χ^2 results from DIS data in Table 11.2. This data is directly affected by the N^{3}LO structure functions constructed approximately in Chapter's 3 to 6. A substantial decrease in the total χ^2 from NNLO is observed across DIS datasets. Considering the results in Table 11.2 in the context

of Table's 10.1 to 10.6, a better fit quality is observed for all DIS and non-DIS datasets than at NNLO with the inclusion of N^{3}LO contributions. As the DIS data makes up over half of the total data included in a global fit, it is the dominant force in deciding the overall form of the PDFs, especially at small-x (discussed further in Section 11.4). Table 11.2 further reinforces the point that the N^{3}LO description is flexible enough to fit to HERA and non-HERA data, without being largely constrained by tensions between the small-x (HERA dominated) and large-x (non-HERA dominated) regions.

11.2. Correlation Results

The correlation matrix shown in Fig. 11.1 illustrates the correlations between extra N^{3}LO theory parameters and the subset of the MSHT20 parameters which are included in the construction of Hessian eigenvectors (see Section 11.3 and [3] for details). It is apparent that the correlations between K-factor parameters for each process (shown in green) and other PDF and theory parameters are usually small, with some exceptions e.g. for the Top_{NLO} parameter. Due to this there is an argument that each process' K-factor parameters could be treated separately from all other parameters in the Hessian prescription (see Section 6.2) which allows for a more flexible PDF set that can be decorrelated from a process. By using the uncorrelated Hessian results for a process NNLO hard cross sections can be transformed to aN^{3}LO and therefore provide more reliable predictions (more details in Chapter 14). This is a fairly intuitive result, since most correlations are showing a natural separation between the process dependent and process independent physics in the DIS picture [1]. Mathematically, the K-factors are directly associated with the hard cross section, whereas other N^{3}LO theory parameters (ρ_{ij} and a_{ij}) are having a direct effect on the PDFs. Fig. 11.1 therefore begins to

[1] The same pattern can be seen for $c^{\text{NLL}}_{\{q,g\}}$ parameters which are involved in the DIS hard cross section.

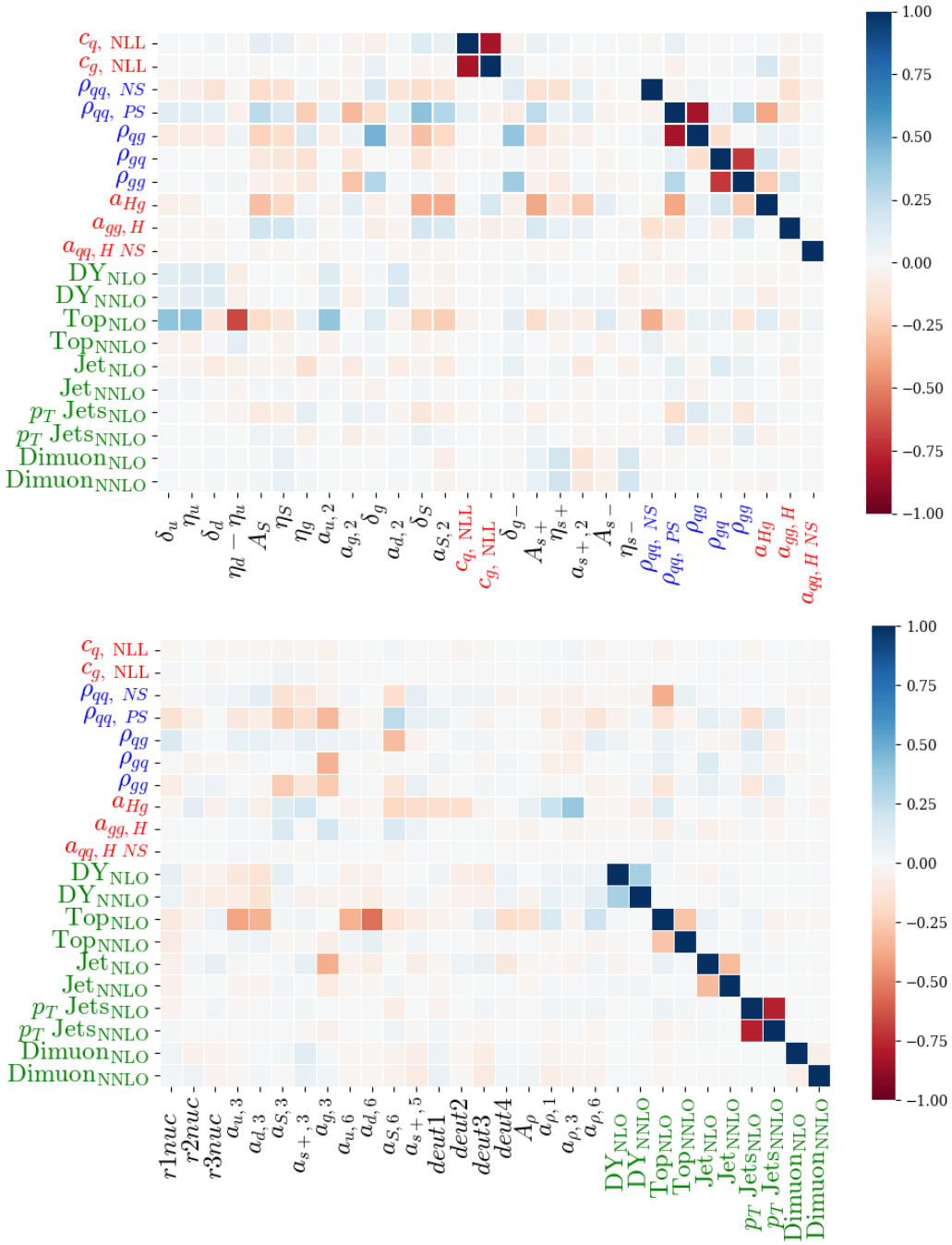

Figure 11.1.: Correlation matrix for all N^{3}LO theory parameters included in the fit against the subset of the MSHT20 parameters (shown in black) used in constructing the Hessian eigenvectors. This is shown for the case where the *K*-factors correlations with the first 42 parameters are included. N^{3}LO theory parameters associated with the splitting functions are coloured blue, the parameters affecting the transition matrix elements and coefficient functions are in red and the *K*-factor parameters are in green.

motivate the inclusion of the 'pure' theory (splitting functions and transition matrix elements) parameters within the standard MSHT eigenvector analysis [3], with the decorrelation of the K-factor parameters, as discussed in Chapter 5. We investigate and compare both treatments (complete correlation and K-factor decorrelation) throughout the rest of this section. We show in Section 11.4 that while the decorrelation of K-factors is not complete, both treatments result in similar uncertainty bands, therefore confirming that the effect of making the assumption of full decorrelation is minimal in practice. Note that although the c_i^{NLL} parameters also show minimal correlation with other parameters, we include these within the 'pure' theory group of parameters (i.e. correlated with ρ_{ij} and a_{ij}) as they are essential ingredients in the underlying DIS theory.

11.3. Eigenvector Results

In the MSHT fitting procedure (described in [3]) the eigenvectors of a Hessian matrix are found, which encapsulate the sources of uncertainties and corresponding correlations. Combining these with the central PDFs, forms the entire PDF set with uncertainties. In this eigenvector analysis a dynamical rescaling of each eigenvector e_i is performed via a tolerance factor t to encapsulate the 68% confidence limit (C.L.).

$$a_i = a_i^0 \pm t e_i, \tag{11.1}$$

where a_i^0 is the best fit parameter. t is then adjusted to give the desired tolerance T for the required confidence interval defined as $T = \sqrt{\Delta\chi^2_{\mathrm{global}}}$ (for 68% C.L.). In a quadratic approximation, for suitably well-behaved eigenvectors, $t = T$ is true. Although for eigenvectors with larger eigenvalues, it is possible to observe significant

deviations from $t = T$. The standard MSHT fitting procedure involves allowing all relevant parameters from [3] to vary when finding the best fit, now including all N^{3}LO theory parameters ($\rho_{ij}, a_{ij}, c_i^{\rm NLL}, K_{\rm NLO/NNLO}$) discussed in this work. After accounting for high degrees of correlation between parameters (described in [64]), the result is a Hessian matrix which in general, depends on a subset of the parameters that were allowed to vary in a best fit and provides a set of suitably well-behaved eigenvectors. The standard MSHT NNLO PDF eigenvectors are based on a set of 32 parameters, reduced from the 52 parameters allowed to vary in the full fit. In the following analysis we are therefore concerned with a smaller number of parameters, specifically the 32 parameters from the standard MSHT fitting procedure plus an extra 20 N^{3}LO parameters (shown in Fig. 11.1).

A standard choice of tolerance T is $T = \sqrt{\Delta\chi^2_{\rm global}} = 1$ for a 68% C.L. limit. However, this assumes all datasets are consistent with Gaussian errors. In practice, due to incomplete theory, tensions between datasets and parameterisation inflexibility, this is known not to be the case in a global PDF fit. To overcome this, a 68% C.L. region for each dataset is defined. Then for each eigenvector, the value of $\sqrt{\chi^2_{\rm global}}$ for each chosen t is recorded (ideally showing a quadratic behaviour). Finally, a value of T is chosen to ensure that all datasets are described within their 68% CL in each eigenvector direction. For a fuller mathematical description of the dynamical tolerance procedure used in MSHT PDF fits, the reader is referred to [64]. In this section we present a demonstration of how well the resultant eigenvectors follow the quadratic assumption based on $t = T$, including the specific choices of dynamical tolerances and which dataset/penalty constrains this tolerance in each eigenvector direction.

PDF + N^{3}LO DIS Theory + N^{3}LO *K*-factor (decorrelated) Parameters

As discussed in Section 11.2, when determining the eigenvectors and therefore PDF uncertainties, we can choose to either include the correlations between the 10 *K*-factor parameters added with the other 42 parameters (encompassing the standard 32 MSHT eigenvector parameters and the 10 new theory parameters from the splitting functions, transition matrix elements and coefficient functions) or to decorrelate the 10 *K*-factor parameters.

In this section we address the scenario where we decorrelate the *K*-factors as

$$H_{ij}^{-1} + \sum_{p=1}^{N_p} K_{ij,p}^{-1} \tag{11.2}$$

and consider each term individually.

Fig. 11.2 shows the map of eigenvectors produced from H_{ij} in Equation (11.2), where we have included the new N^{3}LO DIS theory parameters (splitting functions in blue and coefficient functions/transition matrix elements in red) correlated with the PDF parameters. Eigenvectors 35 and 36 are prime examples of where the eigenvectors have specifically encompassed the correlation/anti-correlation between the two NLL FFNS coefficient function parameters $c_i^{\rm NLL}$ ($i \in \{q, g\}$). Whereas the splitting functions naturally give rise to a much more complicated mixing with other PDF parameters as these directly affect the evolution of the PDFs. Due to the direct impact of ρ_{ij}'s on the PDFs (via DGLAP evolution), combined with the large contributions to the evolution shown at N^{3}LO, this result is as expected.

Another somewhat pleasing aspect is the recovery of a natural separation between eigenvectors associated with the N^{3}LO coefficient function/transition matrix elements

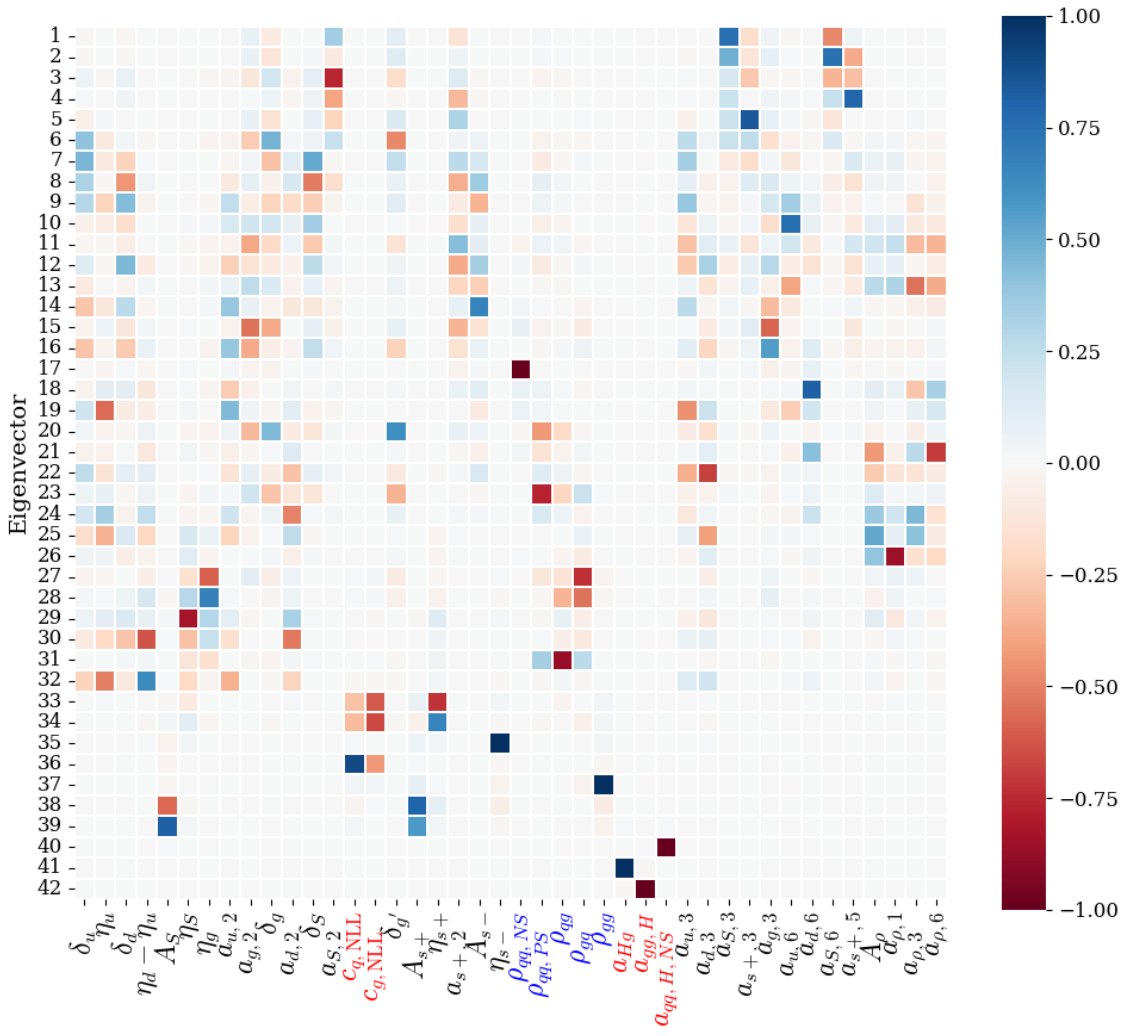

Figure 11.2.: Correlation matrix of the first 42 (total 52) eigenvectors found with the N^{3}LO parameters added into the analysis in the case where the K-factors are decorrelated from these first 42 parameters. Parameters associated with the splitting functions are coloured blue, those affecting the transition matrix elements and coefficient functions are in red.

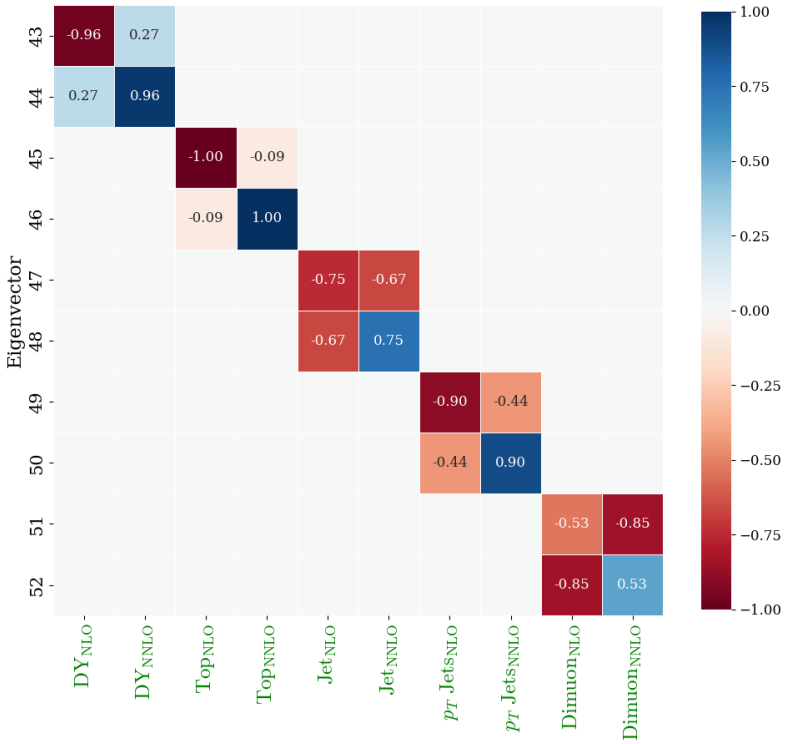

Figure 11.3.: Map of the 10 K-factor eigenvectors found with the N^{3}LO parameters added into the analysis in the case where the K-factors are decorrelated from these first 42 parameters.. Combined with the 42 eigenvectors shown in Fig. 11.2, these form the total 52 eigenvectors in the decorrelated case. Parameters associated with the K-factor parameters are in green.

and our original PDF parameters (incl. N^{3}LO splitting functions). This separation is reminiscent of our DIS picture, whereby the splitting functions are much more intertwined with the raw PDFs and the transition matrix elements have a symbiotic relationship with the coefficient functions (see GM-VFNS description in Chapter 3). Due to this, the form of these eigenvectors has not only some level of physical interpretation inherited from our underlying theory, but also offers a useful way to access the different sources of N^{3}LO additions within the PDF set.

In Fig. 11.3 the eigenvectors resulting from the $\sum_{p=1}^{N_p} K_{ij,p}^{-1}$ terms in Equation (11.2) are shown. These eigenvectors are constructed in pairs, describing the correlation and anti-correlation of the two K-factor parameters (controlling the NLO and NNLO contributions to N^{3}LO) for each process p contained within the corresponding $K_{ij,p}$ correlation matrix.

Table 11.3 shows further information regarding the K-factor parameter limits from each eigenvector. In most cases the parameter limits are well within the allowed variation ($-1 < a < 1$), which is an indication that the data included in the fit is constraining these parameters rather than the individual penalties for each parameter[2].

To assess whether the eigenvectors are violating the quadratic treatment, four examples displaying this behaviour are shown in Fig. 11.4, with a full analysis provided in Appendix E.1. Additionally, Table 11.4 provides a summary of all tolerances found within the eigenvector scans. There is relatively consistent agreement between t and T across all eigenvectors with later eigenvectors (i.e. higher #) generally becoming less quadratic (a feature which is built into the fit). Eigenvectors 31, 41 and 42 displayed

[2]We remind the reader that the Dimuon datasets also include a branching ratio factor which is providing some compensation with these K-factor parameters (as discussed in Chapter 10).

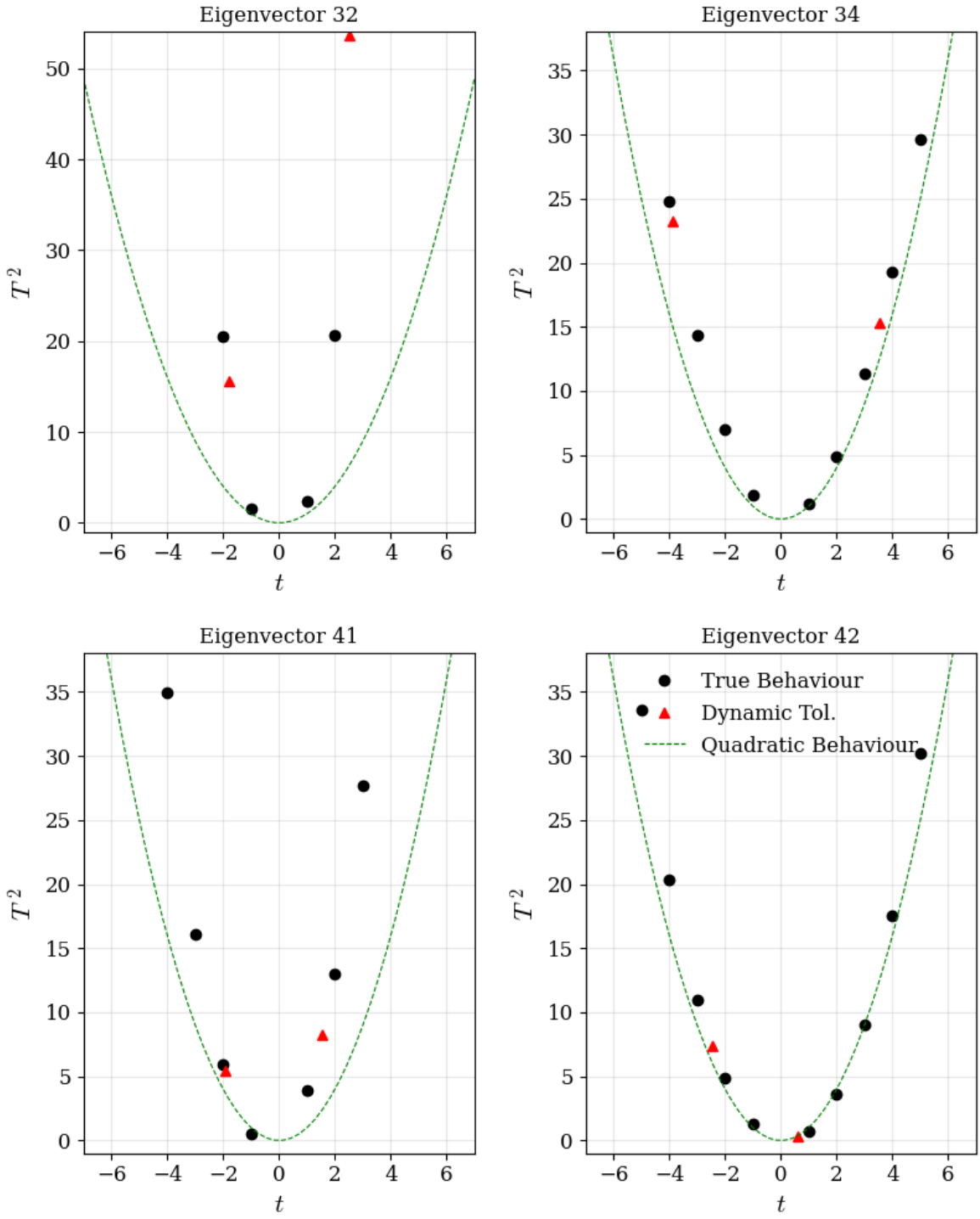

Figure 11.4.: Dynamic tolerance behaviour for 4 selected eigenvectors in the case of decorrelated K-factor parameters. The black dots show the fixed tolerance relations found for integer values of t, whereas the red triangles show the final chosen dynamical tolerances for each eigenvector direction. For an exhaustive analysis of all eigenvectors see Fig. E.1.

Matrix	Central Values		Eigenvector	+ Limit		- Limit		Scale
	$a_{\rm NLO}$	$a_{\rm NNLO}$		$a_{\rm NLO}$	$a_{\rm NNLO}$	$a_{\rm NLO}$	$a_{\rm NNLO}$	
$K_{ij}^{\rm DY}$	-0.247	-0.053	43	-0.386	0.039	-0.146	-0.119	$m/2$
			44	-0.173	0.467	-0.319	-0.559	
$K_{ij}^{\rm Top}$	0.324	0.812	45	-0.015	0.227	0.674	1.476	Section 10.2
			46	0.059	1.295	0.721	0.088	
$K_{ij}^{\rm Jets}$	-0.250	-0.719	47	-0.454	-0.991	0.282	0.008	$p_T^{\rm jet}$
			48	-0.659	-0.060	0.072	-1.237	
$K_{ij}^{p_T\ \rm Jets}$	0.662	-0.105	49	0.468	-0.421	0.916	0.310	p_T
			50	0.558	0.566	0.763	-0.760	
$K_{ij}^{\rm Dimuon}$	-0.694	0.602	51	-1.219	-0.054	-0.272	1.258	Q^2
			52	-1.268	1.013	1.099	-0.680	

Table 11.3.: Limiting values for specific K-factor parameters for each of the processes considered in the decorrelated case. Parameter values are shown in the positive and negative limits for each eigenvector. The scale choices for top quark processes are described in Chapter 10 to be $H_T/4$ for the single differential datasets with the exception of data differential in the average transverse momentum of the top or antitop, p_T^t, $p_T^{\bar{t}}$, for which $m_T/2$ is used. For the double diff. dataset the scale choice is $H_T/4$ and for the inclusive top $\sigma_{t\bar{t}}$ a scale of m_t is chosen.

in Fig. 11.4 are shown in Table 11.4 to be either dominated or limited by at least one new N^{3}LO parameter. Conversely, eigenvector 26 is much more dominated by the original PDF parameters from MSHT20 NNLO. Comparing these cases, the eigenvectors associated more strongly with the N^{3}LO parameters exhibit a similar level of agreement (and occasionally better) with the desired quadratic behaviour as eigenvectors more closely associated with the original PDF parameters.

The last 5 sets of eigenvectors (i.e. the last 10 where a set contains 2 eigenvectors for a particular process) we see in Table 11.4 are the decorrelated K-factor eigenvectors, where there are correlated/anti-correlated eigenvectors for each process. For all K-factor cases, Table 11.4 provides sensible results with either the dominant datasets or parameter penalties constraining each eigenvector direction. One interesting feature one can observe here is a sign of tension between the ATLAS 8 TeV Z p_T [121] and

#	$t+$	$T+$	Limiting Factor (+)	$t-$	$T-$	Limiting Factor (−)	Primary Parameter
1	3.45	3.56	ATLAS 7 TeV high prec. W, Z [116]	2.80	2.93	ATLAS 8 TeV double diff. Z [135]	$a_{S,3}$
2	3.52	3.33	NMC μd F_2 [75]	5.13	5.41	HERA e^+p NC 920 GeV [120]	$a_{S,6}$
3	4.48	4.37	NMC μd F_2 [75]	6.33	6.82	HERA e^+p NC 920 GeV [120]	$a_{g,3}$
4	5.57	5.78	ATLAS 7 TeV high prec. W, Z [116]	2.47	2.42	NMC μd F_2 [75]	$a_{S,2}$
5	6.63	6.72	HERA e^-p NC 575 GeV [120]	4.16	4.39	HERA e^+p NC 920 GeV [120]	$\delta_{g'}$
6	3.97	4.23	DØ II $W \to \nu e$ asym. [74]	2.15	2.14	DØ W asym. [119]	δ_u
7	3.09	3.53	DØ W asym. [119]	6.69	6.44	HERA e^+p NC 920 GeV [120]	δ_S
8	5.97	6.06	LHCb 2015 W, Z [105, 106]	2.85	3.05	DØ W asym. [119]	$a_{u,6}$
9	3.15	3.02	BCDMS μp F_2 [72]	3.07	3.39	DØ W asym. [119]	$a_{u,6}$
10	2.17	2.35	DØ W asym. [119]	5.27	5.37	CMS 8 TeV W [109]	δ_g
11	5.54	5.89	NuTeV νN F_2 [85]	2.55	2.63	NMC μd F_2 [75]	$a_{g,2}$
12	3.58	3.68	CMS 7 TeV $W + c$ [115]	3.22	3.28	NuTeV $\nu N \to \mu\mu X$ [114]	$a_{s+,5}$
13	2.13	2.40	DØ W asym. [119]	2.78	3.13	E866 / NuSea pd/pp DY [104]	A_{s-}
14	4.38	4.92	ATLAS 8 TeV double diff. Z [135]	1.82	1.86	E866 / NuSea pd/pp DY [104]	$a_{\rho,6}$
15	5.08	4.39	NuTeV νN xF_3 [85]	2.09	2.13	NuTeV $\nu N \to \mu\mu X$ [114]	$a_{u,2}$
16	2.97	3.39	E866 / NuSea pd/pp DY [104]	0.92	1.21	E866 / NuSea pd/pp DY [104]	A_ρ
17	2.23	2.61	DØ W asym. [119]	2.81	3.01	E866 / NuSea pd/pp DY [104]	$a_{d,6}$
18	1.68	2.15	E866 / NuSea pd/pp DY [104]	2.51	2.53	NuTeV $\nu N \to \mu\mu X$ [114]	$a_{s+,2}$
19	1.45	1.45	ρ_{qq}^{NS}	1.70	1.75	ρ_{qq}^{NS}	ρ_{qq}^{NS}
20	1.65	1.41	ρ_{qq}^{NS}	1.41	1.68	ρ_{qq}^{NS}	ρ_{qq}^{NS}
21	2.77	3.30	E866 / NuSea pd/pp DY [104]	3.04	2.89	CMS 7 TeV $W + c$ [115]	$a_{s+,2}$
22	2.23	2.45	NuTeV $\nu N \to \mu\mu X$ [114]	1.60	1.99	DØ W asym. [119]	$a_{d,2}$

Table 11.4.: Tolerances resulting from eigenvector scans with decorrelated K-factors for each process. The average tolerance for this set of eigenvectors is $T = 3.12$.

#	$t+$	$T+$	Limiting Factor (+)	$t-$	$T-$	Limiting Factor (−)	Primary Parameter
23	6.08	5.26	BCDMS μp F_2 [72]	1.96	2.18	E866 / NuSea pd/pp DY [104]	η_u
24	5.01	5.91	ATLAS 7 TeV high prec. W, Z [116]	4.77	5.67	HERA e^+p NC 920 GeV [120]	ρ_{qq}^{PS}
25	1.61	1.81	E866 / NuSea pd/pp DY [104]	3.41	3.65	CMS 8 TeV W [109]	$a_{\rho,3}$
26	1.94	2.22	DØ W asym. [119]	2.45	2.90	E866 / NuSea pd/pp DY [104]	$a_{d,3}$
27	1.65	1.68	ρ_{gq}	3.38	4.06	DØ W asym. [119]	ρ_{gq}
28	1.20	1.45	DØ W asym. [119]	3.21	3.61	CMS 8 TeV W [109]	A_{s+}
29	3.87	5.08	ATLAS 8 TeV double diff. Z [135]	2.21	2.86	CMS 8 TeV sing. diff. $t\bar{t}$ [133]	η_g
30	1.06	1.07	DØ W asym. [119]	4.22	4.60	DØ W asym. [119]	$\eta_d - \eta_u$
31	3.58	3.93	CMS 8 TeV W [109]	2.12	2.43	NuTeV νN xF_3 [85]	η_S
32	4.86	6.78	HERA e^+p NC 920 GeV [120]	4.10	4.68	ATLAS 8 TeV Z p_T [121]	ρ_{qg}
33	2.65	3.80	BCDMS μd F_2 [72]	3.34	3.69	CMS 8 TeV W [109]	η_{s+}
34	2.29	3.63	DØ W asym. [119]	2.02	3.28	CMS 8 TeV W [109]	$a_{\rho,1}$
35	4.07	5.08	HERA ep F_2^{charm} [107]	2.40	2.92	HERA ep F_2^{charm} [107]	c_g^{NLL}
36	1.34	1.52	c_q^{NLL}	1.24	1.22	c_g^{NLL}	c_q^{NLL}
37	2.63	3.83	NuTeV $\nu N \to \mu\mu X$ [114]	2.97	3.16	E866 / NuSea pd/pp DY [104]	η_{s-}
38	0.69	0.71	ρ_{gg}	3.76	3.90	ρ_{gq}	ρ_{gg}
39	1.57	5.57	ATLAS 7 TeV high prec. W, Z [116]	1.57	5.01	ATLAS 7 TeV high prec. W, Z [116]	A_S
40	0.88	1.00	$a_{qq,H}^{\text{NS}}$	1.15	1.01	$a_{qq,H}^{\text{NS}}$	$a_{qq,H}^{\text{NS}}$
41	1.71	2.72	HERA ep F_2^{charm} [107]	2.16	2.81	ρ_{gg}	a_{Hg}
42	2.09	2.19	ρ_{gg}	0.60	0.54	$a_{gg,H}$	$a_{gg,H}$
43	2.25	2.77	ATLAS 7 TeV high prec. W, Z [116]	1.62	1.26	CMS double diff. Drell-Yan [103]	DY_{NLO}
44	3.90	3.86	E866 / NuSea pp DY [102]	3.80	4.38	ATLAS 7 TeV high prec. W, Z [116]	DY_{NNLO}
45	1.28	1.22	ATLAS 8 TeV sing. diff. $t\bar{t}$ dilep. [124]	1.45	1.56	Tevatron, ATLAS, CMS $\sigma_{t\bar{t}}$ [89–101]	Top_{NNLO}

Table 11.4.: *(Continued)* Tolerances resulting from eigenvector scans with decorrelated K-factors for each process. The average tolerance for this set of eigenvectors is $T = 3.12$.

#	$t+$	$T+$	Limiting Factor (+)	$t-$	$T-$	Limiting Factor (−)	Primary Parameter
46	1.08	0.92	Top_{NNLO}	1.62	1.34	Top_{NLO}	Top_{NLO}
47	1.47	1.44	CDF II $p\bar{p}$ incl. jets [128]	3.85	4.10	$a_{gg,H}$	Jet_{NLO}
48	3.25	3.29	CMS 2.76 TeV jet [131]	2.56	2.90	Jet_{NNLO}	Jet_{NNLO}
49	2.10	2.35	ATLAS 8 TeV Z p_T [121]	2.75	2.71	ATLAS 8 TeV $W+$jets [126]	p_T Jet_{NLO}
50	2.24	2.28	ATLAS 8 TeV Z p_T [121]	2.19	2.24	ATLAS 8 TeV $W+$jets [126]	p_T Jet_{NNLO}
51	1.02	1.03	$\text{Dimuon}_{\text{NLO}}$	0.82	0.90	$\text{Dimuon}_{\text{NNLO}}$	$\text{Dimuon}_{\text{NNLO}}$
52	0.75	0.77	$\text{Dimuon}_{\text{NLO}}$	2.35	2.33	$\text{Dimuon}_{\text{NLO}}$	$\text{Dimuon}_{\text{NLO}}$

Table 11.4.: *(Continued)* Tolerances resulting from eigenvector scans with decorrelated K-factors for each process. The average tolerance for this set of eigenvectors is $T = 3.12$.

ATLAS 8 TeV $W+$jets [126] datasets where the limiting factors in Table 11.4 for eigenvectors 49 and 50 show that these datasets are preferring a slightly different K-factor.

To provide some extra level of comparison between the eigenvectors shown here and the eigenvectors found in the NNLO case, the average tolerance T for aN^{3}LO (decorrelated K-factors) set is 3.34, compared to the NNLO average T of 3.37.

PDF + N^{3}LO DIS Theory + N^{3}LO K-factor (correlated) Parameters

In this section we address the scenario,

$$H'_{ij} = \left(H_{ij}^{-1} + \sum_{p=1}^{N_p} K_{ij,p}^{-1} \right)^{-1}. \tag{11.3}$$

Moving to an analysis including aN^{3}LO K-factors as correlated parameters with PDF and other N^{3}LO theory parameters. This provides a comparison to the case

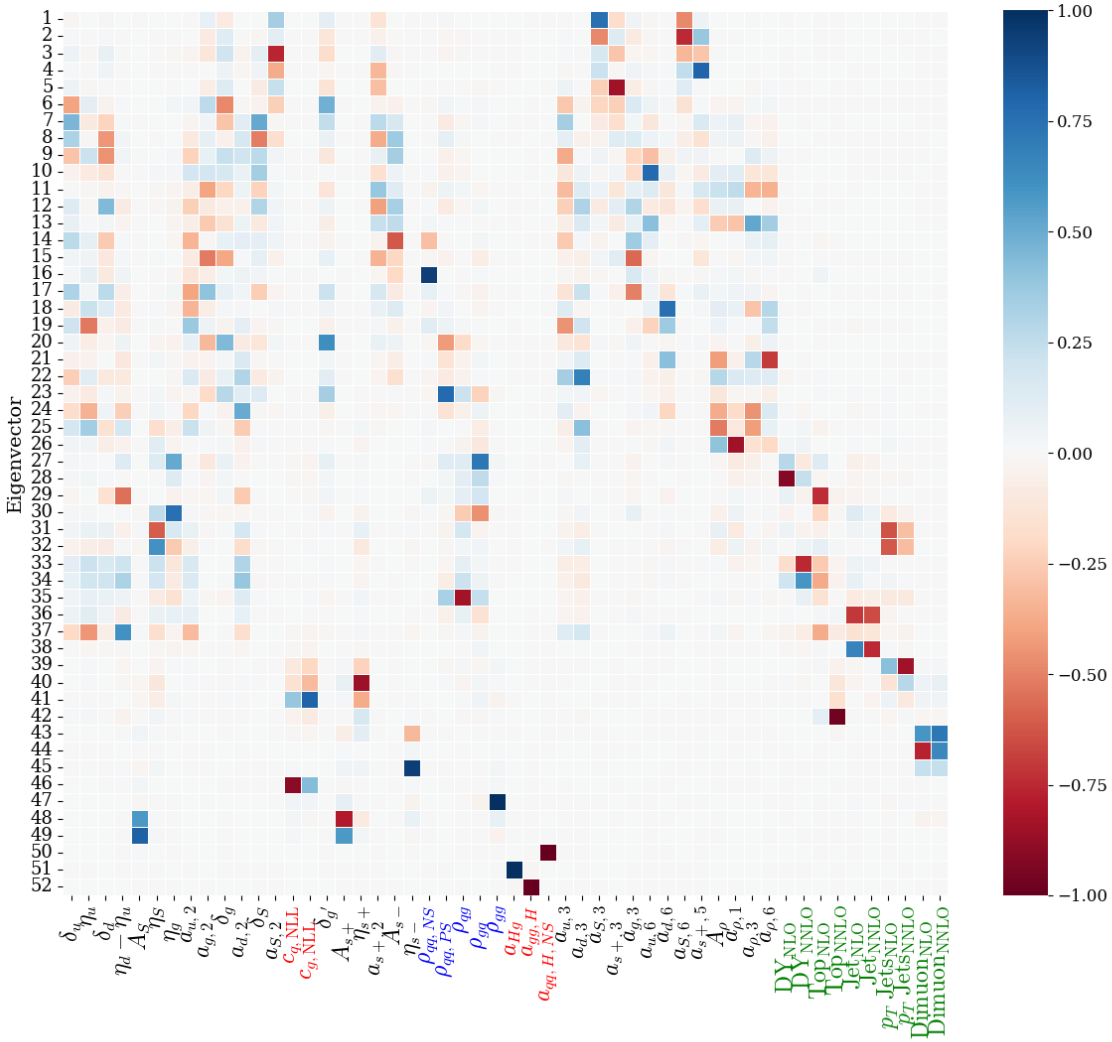

Figure 11.5.: Map of eigenvectors found with the N^{3}LO theory and *K*-factor parameters added into the analysis. Parameters associated with the splitting functions are coloured blue, those affecting the transition matrix elements and coefficient functions are in red and the *K*-factor parameters are in green.

of decorrelated *K*-factors and justification for treating the cross section behaviour separately to the PDF theory behaviour.

Fig. 11.5 shows a map of eigenvectors with the extra 10 N^{3}LO *K*-factor parameters (shown in green) included into the correlations considered. As expected, the result of including the correlations between PDF parameters and aN^{3}LO *K*-factors results in a slightly more intertwined set of eigenvectors (although a high level of decorrelation remains). Specifically, due to the much higher number of DY datasets included in the global fit, these N^{3}LO *K*-factor parameters tend to be included across more of a spread of eigenvectors. On the other hand, the Dimuon *K*-factors are almost entirely isolated within two eigenvectors, similar to the decorrelated case.

Once again, to investigate deviations from the quadratic behaviour, Fig. 11.6 illustrates examples of the tolerance behaviours of selected eigenvectors, with a full analysis provided in Appendix E.2. Further to this, Table 11.5 displays the tolerances and limiting datasets/parameters for the 52 correlated eigenvectors. It is difficult to compare and contrast these results with the decorrelated case, since the eigenvectors are inherently different. However in both cases, the eigenvectors are similarly well behaved, exhibit relatively good consistency between t and T and are therefore providing valid descriptions for a PDF fit.

For most of the 12 eigenvectors with N^{3}LO *K*-factors as primary parameters, there is expected behaviour, with the eigenvectors constrained either by their own penalties or by dominant datasets for the associated process. However, due to the extra correlations considered, there are a small number of eigenvector directions which are not as trivial to explain (e.g. eigenvector 31). We therefore recover the lack of correlation between *K*-factor parameters seen within Fig. 11.1 in the set of correlated PDF

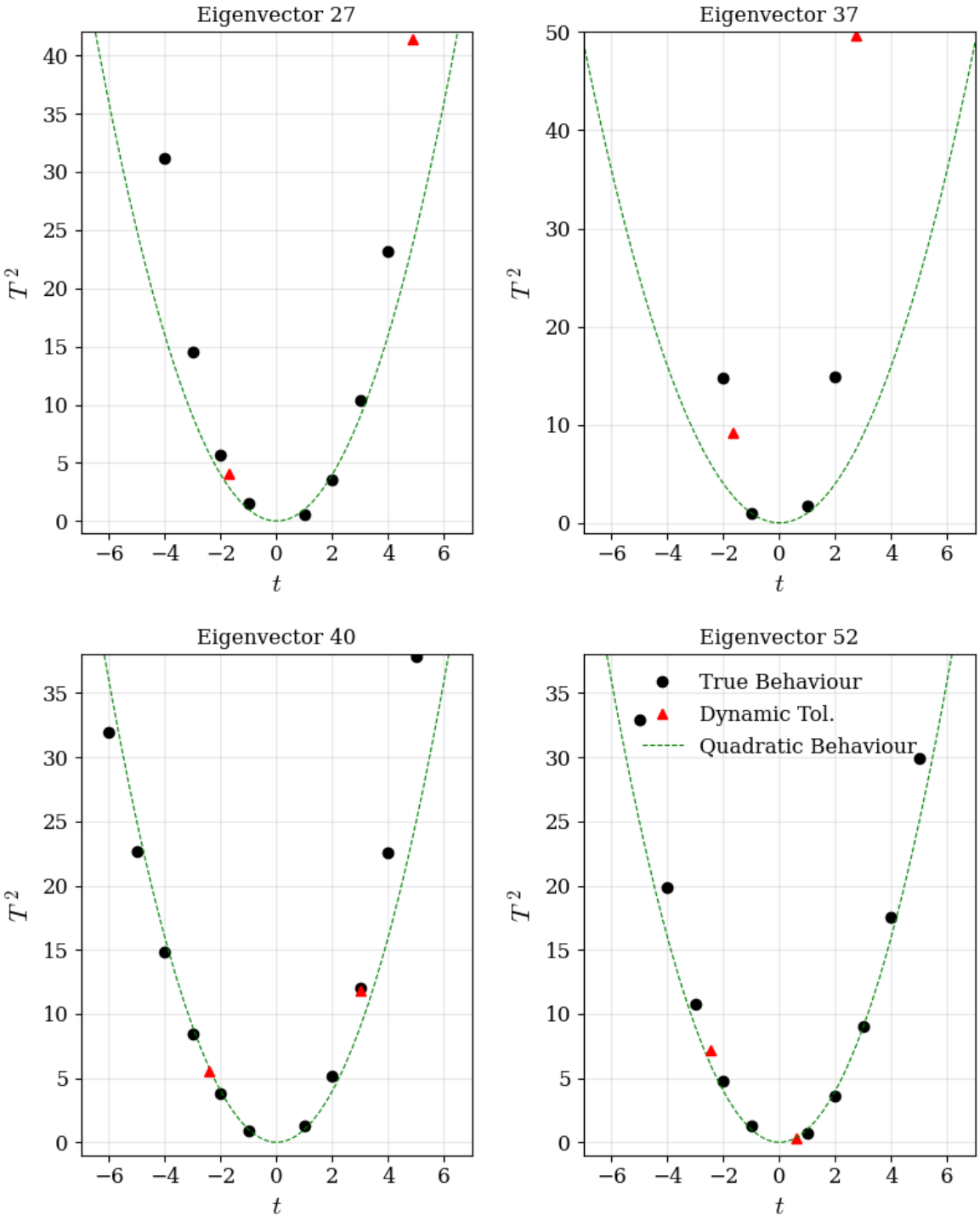

Figure 11.6.: Dynamic tolerance behaviour for 4 selected eigenvectors in the case of correlated K-factor parameters. The black dots show the fixed tolerance relations found for integer values of t, whereas the red triangles show the final chosen dynamical tolerances for each eigenvector direction. For an exhaustive analysis of all eigenvectors see Fig. E.2.

#	$t+$	$T+$	Limiting Factor (+)	$t-$	$T-$	Limiting Factor (−)	Primary Parameter
1	2.87	2.90	ATLAS 8 TeV double diff. Z [135]	3.50	3.47	ATLAS 7 TeV high prec. W, Z [116]	$a_{S,3}$
2	4.22	3.99	NMC μd F_2 [75]	5.14	5.38	HERA e^+p NC 920 GeV [120]	$a_{S,6}$
3	4.54	4.25	ATLAS 8 TeV Z p_T [121]	6.55	6.98	HERA e^+p NC 920 GeV [120]	$a_{g,3}$
4	4.97	5.10	ATLAS 7 TeV high prec. W, Z [116]	2.82	2.74	NMC μd F_2 [75]	$a_{S,2}$
5	4.18	4.29	HERA e^+p NC 920 GeV [120]	6.63	6.59	HERA e^-p NC 575 GeV [120]	$\delta_{g'}$
6	4.00	4.10	DØ II $W \to \nu e$ asym. [74]	2.18	2.08	DØ W asym. [119]	δ_u
7	6.69	6.31	HERA e^+p NC 920 GeV [120]	3.21	3.45	DØ W asym. [119]	δ_S
8	4.65	4.45	CMS W asym. $p_T >$ 25, 30 GeV [81]	2.24	2.32	DØ W asym. [119]	δ_d
9	5.29	5.49	DØ II $W \to \nu\mu$ asym. [134]	2.45	2.25	BCDMS μp F_2 [72]	$a_{u,6}$
10	5.52	5.43	CMS 8 TeV W [109]	2.15	2.20	DØ W asym. [119]	δ_g
11	2.64	2.45	NMC μd F_2 [75]	5.65	5.90	NuTeV νN F_2 [85]	$a_{g,2}$
12	5.76	4.47	CMS 7 TeV $W + c$ [115]	4.44	3.40	NuTeV $\nu N \to \mu\mu X$ [114]	$a_{s+,5}$
13	2.23	2.21	DØ W asym. [119]	2.88	3.03	E866 / NuSea pd/pp DY [104]	A_{s-}
14	4.91	4.75	ATLAS 8 TeV double diff. Z [135]	2.53	2.28	DØ W asym. [119]	$a_{u,2}$
15	6.05	5.57	NuTeV νN xF_3 [85]	1.49	1.41	E866 / NuSea pd/pp DY [104]	$a_{\rho,6}$
16	0.95	0.59	E866 / NuSea pd/pp DY [104]	2.90	3.23	E866 / NuSea pd/pp DY [104]	A_ρ
17	2.86	3.05	NuTeV $\nu N \to \mu\mu X$ [114]	3.27	3.23	CMS 8 TeV W [109]	$a_{d,6}$
18	1.97	1.78	DØ W asym. [119]	1.73	1.82	E866 / NuSea pd/pp DY [104]	$a_{s+,2}$
19	2.36	2.48	CCFR $\nu N \to \mu\mu X$ [114]	2.58	2.40	NuTeV $\nu N \to \mu\mu X$ [114]	$a_{s+,3}$
20	1.57	1.82	ρ_{qq}^{NS}	1.84	1.43	ρ_{qq}^{NS}	ρ_{qq}^{NS}
21	3.03	2.61	ρ_{qq}^{NS}	2.97	3.32	E866 / NuSea pd/pp DY [104]	$a_{s+,2}$
22	2.17	2.10	NuTeV $\nu N \to \mu\mu X$ [114]	1.64	1.77	DØ W asym. [119]	$a_{d,2}$

Table 11.5.: Tolerances resulting from eigenvector scans with correlated K-factors for each process. The average tolerance for this set of eigenvectors is $T = 3.12$.

#	$t+$	$T+$	Limiting Factor (+)	$t-$	$T-$	Limiting Factor (−)	Primary Parameter
23	4.68	4.13	ρ_{qq}^{NS}	1.88	1.78	E866 / NuSea pd/pp DY [104]	η_u
24	4.79	5.59	HERA e^+p NC 920 GeV [120]	4.76	5.42	ATLAS 7 TeV high prec. W, Z [116]	ρ_{qq}^{PS}
25	1.65	1.58	E866 / NuSea pd/pp DY [104]	3.46	3.56	CMS 8 TeV W [109]	$a_{\rho,3}$
26	2.16	2.14	DØ W asym. [119]	2.26	2.43	E866 / NuSea pd/pp DY [104]	$a_{\rho,3}$
27	4.92	5.71	Tevatron, ATLAS, CMS $\sigma_{t\bar{t}}$ [89–101]	1.85	1.64	ρ_{gq}	ρ_{gq}
28	1.19	0.91	DØ W asym. [119]	3.39	3.58	CMS 8 TeV W [109]	A_{s+}
29	3.95	3.47	CMS double diff. Drell-Yan [103]	2.16	2.40	ρ_{gq}	η_g
30	1.79	1.56	CMS double diff. Drell-Yan [103]	2.41	2.59	ATLAS 7 TeV high prec. W, Z [116]	$\mathrm{DY}_{\mathrm{NLO}}$
31	4.43	4.66	DØ W asym. [119]	1.06	0.92	DØ W asym. [119]	$\eta_d - \eta_u$
32	2.94	3.21	ATLAS 8 TeV Z p_T [121]	2.84	2.60	ATLAS 8 TeV W + jets [126]	p_T $\mathrm{Jet}_{\mathrm{NLO}}$
33	3.46	3.68	CMS 8 TeV W [109]	2.44	2.34	NuTeV νN xF_3 [85]	η_S
34	4.61	4.55	DØ W asym. [119]	3.89	4.03	NuTeV νN xF_3 [85]	$\mathrm{DY}_{\mathrm{NNLO}}$
35	4.99	6.80	HERA e^+p NC 920 GeV [120]	3.96	4.29	ATLAS 8 TeV Z p_T [121]	ρ_{qg}
36	6.56	6.80	CMS 8 TeV W [109]	2.06	1.90	CDF II $p\bar{p}$ incl. jets [128]	$\mathrm{Jet}_{\mathrm{NLO}}$
37	2.14	2.95	DØ W asym. [119]	1.86	2.91	CMS 8 TeV W [109]	$a_{\rho,1}$
38	3.77	3.92	CDF II $p\bar{p}$ incl. jets [128]	3.10	3.92	BCDMS μd F_2 [72]	η_{s+}
39	2.62	2.91	$\mathrm{Jet}_{\mathrm{NNLO}}$	3.25	3.28	CMS 2.76 TeV jet [131]	$\mathrm{Jet}_{\mathrm{NNLO}}$
40	1.85	1.77	ATLAS 8 TeV sing. diff. $t\bar{t}$ dilep. [124]	2.34	2.26	Tevatron, ATLAS, CMS $\sigma_{t\bar{t}}$ [89–101]	$\mathrm{Top}_{\mathrm{NLO}}$
41	2.60	2.47	ATLAS 8 TeV W + jets [126]	2.90	2.97	ATLAS 8 TeV sing. diff. $t\bar{t}$ dilep. [124]	p_T $\mathrm{Jet}_{\mathrm{NNLO}}$
42	2.42	2.92	HERA ep F_2^{charm} [107]	4.08	5.04	HERA ep F_2^{charm} [107]	c_g^{NLL}
43	2.02	1.72	$\mathrm{Top}_{\mathrm{NLO}}$	1.07	1.00	$\mathrm{Top}_{\mathrm{NNLO}}$	$\mathrm{Top}_{\mathrm{NNLO}}$
44	0.82	0.78	$\mathrm{Dimuon}_{\mathrm{NNLO}}$	1.00	1.03	$\mathrm{Dimuon}_{\mathrm{NLO}}$	$\mathrm{Dimuon}_{\mathrm{NNLO}}$
45	2.37	2.35	$\mathrm{Dimuon}_{\mathrm{NLO}}$	0.76	0.76	$\mathrm{Dimuon}_{\mathrm{NLO}}$	$\mathrm{Dimuon}_{\mathrm{NLO}}$

Table 11.5.: *(Continued)* Tolerances resulting from eigenvector scans with correlated K-factors for each process. The average tolerance for this set of eigenvectors is $T = 3.12$.

#	$t+$	$T+$	Limiting Factor (+)	$t-$	$T-$	Limiting Factor (−)	Primary Parameter
46	1.34	1.52	$c_q^{\rm NLL}$	1.24	1.22	$c_g^{\rm NLL}$	$c_q^{\rm NLL}$
47	2.62	3.68	NuTeV $\nu N \to \mu\mu X$ [114]	3.00	2.99	E866 / NuSea pd/pp DY [104]	η_{s-}
48	3.76	3.76	ρ_{gq}	0.69	0.68	ρ_{gg}	ρ_{gg}
49	1.54	5.44	ATLAS 7 TeV high prec. W, Z [116]	1.55	4.88	ATLAS 7 TeV high prec. W, Z [116]	A_S
50	0.88	1.00	$a_{qq,H}^{\rm NS}$	1.15	1.01	$a_{qq,H}^{\rm NS}$	$a_{qq,H}^{\rm NS}$
51	2.16	2.71	ρ_{gg}	1.71	2.65	HERA ep $F_2^{\rm charm}$ [107]	a_{Hg}
52	2.09	2.21	ρ_{gg}	0.60	0.54	$a_{gg,H}$	$a_{gg,H}$

Table 11.5.: *(Continued)* Tolerances resulting from eigenvector scans with correlated K-factors for each process. The average tolerance for this set of eigenvectors is $T = 3.12$.

eigenvectors presented here. Further to this, comparing the t and T values found for eigenvectors associated with N^{3}LO K-factors in Table's 11.4 and 11.5, one can observe clear similarities between eigenvectors. This suggests that even when correlating the K-factor parameters, the fit succeeds in decorrelating the individual processes, thereby motivating our original assumption that the correlations with K-factors can be ignored. Another similarity one can observe between Table 11.4 and Table 11.5 is the suggestion of some tension between ATLAS 8 TeV Z p_T [121] and ATLAS 8 TeV $W+$jets [126] datasets seen in the limiting factors of eigenvector 39 in the correlated case.

Eigenvectors 27, 29 and 52 displayed in Fig. 11.6 can be seen from Table 11.5 to be associated with the new N^{3}LO theory parameters. Whereas eigenvector 37 is primarily focused on an original PDF parameter. One can observe a similar level of quadratic behaviour across all four of these eigenvector tolerances. Comparing all eigenvectors in the decorrelated/correlated cases, the behaviours are similarly well behaved. The average tolerance T for the aN^{3}LO (with correlated K-factors) case is 3.57, slightly higher than the NNLO average of 3.37 and the aN^{3}LO (with decorrelated K-factors) average of 3.34.

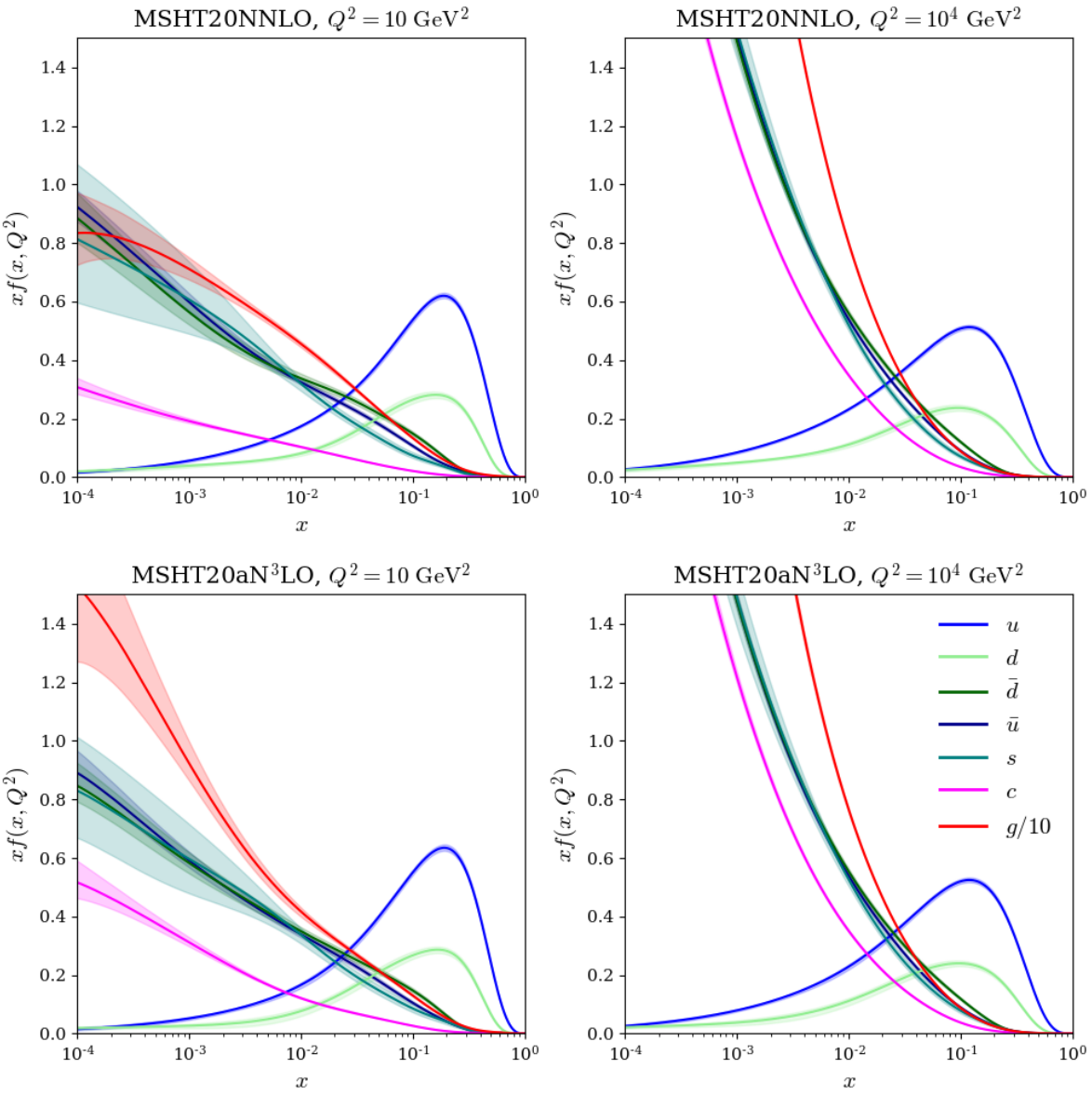

Figure 11.7.: General forms of NNLO (top) and aN^{3}LO (bottom) PDFs at low (left) and high (right) Q^2. Several main features can be compared and contrasted such as the marked increase in the gluon and charm at small-x (note the difference in y-axis scale between NNLO (top) and aN^{3}LO (bottom)).

11.4. PDF Results

Fig. 11.7 displays the overall shape of the PDFs including the N^{3}LO additions compared to the standard NNLO set. We provide this comparison to accompany the

results described in earlier sections. At small-x and low-Q^2 the gluon exhibits a marked enhancement due to the large small-x logarithms inserted at N^{3}LO (similar to the results shown in [4, 15] The changes induced from specific N^{3}LO contributions are investigated in Section 11.8.

Shown in Fig.'s 11.8 and 11.9 are the ratios for each flavour of aN^{3}LO PDF compared to the NNLO set with their 68% confidence intervals at low and high-Q^2 respectively. The shaded aN^{3}LO regions indicate the PDF uncertainty produced with the decorrelated $((H_{ij}^{-1} + \sum_{p=1}^{N_p} K_{ij,\,p}^{-1})^{-1}$) aN^{3}LO K-factors for each process. As a comparison to these shaded regions, the bounds of uncertainty for the fully correlated (H'_{ij}) N^{3}LO K-factor parameters is also provided (red dashed line).

Considering Fig. 11.8 we present the aN^{3}LO PDF set at $Q^2 = 10$ GeV^2 with the bottom quark PDF at $Q^2 = 25$ GeV^2. These PDF ratios better display the substantial increase in the gluon at small-x. The predicted harder small-x gluon is then accommodated for by reductions in the PDFs at large and small-x (including the gluon near $x = 10^{-2}$) from NNLO. Another prominent feature is the enhanced charm and bottom quark at N^{3}LO. Since the heavy flavour quarks are perturbatively calculated in the MSHT framework, this amplification is a feature of the transition matrix element $A_{Hg}^{(3)}$ at high-x, combined with the increase in the gluon PDF at small-x (as these two ingredients are convoluted together). Comparing with Fig. 95 in [3], we observe that the approximate N^{3}LO charm quark now follows a much closer trend to the CT18 PDF and is therefore even more significantly different from the NNPDF NNLO fitted charm at large-x than MSHT20 at NNLO. In the high-Q^2 setting shown in Fig. 11.9 we observe similar albeit less drastic effects to those described above.

Also contained in Fig.'s 11.8 and 11.9 are the relative forms of NNLO PDFs when fit to all non-HERA data (full χ^2 results are provided in Appendix D). Comparing

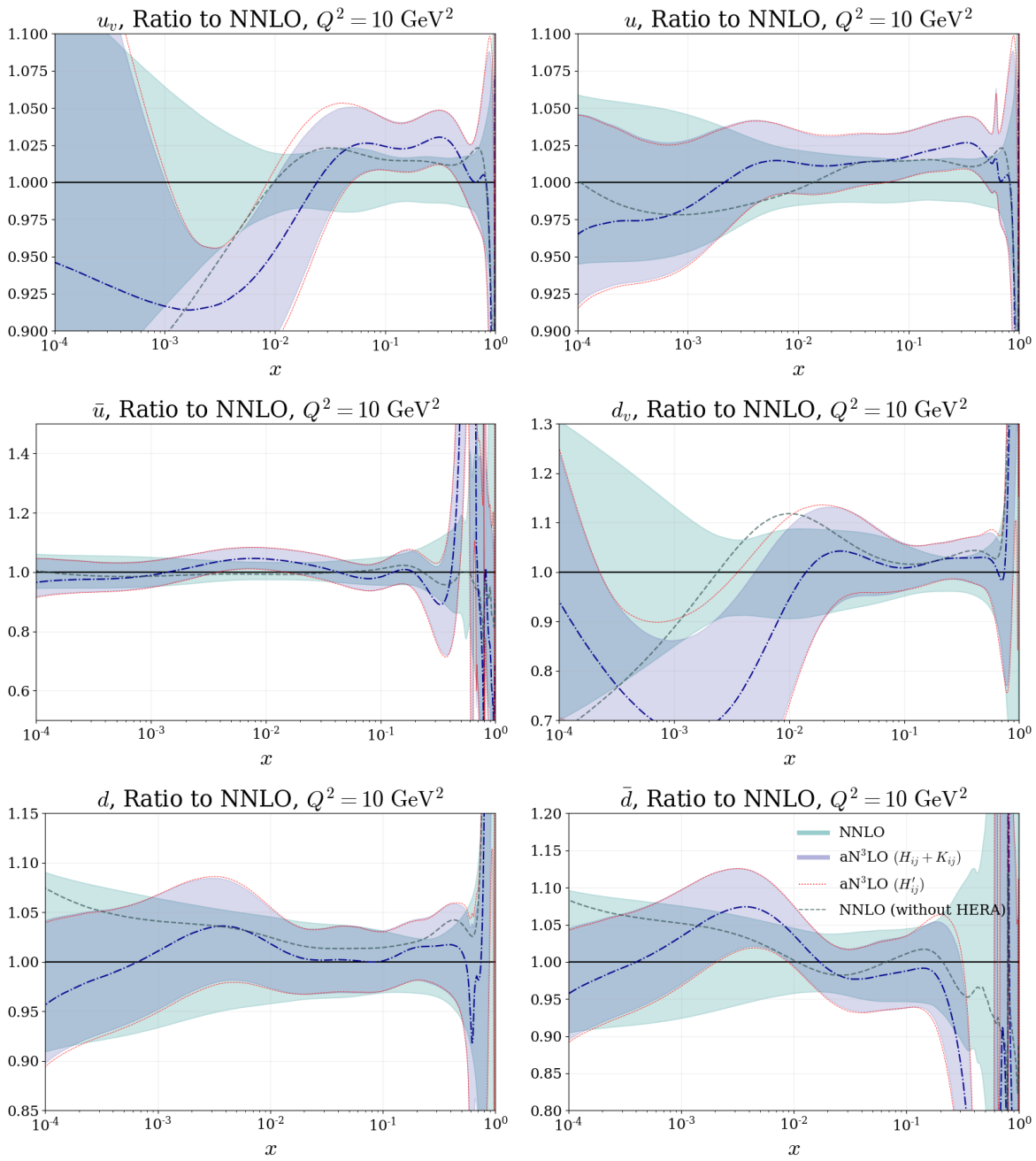

Figure 11.8.: Low-Q^2 ratio plots showing the aN^{3}LO 68% confidence intervals with decorrelated ($H_{ij} + K_{ij}$) and correlated (H'_{ij}) K-factor parameters, compared to NNLO 68% confidence intervals. Also shown are the central values at NNLO when fit to all non-HERA datasets which show similarities with N^{3}LO in the large-x region of selected PDF flavours. All plots are shown for $Q^2 = 10$ GeV^2 with the exception of the bottom quark shown for $Q^2 = 25$ GeV^2.

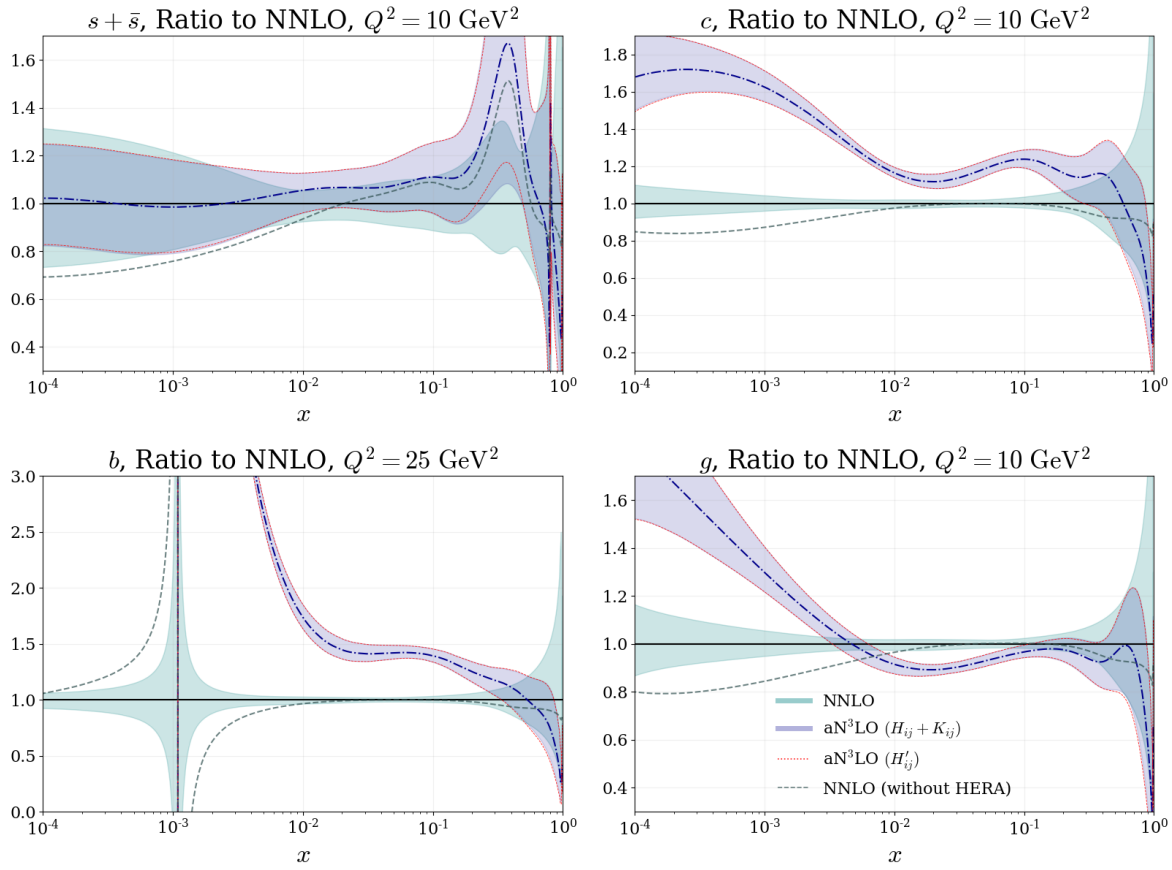

Figure 11.8.: *(Continued)* Low-Q^2 ratio plots showing the aN^{3}LO 68% confidence intervals with decorrelated ($H_{ij} + K_{ij}$) and correlated (H'_{ij}) K-factor parameters, compared to NNLO 68% confidence intervals. Also shown are the central values at NNLO when fit to all non-HERA datasets which show similarities with N^{3}LO in the large-x region of selected PDF flavours. All plots are shown for $Q^2 = 10$ GeV^2 with the exception of the bottom quark shown for $Q^2 = 25$ GeV^2.

the *non*-HERA NNLO PDFs with aN^{3}LO PDFs, there are some similarities in the shapes and magnitudes of a handful of PDFs in the intermediate to large-x regime, most noticeably the light quarks. At small-x the HERA data heavily constrains the PDF fit and therefore these similarities rapidly break down. However, this analysis displays further evidence that including N^{3}LO contributions, even though approximate, reduces tensions between the HERA and non-HERA data (when considering the reduction in tension seen in Table D.1). The aN^{3}LO PDFs are seemingly able to fit to HERA and non-HERA datasets with superior flexibility than at NNLO.

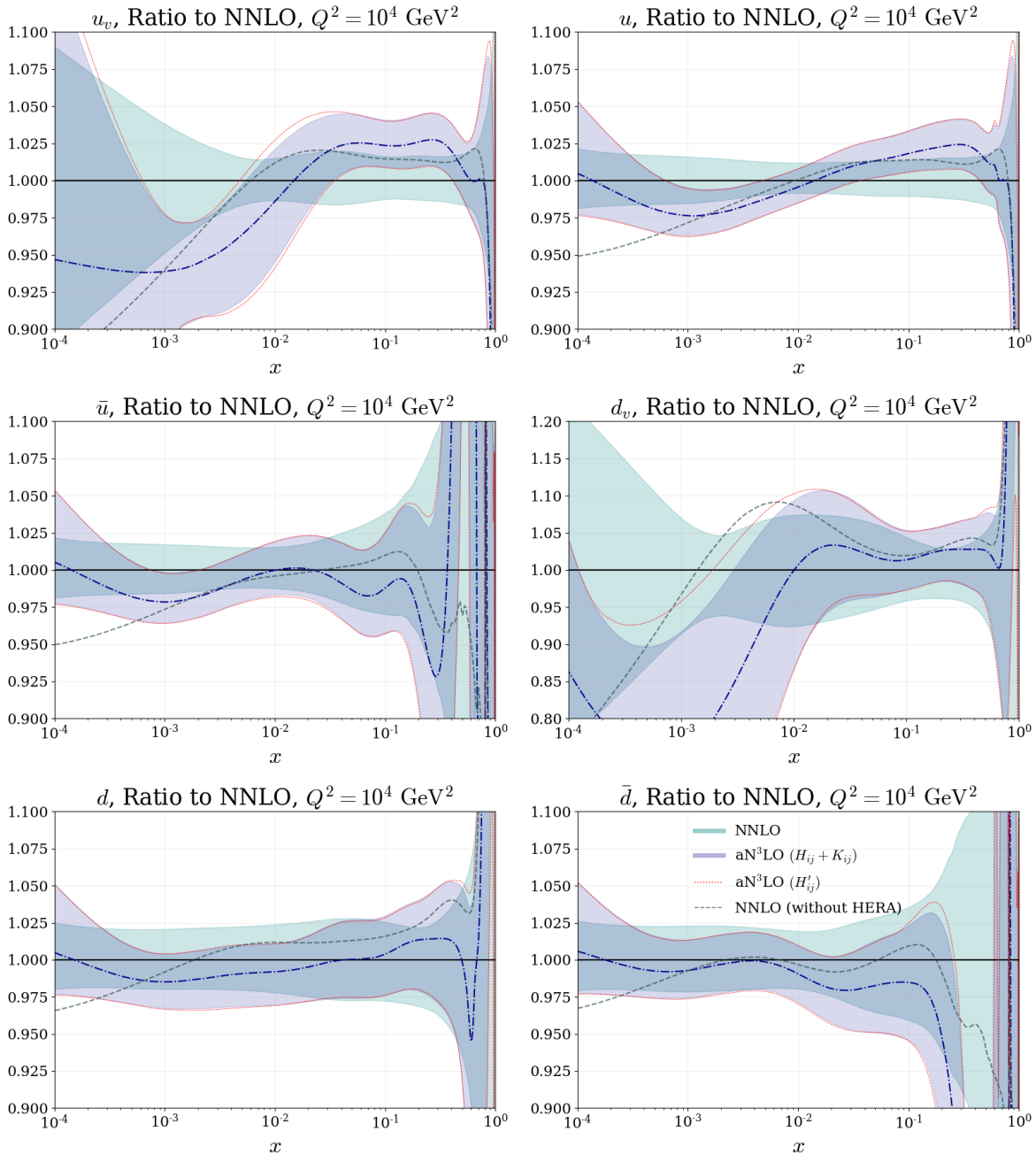

Figure 11.9.: High-Q^2 ratio plots showing the aN^{3}LO 68% confidence intervals with decorrelated ($H_{ij} + K_{ij}$) and correlated (H'_{ij}) K-factor parameters, compared to NNLO 68% confidence intervals. Also shown are the central values at NNLO when fit to all non-HERA datasets which show similarities with N^{3}LO in the large-x region of selected PDF flavours. All plots are shown for $Q^2 = 10^4$ GeV^2.

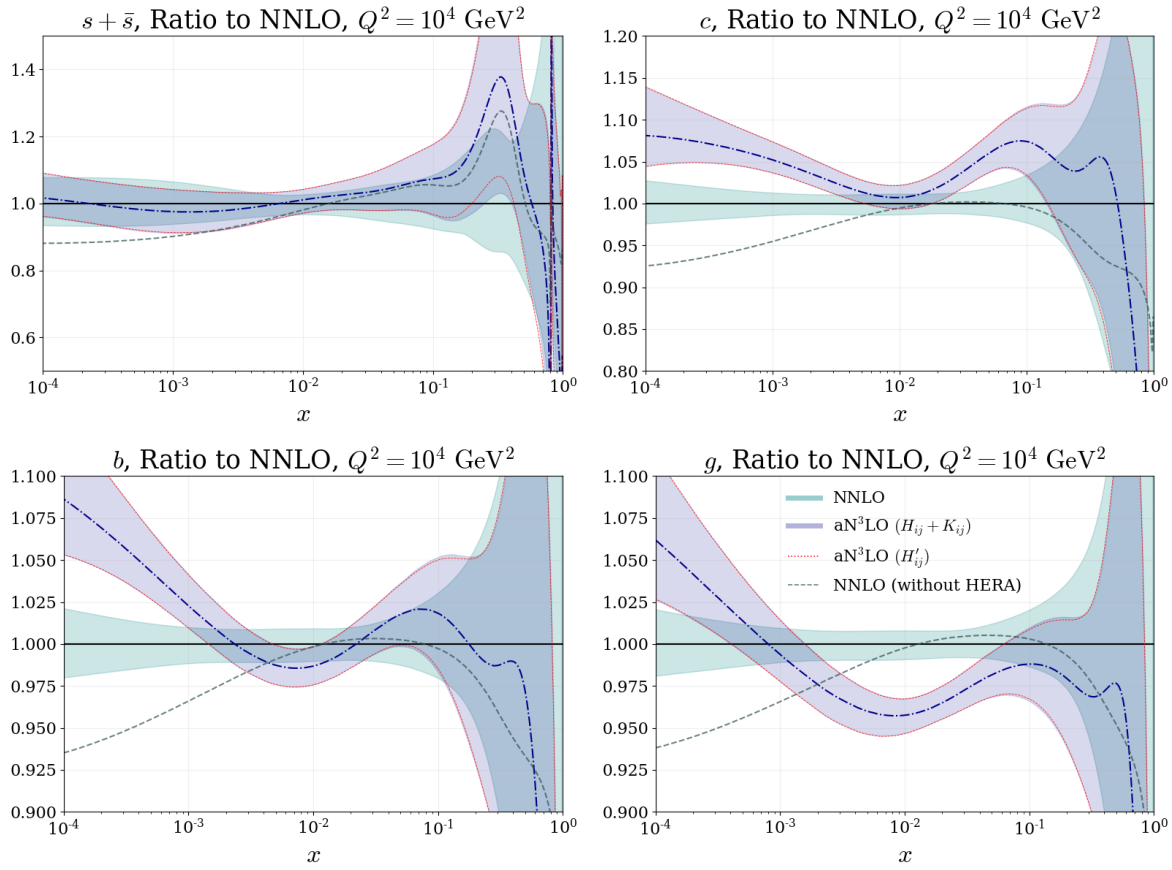

Figure 11.9.: *(Continued)* High-Q^2 ratio plots showing the aN^{3}LO 68% confidence intervals with decorrelated ($H_{ij}+K_{ij}$) and correlated (H'_{ij}) K-factor parameters, compared to NNLO 68% confidence intervals. Also shown are the central values at NNLO when fit to all non-HERA datasets which show similarities with N^{3}LO in the large-x region of selected PDF flavours. All plots are shown for $Q^2 = 10^4$ GeV^2.

While in principle the negativity of quarks is possible in the $\overline{MS}$ scheme, it is unlikely to be correct at very high scales and the behaviour can lead to issues concerning negative cross section predictions [155, 156]. In the case of the $\bar{d}$, the form of this PDF has a negative central value above $x \sim 0.5$ with a minimum of ~ -0.001 at $x \sim 0.6$. It is also noted that although the $\bar{d}$ central value becomes negative in this region, it is still positive within PDF uncertainties. These features are not uncommon in PDF analyses and are discussed in detail in [8]. The proposed smoothing of parameterisations employed in [8] ensures the definite positive nature of PDFs in the high-x region.

Comparing the negativity of the approximate N^{3}LO $\bar{d}$ PDF with that in [8], the $\bar{d}$ PDF presented here is much less negative and positive within PDF uncertainties. Due to this and the fact that this effect is only apparent in the $\bar{d}$, we present these PDFs as they are. We also note that in the current MSHT20 fit, recent results surrounding the $\bar{d}/\bar{u}$ from the SeaQuest collaboration [19] are not included at the time of writing. It is therefore only the E866 / NuSea pd/pp DY dataset [104] that is constraining this ratio, which is not as precise as the more recent results. However SeaQuest results suggest a preference for a higher $\bar{d}$ at large-x, therefore including this data may in fact help constrain the high-x $\bar{d}$ behaviour seen here.

Fig.'s 11.10 and 11.11 express the aN^{3}LO PDFs with decorrelated (green shaded region) and correlated (red dashed lines) aN^{3}LO K-factors at low and high-Q^2 respectively (again with the bottom quark provided at $Q^2 = 25$ GeV^2 at low-Q^2) as a ratio to the N^{3}LO central value. For comparison we also include the level of uncertainty predicted with all N^{3}LO theory fixed (blue shaded region) i.e. only considering the variation *without* N^{3}LO theoretical uncertainty.

Comparing the two different aN^{3}LO sets in Fig.'s 11.10 and 11.11, in general there is good agreement between the total uncertainties considering the cases with correlated (red dash) and decorrelated (green shaded) aN^{3}LO K-factors. The differences that are apparent between between the two aN^{3}LO cases, are relatively small across all PDFs, with slightly larger effects only where the PDF itself tends towards zero i.e. valence quarks at small-x.

A larger distinction is observed when comparing the sets *with* and *without* theoretical uncertainty (where N^{3}LO theory is fixed at the best fit value). In general there is an expected substantial increase in the PDF uncertainties when taking into account the MHOUs for the gluon (and therefore the heavy quarks). In particular, the form of the

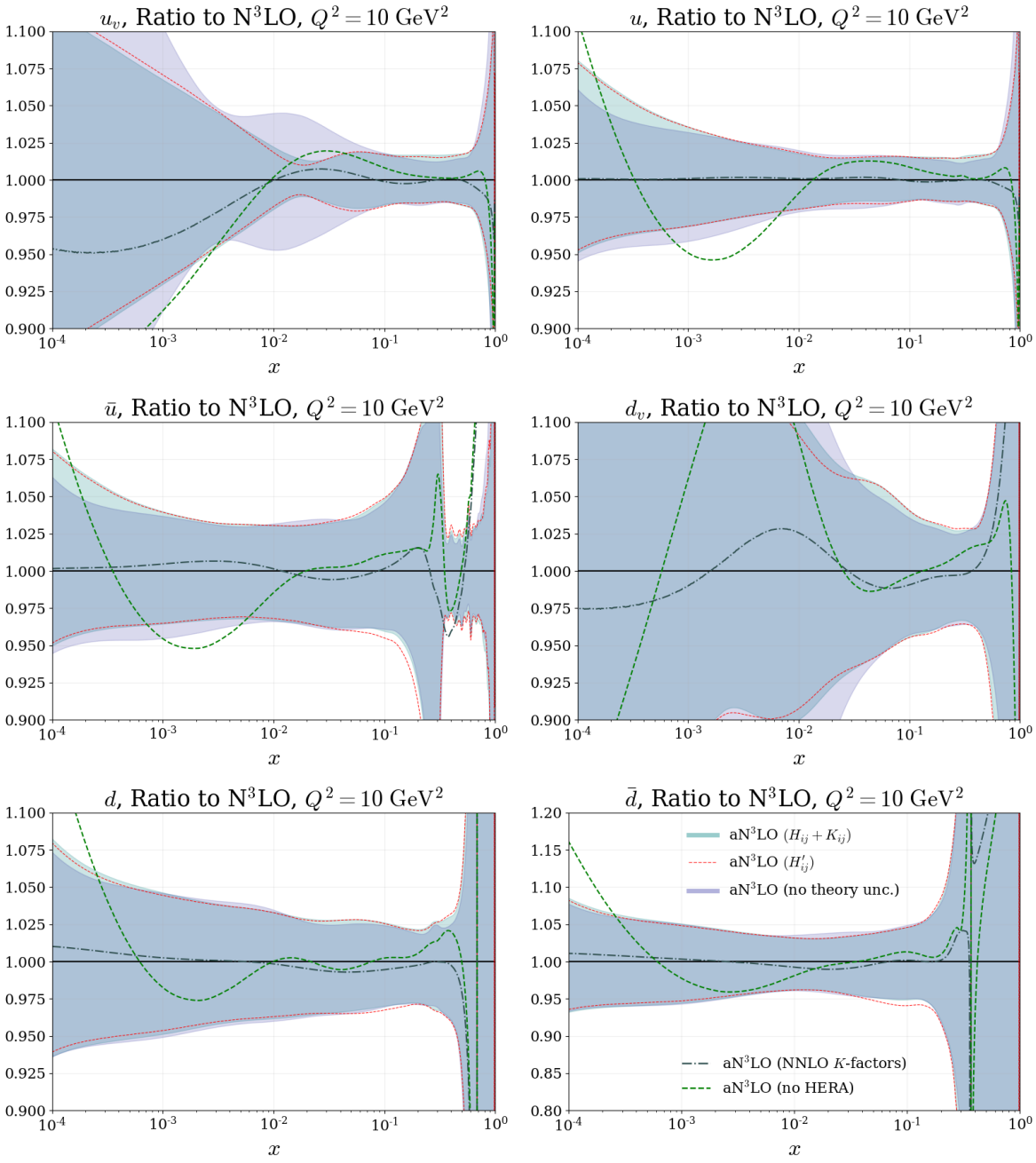

Figure 11.10.: Low-Q^2 ratio plots showing the aN^{3}LO 68% confidence intervals with decorrelated and correlated K-factor parameters, compared to the aN^{3}LO central value. Also shown are the central values at aN^{3}LO when fit to all non-HERA datasets and the central values with all K-factors set at NNLO. All plots are shown for $Q^2 = 10\,\text{GeV}^2$ with the exception of the bottom quark shown for $Q^2 = 25\,\text{GeV}^2$.

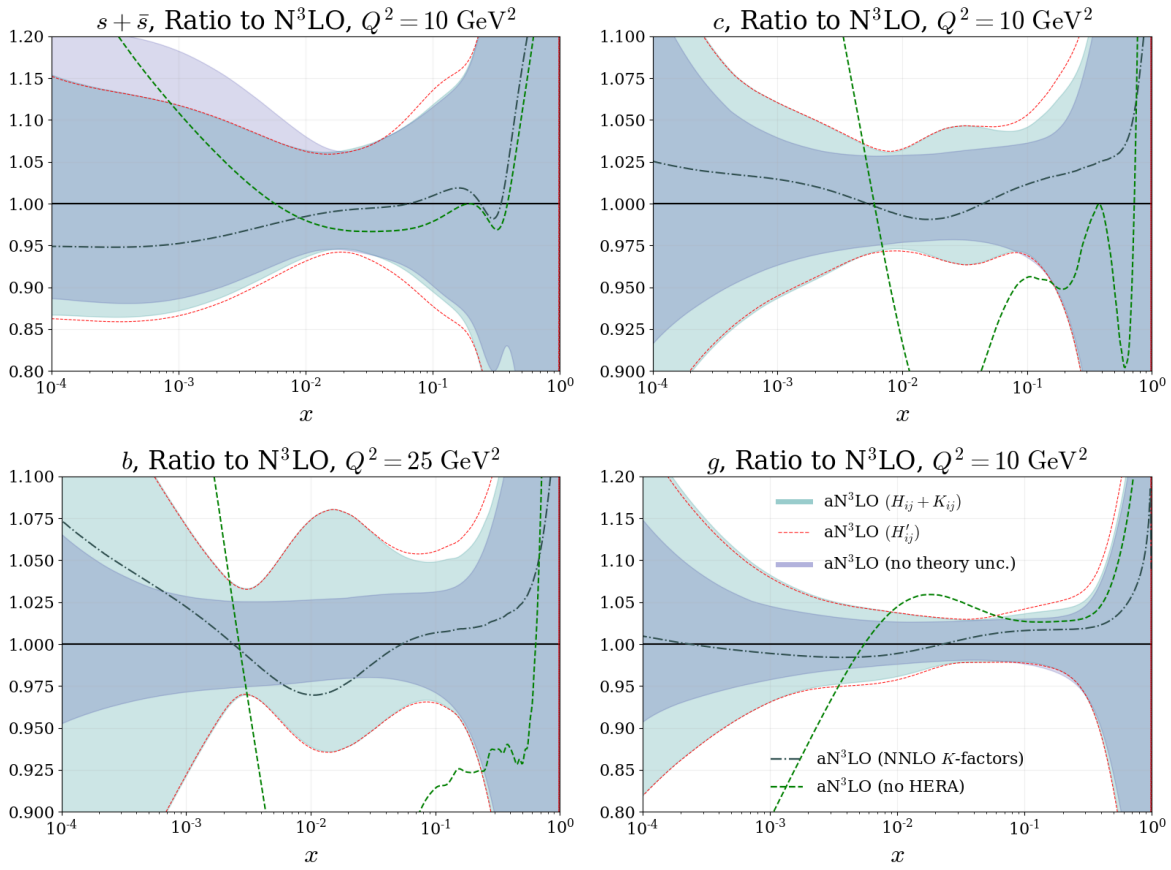

Figure 11.10.: *(Continued)* Low-Q^2 ratio plots showing the aN^{3}LO 68% confidence intervals with decorrelated and correlated K-factor parameters, compared to the aN^{3}LO central value. Also shown are the central values at aN^{3}LO when fit to all non-HERA datasets and the central values with all K-factors set at NNLO. All plots are shown for $Q^2 = 10$ GeV^2 with the exception of the bottom quark shown for $Q^2 = 25$ GeV^2.

N^{3}LO bottom quark uncertainty is reminiscent of the $(H + \overline{H})$ prediction from Fig. 8.5. One can therefore directly observe the effect of the A_{Hg} MHOU on the bottom quark directly above its mass threshold. In other areas, the *without* theoretical uncertainty PDF set exhibits a comparable uncertainty to aN^{3}LO and is even shown to increase the overall 68% confidence intervals in certain regions of (x, Q^2) due to N^{3}LO parameters being fixed (i.e. u_v and d_v PDFs in Fig. 11.10 and Fig. 11.11). As the fit now resides in a different χ^2 landscape where a best fit has been achieved through fitting the N^{3}LO

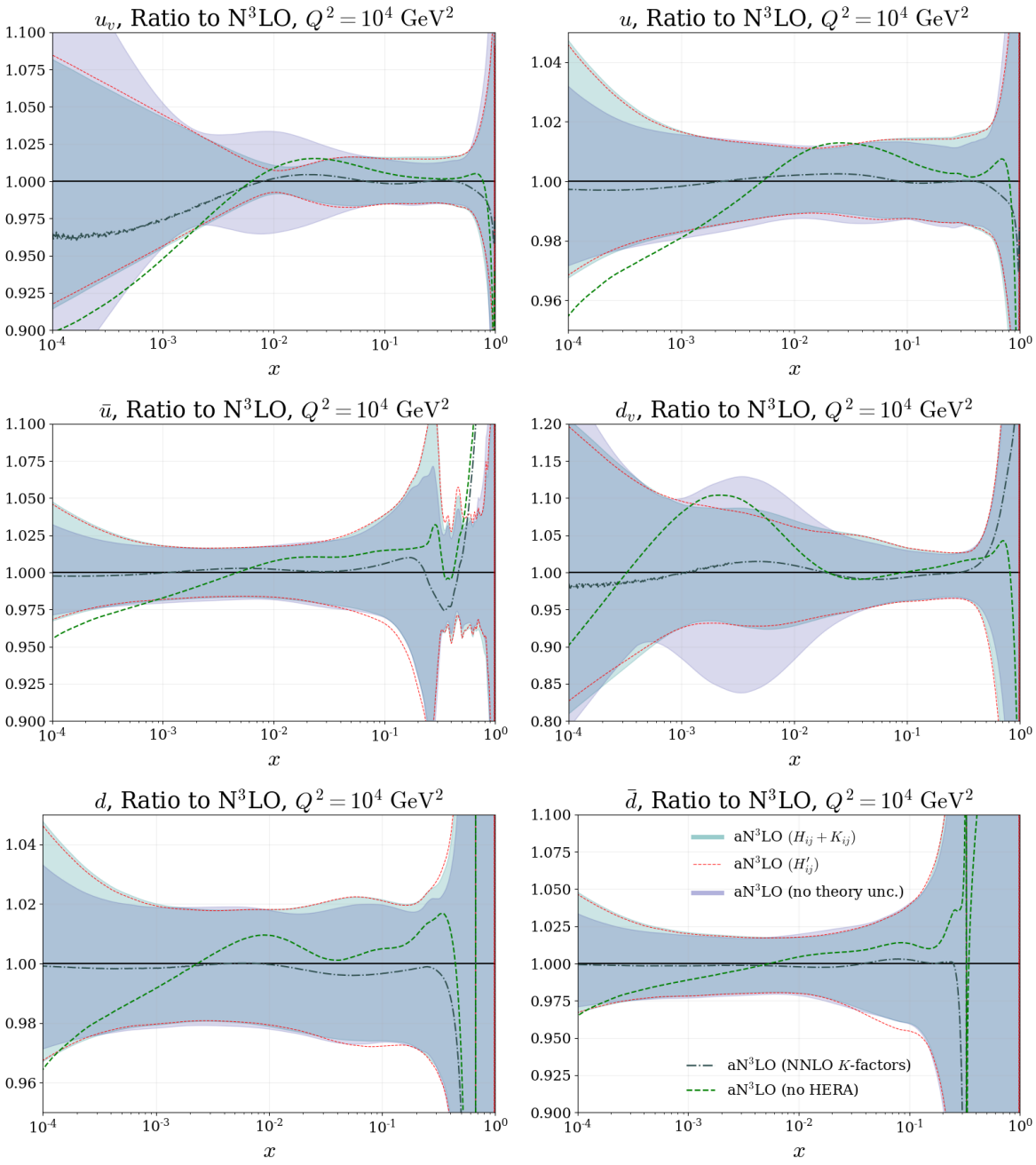

Figure 11.11.: High-Q^2 ratio plots showing the aN^{3}LO 68% confidence intervals with decorrelated and correlated K-factor parameters, compared to the aN^{3}LO central value. Also shown are the central values at aN^{3}LO when fit to all non-HERA datasets and the central values with all K-factors set at NNLO. All plots are shown for $Q^2 = 10^4$ GeV^2.

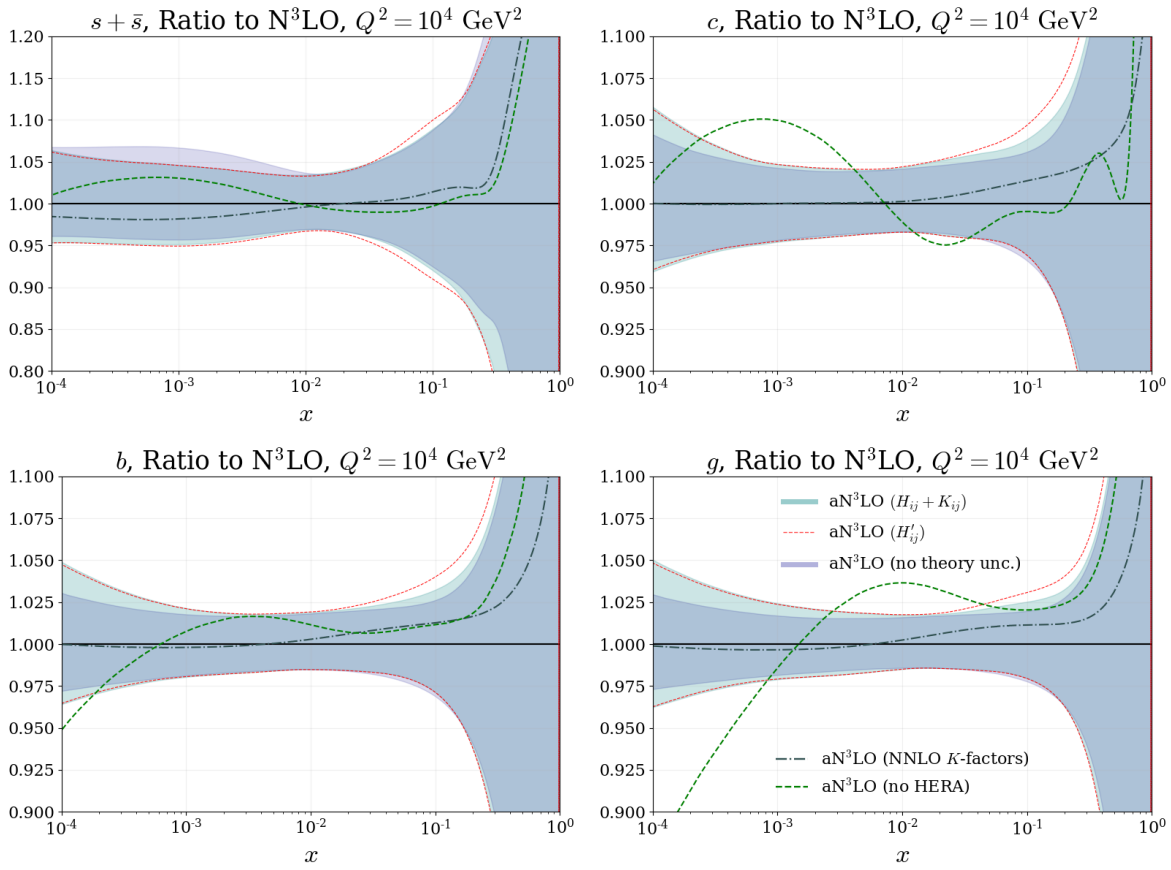

Figure 11.11.: *(Continued)* High-Q^2 ratio plots showing the aN^{3}LO 68% confidence intervals with decorrelated and correlated K-factor parameters, compared to the aN^{3}LO central value. Also shown are the central values at aN^{3}LO when fit to all non-HERA datasets and the central values with all K-factors set at NNLO. All plots are shown for $Q^2 = 10^4$ GeV^2.

theory, fixing the aN^{3}LO theory parameters is likely to have a substantial effect across all PDFs.

An important point made by Fig.'s 11.10 and 11.11 is that that the difference between the decorrelated and correlated cases is much smaller than the difference of not including theoretical uncertainties at all (blue shaded region). This analysis therefore provides evidence to support the original assumption of being able to decorrelate the cross section (aN^{3}LO K-factors) and PDF theory (including other N^{3}LO theory).

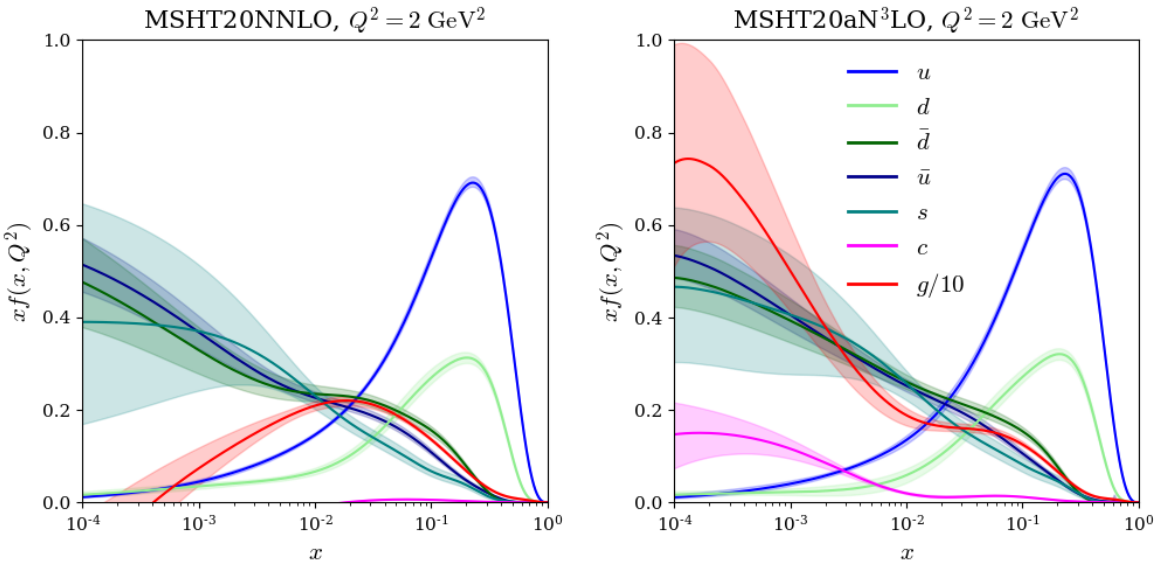

Figure 11.12.: General forms of NNLO (left) and aN^{3}LO (right) PDFs at $Q^2 = 2$ GeV^2. Axis are set to the same scale to highlight the main differences between NNLO and aN^{3}LO. Specifically in the gluon and heavy flavour sectors.

Along with the separate cases of uncertainty illustrated in Fig.'s 11.10 and 11.11, we also display the central values of an aN^{3}LO fit to all non-HERA data and an aN^{3}LO fit with NNLO K-factors. Examining the form of the no HERA aN^{3}LO PDFs for $x > 10^{-2}$, we show some agreement with the standard N^{3}LO central value across most PDFs (more so at high-Q^2 than low-Q^2). Whereas the form at small-x gives some insight into the importance of HERA data in constraining PDFs in this region. In slightly better agreement across all x are the aN^{3}LO PDFs with NNLO K-factors, which complement the χ^2 results in Section 10 and Section 11.1 arguing that the form (and fit results) of aN^{3}LO PDFs is mostly determined from the extra PDF + DIS coefficient function N^{3}LO additions i.e. not aN^{3}LO K-factors which prefer a softer high-x gluon (similar to the N^{3}LO no HERA case – also shown in Fig.'s 11.10 and 11.11).

11.5. MSHT20aN^{3}LO PDFs at $Q^2 = 2$ GeV^2

Fig. 11.12 compares the MSHT NNLO and aN^{3}LO PDF sets at $Q^2 = 2$ GeV^2. In this very low-Q^2 regime, some major differences are evident between NNLO and aN^{3}LO sets at $Q^2 = 2$ GeV^2, especially towards small-x. For example, the gluon PDF is predicted to be much harder across this region, such that it is now positive across all x values considered here. The effect of this can be immediately seen in the sea and heavy quarks.

Since the charm quark is directly coupled to the gluon PDF (through a convolution with A_{Hg}), the charm PDF receives a notable enhancement at small-x and also remains positive across all x values considered[3]. Another interesting feature is the reduction in uncertainty of the strange quark at small-x. It may seem counter intuitive to have an uncertainty reduction by adding sources of theoretical uncertainty, however we should recall that the underlying theory has also been altered. Although one can expect an uncertainty increase in PDFs across (x, Q^2), there are exceptions to this e.g. where tensions are relieved by introducing the N^{3}LO theory. The shift in the χ^2 landscape then has the potential to result in more precise regions of (x, Q^2) (in this case manifesting in an uncertainty reduction for the strange quark towards small-x).

Fig. 11.13 displays the ratios of the aN^{3}LO MSHT PDFs to their NNLO counterparts at $Q^2 = 2$ GeV^2. Here the specific shifts of each PDF are displayed more clearly. We note that there are many similar features shown here to those discussed for Fig.'s 11.8 and 11.9. Even in this very low-Q^2 regime, the uncertainty difference between correlated and decorrelated aN^{3}LO K-factor PDF sets is minimal in all relevant regions of x.

[3]Since this is a convolution, it is the higher small-x gluon, combined with the high-x enhancement of A_{Hg} at N^{3}LO which gives rise to this increase in the charm PDF.

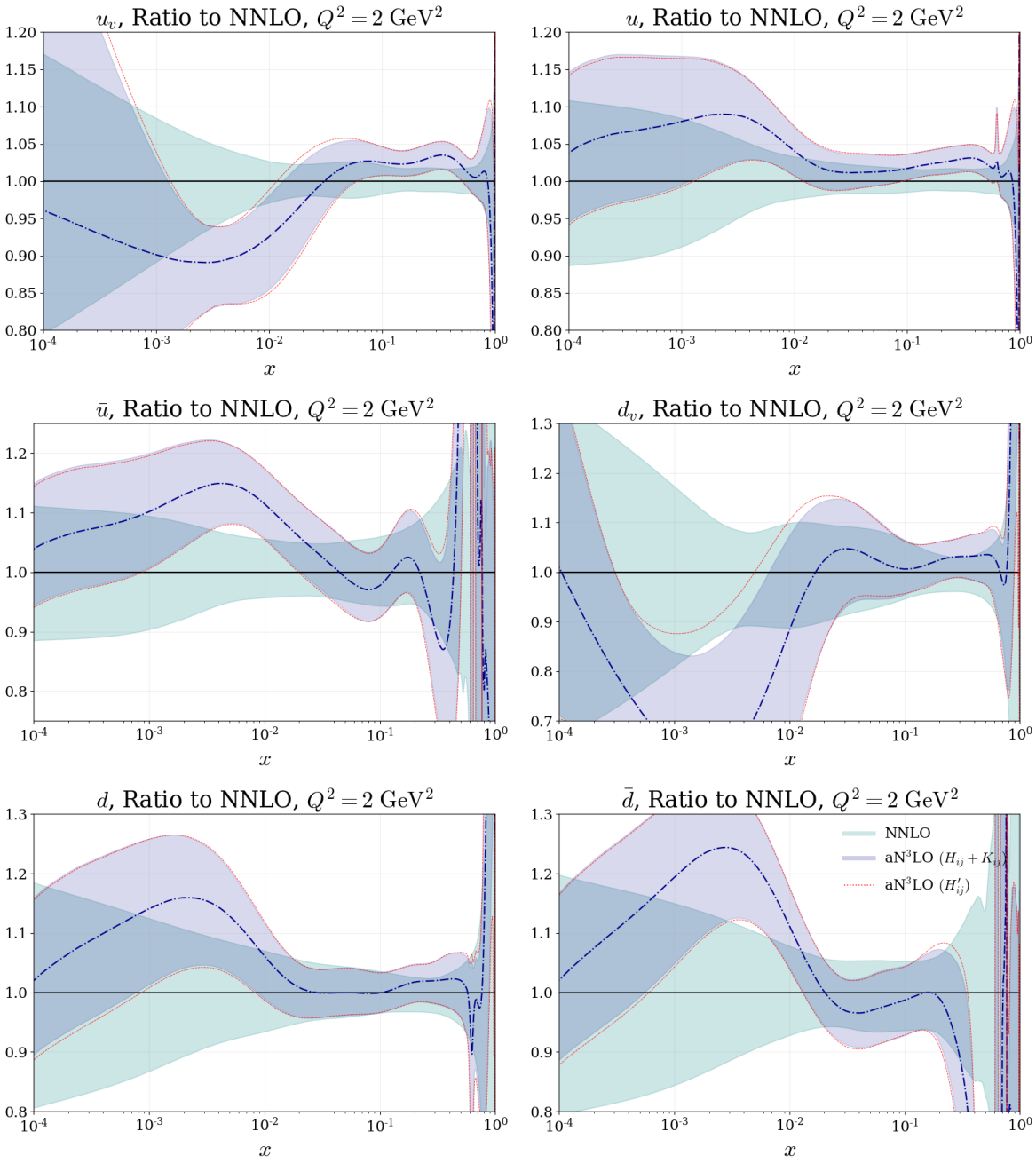

Figure 11.13.: Very low-Q^2 ratio plots showing the aN^{3}LO 68% confidence intervals with decorrelated and correlated K-factor parameters, compared to NNLO 68% confidence intervals. All plots are shown for $Q^2 = 2$ GeV^2.

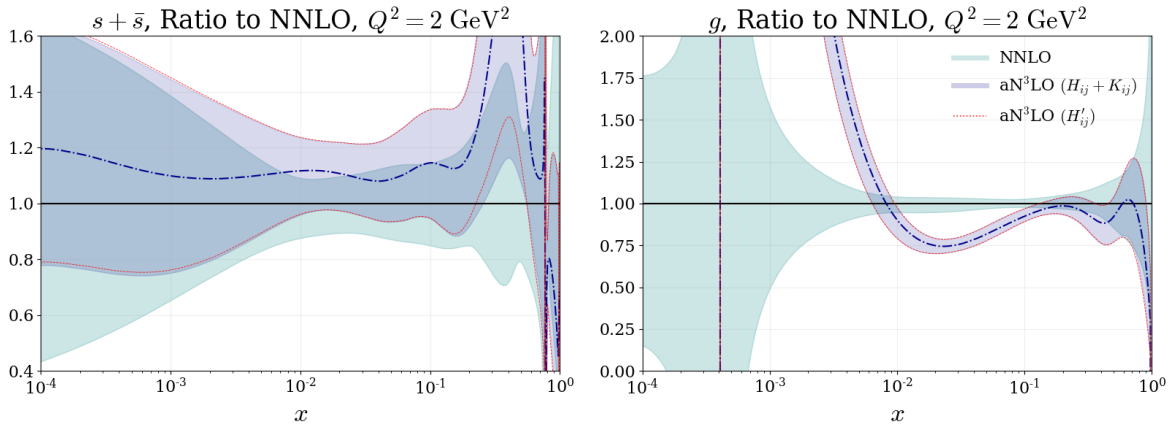

Figure 11.13.: *(Continued)* Very low-Q^2 ratio plots showing the aN^{3}LO 68% confidence intervals with decorrelated and correlated K-factor parameters, compared to NNLO 68% confidence intervals. All plots are shown for $Q^2 = 2$ GeV^2.

11.6. Effect of a $x < 10^{-3}$ cut at aN^{3}LO

In this section we include results from a global PDF fit with all small-x ($x < 10^{-3}$) data omitted. This analysis is provided to shed some light on the tensions between regions of x at aN^{3}LO while also providing some context with regards to the form of the PDFs in different regions of x.

Immediately, in Fig. 11.14, one can observe that omitting all small-x data results in a set of less constrained PDFs for $x < 10^{-3}$ (most notably in the gluon sector). However, also in Fig. 11.14 it can be observed that overall, the large-x behaviour of these PDFs is very similar across both fits, indicating that the fit is able to sufficiently fit to both large and small x regions simultaneously. We provide this analysis as a cross-check to further support the reliability of our procedure, showing that the small-x behaviour is seemingly not attempting to fit to any all order result at the expense of the large-x description. We also note that while there is some change in the central values of the PDFs at small x, in most cases this is very well within uncertainties, and at most at the level of about one standard deviation, particularly for the gluon for x just below 10^{-3}.

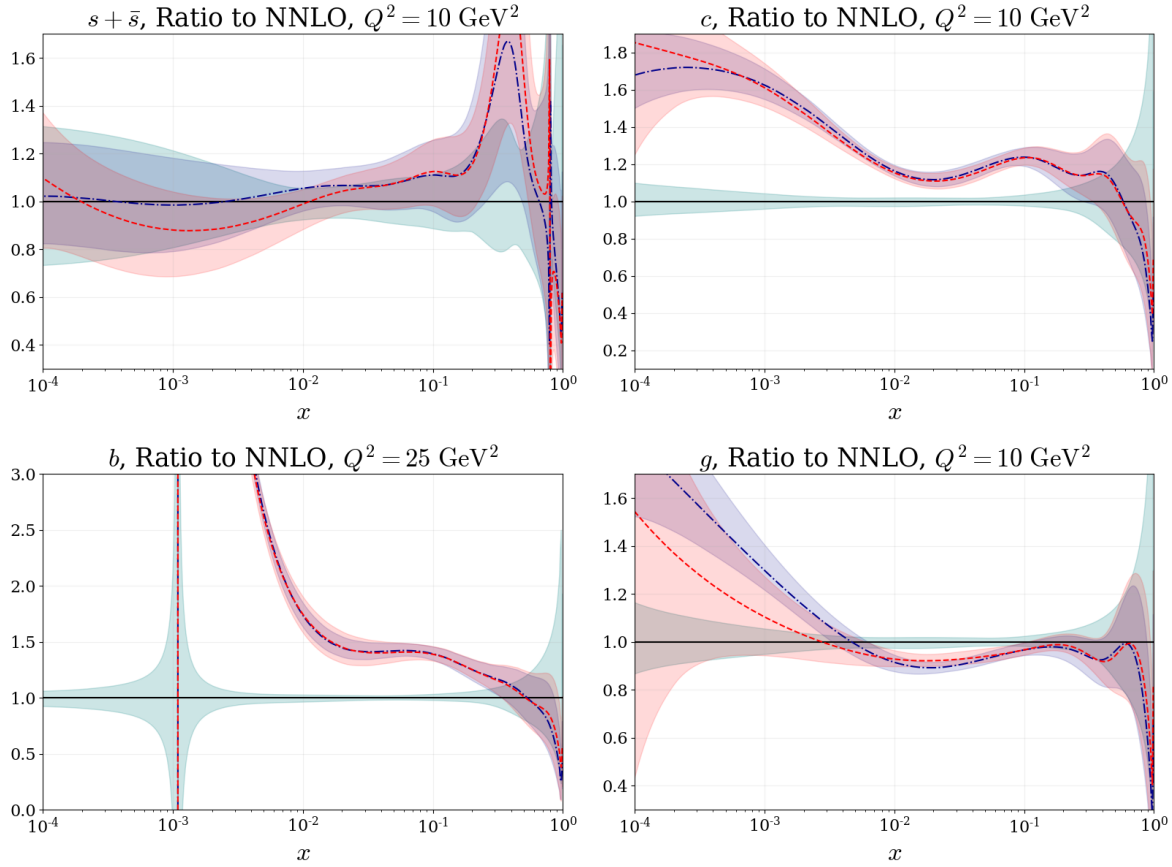

Figure 11.14.: Low-Q^2 PDF ratios showing aN^{3}LO PDFs fitted with and without small-x ($< 10^{-3}$) data included in a global fit. All plots are shown for $Q^2 = 10$ GeV^2 with the exception of the bottom quark shown for $Q^2 = 25$ GeV^2.

Parameter	Default Fit			Small-x cut Fit		
	Central	+ Limit	− Limit	Central	+ Limit	− Limit
Low-Q^2 Coefficient						
$c_q^{\rm NLL}$	−3.868	−1.891	−6.132	−5.822	−4.333	−10.373
$c_g^{\rm NLL}$	−5.837	−4.444	−7.429	−6.995	−3.701	−7.991
Transition Matrix Elements						
$a_{qq,H}^{\rm NS}$	−64.411	−38.778	−91.850	−65.103	−40.073	−93.225
a_{Hg}	12214.000	12966.856	11279.376	12524.000	13831.976	11286.843
$a_{gg,H}$	−1951.600	−1577.155	−3418.568	−1392.600	−512.817	−2190.354
Splitting Functions						
ρ_{qq}^{NS}	0.007	0.015	−0.002	0.006	0.020	−0.005
ρ_{qq}^{PS}	−0.501	−0.254	−0.644	−0.505	−0.285	−0.692
ρ_{qg}	−1.754	−1.157	−1.897	−1.309	−0.620	−1.881
ρ_{gq}	−1.784	−1.548	−2.212	−1.622	−1.367	−1.877
ρ_{gg}	19.245	21.505	9.025	12.997	16.142	6.611

Table 11.6.: Posterior predicted $\pm 1\sigma$ limits on aN^{3}LO theoretical nuisance parameters for splitting functions, transition matrix elements and coefficient functions.

This limited shift in the best fit PDFs suggests that while effects beyond N^{3}LO are not insignificant at very low x, they are also not dominating the pull on the fit.

11.7. Posterior N^{3}LO Theory Parameters

Following from the previous section, it is also interesting to examine where the aN^{3}LO theory contributions and their uncertainties reside after a global PDF fit.

Displayed in Table 11.6 are the predicted posterior limits on each (non K-factor) aN^{3}LO theory parameter. Here one can directly compare these variations with the prior variations decided in earlier Sections. Also provided is a comparison of these posterior limits across a fit with and without small-x ($x < 10^{-3}$) data included. This comparison complements the previous section by showing a similar trend in the

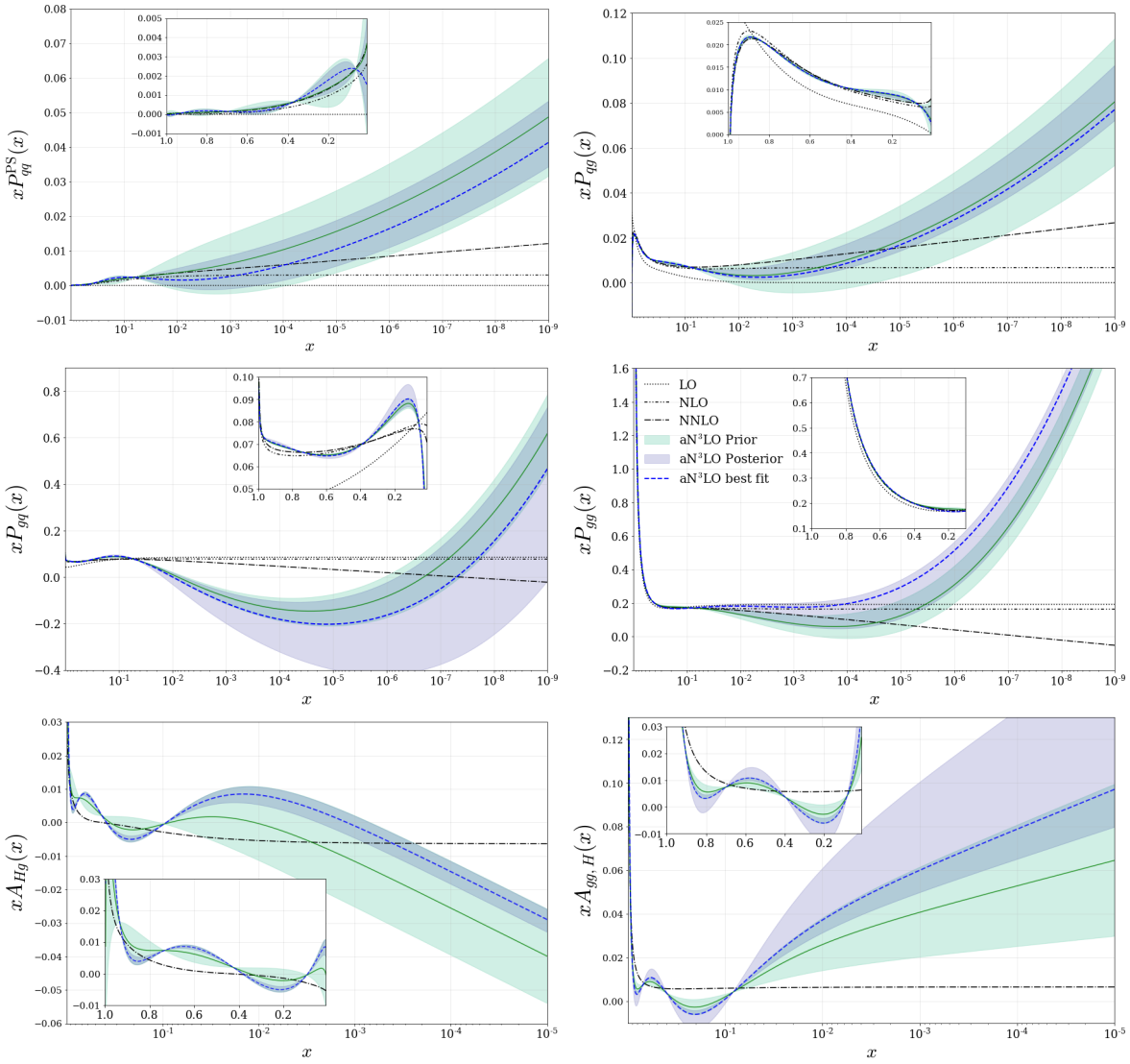

Figure 11.15.: Posterior variations of the aN^{3}LO splitting functions and transition matrix elements predicted from a full global fit.

central values predicted in both cases (i.e. with an overlap of uncertainties). As with the PDFs, there is some evidence of tensions, but these are clearly not severe, and the central values of many parameters are extremely stable. Furthermore this is evidence that the small-x behaviour is not likely to be dominating the behaviour of aN^{3}LO parameters in a manner which is adversarial to the preference of data at $x > 10^{-3}$.

Fig. 11.15 displays a comparison of the prior and posterior variations predicted for the perturbative expansions of relevant splitting functions and transition matrix elements discussed in Chapter's 7 and 8. We exclude the non-singlet quantities from this comparison as the variations predicted for these quantities are very similar to their priors (as can be seen in Table 11.6) and have a small overall effect on the PDFs. It is true that once a fit is performed, the variation of the aN^{3}LO theoretical nuisance parameters becomes less sensitive to the prior variation, suggesting that the initial uncertainty estimate was conservative. Nevertheless in Fig. 11.15, one can observe that all posterior variations overlap with their corresponding priors, in most cases quite considerably. We also note that the most drastic differences between prior and posterior variations are expectedly relating to the gluon PDF.

Fig. 11.16 contains a comparison between the aN^{3}LO functions posterior variations with and without small-x ($x < 10^{-3}$) data included in a global fit. These results accompany those presented in Table 11.6 and further display the agreement between the two fits. In all cases the predicted variations overlap with most central values being stable (i.e. contained within the uncertainty predictions). Therefore providing evidence that the aN^{3}LO predictions are consistent across all values of x and not being heavily determined by, for example, the small-x region.

11.8. N^{3}LO Contributions

In this section all but one N^{3}LO contribution will be switched off, in particular only splitting functions, or only heavy or light flavour coefficient functions with their relevant transition matrix elements. In all cases the aN^{3}LO K-factors are left free to allow the fit some freedom in manipulating the cross sections of other datasets. In

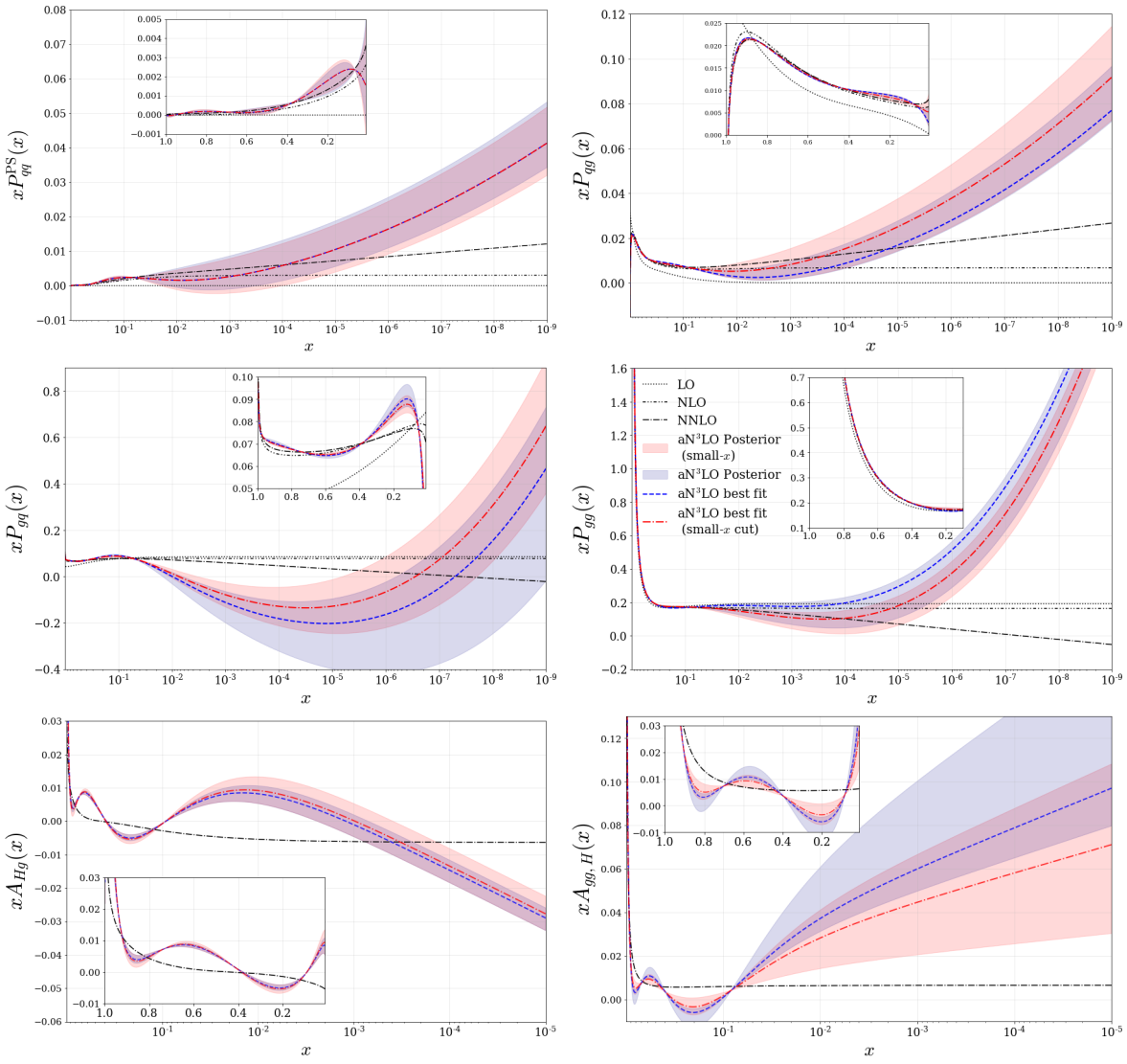

Figure 11.16.: Posterior variations of the aN^{3}LO splitting functions and transition matrix elements predicted from a full global fit (blue shaded band) compared to a fit with small-x ($x < 10^{-3}$) data removed from a fit (red shaded band).

practice however, fixing these K-factors at the NNLO values has a minimal effect on the shape of the PDFs in all cases (as demonstrated in Fig. 11.10 and 11.11).

The deconstructed aN^{3}LO PDFs as a ratio to the NNLO MSHT PDFs for various flavours at $Q^2 = 10\,\text{GeV}^2$ (with the bottom quark given at $Q^2 = 25\,\text{GeV}^2$) are shown in Fig. 11.17. Across the more tightly constrained light quark PDFs, all contributions lie very close to the aN^{3}LO $\pm 1\sigma$ uncertainty bands (blue shaded region and solid line). The additive and compensating nature of these contributions is also clear in a handful of the ratios from Fig. 11.17. In other areas the full description is biased towards a single contribution, for example the charm and bottom quarks follow the contribution from heavy flavours as one may expect. Conversely, to some extent the gluon follows the splitting functions much more closely as these contributions indirectly couple the gluon to the more constraining data.[4]

11.9. α_s Variation

As in the standard MSHT20 NNLO PDF fit, we present the best fit aN^{3}LO PDFs with $\alpha_s(m_Z) = 0.118$, the common value chosen in the PDF4LHC combination [8]. However, investigating the true minima in $\alpha_s(m_Z)$, the χ^2 profiles in Fig. 11.18 prefer a value of around $\alpha_s(m_Z) = 0.1170$. This result follows the trend from lower orders whereby the best fit values are $\alpha_s(m_Z) = 0.1174 \pm 0.0013$ at NNLO and $\alpha_s(m_Z) = 0.1203 \pm 0.0015$ at NLO [143]. Following from NNLO, the aN^{3}LO $\alpha_s(m_Z)$ prediction is also slightly lower than the NNLO world average central value at around $\alpha_s(m_Z) = 0.1179 \pm 0.0010$ [213]. In any case, the preferred aN^{3}LO $\alpha_s(m_Z)$ value stated here is in agreement with the

[4] An exception to this can be seen around $x \sim 10^{-2}$ where the contributions act cumulatively. We make this point as this region of x is of interest for Higgs calculations such as those discussed in Chapter 12

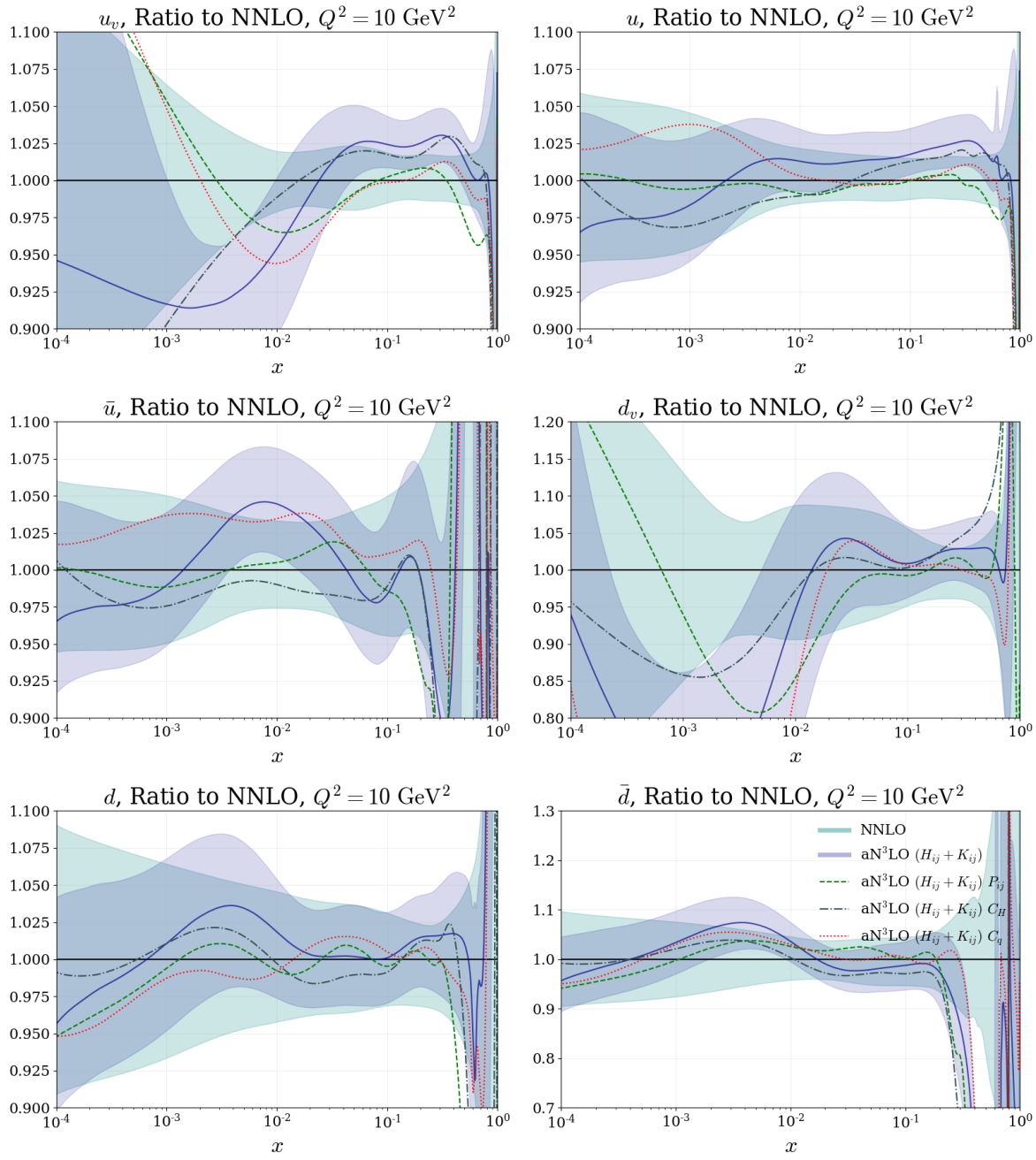

Figure 11.17.: Low-Q^2 PDF ratios showing aN^{3}LO (with decorrelated K-factors) 68% confidence intervals compared to NNLO 68% confidence intervals with varying theory contributions. All plots are shown for $Q^2 = 10\,\text{GeV}^2$ with the exception of the bottom quark shown for $Q^2 = 25\,\text{GeV}^2$. The PDFs included are: NNLO (green shaded), All N^{3}LO contributions (blue shaded), only splitting functions (green dashed), only heavy flavour coefficient functions and transition matrix elements (dark grey dash-dot) and only light flavour coefficient functions and transition matrix elements (red dotted).

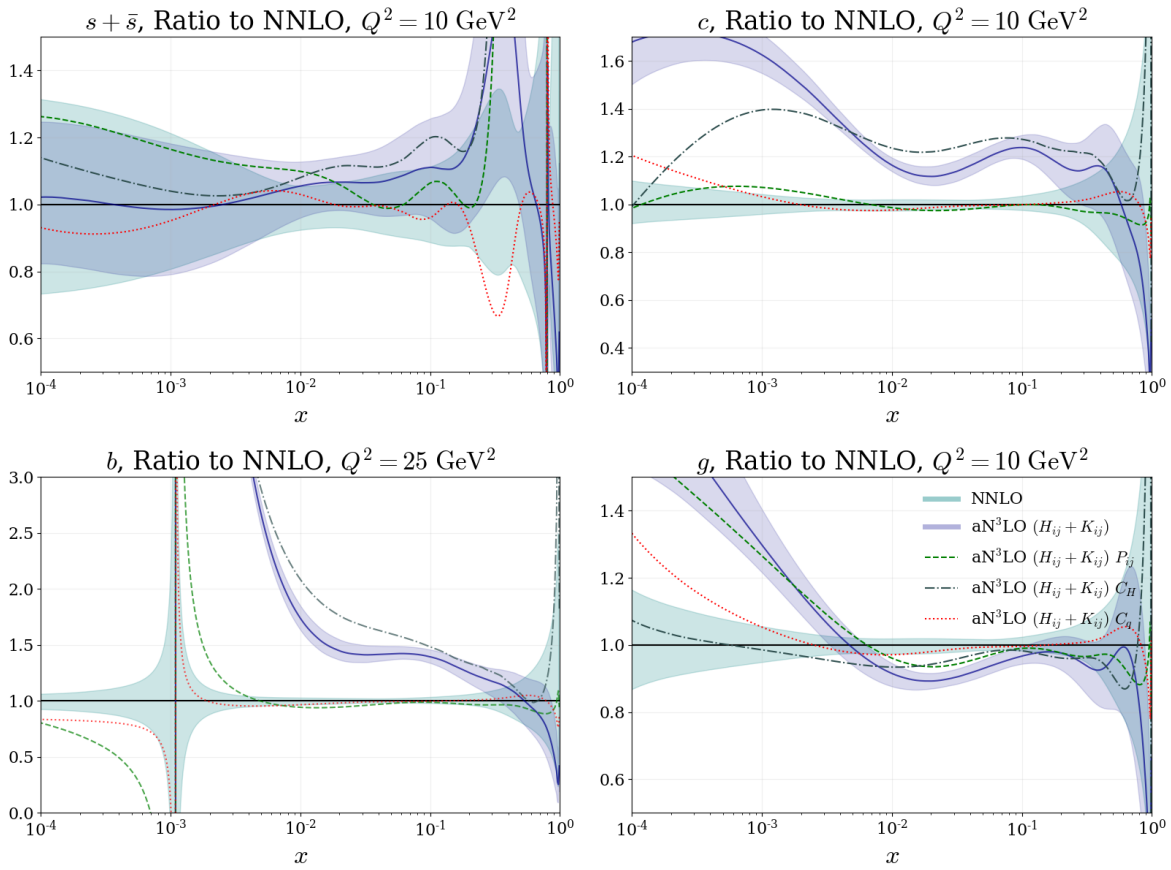

Figure 11.17.: *(Continued)* Low-Q^2 PDF ratios showing aN^{3}LO (with decorrelated K-factors) 68% confidence intervals compared to NNLO 68% confidence intervals with varying theory contributions. All plots are shown for $Q^2 = 10$ GeV^2 with the exception of the bottom quark shown for $Q^2 = 25$ GeV^2. The PDFs included are: NNLO (green shaded), All N^{3}LO contributions (blue shaded), only splitting functions (green dashed), only heavy flavour coefficient functions and transition matrix elements (dark grey dash-dot) and only light flavour coefficient functions and transition matrix elements (red dotted).

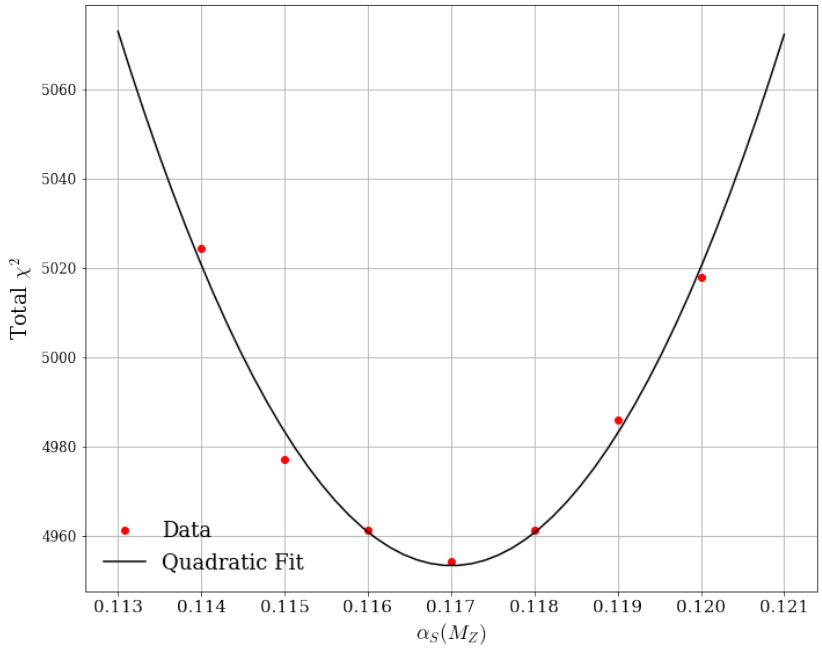

Figure 11.18.: Quadratic fit to the total χ^2 results from various $\alpha_s(m_Z)$ starting scales. The minimum of the quadratic fit provides a rough estimate of $\alpha_s(m_Z) = 0.1170$ at aN^{3}LO.

MSHT20 NNLO result and the world average within uncertainties. A full analysis is left for a future publication.

11.10. Charm Mass Dependence

In a standard MSHT fit [3], aN^{3}LO PDFs are produced with the charm pole mass $m_c = 1.40$ GeV. Fig. 11.19 displays the χ^2 results when varying this charm mass. The predicted minimum at NNLO (for MSHT20 PDFs) is in the range $m_c = 1.35 - 1.40$ GeV [143], whereas at aN^{3}LO we show a minimum in the region of $m_c = 1.42 - 1.47$ GeV. This aN^{3}LO result therefore shows a slightly better agreement with the world average [213][5] of $m_c = 1.5 \pm 0.2$ GeV.

[5]There is some ambiguity in this value since the transformation from $\overline{MS}$ to the pole mass definition is not well-defined (see [143] for more details).

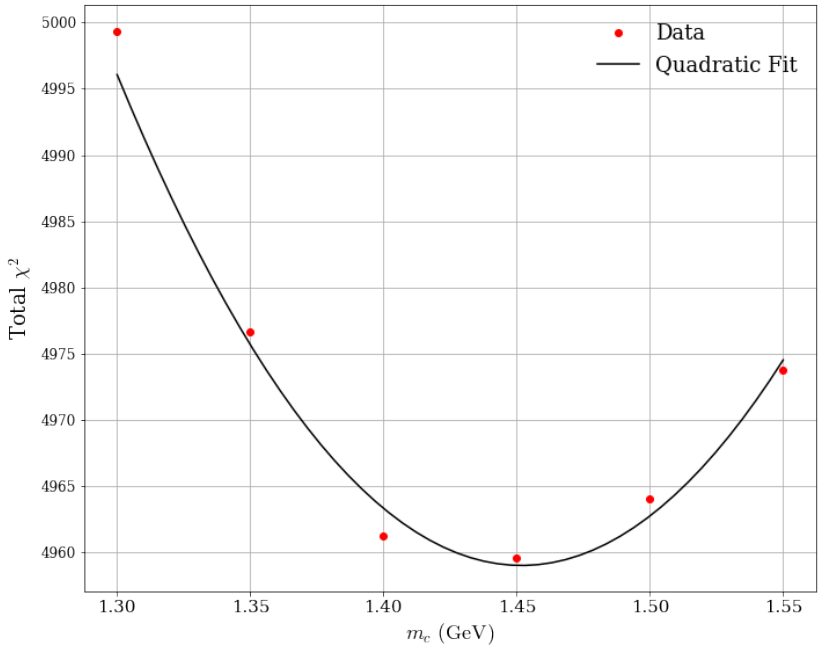

Figure 11.19.: Quadratic fit to the total χ^2 results from various charm masses (m_c). The minimum of the quadratic fit provides a rough estimate of $m_c = 1.45$ GeV at aN^{3}LO.

Considering Fig. 11.20, one is then able to analyse the effect of this slightly higher charm mass on the form of the PDFs. As one can expect, the charm PDF is subject to the largest difference and is suppressed by a higher m_c. The extra suppression from a higher charm mass allows the fit to suppress the $c + \bar{c}$ sea contribution. This is then compensated by an increase in the $\bar{u}$ and $\bar{d}$ distributions which stabilises the overall sea contribution.

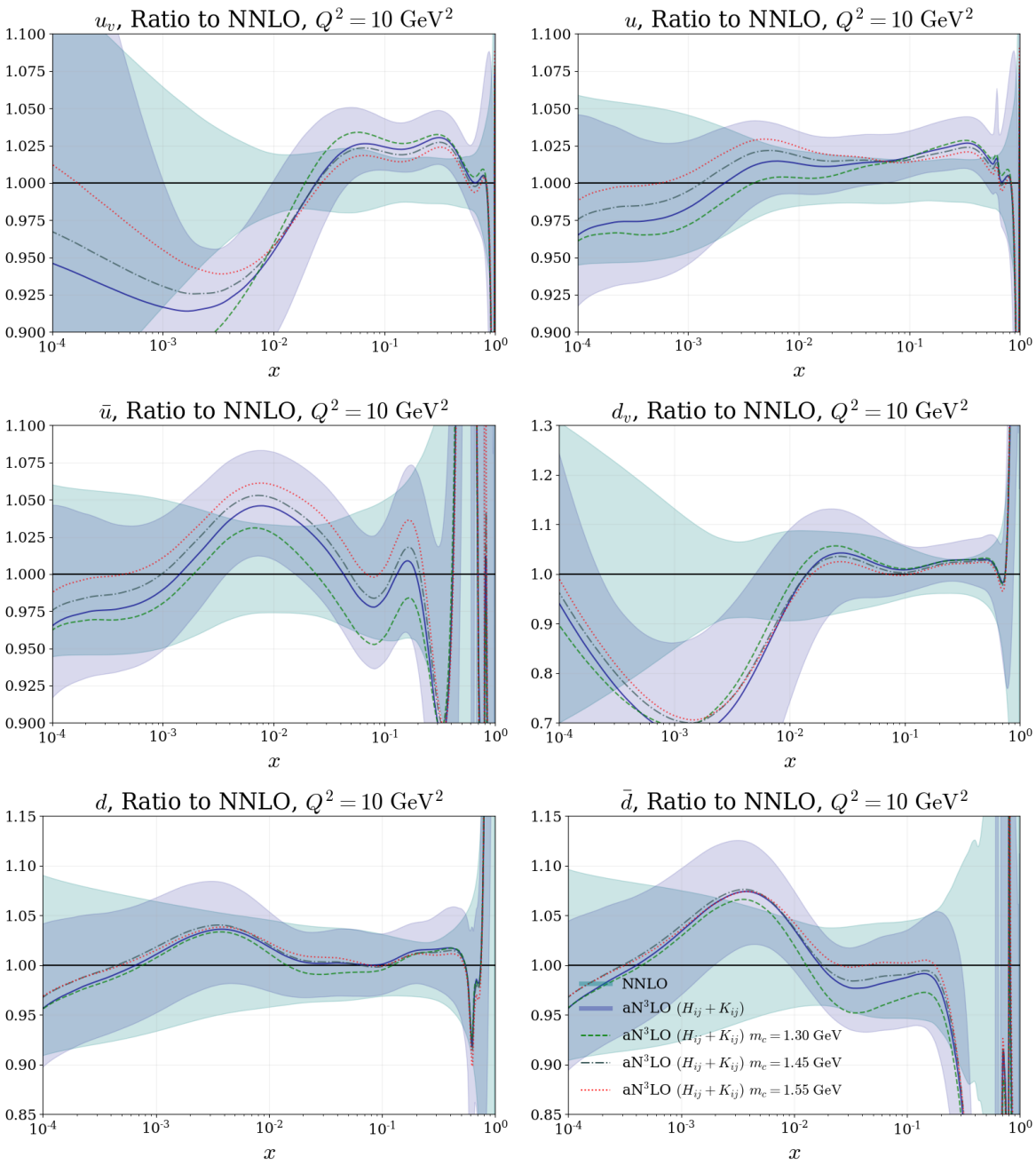

Figure 11.20.: Low-Q^2 PDF ratios showing aN^{3}LO (with decorrelated K-factors) 68% confidence intervals compared to NNLO 68% confidence intervals with varying fixed values for the charm mass. All plots are shown for $Q^2 = 10$ GeV^2 with the exception of the bottom quark shown for $Q^2 = 25$ GeV^2. The PDFs included are: $m_c = 1.40$ GeV (standard MSHT20 choice) (blue solid), $m_c = 1.30$ GeV (green dashed), $m_c = 1.45$ GeV (grey dotted dashed) $m_c = 1.50$ GeV (red dotted).

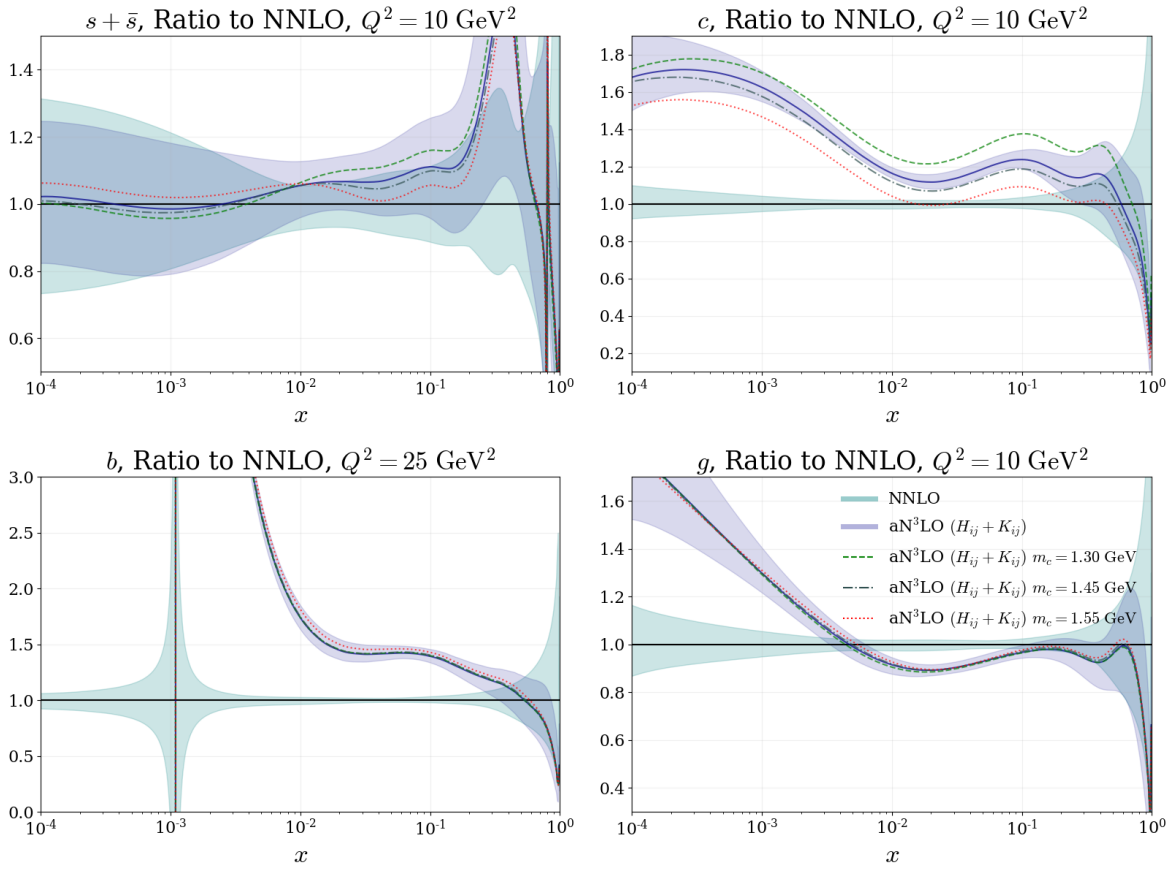

Figure 11.20.: *(Continued)* Low-Q^2 PDF ratios showing aN^{3}LO (with decorrelated K-factors) 68% confidence intervals compared to NNLO 68% confidence intervals with varying fixed values for the charm mass. All plots are shown for $Q^2 = 10$ GeV^2 with the exception of the bottom quark shown for $Q^2 = 25$ GeV^2. The PDFs included are: $m_c = 1.40$ GeV (standard MSHT20 choice) (blue solid), $m_c = 1.30$ GeV (green dashed), $m_c = 1.45$ GeV (grey dotted dashed) $m_c = 1.50$ GeV (red dotted).

Chapter 12.

N^{3}LO Predictions

With the increasing number of hard cross section calculations at N^{3}LO, there is a growing demand for N^{3}LO accuracy in PDFs. In this section we investigate the effect of the MSHT approximate N^{3}LO PDFs on Higgs production via gluon fusion and vector boson fusion (VBF). The hard cross sections for these processes have been calculated to N^{3}LO accuracy [195–204, 214, 215]. We present a full N^{3}LO computation for each prediction with our approximate N^{3}LO PDFs, including theoretical uncertainties. In future work, the intention will be to expand this analysis to include results for N^{3}LO DY [191] and approximate N^{3}LO top production [194] cross sections.

Note that in this Section we follow the notation used previously and denote the aN^{3}LO results with decorrelated K-factors as $(H_{ij} + K_{ij})^{-1}$ and those with correlated K-factors with ${H'_{ij}}^{-1}$. In all cases, scale variations are found via the 9-point prescription [9] for results with NNLO PDFs. Whereas for aN^{3}LO PDFs, although the extra information introduced is at N^{3}LO, the data (and therefore all relevant theory nuisance parameters) which are included in the global fit are sensitive to all orders. In particular, we include

σ order	PDF order	$\sigma + \Delta\sigma_+ - \Delta\sigma_-$ (pb)	σ (pb) $+ \Delta\sigma_+ - \Delta\sigma_-$ (%)
PDF uncertainties			
N^{3}LO	aN^{3}LO (no theory unc.)	44.164 + 1.339 - 1.382	44.164 + 3.03% - 3.13%
	aN^{3}LO ($H_{ij} + K_{ij}$)	44.164 + 1.473 - 1.395	44.164 + 3.34% - 3.15%
	aN^{3}LO (H'_{ij})	44.164 + 1.515 - 1.354	44.164 + 3.43% - 3.07%
	NNLO	47.817 + 0.558 - 0.581	47.817 + 1.17% - 1.22%
NNLO	NNLO	46.206 + 0.541 - 0.564	46.206 + 1.17% - 1.22%
PDF + Scale uncertainties			
N^{3}LO	aN^{3}LO (no theory unc.)	44.164 + 1.339 - 2.214	44.164 + 3.03% - 5.01%
	aN^{3}LO ($H_{ij} + K_{ij}$)	44.164 + 1.473 - 2.222	44.094 + 3.34% - 5.03%
	aN^{3}LO (H'_{ij})	44.164 + 1.515 - 2.196	44.164 + 3.43% - 4.97%
	NNLO	47.817 + 0.577 - 2.210	47.817 + 1.21% - 4.62%
NNLO	NNLO	46.206 + 4.284 - 5.414	46.206 + 9.27% - 11.72%

Table 12.1.: Higgs production cross section results via gluon fusion ($\sqrt{s} = 13$ TeV) using N^{3}LO and NNLO hard cross sections combined with NNLO and aN^{3}LO PDFs. All PDFs are at the standard choice $\alpha_s(m_Z) = 0.118$. These results are found with $\mu = m_H/2$ unless stated otherwise, with the values for $\mu = m_H$ supplied in Table F.1.

theoretical uncertainties into our aN^{3}LO fit which incorporate MHO effects on the PDFs. Therefore we argue (and in these cases demonstrate) that the factorisation scale variation is contained within the PDF uncertainties. Therefore it is only the renormalisation scale which requires variation in predictions involving aN^{3}LO PDFs[1].

12.1. Higgs Production – Gluon Fusion: $gg \to H$

Table 12.1 and Fig. 12.1 (left) show predictions at a central scale of $\mu = \mu_f = \mu_r = m_H/2$ (where $m_H = 125$ GeV) for the Higgs production cross section via gluon fusion[2]

[1] This is to quantify the theoretical MHOU in the hard cross section, whereas the aN^{3}LO PDFs now come with an estimated MHOU.

[2] Results are obtained with the code `ggHiggs` [195–204, 216].

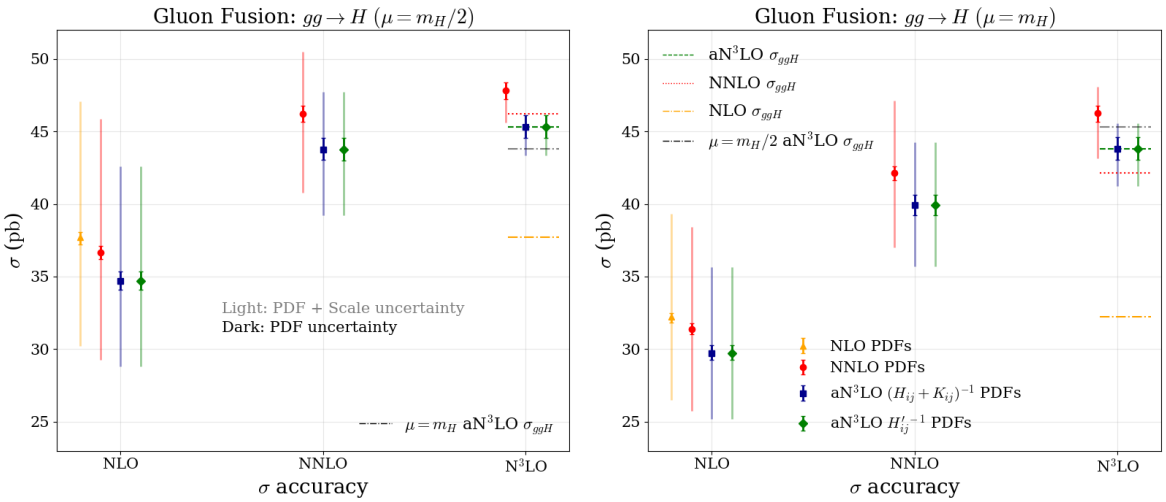

Figure 12.1.: Higgs production cross section results via gluon fusion ($\sqrt{s} = 13$ TeV) at two central scales: $\mu = m_H/2$ (left) and $\mu = m_H$ (right). Displayed are the results for aN^{3}LO PDFs with decorrelated K-factors ($(H_{ij} + K_{ij})^{-1}$), correlated K-factors ($H'^{-1}_{ij} = (H_{ij} + K_{ij})^{-1}$) each with a scale variation band from varying μ_r by a factor of 2. In the NNLO and NLO PDF cases, both scales μ_f and μ_r are varied by a factor of 2 following the 9-point convention [9].

at the LHC for $\sqrt{s} = 13$ TeV where m_H is the Higgs mass. Fig. 12.1 (right) displays the same analysis for the gluon fusion cross section with $\mu = \mu_f = \mu_r = m_H$ (numerical results provided in Table F.1).

Considering the $\mu = m_H/2$ and $\mu = m_H$ central value results displayed in Table 12.1 and Fig. 12.1, it can be observed that aN^{3}LO PDFs predict a lower central value than NNLO PDFs across all hard cross section orders. One can also notice an overlap in all cases between predictions from NNLO and aN^{3}LO PDFs for both choices of central scale. However for $\mu = m_H/2$, whilst the error bands for predictions with N^{3}LO hard cross section and NNLO and N^{3}LO PDFs overlap, their central values are outside each other's respective error bands. Since estimating MHOUs via scale variations is a somewhat ambiguous procedure (and is therefore estimated conservatively to reflect this), these results highlight the benefit of being able to exploit a higher level of control over MHOUs i.e. via nuisance parameters. By predicting a different central value

we include a more accurate estimation for higher order predictions which may not be contained within scale variations, especially at unmatched orders in perturbation theory.

Examining the predicted central values further, Fig. 12.1 suggests that the increase in the cross section theory at N^{3}LO is compensated by the PDF theory at N^{3}LO, suggesting a cancellation between terms in the PDF and cross section theory at N^{3}LO. This point is important to consider when combining unmatched orders in physical calculations, since we must be open to the possibility that unmatched cancellations in physical calculations can lead to inaccurate predictions, as our results suggest here.

Further to this, the change in the gluon PDF is largely driven by the predicted form of P_{qg} at aN^{3}LO and DIS data. Therefore the relevant changes in the gluon at aN^{3}LO are most likely due to indirect effects i.e. not directly related to gluon fusion predictions. Due to this, there is no reason to believe that the observed level of convergence should happen at aN^{3}LO for both choices of μ. However, owing to the inclusion of known information at higher orders, one can be confident that the prediction is more accurate than NNLO, whichever way it moves.

Comparing PDF uncertainty values calculated using NNLO and aN^{3}LO PDFs, another prominent feature one can notice in Table 12.1 is an increase in PDF uncertainties. We find that the PDF uncertainty without N^{3}LO theory uncertainties included (i.e. using only the eigenvector description from the first 32 eigenvectors and with N^{3}LO parameters fixed at the best fit) also includes a marginal increase in the positive direction compared to NNLO. Mathematically, the reason for this comes back to the fact that the best fit is inherently different from the NNLO theory, residing in a completely novel χ^2 landscape. In turn, this means it is not guaranteed that the PDF uncertainty

will remain consistent across the distinct PDF sets[3]. In the case of gluon fusion, the leading contribution to the positive uncertainty direction is an eigenvector primarily dominated by PDF parameters, while in the negative direction a N^{3}LO splitting function parameter dominates (eigenvector 9 and 31 in the $(H_{ij} + K_{ij})^{-1}$ N^{3}LO case – see Table 11.4). As discussed in Section 11.8, the gluon predominantly follows the splitting function contributions, therefore it is not surprising that this eigenvector is having a noticeable effect. Phenomenologically, the increase in predicted uncertainties from the inclusion of the theoretical uncertainties is a reflection of the estimated PDF MHOUs in this particular cross section and acts to replace factorisation scale variation. As a consistency check, we find that when performing a 9-point scale variation procedure with aN^{3}LO PDFs, the values calculated (for both choices of μ) are within the predicted PDF uncertainties. This is therefore a further verification of our MHOUs and that the μ_f variation is intrinsic in the PDF uncertainties.

Finally Fig. 12.1 also demonstrates the increased stability of predictions when considering the two different central scales μ at N^{3}LO. As predicted from perturbation theory, the scale dependence is reduced and central values become more in agreement when increasing the order of either the PDFs or hard cross section. Furthermore, the aN^{3}LO σ central predictions for both choices of μ are contained within the uncertainty bands of each other. This is true by definition for the NNLO PDFs since the factorisation scale μ_f variation includes both choices of μ, whereas for aN^{3}LO PDFs this result is not guaranteed and is therefore intrinsic in the PDF (and renormalisation scale μ_r variation) uncertainty.

[3] As we can see from Section 11.4, the theory uncertainty is also not guaranteed to add to the total uncertainty (and in fact acts to reduce the uncertainty in some areas of (x, Q^2)).

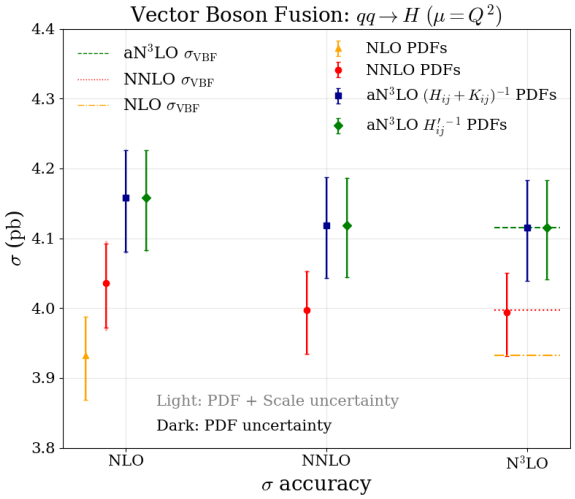

Figure 12.2.: Higgs production cross section results via vector boson fusion (with $\sqrt{s} = 13$ TeV) at a central scale set to the vector boson momentum. Displayed are the results for aN^{3}LO PDFs with decorrelated K-factors ($(H_{ij} + K_{ij})^{-1}$), correlated K-factors ($H'^{-1}_{ij} = (H_{ij} + K_{ij})^{-1}$) each with a scale variation band from varying μ_r by a factor of 2. In the NNLO and NLO PDF cases, both scales μ_f and μ_r are varied by a factor of 2 following the 9-point convention [9]. Note that the light bands are almost invisible in this plot due to the scale variations being extremely small.

12.2. Higgs Production – Vector Boson Fusion: $qq \to H$

Table 12.2 and Fig. 12.2 show the predictions at various orders in α_s for Higgs production cross sections via vector boson fusion[4] at the LHC for $\sqrt{s} = 13$ TeV up to N^{3}LO [214, 215]. The predictions shown are calculated with $\mu_f^2 = \mu_r^2 = Q^2$ as the central scale where Q^2 is the vector boson squared momentum.

For this process one can follow the increase in the cross section as higher order PDFs are used. Contrasting with the case of gluon fusion, Fig. 12.2 displays little cancellation between the terms added in the aN^{3}LO PDF description and the N^{3}LO cross section. However, the cross section for VBF produces around a $\sim 3-4\%$ change order by order

[4] Results are obtained with the inclusive part of the code proVBFH [214, 215, 217].

σ order	PDF order	$\sigma + \Delta\sigma_+ - \Delta\sigma_-$ (pb)	σ (pb) $+ \Delta\sigma_+ - \Delta\sigma_-$ (%)
PDF uncertainties			
N^{3}LO	aN^{3}LO (no theory unc.)	4.1378 + 0.0737 - 0.0926	4.1378 + 1.78% - 2.23%
	aN^{3}LO ($H_{ij} + K_{ij}$)	4.1378 + 0.0867 - 0.0869	4.1378 + 2.10% - 2.10%
	aN^{3}LO (H'_{ij})	4.1378 + 0.0829 - 0.0889	4.1378 + 2.00% - 2.15%
	NNLO	3.9941 + 0.0558 - 0.0631	3.9941 + 1.40% - 1.58%
NNLO	NNLO	3.9974 + 0.0557 - 0.0633	3.9974 + 1.39% - 1.58%
PDF + Scale uncertainties			
N^{3}LO	aN^{3}LO (no theory unc.)	4.1378 + 0.0737 - 0.0926	4.1378 + 1.78% - 2.23%
	aN^{3}LO ($H_{ij} + K_{ij}$)	4.1378 + 0.0867 - 0.0869	4.1378 + 2.10% - 2.10%
	aN^{3}LO (H'_{ij})	4.1378 + 0.0829 - 0.0889	4.1378 + 2.00% - 2.15%
	NNLO	3.9941 + 0.0560 - 0.0631	3.9941 + 1.40% - 1.58%
NNLO	NNLO	3.9974 + 0.0576 - 0.0642	3.9974 + 1.44% - 1.61%

Table 12.2.: Higgs production cross section results via the vector boson fusion process (with $\sqrt{s} = 13$ TeV) using N^{3}LO and NNLO hard cross sections combined with NNLO and aN^{3}LO PDFs. All PDFs are at the standard choice $\alpha_s(m_Z) = 0.118$. These results are found with $\mu = Q^2$ where Q^2 is the vector boson momentum.

σ order	PDF order	$\sigma + \Delta\sigma_+ - \Delta\sigma_-$ (pb)	σ (pb) $+ \Delta\sigma_+ - \Delta\sigma_-$ (%)
N^{3}LO	aN^{3}LO $n_f = 5$	4.1378 + 0.0867 - 0.0869	4.1378 + 2.10% - 2.10%
	aN^{3}LO $n_f = 4$	4.0510 + 0.0853 - 0.0859	4.0510 + 2.11% - 2.12%
	aN^{3}LO $n_f = 3$	2.7066 + 0.0610 - 0.0695	2.7066 + 2.26% - 2.57%
NNLO	NNLO $n_f = 5$	3.9974 + 0.0557 - 0.0633	3.9974 + 1.39% - 1.58%
	NNLO $n_f = 4$	3.9118 + 0.0561 - 0.0634	3.9118 + 1.44% - 1.62%
	NNLO $n_f = 3$	2.6845 + 0.0539 - 0.0641	2.6845 + 2.01% - 2.39%

Table 12.3.: Higgs production cross section results via the vector boson fusion process (with $\sqrt{s} = 13$ TeV) using N^{3}LO and NNLO hard cross sections combined with NNLO and decorrelated aN^{3}LO PDFs whilst varying the number of active flavours n_f. All PDFs are at the standard choice $\alpha_s(m_Z) = 0.118$. These results are found with $\mu = Q^2$ where Q^2 is the vector boson momentum.

and is therefore fairly constant. Considering this relatively small difference between orders, this lack of cancellation is not a major concern. Further to this, the vector boson fusion process is much more reliant on the quark sector which, compared to the gluon, is relatively constant order by order (see Section 11.4). The reason for this stems from the more direct data constraints on the shape of quark PDFs.

Comparing the aN^{3}LO VBF cross section (with MHO theoretical uncertainties) with the NNLO cross section result (with NNLO PDFs) including MHOUs via scale variations, we see that the scale variation MHOUs are negligible against the PDF uncertainties at aN^{3}LO. This result is in part due to the fact that the scale variation for aN^{3}LO is only being included for the renormalisation scale. However at NNLO, the extra MHOU predicted was still only a small contribution. Therefore considering these results further, the effects of higher orders in both cases are expected to be small, which provides some agreement with the argument that there is little scope for cancellation between orders for VBF. As for the gluon fusion prediction in Section 12.1, we confirm that any further factorisation scale variation (i.e. using the 9-point prescription) is contained within the predicted PDF uncertainties; hence further motivating our previous argument that factorisation scale variation is not necessary with aN^{3}LO PDFs.

Another feature of the VBF results is that the level of uncertainty at full aN^{3}LO is only increased slightly from the calculation involving NNLO PDFs. Comparing this to the gluon fusion results, where the uncertainty was more noticeably increased in both directions, it is evident that these approximate N^{3}LO additions are having a smaller effect on the VBF calculation. Once again, the origin of this is due to the nature of the process. VBF involves mostly the quark sector and is therefore much less affected by the extra N^{3}LO theory we have introduced (due to direct constraints from data). As

we have presented in previous sections, most of the uncertainty in the N^{3}LO theory resides in the small-x regime which is more directly probed by the gluon sector than in the quark sector.

Lastly we briefly discuss the n_f dependence of the VBF cross section. In VBF the scaling of contributions follows as n_f^2 due to the presence of two input quark flavours in the process. In Table 12.3 we observe that the VBF cross section receives a large contribution when including the charm quark ($n_f = 3 \to 4$) due to this scaling. We also show that at aN^{3}LO, this is where most of the difference in the central value and uncertainty from NNLO is accounted for. This is a consequence of the predicted enhancement of the charm PDF at aN^{3}LO, discussed in Section 11.4. Beyond $n_f = 4$ the bottom contribution to VBF in the $W^\pm$ channel (the dominant channel) is heavily suppressed, since due to the CKM elements b must transition to t most of the time. Therefore the VBF cross section only receives a small contribution moving from $n_f = 4$ to $n_f = 5$.

Chapter 13.

PDFs in the High-x Region

In the high-x region there is little data available to constrain PDFs at the time of writing. However, with the recent experimental results from the SeaQuest collaboration and the highly anticipated EIC on the horizon, this elusive region is becoming much more popular in particle phenomenology.

13.1. Negative $\bar{d}$ PDFs at low-Q^2

In this thesis, a set of aN^{3}LO PDFs has been presented whereby a global minimum is achieved with a slightly negative low-Q^2 $\bar{d}$ at high-x, as discussed in Chapter 11. Investigating this negative $\bar{d}$ mode further, it can also be shown that a negative $\bar{d}$ mode is also present at NNLO with a near degenerate global χ^2 compared to the standard MSHT20 NNLO set [3].

Dataset	N_{pts}	χ^2	$\Delta\chi^2$ from NNLO
BCDMS μp F_2 [72]	163	182.3	+3.5
BCDMS μd F_2 [72]	151	140.7	−5.8
E866 / NuSea pd/pp DY [104]	15	7.9	−1.8
NuTeV $\nu N \to \mu\mu X$ [114]	84	55.9	−3.3
HERA e^+p NC 920 GeV [120]	402	516.4	+4.3
LHCb 2015 W, Z [105, 106]	67	105.5	+5.7
DØ W asym. [119]	14	16.0	+4.4
Total	4369	5115.8	+2.1

Table 13.1.: A selection of χ^2 results comparing the two near degenerate NNLO minima with positive and negarive $\bar{d}$ PDFs.

Table 13.1 displays a selection of χ^2 changes between the two near degenerate NNLO minima. Of particular interest is the $\Delta\chi^2 = -1.8$ in the E866 DY ratio data [104] which prefers a negative high-x $\bar{d}$ PDF at low-Q^2. While this is a relatively small change in χ^2, it is a smaller number of data points which make up the main constraint for the high-x $\bar{d}$ description. Therefore it is this data which is driving the fit to find a minima with a negative high-x $\bar{d}$ at N^{3}LO and also at NNLO.

Fig. 13.1 presents the form of these NNLO PDFs at low-Q^2, clearly highlighting the areas in which these two degenerate fits differ. Towards small-x in all cases the two sets of PDFs are in agreement within uncertainties. However for the light sea quarks ($\bar{u}$, $\bar{d}$, $s + \bar{s}$), this agreement breaks down at high-x ($x > 0.2$). At this point one can observe that the fit has produced a near degenerate global minima with a reduction in the $\bar{d}$ PDF magnitude which is negative ($\sim -10^{-3}$) between $0.4 < x < 0.9$.

These results confirm that the negative $\bar{d}$ found in Chapter 11 at aN^{3}LO is not a direct feature of any N^{3}LO approximations and is in fact present at NNLO (although this was not found before). Having said this, it is true that extending our theoretical

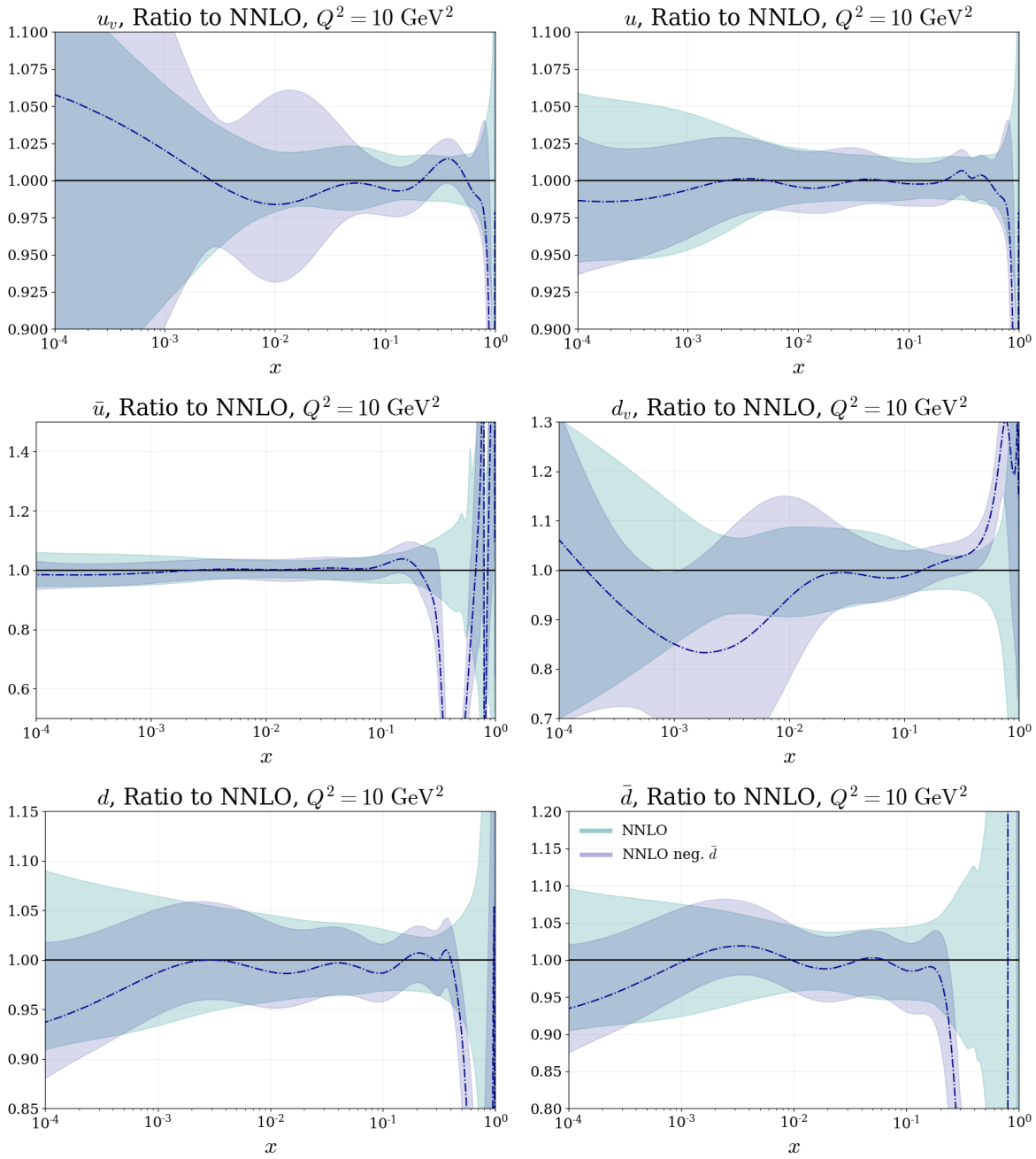

Figure 13.1.: Low-Q^2 ratio plots showing a NNLO negative $\bar{d}$ mode 68% confidence intervals, compared to the standard MSHT20 NNLO 68% confidence intervals. All plots are shown for $Q^2 = 10$ GeV^2 with the exception of the bottom quark shown for $Q^2 = 25$ GeV^2.

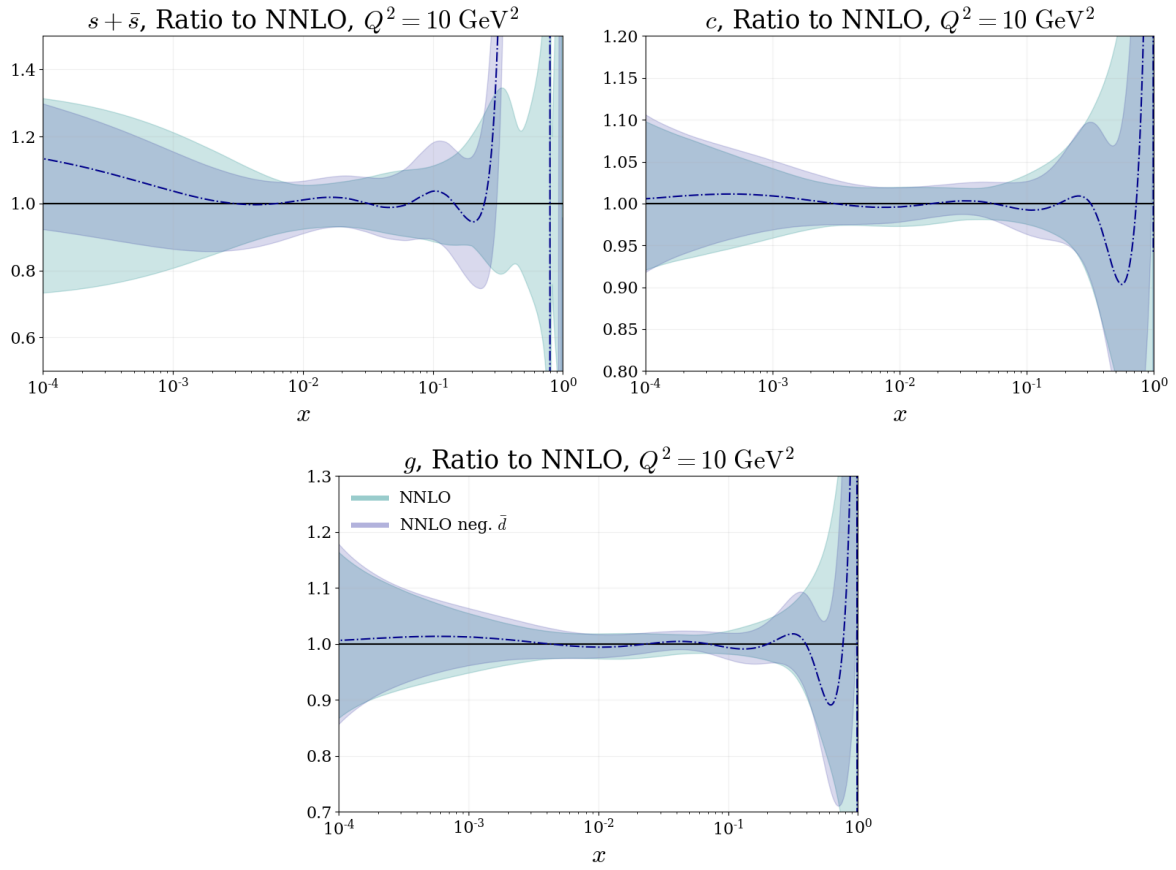

Figure 13.1.: *(Continued)* Low-Q^2 ratio plots showing a NNLO negative $\bar{d}$ mode 68% confidence intervals, compared to the standard MSHT20 NNLO 68% confidence intervals. All plots are shown for $Q^2 = 10$ GeV^2 with the exception of the bottom quark shown for $Q^2 = 25$ GeV^2.

description to N^{3}LO results in a clear preference for a negative high-x $\bar{d}$ at low-Q^2. This is most likely due to the increased flexibility allowed at aN^{3}LO, which in turn allows the fit to better fit the high-x E866 which is known to prefer a negative $\bar{d}$ in this region. In the following section, we will investigate how this description changes with the inclusion of SeaQuest data.

Dataset	N_{pts}	χ^2	$\Delta\chi^2$ from NNLO (with SQ)	$\Delta\chi^2$ from aN^{3}LO (w/o SQ)
NMC $\mu n/\mu p$ [88]	148	136.3	$+1.9$	$+4.7$
E866 / NuSea pp DY [102]	184	219.7	-9.8	$+4.3$
E866 / NuSea pd/pp DY [104]	15	19.2	$+0.2$	$+10.8$
LHCb 2015 W, Z [105, 106]	67	99.2	$+1.2$	-4.0
CMS 7 TeV jets [118]	158	190.6	$+13.0$	$+3.8$
CMS 8 TeV jets [122]	174	267.7	$+6.1$	-3.6
SeaQuest [19]	6	8.2	$+0.1$	-
Total	4369	4994.5	-144.7	$+25.1(+8.2)$

Table 13.2.: Selective breakdown of χ^2 results from relevant datasets included in a global fit with SeaQuest data added. Note that the total from from aN^{3}LO includes an extra $\Delta\chi^2 = +8.2$ from the addition of SeaQuest data which must be taken into account when comparing the two fits.

13.2. Inclusion of SeaQuest Data

As discussed in Chapter 11 and in the previous section, it is hoped that the high-x SeaQuest data [19] can alleviate an issue found with the positivity of the high-x $\bar{d}$ PDF at low-Q^2. In particular, the SeaQuest data provides a higher ratio for the $(\bar{d}/\bar{u})$ around $x \sim 0.4$ than the previously included E866 ratio data.

Table 13.2 summarises the largest χ^2 changes from performing a fit at aN^{3}LO with SeaQuest data compared to a NNLO fit with SeaQuest data and the standard aN^{3}LO fit discussed in Chapter 11. Comparing with the previous aN^{3}LO results, one can observe that the fit quality unsurprisingly gets slightly worse due to the tension introduced between E866 data and the new SeaQuest data, an effect which is also seen at NNLO. However there are also some smaller indirect effects which result in a slightly better fit to the LHCb 2015 W, Z [105, 106] data along with a variety of other small effects across

multiple datasets, some of which are also shown in Table 13.2. Overall these small shifts cancel out globally and we find that the $\Delta\chi^2_{\text{global}} = +16.9$ (ignoring any extra χ^2 directly from the SeaQuest data) can be almost entirely attributed to the E866 data.

Fig. 13.2 displays the effect of SeaQuest data on the form of the NNLO and aN^{3}LO PDFs as a ratio to the standard MSHT20 NNLO PDF set. For both the NNLO and aN^{3}LO PDF sets, the effect of adding SeaQuest data has a similar effect on the high-x light quarks. For example, the high-x $\bar{d}$ PDF shows a substantial increase in both NNLO and aN^{3}LO fits when including SeaQuest data. Accompanying this effect is also a decrease in the $\bar{u}$ and sea strangeness at high-x, in order to preserve momentum conservation.

As expected, the gluon remains very similar with the addition of the SeaQuest data at both NNLO and aN^{3}LO. As a result of this, since the heavy quarks are directly coupled to the gluon, the heavy quarks are also unaffected by the extra SeaQuest data.

Fig. 13.3 (top left) displays the $(\bar{d}/\bar{u})$ ratio at NNLO and aN^{3}LO and the direct effect of SeaQuest data on this ratio. One can observe that the aN^{3}LO ratio is completely reversed from the PDFs presented in Chapter 11 to be very similar to the NNLO result with SeaQuest data added in. Fig. 13.3 also illustrates a reduction in the uncertainties in this ratio at aN^{3}LO where these uncertainties are comparable to those found at NNLO with SeaQuest. Along with the χ^2 results shown in Table 13.2, this result therefore confirms that both aN^{3}LO and NNLO PDF sets are able to fit SeaQuest data similarly well.

To further accompany the results above, and display where the main differences lie at aN^{3}LO are, Fig. 13.3 also shows the new aN^{3}LO set (with SeaQuest) as a ratio of the set presented in Chapter 11. The main differences clearly lie in the aN^{3}LO $\bar{u}, \bar{d}$

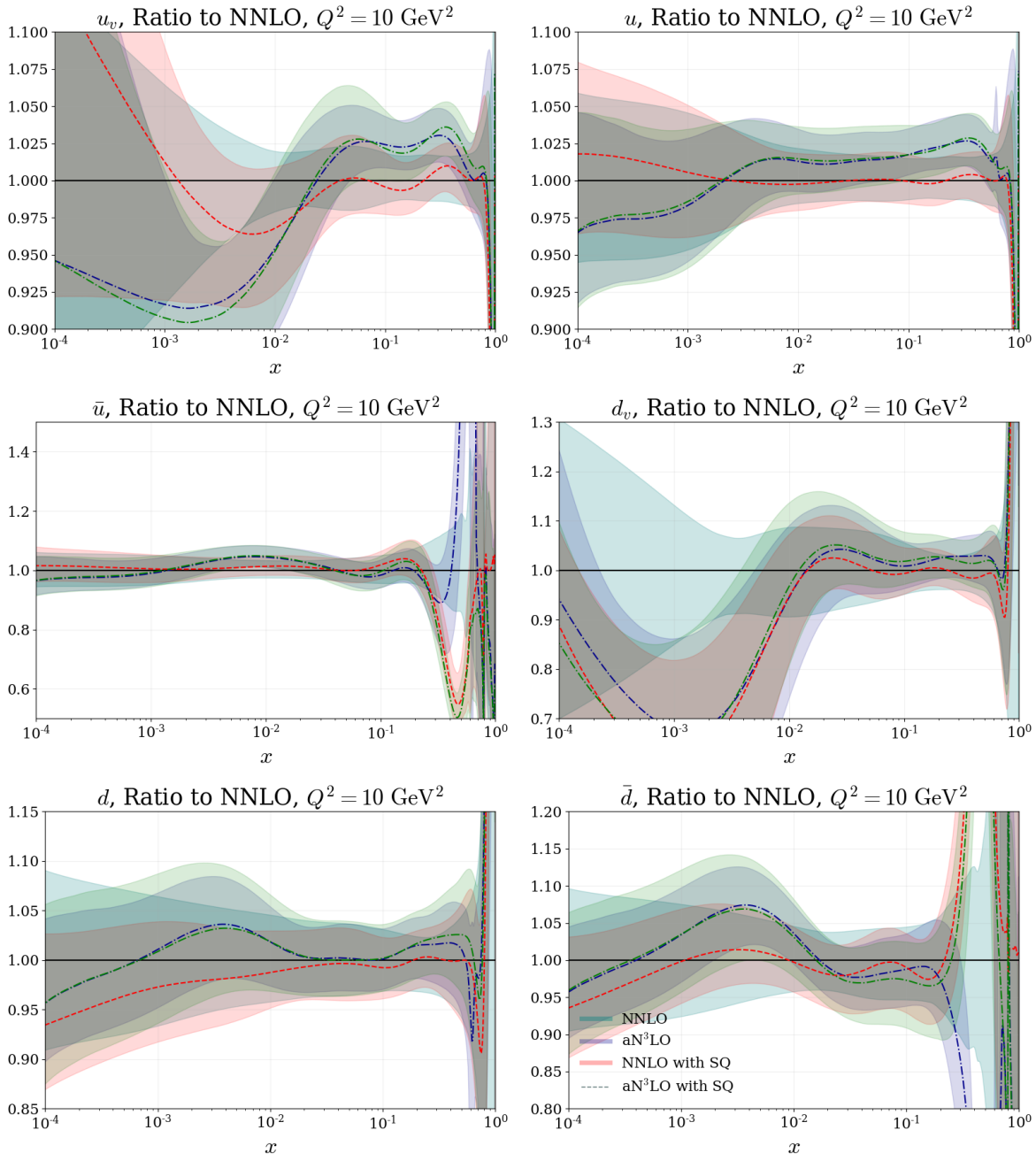

Figure 13.2.: Low-Q^2 ratio plots showing the 68% confidence intervals for aN^{3}LO and NNLO PDFs with and without SeaQuest data included in a fit, compared to the standard MSHT20 NNLO 68% confidence intervals (i.e. without SeaQuest data). All plots are shown for $Q^2 = 10$ GeV^2 with the exception of the bottom quark shown for $Q^2 = 25$ GeV^2.

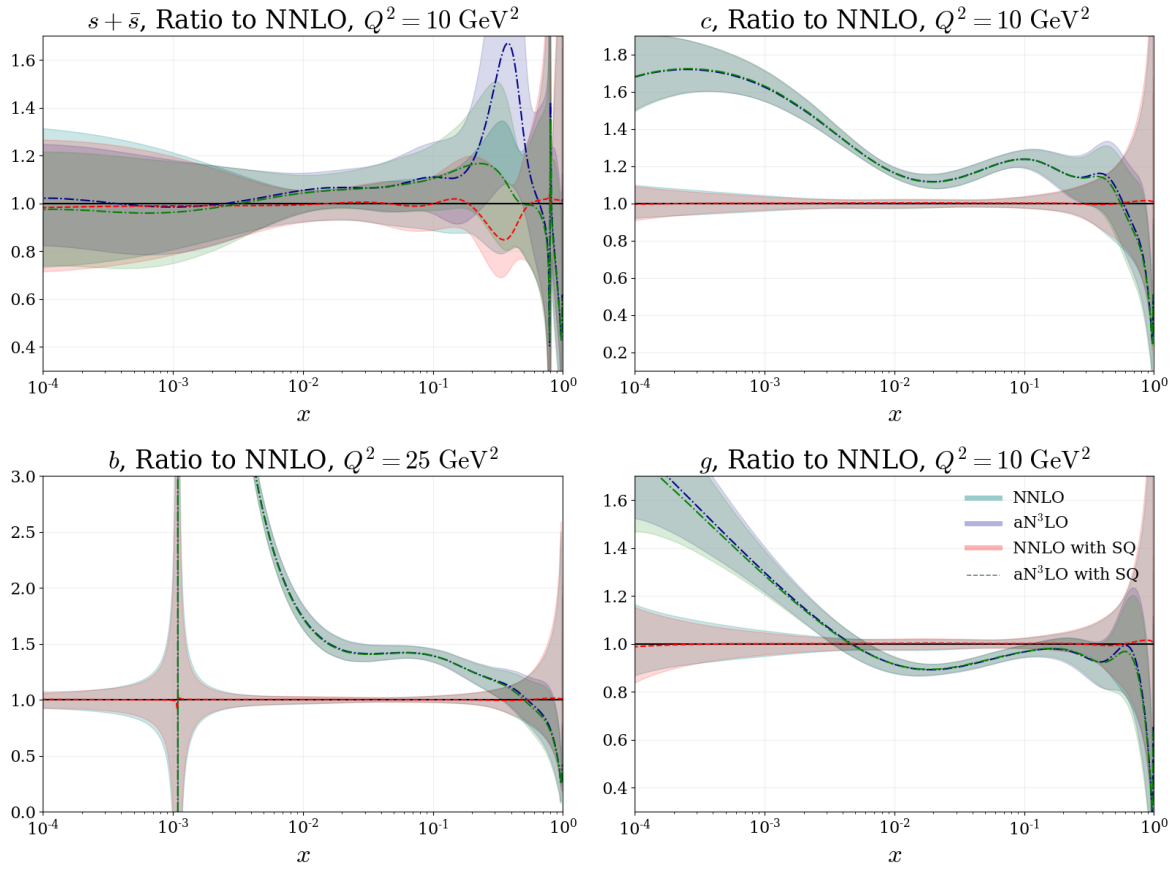

Figure 13.2.: *(Continued)* Low-Q^2 ratio plots showing the 68% confidence intervals for aN^{3}LO and NNLO PDFs with and without SeaQuest data included in a fit, compared to the standard MSHT20 NNLO 68% confidence intervals (i.e. without SeaQuest data). All plots are shown for $Q^2 = 10$ GeV^2 with the exception of the bottom quark shown for $Q^2 = 25$ GeV^2.

and strange PDFs at in Fig. 13.3. However, these plots also show the orthogonality between the small and high-x behaviour with virtually all changes in the PDFs being focused almost entirely in the high-x region.

13.3. Inclusion of Dijet Data

Including data with dijets in the final state is beneficial as this data is sensitive to some of the highest mass scales accessible at the LHC. Also the increased tension observed

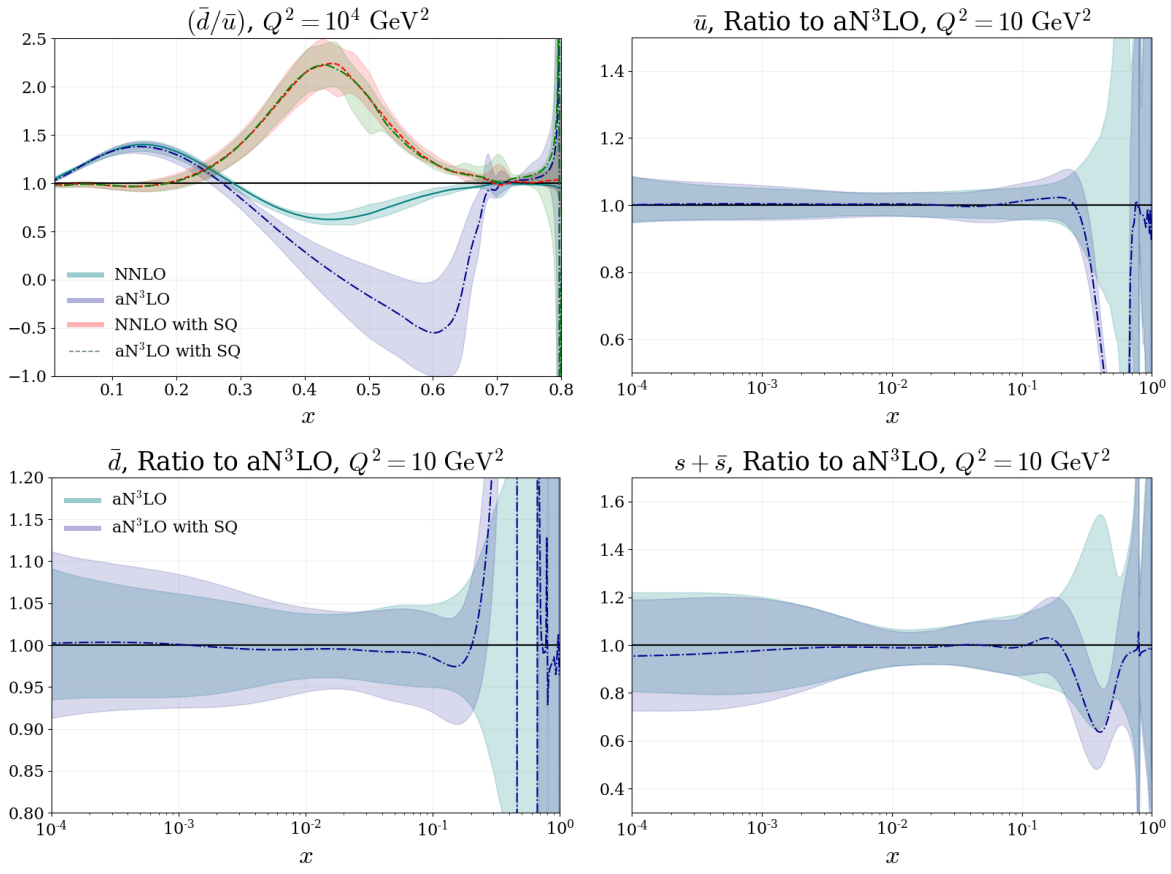

Figure 13.3.: Comparison of NNLO and aN^{3}LO PDFs fitted with and without SeaQuest data. The $(\bar{d}/\bar{u})$ ratios (top left) are shown for NNLO and aN^{3}LO PDFs with and without SeaQuest data added into the global fit. Low-Q^2 ($Q^2 = 10$ GeV^2) ratio plots (top right and bottom) also display the main differences between aN^{3}LO 68% confidence intervals found with SeaQuest compared to aN^{3}LO 68% confidence intervals found without SeaQuest data.

	N_{pts}	NNLO		aN^{3}LO	
		χ^2/N_{pts}	χ^2	χ^2/N_{pts}	χ^2
ATLAS 7 TeV jets [113]	140	1.58	221.2	1.54	215.6
CMS 7 TeV jets [118]	158	1.11	175.4	1.18	186.4
CMS 8 TeV jets [122]	174	1.50	261.0	1.56	271.4
Total (jets)	472	1.39	656.1	1.43	675.0
Total	4363	1.17	5121.3	1.14	4961.2

	N_{pts}	NNLO		aN^{3}LO	
		χ^2/N_{pts}	χ^2	χ^2/N_{pts}	χ^2
ATLAS 7 TeV dijets [218]	90	1.05	94.5	1.12	100.8
CMS 7 TeV dijets [219]	54	1.43	77.2	1.39	75.1
CMS 8 TeV dijets [220]	122	1.04	126.9	0.83	101.3
Total (dijets)	266	1.12	297.9	1.04	276.7
Total	4157	1.14	4756.0	1.10	4555.6

Table 13.3.: Breakdown of χ^2 results from jets (top) and dijets (bottom) datasets included in a global fit for NNLO and aN^{3}LO PDFs. χ^2 results are shown per data point (χ^2/N_{pts}) to provide a fair comparison across datasets with a varying number of points.

in a global fit with single inclusive jets final states (which was shown to be even more apparent at aN^{3}LO than at NNLO) provides an extra motivation to consider dijet final states as opposed to single inclusive jets.[1]

Table 13.3 compares the χ^2 results from global fits with single inclusive jet (left) and with dijet final states (right). Comparing across the two orders, it is apparent that including aN^{3}LO theory disfavours jet data overall compared to NNLO, whereas for dijets there is a preference for aN^{3}LO theory from NNLO.

Considering the overall fit quality of both final states, it is clear to see that both the NNLO and aN^{3}LO fits prefer a dijet description of the $7+8$ TeV ATLAS and CMS data. Overall the aN^{3}LO description with dijets produces not only the best fit quality for this data but also a manages to fit the rest of the data very slightly better ($\Delta\chi^2 \sim -10$) than the results presented in Chapter 11.

[1] or *as well as*, if correlations can be made available in the future.

Considering the total difference in the global aN^{3}LO χ^2, Table 13.3 displays a reduction of $\Delta\chi^2 = -200.4$ in the dijet description from NNLO. This reduction is ~ 40 better than the reduction seen for a fit including jet data, therefore providing further evidence for an overall preference towards a dijet description.

The form of NNLO and aN^{3}LO PDFs with dijets is compared and contrasted with PDFs produced with single inclusive jet data also at NNLO and aN^{3}LO. In both cases, the switch from jets to dijets produces similar PDF results, with any more substantial changes restricted to the high-x gluon. There are also very small changes in the sea quarks such as a reduction at very high-x for the NNLO $\bar{d}$ and $\bar{u}$. However at aN^{3}LO, this reduction was already apparent with single inclusive jets, therefore these PDFs are more similar in these regions than at NNLO.

Fig. 13.5 provides a more in-depth comparison of the high-x gluon behaviour with jets or dijets. It can be observed that the effect of including $7+8$ TeV dijet data allows for a softer gluon at very high-x ($x > 0.5$) at NNLO, with a slightly harder gluon predicted between $0.1 < x < 0.5$. At aN^{3}LO this very high-x reduction is seen when considering jets to some level, however is also slightly more significant when switching to dijet data. A noteable difference between the two orders is the differences in the gluon between $0.1 < x < 0.5$, where the aN^{3}LO description is allowing for a softer central prediction throughout this entire region with dijets compared to NNLO. It can also be seen that below around $x \sim 0.1$, the gluon PDF becomes almost identical for the case of fitting jets or dijets in both NNLO and aN^{3}LO cases.

Inspecting Fig. 13.4 once more, one can observe the parallels between the heavy quark predictions and those discussed for the gluon. In particular, the charm and bottom PDFs tend to follow the general trend discussed for the high-x gluon due to the direct coupling between these partons.

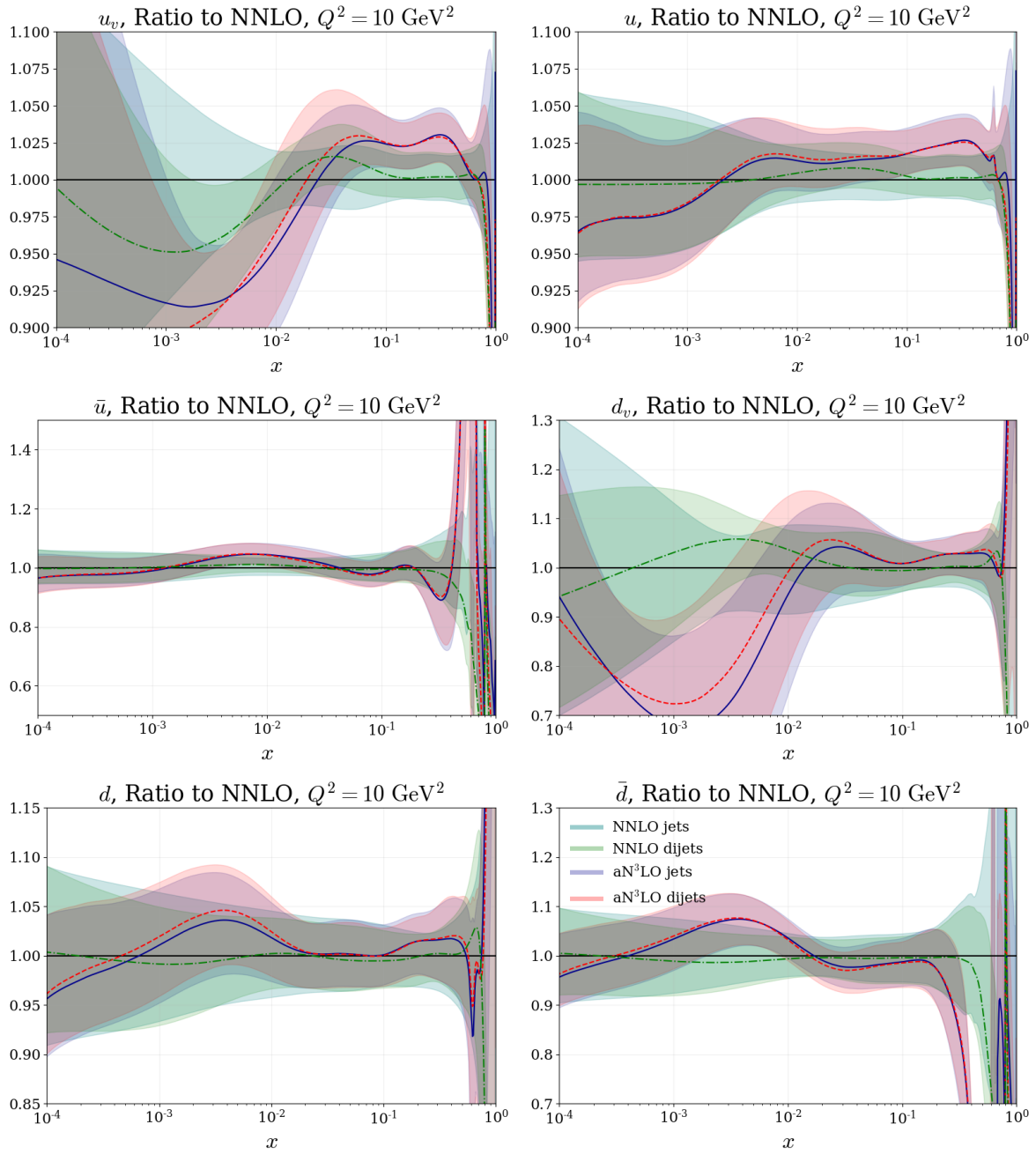

Figure 13.4.: Low-Q^2 ratio plots showing the NNLO and aN^{3}LO 68% confidence intervals with $7 + 8$ TeV jets or $7 + 8$ TeV dijets included in a gloabl fit, compared to the standard MSHT20 NNLO ($7 + 8$ TeV jets) 68% confidence intervals. All plots are shown for $Q^2 = 10\,\text{GeV}^2$ with the exception of the bottom quark shown for $Q^2 = 25\,\text{GeV}^2$.

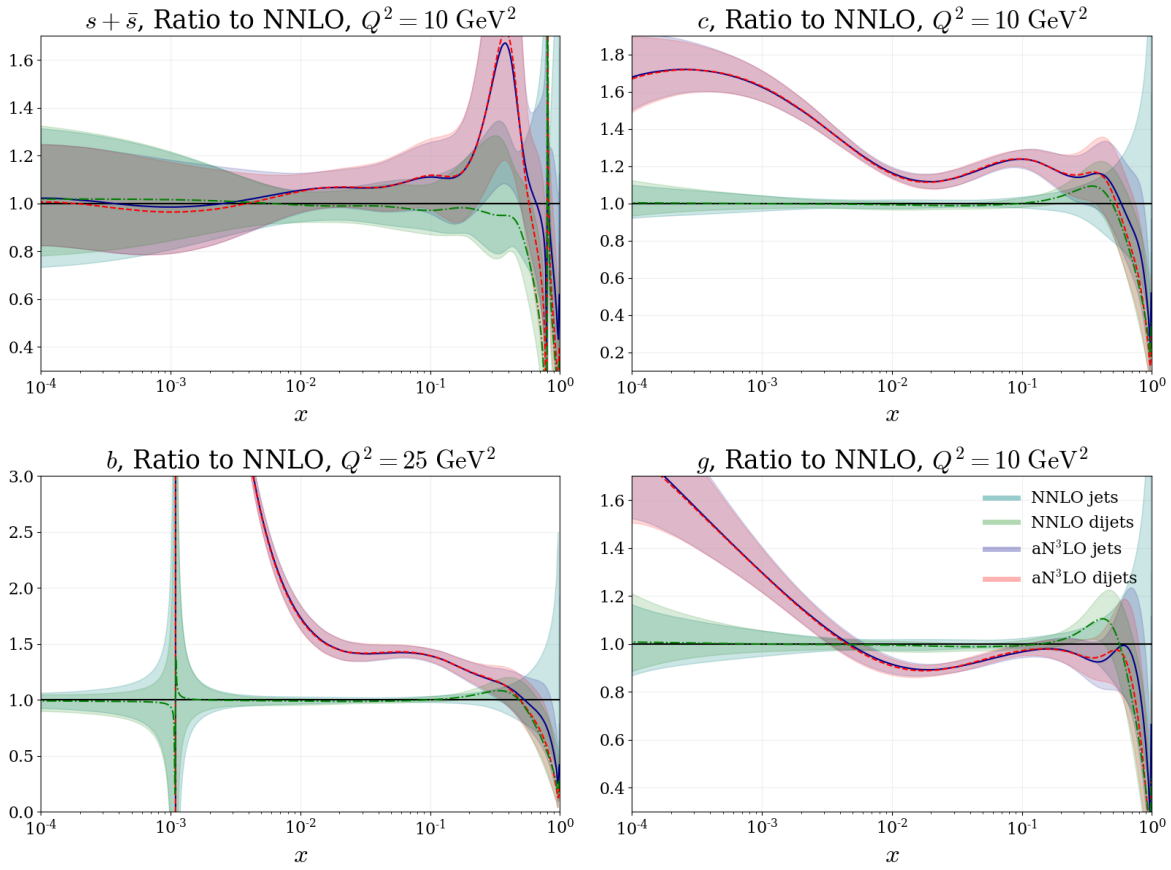

Figure 13.4.: *(Continued)* Low-Q^2 ratio plots showing the NNLO and aN^{3}LO 68% confidence intervals with $7+8$ TeV jets or $7+8$ TeV dijets included in a gloabl fit, compared to the standard MSHT20 NNLO ($7+8$ TeV jets) 68% confidence intervals. All plots are shown for $Q^2 = 10$ GeV^2 with the exception of the bottom quark shown for $Q^2 = 25$ GeV^2.

13.4. Combined Fit with Dijets and SeaQuest Data

In this section, the previous two sections will be combined to show the combined effects of fitting to $7+8$ TeV dijet final states alongside the added SeaQuest data.

Table 13.4 summarises the χ^2 results from a global fit including dijet and SeaQuest data. These results show a similar fit quality across all common datasets to the original

Dataset	N_{pts}	χ^2	$\Delta\chi^2$ from NNLO	$\Delta\chi^2$ from N^{3}LO
BCDMS μp F_2 [72]	163	172.5	−7.7	−1.9
BCDMS μd F_2 [72]	151	150.2	+4.2	+5.9
NMC μp F_2 [75]	123	121.9	−2.2	+0.4
NMC μd F_2 [75]	123	105.4	−7.3	+1.2
SLAC ep F_2 [78,79]	37	32.0	+0.0	+0.5
SLAC ed F_2 [78,79]	38	22.5	−0.5	−0.3
E665 μd F_2 [82]	53	63.8	+4.1	−0.1
E665 μp F_2 [82]	53	67.5	+2.8	−0.1
NuTeV νN F_2 [85]	53	34.7	−3.6	−1.0
NuTeV νN xF_3 [85]	42	36.1	+5.5	+1.3
NMC $\mu n/\mu p$ [88]	148	136.4	+5.6	+4.8
E866 / NuSea pp DY [102]	184	219.9	−5.2	+4.5
E866 / NuSea pd/pp DY [104]	15	19.2	+8.8	+10.8
HERA ep F_2^{charm} [107]	79	145.6	+13.3	+2.0
NMC/BCDMS/SLAC/HERA F_L [72,75,79,110–112]	57	45.5	−23.0	−0.2
CCFR $\nu N \to \mu\mu X$ [114]	86	68.1	+0.3	−0.2
NuTeV $\nu N \to \mu\mu X$ [114]	84	59.0	+0.5	+2.3
CHORUS νN F_2 [117]	42	29.9	−0.3	+0.7
CHORUS νN xF_3 [117]	28	18.2	−0.2	+0.1
HERA e^+p CC [120]	39	50.2	−1.8	+0.5
HERA e^-p CC [120]	42	64.7	−5.5	−0.2
HERA e^+p NC 820 GeV [120]	75	84.8	−5.1	+0.5
HERA e^-p NC 460 GeV [120]	209	247.4	−0.9	−0.4
HERA e^+p NC 920 GeV [120]	402	474.0	−38.7	−0.1
HERA e^-p NC 575 GeV [120]	259	248.5	−14.5	+0.0
HERA e^-p NC 920 GeV [120]	159	242.6	−1.8	−0.4
CDF II $p\bar{p}$ incl. jets [128]	76	62.6	+2.2	−3.9
DØ II Z rap. [130]	28	17.1	+0.8	−0.3
CDF II Z rap. [132]	28	38.4	+1.2	−2.2
DØ II $W \to \nu\mu$ asym. [134]	10	15.6	−1.7	−0.9
CDF II W asym. [73]	13	19.0	+0.0	+0.8

Table 13.4.: Full breakdown of χ^2 results for the aN^{3}LO PDF fit. The global fit includes the N^{3}LO treatment for transition matrix elements, coefficient functions, splitting functions and K-factor additions with their variational parameters determined by the fit.

Dataset	N_{pts}	χ^2	$\Delta\chi^2$ from NNLO	$\Delta\chi^2$ from N^{3}LO
DØ II $W \to \nu e$ asym. [74]	12	31.2	-2.7	$+0.5$
DØ II $p\bar{p}$ incl. jets [76]	110	113.9	-6.3	$+0.6$
ATLAS W^+, W^-, Z [77]	30	30.0	$+0.0$	$+0.0$
CMS W asym. $p_T > 35$ GeV [80]	11	6.7	-1.2	-0.1
CMS W asym. $p_T > 25, 30$ GeV [81]	24	7.8	$+0.4$	-0.1
LHCb $Z \to e^+e^-$ [83]	9	22.6	-0.2	-0.7
LHCb W asym. $p_T > 20$ GeV [84]	10	12.6	$+0.1$	$+0.0$
CMS $Z \to e^+e^-$ [86]	35	17.8	-0.2	$+0.2$
ATLAS High-mass Drell-Yan [87]	13	18.2	-0.7	-0.1
Tevatron, ATLAS, CMS $\sigma_{t\bar{t}}$ [89–101]	17	14.3	-0.3	$+0.0$
CMS double diff. Drell-Yan [103]	132	133.5	-10.9	$+0.4$
LHCb 2015 W, Z [105,106]	67	99.6	$+0.3$	-3.5
LHCb 8TeV $Z \to ee$ [108]	17	30.1	$+3.9$	-0.2
CMS 8 TeV W [109]	22	10.9	-1.8	-0.6
CMS 7 TeV $W + c$ [115]	10	10.6	$+2.0$	-0.2
ATLAS 7 TeV high prec. W, Z [116]	61	117.5	$+0.9$	-1.7
DØ W asym. [119]	14	13.7	$+1.7$	$+1.5$
ATLAS 8 TeV Z p_T [121]	104	107.6	-80.9	-0.9
ATLAS 8 TeV sing. diff. $t\bar{t}$ [123]	25	24.1	-1.5	-0.1
ATLAS 8 TeV sing. diff. $t\bar{t}$ dilep. [124]	5	2.2	-1.2	-0.5
ATLAS 8 TeV High-mass DY [125]	48	62.0	$+4.9$	-0.8
ATLAS 8 TeV W + jets [126]	30	18.7	$+0.6$	-0.1
CMS 8 TeV double diff. $t\bar{t}$ [127]	15	23.6	$+1.1$	$+0.1$
ATLAS 8 TeV W [129]	22	53.2	-4.2	$+0.2$
CMS 2.76 TeV jet [131]	81	107.1	$+4.2$	-2.7
CMS 8 TeV sing. diff. $t\bar{t}$ [133]	9	9.3	-3.9	-1.0
ATLAS 8 TeV double diff. Z [135]	59	81.1	-4.5	$+0.6$
Total	3891	4302.0	-161.7	$+14.8$
ATLAS 7 TeV dijets [218]	90	100.9	-	-
CMS 7 TeV dijets [219]	54	75.5	-	-
CMS 8 TeV dijets [220]	122	100.4	-	-
SeaQuest [19]	6	8.0	-	-

Table 13.4.: *(Continued)* Full breakdown of χ^2 results for the aN^{3}LO PDF fit. The global fit includes the N^{3}LO treatment for transition matrix elements, coefficient functions, splitting functions and K-factor additions with their variational parameters determined by the fit.

Low-Q^2 Coefficient			
$c_q^{\mathrm{NLL}} = -3.802$	0.010	$c_g^{\mathrm{NLL}} = -5.810$	0.819
Transition Matrix Elements			
$a_{Hg} = 12326.000$	0.652	$a_{qq,H}^{\mathrm{NS}} = -64.682$	0.002
$a_{gg,H} = -1893.200$	0.698		
Splitting Functions			
$\rho_{qq}^{NS} = 0.006$	0.007	$\rho_{gq} = -1.777$	0.713
$\rho_{qq}^{PS} = -0.484$	0.147	$\rho_{gg} = 18.685$	3.017
$\rho_{qg} = -1.797$	0.030		
K-factors			
$\mathrm{DY}_{\mathrm{NLO}} = -0.273$	0.074	$\mathrm{DY}_{\mathrm{NNLO}} = -0.142$	0.020
$\mathrm{Top}_{\mathrm{NLO}} = 0.002$	0.000	$\mathrm{Top}_{\mathrm{NNLO}} = 0.652$	0.425
$\mathrm{Jet}_{\mathrm{NLO}} = 0.567$	0.322	$\mathrm{Jet}_{\mathrm{NNLO}} = -0.757$	0.573
$p_T\mathrm{Jets}_{\mathrm{NLO}} = 0.556$	0.310	$p_T\mathrm{Jets}_{\mathrm{NNLO}} = -0.071$	0.005
$\mathrm{Dimuon}_{\mathrm{NLO}} = -0.458$	0.210	$\mathrm{Dimuon}_{\mathrm{NNLO}} = 0.865$	0.748
$\mathrm{Dijet}_{\mathrm{NLO}} = 0.449$	0.202	$\mathrm{Dijet}_{\mathrm{NNLO}} = -0.127$	0.016
$\mathrm{N^3LO}$ Penalty Total	9.000 / 22	Average Penalty	0.409
		Total	4586.8 / 4163

Table 13.4.: *(Continued)* Full breakdown of χ^2 results for the $\mathrm{aN^3LO}$ PDF fit. The global fit includes the $\mathrm{N^3LO}$ treatment for transition matrix elements, coefficient functions, splitting functions and K-factor additions with their variational parameters determined by the fit.

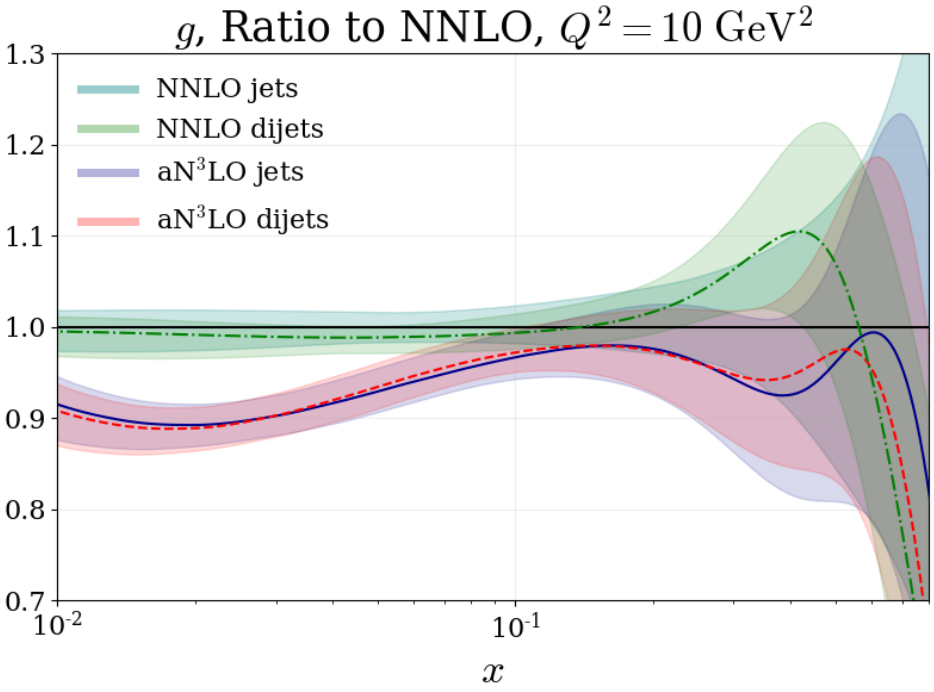

Figure 13.5.: Effect of including a dijet description for $7+8$ TeV LHC data in a global fit on the high-x gluon at NNLO and aN^{3}LO.

aN^{3}LO fit (with single inclusive jets) reported in Chapter 11. Inspecting these results in more detail, the main differences from a single inclusive jet fit at aN^{3}LO is the worsening fit quality to E866 data as a result of the tension between these data and the included SeaQuest data. Note that a similar increase can be seen at NNLO for the E866 / NuSea pd/pp DY [104] data, confirming this is a tension effect and not a result of any N^{3}LO theory. The overall fit quality per data point is also reduced to $\chi^2/N_{\text{pts}} = 1.102$ from $\chi^2/N_{\text{pts}} = 1.140$ ($\chi^2/N_{\text{pts}} = 1.136$) for the single inclusive jet case with (without) SeaQuest included and from $\chi^2/N_{\text{pts}} = 1.149$ for a NNLO fit to dijet and SeaQuest data.

In terms of the aN^{3}LO theory, we find a very similar set of parameters and therefore penalties as those found in Chapter 11. Note that Table 13.4 also includes the aN^{3}LO

K-factor parameters used in the same way as described in Chapter 10 to provide a rough approximation for the N^{3}LO dijet hard cross sections.

Fig. 13.6 illustrates the combined effects of including dijets and SeaQuest data in a global fit at NNLO and aN^{3}LO. It can be observed that the two effects are virtually orthogonal, with the high-x gluon seemingly being sensitive only to the dijets and displaying very similar effects to those seen in Fig. 13.4. Similarly, the effects from Sect. 13.2 are also present in Fig. 13.6 and are seemingly unaffected by the inclusion of dijets.

From these results, we can therefore conclude that at both NNLO and aN^{3}LO, the PDFs are able to fit both SeaQuest and dijet data well, with no indirect effects or tensions between these high-x datasets. On top of this, a better overall fit quality per data point can be achieved while also pushing the PDFs to be positive without directly demanding positivity.

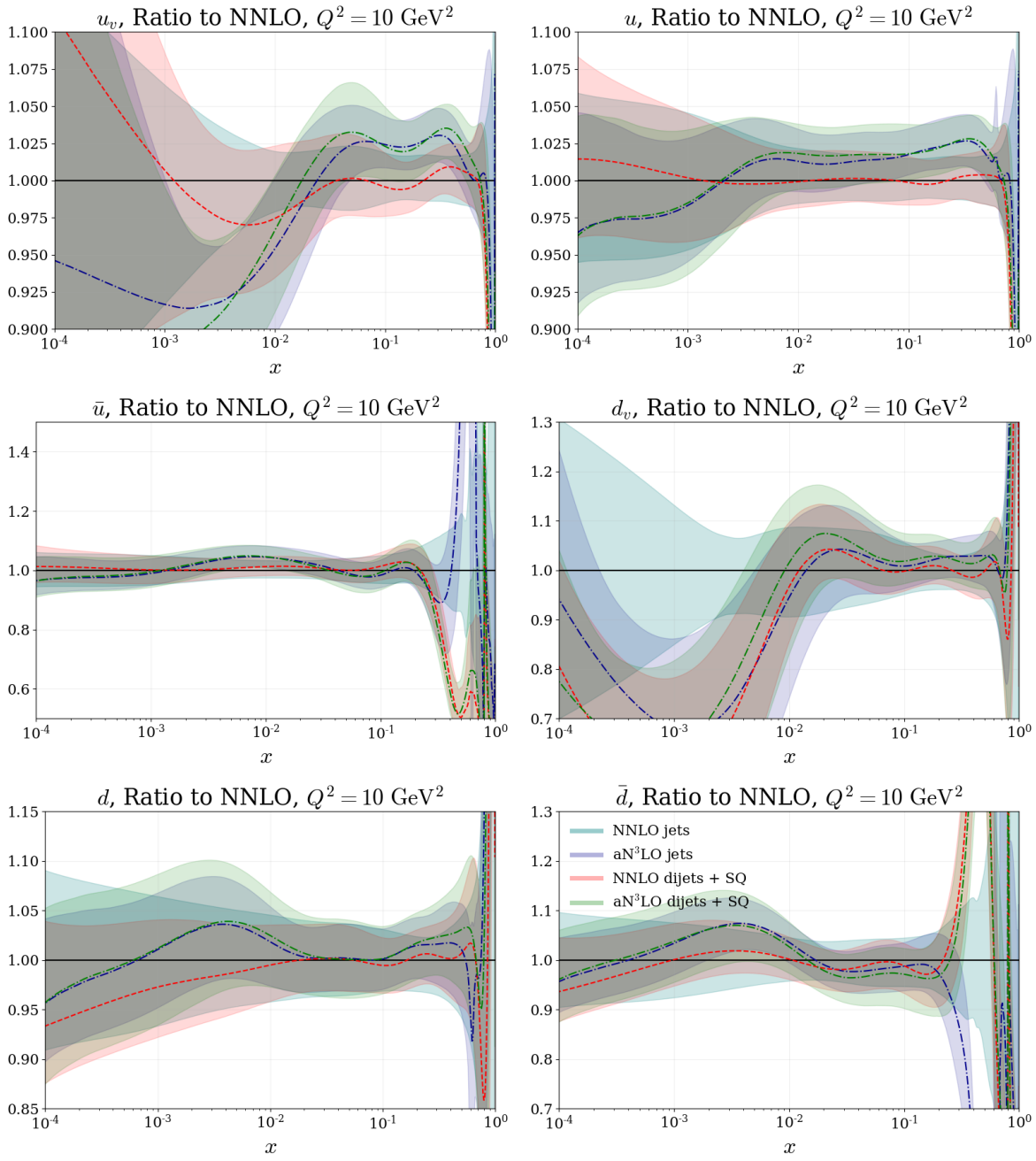

Figure 13.6.: Low-Q^2 ratio plots showing the NNLO and aN^{3}LO 68% confidence intervals with $7 + 8$ TeV jets or $7 + 8$ TeV dijets + SeaQuest data included in a global fit, compared to the standard MSHT20 NNLO ($7 + 8$ TeV jets) 68% confidence intervals. All plots are shown for $Q^2 = 10\,\text{GeV}^2$ with the exception of the bottom quark shown for $Q^2 = 25\,\text{GeV}^2$.

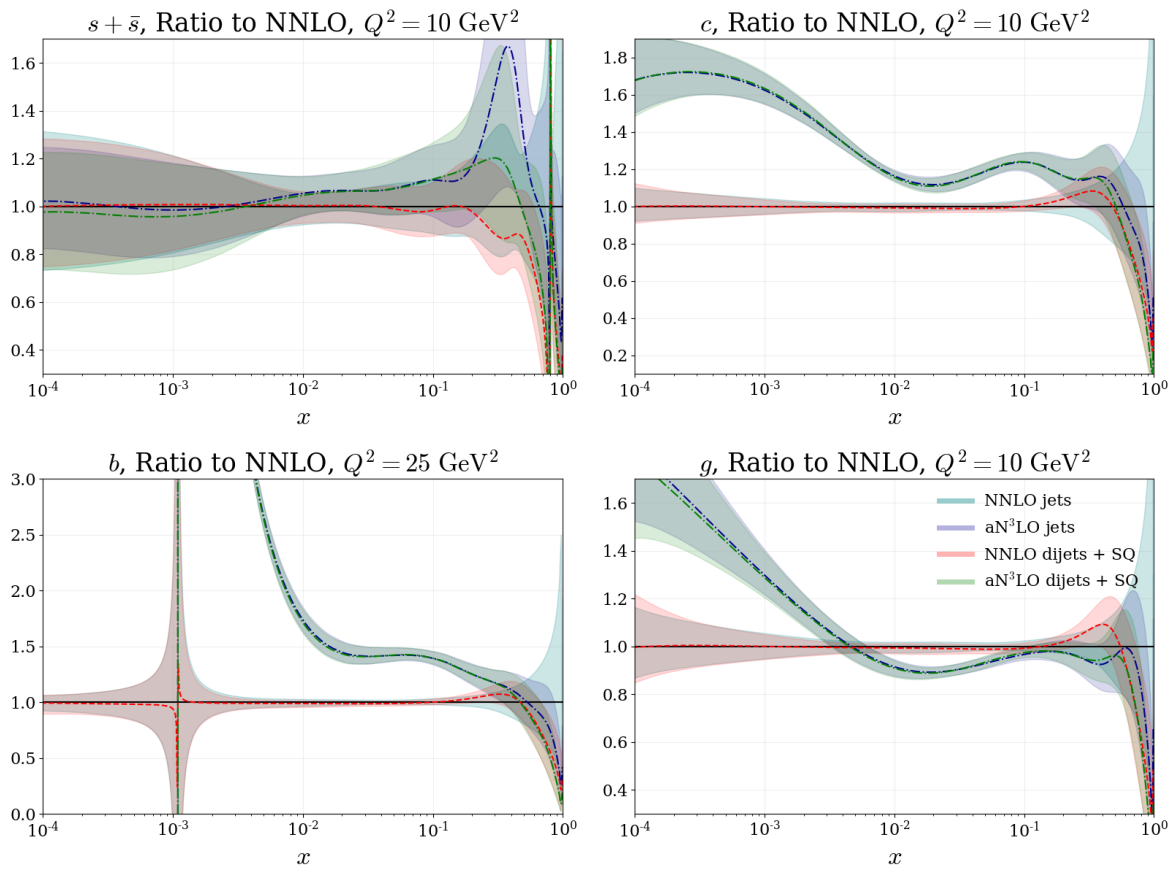

Figure 13.6.: *(Continued)* Low-Q^2 ratio plots showing the NNLO and aN^{3}LO 68% confidence intervals with $7 + 8$ TeV jets or $7 + 8$ TeV dijets + SeaQuest data included in a global fit, compared to the standard MSHT20 NNLO ($7 + 8$ TeV jets) 68% confidence intervals. All plots are shown for $Q^2 = 10$ GeV^2 with the exception of the bottom quark shown for $Q^2 = 25$ GeV^2.

Chapter 14.

Availability and Recommended Usage of MSHT20 aN^{3}LO PDFs

We provide the MSHT20 aN^{3}LO PDFs in LHAPDF format [221]:

http://lhapdf.hepforge.org/

as well as on the repository:

http://www.hep.ucl.ac.uk/msht/

The approximate N^{3}LO functions (for $P_{ij}(x)$ and $A_{ij}(x)$) are provided as lightweight FORTRAN functions or as part of a Python framework in the repository:

https://github.com/MSHTPDF/N3LO_additions

We present the aN^{3}LO eigenvector sets with and without correlated K-factors as discussed in Chapter 11, with the default set being provided with decorrelated K-factors.

MSHT20an3lo_as118

MSHT20an3lo_as118_Kcorr

Both these PDF sets contain a central PDF accompanied by 104 eigenvector directions (describing 52 eigenvectors) and can be used in exactly the same way as previous MSHT PDF sets i.e. the MSHT20 NNLO PDFs with 64 eigenvector directions.

Further to this, the aN^{3}LO eigenvector sets discussed in Chapter 13 for global fits including $7 + 8$ TeV dijet final states and/or SeaQuest data will be made available in a future publication (these will be added to both the web pages listed above). The PDF sets fitted to dijet final states will contain a central PDF accompanied by 108 eigenvector directions (describing 54 eigenvectors) and can be used in exactly the same way as previous MSHT PDF sets i.e. the MSHT20 NNLO PDFs with 64 eigenvector directions. Note the extra eigenvector directions correspond to the extra K-factors introduced in the aN^{3}LO theory.

As presented in this work, the aN^{3}LO PDFs include an estimation for MHOUs (the leading theoretical uncertainty) within their PDF uncertainties. Due to this, we argue and motivate in Chapter 12 that factorisation scale variations are no longer necessary in calculations involving aN^{3}LO PDFs. However the renormalisation scale should continue to be varied to provide estimates of MHOUs in the hard cross section piece of physical calculations.

In the case that the hard cross section for a process is available up to N^{3}LO the recommendation is to use the aN^{3}LO PDFs, since unmatched ingredients in cross section calculations can ignore important cancellations (between the PDFs and hard cross section).

If a process is included within the global fit and the hard cross section is known only up to NNLO (i.e. those discussed in Chapter 10), we recommend the use of the decorrelated version of the aN^{3}LO PDF set. Using these PDFs and the details provided in Table 11.3, the hard cross section can be transformed from NNLO to approximate N^{3}LO. From here the two approximate N^{3}LO ingredients can be used together to give a full approximate N^{3}LO result.

If a process is not included in the global PDF fit and the hard cross section is known only up to NNLO, the standard NNLO PDF set remains the default choice. However, we recommend the use of these aN^{3}LO PDFs as an estimate of potential MHOUs. In this case the aN^{3}LO PDF set + NNLO hard cross section prediction should be reflected in any MHOU estimates for the full NNLO prediction. For example, when the hard cross section is known only up to NNLO Equation (3.13) from [203] can be adapted to be,

$$\delta(\text{PDF}-\text{TH}) = \frac{1}{2}\left|\frac{\sigma^{(2)}_{\text{aN}^3\text{LO}} - \sigma^{(2)}_{\text{NNLO}}}{\sigma^{(2)}_{\text{aN}^3\text{LO}}}\right| \tag{14.1}$$

where $\delta(\text{PDF}-\text{TH})$ is the predicted PDF theory uncertainty on the σ prediction, $\sigma^{(2)}_{\text{aN}^3\text{LO}}$ is the NNLO hard cross section with aN^{3}LO PDFs and $\sigma^{(2)}_{\text{NNLO}}$ is the full NNLO result. A caveat to this treatment is that the theory uncertainty is sensitive to unmatched cancellations and should therefore be used with care (and caution), therefore the NNLO set remains the default in evaluating PDF uncertainties.

Chapter 15.

Conclusion

This thesis has presented the first approximate N^{3}LO global PDF fit. This has been achieved by following the MSHT20 framework [3], where the aN^{3}LO PDF set also incorporates estimates for theoretical uncertainties from MHOs. In addition, the framework presented for obtaining these PDFs provides a means of utilising higher order information as and when it is available. In contrast, previously, complete information of the next order was required for theoretical calculations in PDF fits. This provides a significant advantage moving forward in precision phenomenology, since as we move to higher orders, this information takes increasingly longer to calculate. We have analysed the resulting set of PDFs, denoted MSHT20aN^{3}LO, and made two sets available as described in Chapter 14. These aN^{3}LO PDF fits have been performed to the same set of global hard scattering data and PDF parameterisations included for the MSHT20 NNLO PDF fits.

The NNLO theoretical framework for MSHT20 PDFs has been extended in Chapter 5 to include the addition of general N^{3}LO theory parameters into the fit. Subse-

quently, we have outlined how these N^{3}LO theory parameters can be included into the Hessian procedure as controllable nuisance parameters where they are not yet known. Two methods of handling subsets of the N^{3}LO theory parameters in the Hessian matrix have then been discussed i.e. including or ignoring correlations with aN^{3}LO K-factors across distinct processes. Finally in Chapter 6 we explained in detail the approximation framework which can be employed to provide approximate parameterisations for each N^{3}LO function considered.

In Chapter 7 to Chapter 10 we have presented the N^{3}LO additions to the relevant splitting functions, transition matrix elements, heavy coefficient functions and K-factors. We present usable and computationally efficient approximations to N^{3}LO based on known information in the small and large-x regimes and the available Mellin moments (and make these available as described in Chapter 14). In all cases the best fit prediction for each N^{3}LO function is in good agreement with the prior expected behaviour. Also in Chapter 10, we find good agreement with recent progress towards N^{3}LO DY and top production K-factors [192, 194]. As more information becomes available surrounding each of these functions, the framework we present here can be easily adapted, aiding in the reduction in sources of MHOUs from N^{3}LO. As we have stressed, we interpret our theoretical uncertainty as being mainly due to the remaining uncertainty at N^{3}LO, but with some small, but significant contribution from even higher orders, particularly at small-x. Our results seem consistent with this interpretation. However, in the future we expect the N^{3}LO description to become more exact. Hence, at some point remaining N^{3}LO uncertainty will become comparable to, or smaller than effects beyond N^{3}LO. At that point we would have to modify our procedure. However, we expect that once N^{3}LO is largely known, there will then also be more information known about even higher orders (i.e. N^{4}LO), which could then be incorporated in a similar manner to maintain an estimate for MHOUs. Alternatively,

in the event that the available information is not suitable to provide approximations (or indeed to complement these approximations), a treatment similar in principle, but more sophisticated in practice, to that of the K-factors may be adopted for DIS quantities. On this note, we acknowledge that the method of constructing aN^{3}LO K-factor's for non-(inclusive) DIS processes presented here is a first step towards a more robust and flexible procedure which is left for future work.

Combining together all N^{3}LO information, in Chapter 11 the results of an approximate N^{3}LO global PDF fit are presented. The new MSHT20 approximate N^{3}LO PDFs show a significant reduction in χ^2 from the MSHT20 NNLO PDF set, with the leading NNLO tensions between HERA and non-HERA datasets heavily reduced at aN^{3}LO (most notably with the ATLAS 8 TeV Z p_T dataset [121]). With this being said, the aN^{3}LO set does fit selected Jets datasets worse in an aN^{3}LO global fit than at NNLO, although these are an exception to the behaviour seen for the other datasets. In performing a fit not including ATLAS 8 TeV Z p_T data we provide evidence that similar tensions seen at NNLO (see [3]) remain between this dataset and jet production data at aN^{3}LO. Further to this, we show that since HERA and ATLAS 8 TeV Z p_T data are more in agreement in the form of the high-x gluon at aN^{3}LO, one can observe that the tension with the jet production data is shared between HERA and ATLAS 8 TeV Z p_T data.

Investigating the correlations present within an aN^{3}LO PDF fit, a natural separation between process independent and process dependent parameters can be observed. With this motivation, a PDF set with decorrelated aN^{3}LO K-factor eigenvectors is constructed. The validity of this is then also verified by comparison with a second PDF set which includes correlations between all parameters. Each of these sets exhibits similarly well behaved eigenvectors and levels of dynamical tolerance.

Considering the form of the individual PDFs, the aN^{3}LO PDFs include a much harder gluon at small-x due to contributions from the splitting functions as discussed in Section 11.8. This enhancement then translates into an increase in the charm and bottom PDFs due to the gluon input into the heavy flavour sector via the transition matrix elements. Further to this, at very low-Q^2 the result of the N^{3}LO additions is a non-negative charm and gluon PDF at small-x. As a consistency check, the fit dependence on α_s and m_c has been investigated. In both of these cases we show a preference for values which suppress the heavy flavour contributions (slightly lower α_s and slightly higher m_c than NNLO). Considering the predicted aN^{3}LO α_s, we observe a slightly lower than 1σ effect when comparing with the NNLO world average. While an extensive analysis of the aN^{3}LO α_s value is left for further study, since the world average is determined by NNLO results, one could expect a small systematic effect from moving to N^{3}LO.

Taking this analysis further and using the approximate N^{3}LO PDFs as input to N^{3}LO cross section calculations, we consider the cases of gluon and vector boson fusion in Higgs production in Chapter 12. We present the first aN^{3}LO calculation for these cross sections and show how the aN^{3}LO prediction differs from the case with NNLO PDFs including scale variations, highlighting the importance of matching orders in calculations. In VBF we provide an example where cancellation is not realised between orders. However in this case the quark sector is much more constrained and due to the smaller variation between orders, there is naturally less scope for cancellation.

Finally in Chapter 13, the datasets included in an MSHT20 global fit have been extended to include SeaQuest and $7+8$ TeV dijet final states. With the addition of high-x SeaQuest data, we investigate how the high-x $\bar{d}$ PDF at low-Q^2 no longer becomes

negative and also that a similar negative $\bar{d}$ mode was present at NNLO without SeaQuest (with a near discrete minima). These results confirm that the observed negativity is not a direct feature of the aN^{3}LO theory and is in fact, a result of the extra flexibility introduced when performing a fit at aN^{3}LO. For the dijets data, the PDFs are also presented in Chapter 13 which show the effects introduced in the high-x gluon. Towards the end of this Chapter, a final set of PDFs are investigated which are fitted to SeaQuest and dijet data, which exhibit all the features discussed for fitting these datasets separately while also resulting in a slightly better overall fit quality than for a fit with single inclusive jet data.

In summary, we have presented a set of approximate N^{3}LO PDFs that are able to more accurately predict physical quantities involving PDFs (given that all ingredients in these calculations are included at N^{3}LO or aN^{3}LO). In producing these PDFs, we have provided a more controllable method for estimating theoretical uncertainties from MHOs in a PDF fit than scale variations. While some ambiguity remains in this method in how the prior variations are chosen, we argue that the current knowledge and intuition surrounding each source of uncertainty can be utilised as and when available. This is therefore much more in line with what one can expect a theoretical uncertainty to encompass. Another potential shortcoming is the possibility of fitting to sources of uncertainty other than higher orders (or higher order corrections elsewhere in theory calculations included in a PDF fit). Although this is a possibility, the position of the considered sources of uncertainty in the underlying theory combined with the prior variations and penalties should act to minimise this effect. In any case, if a separate source of uncertainty is significantly affecting the fit, this will present itself as a source of tension with the N^{3}LO penalties and the χ^2 (and PDF uncertainty) will be adapted accordingly.

In future work it will be interesting to investigate the effects in the high-x gluon, which is a region of phenomenological importance and where the interpretation of LHC constraints is not always straightforward. We also note that there are N^{3}LO results available from di-lepton rapidity in DY processes [192]. Considering the results in Chapter 10 which display an agreement with these recent results, we hope that these approximate N^{3}LO PDFs may be of interest in this analysis. Similarly for recent results considering top production [194]. Furthermore, any approximate information from these results could be included in the N^{3}LO K-factor priors, which was not done for this iteration of the aN^{3}LO PDFs. Further to this, the treatment of K-factors presented here could be re-imagined to include a more extensive description. Finally, in order to continually improve the description of aN^{3}LO PDFs, the inclusion of more sub-leading sources of MHOUs could be addressed. With the upcoming wealth of experimental data from future colliders such as the HL-LHC and the EIC, it will be of interest to gain a better understanding of the transition matrix elements and also describe better the charged current and longitudinal structure functions, where currently theoretical uncertainties are much smaller than the experimental uncertainties.

Appendix A.

Higher Order Convolutions

In this section we present some of the complicated analytical solutions that accompany the work done in Chapter 5. These functions were calculated by hand via a transformation into Mellin space which transforms the convolution into a multiplication. After the full function is obtained in Mellin space, the x-space solutions provided below are obtained via an inverse Mellin transform for each term.

$$\left[P_{qq}^{(0)} \otimes P_{qq}^{(0)}\right](x) = \left[\frac{4\,(1+x^2)\,\ln(1-x)+x^2+5}{1-x}\right]_+ - (3x^2+1)\,\frac{\ln x}{1-x} - 4 + \left(\frac{31}{4} - \frac{2\pi^2}{3}\right)\delta(1-x) \quad \text{(A.1)}$$

$$\left[P_{qq}^{(0)} \otimes P_{qg}^{(0)}\right](x) = C_F T_R \Bigg\{ (4x^2 - 4x + 2)\ln(1-x) - (4x^2 - 2x + 1)\ln x + 2x - \frac{1}{2} \Bigg\} + \left(\frac{11C_A - 4n_f T_R}{6}\right)(2x^2 - 2x + 1) \quad \text{(A.2)}$$

$$\left[P_{qg}^{(0)} \otimes P_{gq}^{(0)}\right](x) \quad = \quad C_F T_R \left\{ 2(1 + x)\ln x - \frac{4}{3}x^2 + \frac{4}{3x} - x + 1 \right\} \quad \text{(A.3)}$$

$$\left[P_{qg}^{(0)} \otimes P_{gg}^{(0)}\right](x) = 2C_A T_R \Bigg\{ (2x^2 - 2x + 1)\ln(1-x) + (1 + 4x)\ln x - \frac{31}{6}x^2 + 7x + \frac{2}{3x} - \frac{5}{2} \Bigg\} + T_R \left(\frac{11C_A - 4n_f T_R}{6}\right)(2x^2 - 2x + 1) \quad \text{(A.4)}$$

$$\begin{aligned}\left[C_{2,q}^{(1)} \otimes P_{qq}^{(0)}\right](x) = {} & 4\left[(1 + x^2)\,\frac{\ln^2(1-x)}{1-x}\right]_+ + \left[\frac{1}{1-x}\left(\frac{32}{3}\,\mathrm{Li}_2(x) - \frac{64}{3}\zeta_2 - 15\right)\right]_+ \\ & + \frac{4}{3}\left[\frac{\ln(1-x)}{1-x}\,(1 + 2x - 6x^2)\right]_+ + \frac{\ln^2 x}{1-x}\,\frac{2}{3}\,(1 + 3x^2) \\ & + \frac{4}{3}\,(9 - x^2)\,\frac{\mathrm{Li}_2(1-x)}{1-x} + \frac{20}{3}\,(1 + x)\,\ln x \ln(1-x) \\ & + \frac{\ln x}{1-x}\,\frac{8}{3}\,(2x^2 - x - 1) + \frac{16}{3}\,\zeta_2\,(1 + x) + 14 \\ & + 8\,x - \left(\frac{106}{3} + \zeta_3\right)\delta(1-x) \quad \text{(A.5)}\end{aligned}$$

$$\left[C_{2,q}^{(1)} \otimes P_{qg}^{(0)}\right](x) = T_R C_F \Bigg\{ \left(2x^2 - 2x + 1\right) \ln^2(1-x) - (6x^2 - 8x + \frac{7}{2}) \ln(1-x) + (2x^2 - x + \frac{1}{2}) \ln^2 x + \left(6x^2 - 4x - \frac{1}{2}\right) \ln x - (1+2x) \mathrm{Li}_2(x) + (-4x^2 + 2x - 1) \ln x \ln(1-x) + x^2 - 3x + 2 - \left(2\zeta_2 + \frac{9}{2}\right)(2x^2 - 2x + 1) \Bigg\} \quad \text{(A.6)}$$

$$\left[C_{2,g}^{(1)} \otimes P_{gq}^{(0)}\right](x) = T_R C_F \Bigg\{ \left(-\frac{4}{3}x^2 - x + \frac{4}{3x} + 1\right) \ln(1-x) - (1+x) \ln^2 x + \left(\frac{4}{3}x^2 - 5x - 1\right) \ln x - 2(1+x) \mathrm{Li}_2(x) + \frac{16}{3}x^2 + \frac{2}{3}x + \frac{2}{3x} - \frac{20}{3} + 2\zeta_2(1+x) \Bigg\} \quad \text{(A.7)}$$

$$\left[C_{2,g}^{(1)} \otimes P_{gg}^{(0)}\right](x) = 2C_A T_R \Bigg\{ \left(2x^2 - 2x + 1\right) \ln^2(1-x) - \left(2x^2 - 4x + 2\right) \ln x \ln(1-x) - \left(\frac{79}{6}x^2 - 11x + \frac{7}{6}\right) \ln(1-x) + \frac{1}{3x} - \frac{121}{6}x + 4\zeta_2 x + \zeta_2 - \left(2x + \frac{1}{2}\right) \ln^2 x - \frac{43}{12} + \left(\frac{281}{12} - 2\zeta_2\right) x^2 - (2x+2) \mathrm{Li}_2(x) + \left(\frac{31}{6}x^2 - 16x - \frac{1}{2}\right) \ln x + (2x-1) \mathrm{Li}_2(1-x) \Bigg\} \quad \text{(A.8)}$$

Appendix B.

Renormalisation Group Invariance

A general RG invariant function $C(\alpha_s(\mu^2), \frac{\mu^2}{Q^2})$ is required to obey the RG equation,

$$\mu^2 \frac{d}{d\mu^2} C(\alpha_s(\mu^2), \frac{\mu^2}{Q^2}) = 0. \tag{B.1}$$

We define two new variables for the convenience of this derivation as,

$$\xi = \ln \frac{Q^2}{\Lambda^2} \qquad\qquad \chi = \ln \frac{\mu^2}{Q^2}, \tag{B.2}$$

also note the change of variables gives,

$$\frac{d}{d\mu^2} = \frac{1}{\mu^2} \frac{d}{d\chi}. \tag{B.3}$$

Now we have the RG equation in a simpler form,

$$\frac{d}{d\chi} C(\alpha_s(\xi + \chi), \chi) = 0 \tag{B.4}$$

We can expand this equation out by use of the chain rule as follows,

$$0 = \frac{d}{d\chi}\alpha_s(\xi+\chi)\frac{\partial}{\partial\alpha_s}C(\alpha_s(\xi+\chi),\chi)\Big|_\chi + \frac{\partial}{\partial\chi}C(\alpha_s(\xi+\chi),\chi)\Big|_{\alpha_s} \tag{B.5}$$

$$= \frac{d}{d\xi}\alpha_s(\xi+\chi)\frac{\partial}{\partial\alpha_s}C(\alpha_s(\xi+\chi),\chi)\Big|_\chi + \frac{\partial}{\partial\chi}C(\alpha_s(\xi+\chi),\chi)\Big|_{\alpha_s} \tag{B.6}$$

$$= \frac{\partial}{\partial\xi}C(\alpha_s(\xi+\chi),\chi)\Big|_\chi + \frac{\partial}{\partial\chi}C(\alpha_s(\xi+\chi),\chi)\Big|_{\alpha_s} \tag{B.7}$$

This then reveals a new relationship between the partial derivatives of an RG invariant quantity with respect to our new variables, which will be useful in the next step.

Performing a Taylor expansion around the point where $\mu^2 = Q^2$ or $\chi = 0$ gives us the following expression,

$$C(\alpha_s(\xi+\chi),\chi) = C(\alpha_s(\xi+\chi),0) + \chi\frac{\partial}{\partial\chi}C(\alpha_s(\xi+\chi),0)\Big|_{\alpha_s} \tag{B.8}$$

$$+ \frac{1}{2}\chi^2\frac{\partial^2}{\partial\chi^2}C(\alpha_s(\xi+\chi),0)\Big|_{\alpha_s} + ... \tag{B.9}$$

Then using the relation we just derived from the RG group equation, we can state,

$$C(\alpha_s(\xi+\chi),\chi) = C(\alpha_s(\xi+\chi),0) - \chi\frac{\partial}{\partial\xi}C(\alpha_s(\xi+\chi),0)\Big|_{\alpha_s} \tag{B.10}$$

$$+ \frac{1}{2}\chi^2\frac{\partial^2}{\partial\xi^2}C(\alpha_s(\xi+\chi),0)\Big|_{\alpha_s} + ... \tag{B.11}$$

The above equation is in general how any RG invariant quantity can be described in terms of a Taylor expansion and is how expressions used in this report are formulated. With the use of (B.12) and the subsequent perturbative expansion of the β-function and $C(\alpha_s,0)$ in terms of α_s, we are then able to find an order by order expansion for

$C(\alpha_s(\mu^2), \frac{\mu^2}{Q^2})$.

$$\frac{d}{d\xi}C(\alpha_s(\xi),0) = \frac{d\alpha_s}{d\xi}\frac{\partial}{\partial\alpha_s}C(\alpha_s(\xi),0) = \beta(\alpha_s(\xi))\frac{\partial}{\partial\alpha_s}C(\alpha_s(\xi),0) \tag{B.12}$$

Note that the beta function has the perturbative expansion shown in (B.13), beginning at the 1-loop correction.

$$\beta(\alpha_s(\mu^2)) = \alpha_s^2(Q^2)\beta_0 + \alpha_s^3(Q^2)\beta_1 + \alpha_s^4(Q^2)\beta_2 + ... \tag{B.13}$$

Appendix C.

List of N^3LO Ingredients

Table's C.1 and C.2 summarise the available (at the time of writing) and used information regarding the N^3LO splitting functions and coefficient functions respectively. The formalism presented in Chapter 5 currently makes use of all this information and is able to be adapted as and when more information becomes available.

N^{3}LO Function	No. of Moments	Moments (Even only)	Small-x	Large-x
P_{qq}^{NS}	8	$N = 2 - 16$ [159]	[159]	[159]
P_{qq}^{PS}	4	$N = 2 - 8$ [171, 172]	LL [164]	N/A
P_{qg}	4	$N = 2 - 8$ [171, 172]	LL [164]	N/A
P_{gq}	4	$N = 2 - 8$ [171, 172]	LL [165–167]	N/A
P_{gg}	4	$N = 2 - 8$ [171, 172]	LL & NLL [165–169]	N/A
$A_{qq,H}^{\text{NS}}$	7	$N = 2 - 14$ [179]	N/A	N/A
A_{Hq}^{PS}	6	$N = 2 - 12$ [179]	[181]	[181]
A_{Hg}	5	$N = 2 - 10$ [179]	LL [178]	N/A
$A_{gq,H}$	7	$N = 2 - 14$ [179]	[182]	[182]
$A_{gg,H}$	5	$N = 2 - 10$ [179]	N/A	N/A

Table C.1.: List of all the N^{3}LO ingredients used to construct the approximate N^{3}LO splitting functions and transition matrix elements. Where only a citation is provided, extensive knowledge i.e. beyond NLL is used. This table is a non-exhaustive list of the current knowledge about these functions, however information beyond that which is provided here is not currently in a usable format for phenomological studies.

GM-VFNS N^{3}LO Function	Known N^{3}LO Components
$C_{H,q}$	$C_{H,q}^{(3),\,\text{FF}}\left(Q^2 \leq m_h^2\right)$ LL [176–178], $C_{H,q}^{\text{VF},\,(3)}$ [185]
$C_{H,g}$	$C_{H,g}^{(3),\,\text{FF}}\left(Q^2 \leq m_h^2\right)$ LL [176–178], $C_{H,q}^{\text{ZM},\,(3)}$ [185]
$C_{q,q}^{\text{NS}}$	$C_{q,q,\,\text{NS}}^{\text{ZM},\,(3)}$ [185]
$C_{q,q}^{\text{PS}}$	$C_{q,q,\,\text{PS}}^{\text{ZM},\,(3)}$ [185]
$C_{q,g}$	$C_{q,g}^{\text{ZM},\,(3)}$ [185]

Table C.2.: List of all N^{3}LO ingredients used to construct the approximate N^{3}LO GM-VFNS coefficient functions. Note that lower order components that contribute to these functions are also known and are cited in the text. This table only considers contributing 3-loop functions.

Appendix D.

χ^2 Results without HERA

D.1. NNLO

Table D.1 shows the differences in χ^2 found when omitting HERA data from a PDF fit using the MSHT NNLO PDFs. This table is copied here from [3] for the ease of the reader. We see similarities between these results and the $\Delta\chi^2$'s seen in the case of N^{3}LO PDFs. Specifically the ATLAS 8 TeV Z p_T displaying a substantial reduction from the global NNLO fit. This therefore provides evidence that the inclusion of the N^{3}LO contributions is aiding in reducing tensions between the HERA and non-HERA datasets.

Dataset	N_{pts}	χ^2	$\Delta\chi^2$
BCDMS μp F_2 [72]	163	174.7	−5.5
BCDMS μd F_2 [72]	151	143.9	−2.1
NMC μp F_2 [75]	123	119.6	−4.5
NMC μd F_2 [75]	123	96.6	−16.1
SLAC ep F_2 [78,79]	37	33.0	+0.9
SLAC ed F_2 [78,79]	38	24.1	+1.1
E665 μd F_2 [82]	53	63.5	+3.9
E665 μp F_2 [82]	53	68.9	+4.3
NuTeV νN F_2 [85]	53	38.0	−0.3
NuTeV νN xF_3 [85]	42	27.5	−3.2
NMC $\mu n/\mu p$ [88]	148	132.7	+1.9
E866 / NuSea pp DY [102]	184	228.0	+2.9
E866 / NuSea pd/pp DY [104]	15	9.1	−1.3
CCFR $\nu N \to \mu\mu X$ [114]	86	66.2	−1.5
NuTeV $\nu N \to \mu\mu X$ [114]	84	49.0	−9.5
CHORUS νN F_2 [117]	42	29.6	−0.6
CHORUS νN xF_3 [117]	28	18.2	−0.3
CDF II $p\bar{p}$ incl. jets [128]	76	60.9	+0.5
DØ II Z rap. [130]	28	16.6	+0.3
CDF II Z rap. [132]	28	38.7	+1.5
DØ II $W \to \nu\mu$ asym. [134]	10	17.4	+0.1
CDF II W asym. [73]	13	19.0	+0.0
DØ II $W \to \nu e$ asym. [74]	12	30.0	−3.9
DØ II $p\bar{p}$ incl. jets [76]	110	119.3	−0.9
ATLAS W^+, W^-, Z [77]	30	29.5	−0.4

Table D.1.: The change in χ^2 for a NNLO fit(with negative indicating an improvement in the fit quality) when the combined HERA data sets including F_L and heavy flavour data are removed, illustrating the tensions of these data sets with several of the other data sets in the global fit. $\Delta\chi^2$ represents the change from a full global fit at the same order in α_s.

Dataset	N_{pts}	χ^2	$\Delta\chi^2$
CMS W asym. $p_T > 35$ GeV [80]	11	6.6	−1.2
CMS W asym. $p_T > 25, 30$ GeV [81]	24	7.5	+0.1
LHCb $Z \to e^+e^-$ [83]	9	24.2	+1.5
LHCb W asym. $p_T > 20$ GeV [84]	10	12.1	−0.3
CMS $Z \to e^+e^-$ [86]	35	17.3	−0.6
ATLAS High-mass Drell-Yan [87]	13	16.9	−2.0
Tevatron, ATLAS, CMS $\sigma_{t\bar{t}}$ [89–101]	17	14.2	−0.4
CMS double diff. Drell-Yan [103]	132	134.2	−10.3
LHCb 2015 W, Z [105, 106]	67	97.4	−1.9
LHCb 8 TeV $Z \to ee$ [108]	17	24.4	−1.8
CMS 8 TeV W [109]	22	13.7	+0.9
ATLAS 7 TeV jets [113]	140	228.0	+6.5
CMS 7 TeV $W + c$ [115]	10	9.2	+0.6
ATLAS 7 TeV high prec. W, Z [116]	61	116.8	+0.2
CMS 7 TeV jets [118]	158	179.5	+3.8
DØ W asym. [119]	14	11.3	−0.8
ATLAS 8 TeV Z p_T [121]	104	149.3	−39.2
CMS 8 TeV jets [122]	174	259.5	−1.8
ATLAS 8 TeV sing. diff. $t\bar{t}$ [123]	25	24.5	−1.1
ATLAS 8 TeV sing. diff. $t\bar{t}$ dilep. [124]	5	2.3	−1.1
ATLAS 8 TeV High-mass DY [125]	48	60.9	+3.7
ATLAS 8 TeV W + jets [126]	30	16.4	−1.7
CMS 8 TeV double diff. $t\bar{t}$ [127]	15	23.3	+0.8
ATLAS 8 TeV W [129]	22	54.4	−3.0
CMS 2.76 TeV jet [131]	81	102.9	+0.0
CMS 8 TeV sing. diff. $t\bar{t}$ [133]	9	10.6	−2.6
ATLAS 8 TeV double diff. Z [135]	59	108.3	+22.7
Total	3042	3379.6	−61.6

Table D.1.: *(Continued)* The change in χ^2 (with negative indicating an improvement in the fit quality) when the combined HERA data sets including F_L and heavy flavour data are removed, illustrating the tensions of these data sets with several of the other data sets in the global fit. $\Delta\chi^2$ represents the change from a full global fit at the same order in α_s.

D.2. aN^{3}LO

Table D.2 shows the differences in χ^2 found when omitting HERA data from a PDF fit using the MSHT aN^{3}LO PDFs. These results show that at aN^{3}LO the fit no longer experiences large tensions between HERA and ATLAS 8 TeV Z p_T [121] datasets. The main tensions at N^{3}LO are now concerning the Jets data with HERA (and most likely some non-HERA datasets). This result is not unexpected due to the known issues surrounding jets especially as we move to higher precision [207].

Dataset	N_{pts}	χ^2	$\Delta\chi^2$
BCDMS μp F_2 [72]	163	175.8	+1.4
BCDMS μd F_2 [72]	151	144.2	−0.0
NMC μp F_2 [75]	123	113.6	−7.8
NMC μd F_2 [75]	123	87.6	−16.6
SLAC ep F_2 [78,79]	37	30.7	−0.9
SLAC ed F_2 [78,79]	38	23.2	+0.4
E665 μd F_2 [82]	53	65.2	+1.3
E665 μp F_2 [82]	53	69.0	+1.5
NuTeV νN F_2 [85]	53	35.4	−0.4
NuTeV νN xF_3 [85]	42	29.2	−5.6
NMC $\mu n/\mu p$ [88]	148	131.1	−0.5
E866 / NuSea pp DY [102]	184	217.6	+2.3
E866 / NuSea pd/pp DY [104]	15	8.2	−0.2
CCFR $\nu N \to \mu\mu X$ [114]	86	67.0	−1.3
NuTeV $\nu N \to \mu\mu X$ [114]	84	47.6	−9.1
CHORUS νN F_2 [117]	42	29.0	−0.2
CHORUS νN xF_3 [117]	28	18.5	+0.4
CDF II $p\bar{p}$ incl. jets [128]	76	65.9	−0.6
DØ II Z rap. [130]	28	17.7	+0.3
CDF II Z rap. [132]	28	42.1	+1.5
DØ II $W \to \nu\mu$ asym. [134]	10	18.9	+2.4
CDF II W asym. [73]	13	19.2	+0.9
DØ II $W \to \nu e$ asym. [74]	12	31.0	+0.2
DØ II $p\bar{p}$ incl. jets [76]	110	114.2	+0.9
ATLAS W^+, W^-, Z [77]	30	29.5	−0.5

Table D.2.: The change in χ^2 for an N^{3}LO fit (with negative indicating an improvement in the fit quality) when the combined HERA data sets including F_L and heavy flavour data are removed, illustrating the tensions of these data sets with several of the other data sets in the global fit. $\Delta\chi^2$ represents the change from a full global fit at the same order in α_s.

Dataset	N_{pts}	χ^2	$\Delta\chi^2$
CMS W asym. $p_T > 35$ GeV [80]	11	7.0	+0.2
CMS W asym. $p_T > 25, 30$ GeV [81]	24	7.8	−0.2
LHCb $Z \to e^+e^-$ [83]	9	22.5	−0.7
LHCb W asym. $p_T > 20$ GeV [84]	10	12.6	+0.0
CMS $Z \to e^+e^-$ [86]	35	17.1	−0.5
ATLAS High-mass Drell-Yan [87]	13	17.5	−0.9
Tevatron, ATLAS, CMS $\sigma_{t\bar{t}}$ [89–101]	17	14.4	+0.1
CMS double diff. Drell-Yan [103]	132	129.5	−3.7
LHCb 2015 W, Z [105, 106]	67	96.7	−6.5
LHCb 8TeV $Z \to ee$ [108]	17	27.9	−2.4
CMS 8 TeV W [109]	22	11.6	+0.1
ATLAS 7 TeV jets [113]	140	217.7	+1.8
CMS 7 TeV $W + c$ [115]	10	10.8	+0.0
ATLAS 7 TeV high prec. W, Z [116]	61	118.0	−1.3
CMS 7 TeV jets [118]	158	187.8	+1.0
DØ W asym. [119]	14	10.1	−2.0
ATLAS 8 TeV Z p_T [121]	104	121.2	+12.8
CMS 8 TeV jets [122]	174	259.8	−11.5
ATLAS 8 TeV sing. diff. $t\bar{t}$ [123]	25	24.1	−0.2
ATLAS 8 TeV sing. diff. $t\bar{t}$ dilep. [124]	5	3.0	+0.3
ATLAS 8 TeV High-mass DY [125]	48	65.2	+2.4
ATLAS 8 TeV W + jets [126]	30	18.0	−0.8
CMS 8 TeV double diff. $t\bar{t}$ [127]	15	22.8	−0.8
ATLAS 8 TeV W [129]	22	48.0	−5.0
CMS 2.76 TeV jet [131]	81	103.0	−6.8
CMS 8 TeV sing. diff. $t\bar{t}$ [133]	9	12.3	+2.0
ATLAS 8 TeV double diff. Z [135]	59	86.1	+5.7

Table D.2.: *(Continued)* The change in χ^2 for an N^{3}LO fit (with negative indicating an improvement in the fit quality) when the combined HERA data sets including F_L and heavy flavour data are removed, illustrating the tensions of these data sets with several of the other data sets in the global fit. $\Delta\chi^2$ represents the change from a full global fit at the same order in α_s.

Low-Q^2 Coefficient			
$c_q^{\rm NLL} = -3.844$	0.006	$c_g^{\rm NLL} = -3.875$	0.004
Transition Matrix Elements			
$a_{Hg} = 17788.000$	5.607	$a_{qq,H}^{\rm NS} = -63.950$	0.000
$a_{gg,H} = -1334.500$	0.001		
Splitting Functions			
$\rho_{qq}^{NS} = 0.007$	0.000	$\rho_{gq} = -1.647$	0.001
$\rho_{qq}^{PS} = -0.579$	0.429	$\rho_{gg} = 9.237$	0.023
$\rho_{qg} = -1.343$	0.131		
K-factors			
$\text{DY}_{\rm NLO} = -0.291$	0.085	$\text{DY}_{\rm NNLO} = -0.228$	0.052
$\text{Top}_{\rm NLO} = -0.204$	0.042	$\text{Top}_{\rm NNLO} = 0.412$	0.170
$\text{Jet}_{\rm NLO} = -0.254$	0.065	$\text{Jet}_{\rm NNLO} = -0.861$	0.741
$p_T\text{Jets}_{\rm NLO} = 0.461$	0.213	$p_T\text{Jets}_{\rm NNLO} = 0.016$	0.000
$\text{Dimuon}_{\rm NLO} = -0.329$	0.109	$\text{Dimuon}_{\rm NNLO} = 0.587$	0.345
		Total	3311.8 / 3042
		$\Delta\chi^2$ from N^{3}LO	-48.0

Table D.2.: *(Continued)* The change in χ^2 for an N^{3}LO fit (with negative indicating an improvement in the fit quality) when the combined HERA data sets including F_L and heavy flavour data are removed, illustrating the tensions of these data sets with several of the other data sets in the global fit. $\Delta\chi^2$ represents the change from a full global fit at the same order in α_s.

Appendix E.

Dynamic Tolerances

In this section we provide an exhaustive breakdown of the $\Delta\chi^2_{\text{global}}$ behaviour for all eigenvectors found where N^{3}LO K-factor parameters are considered completely decorrelated ($H_{ij} + K_{ij}$) or correlated (H'_{ij}) with all other parameters.

E.1. Case 1: Decorrelated K-factor Parameters

Fig. E.1 displays the tolerance landscape for each eigenvector found from the decorrelated ($H_{ij} + K_{ij}$) Hessian described in Chapter 5. Across all 52 eigenvectors (42 PDF + N^{3}LO DIS theory and 10 N^{3}LO K-factor) we show an overall general agreement with the quadratic assumption similar to that found at NNLO.

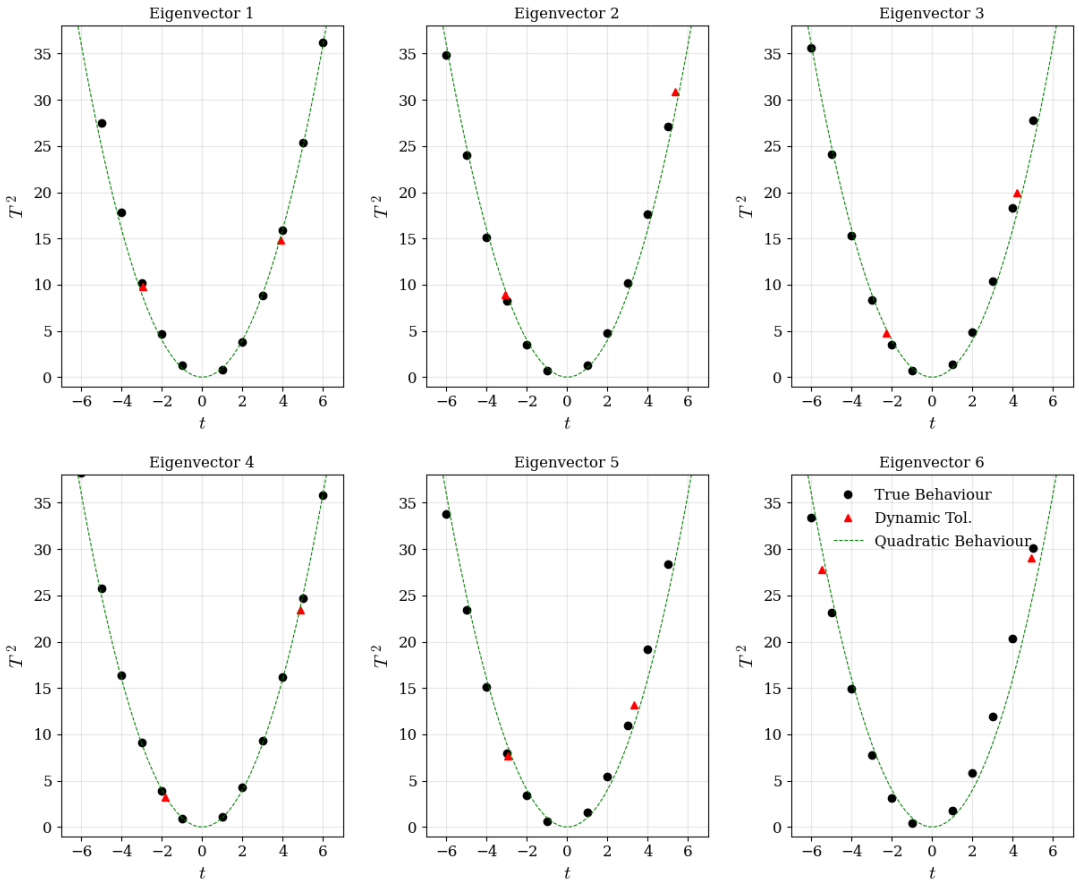

Figure E.1.: Dynamic tolerances for each eigenvector direction in the case of complete decorrelation between the theory and PDF parameters, and the K-factor parameters included in the PDF fit.

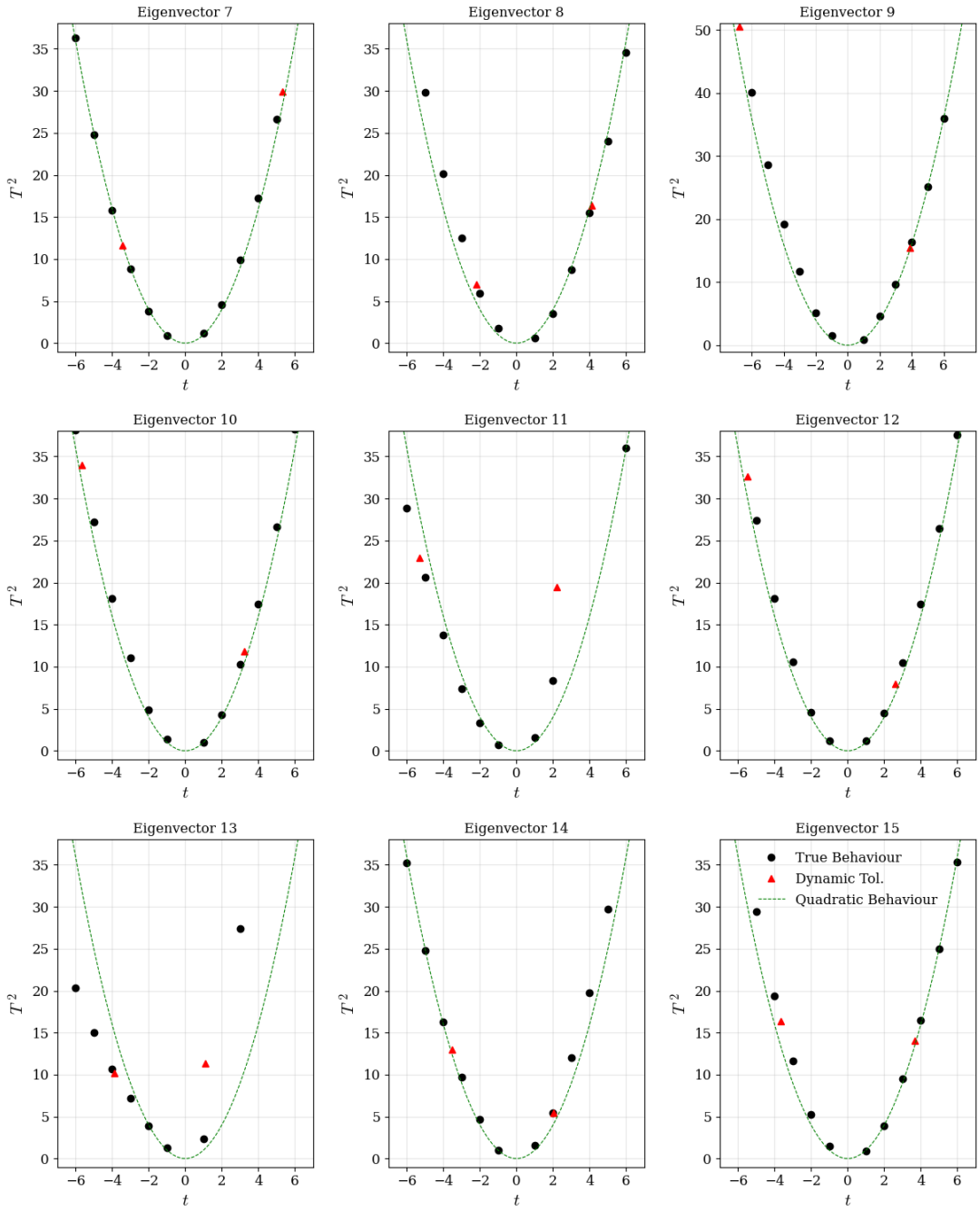

Figure E.1.: *(Continued)* Dynamic tolerances for each eigenvector direction in the case of complete decorrelation between the theory and PDF parameters, and the K-factor parameters included in the PDF fit.

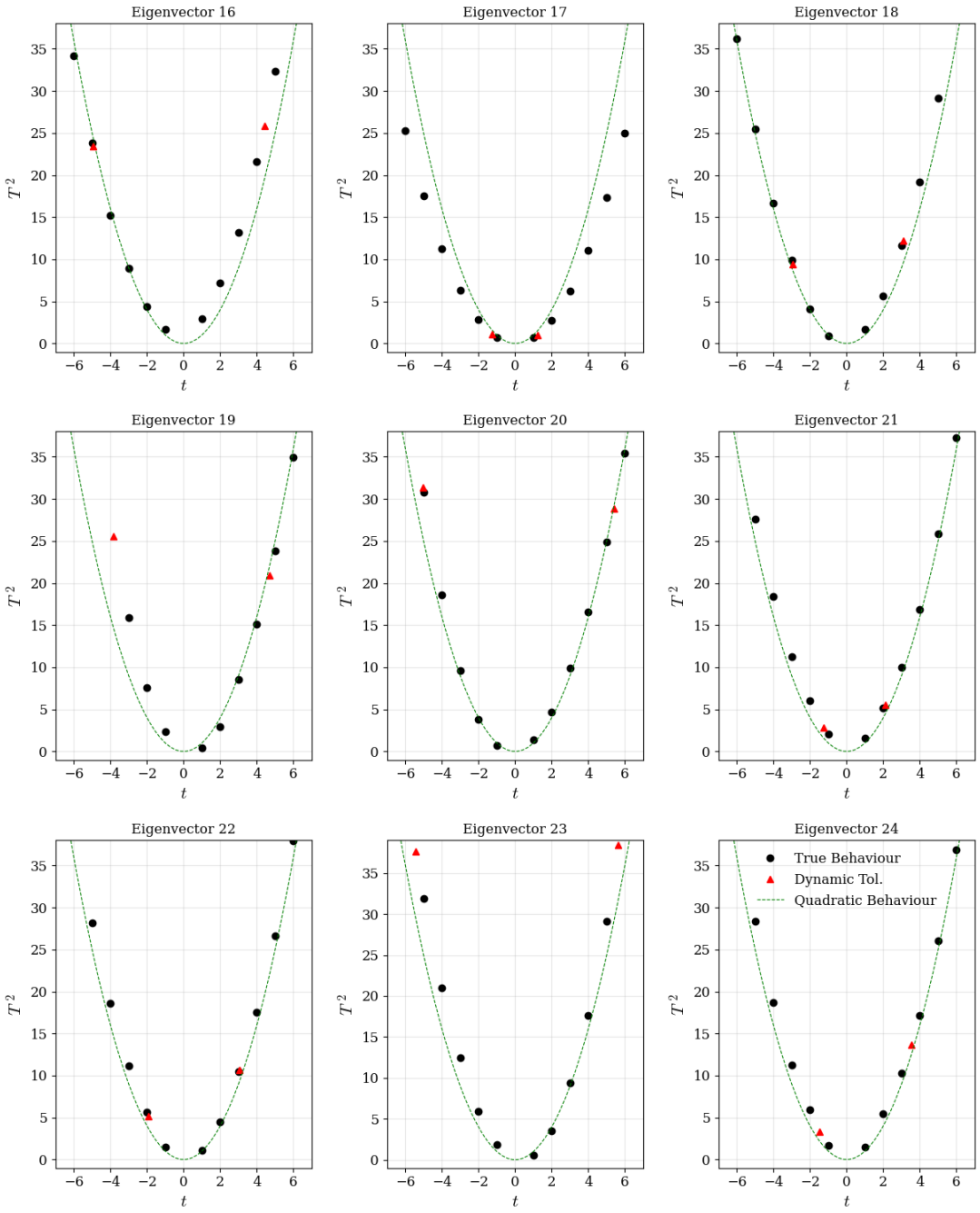

Figure E.1.: *(Continued)* Dynamic tolerances for each eigenvector direction in the case of complete decorrelation between the theory and PDF parameters, and the K-factor parameters included in the PDF fit.

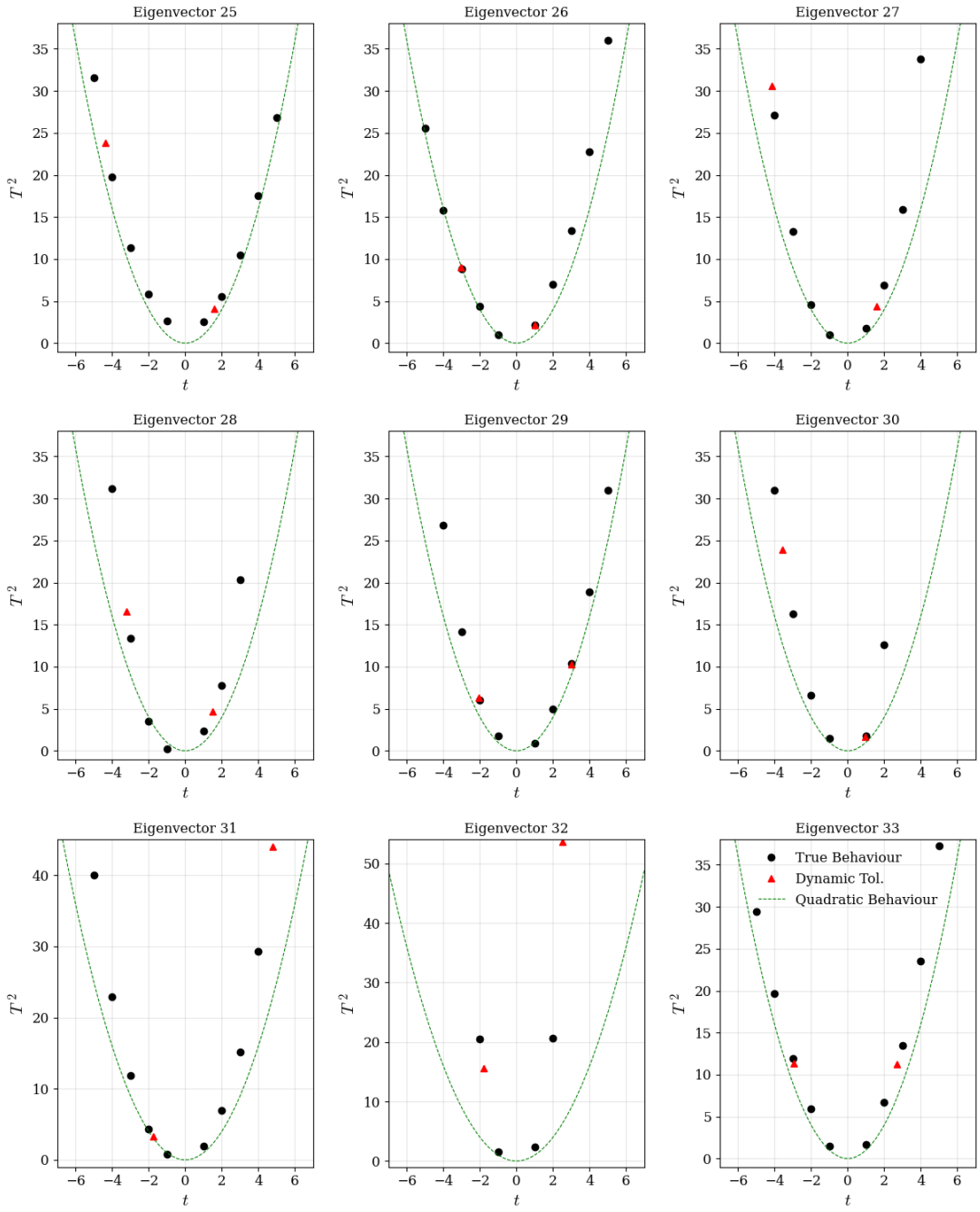

Figure E.1.: *(Continued)* Dynamic tolerances for each eigenvector direction in the case of complete decorrelation between the theory and PDF parameters, and the K-factor parameters included in the PDF fit.

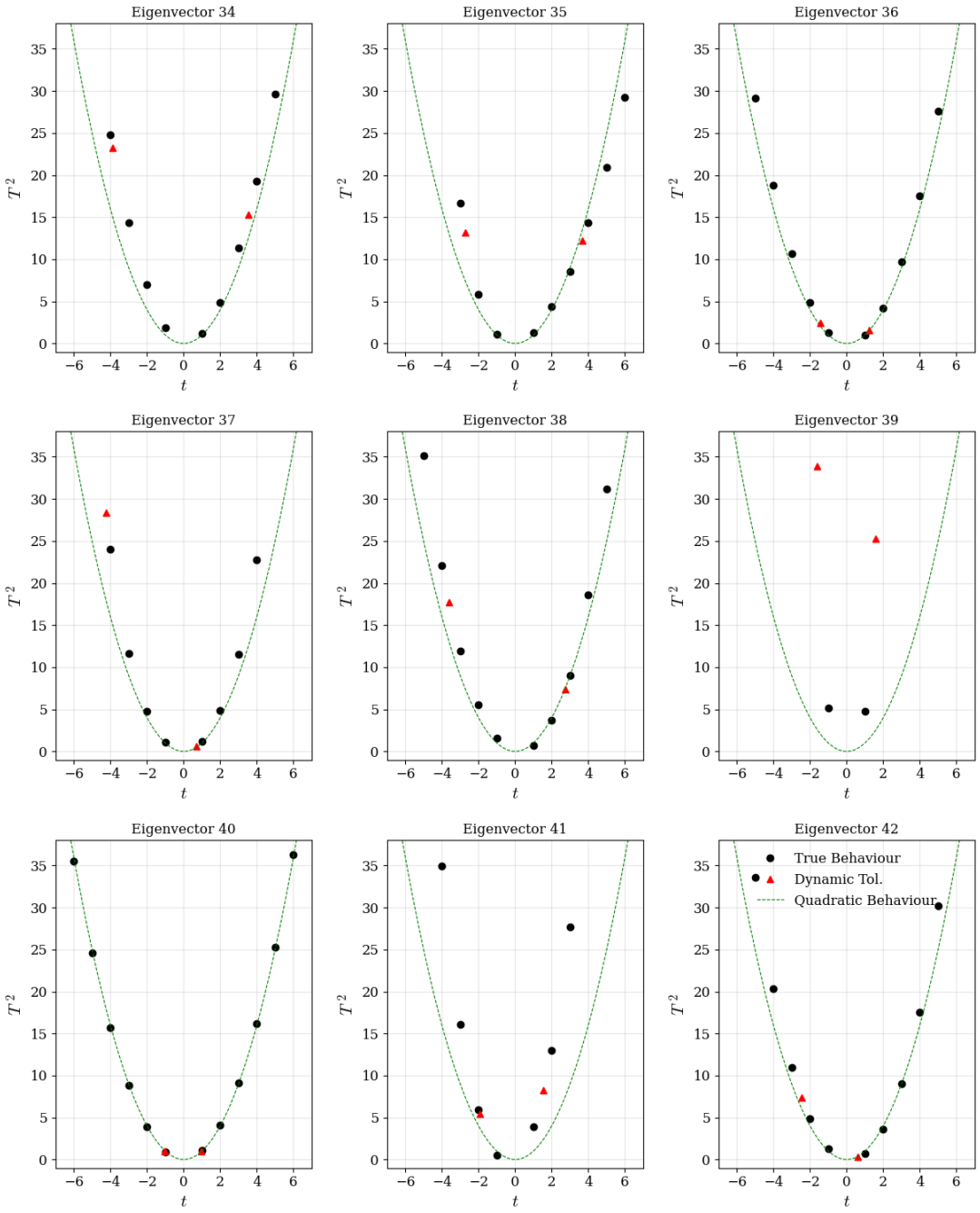

Figure E.1.: *(Continued)* Dynamic tolerances for each eigenvector direction in the case of complete decorrelation between the theory and PDF parameters, and the K-factor parameters included in the PDF fit.

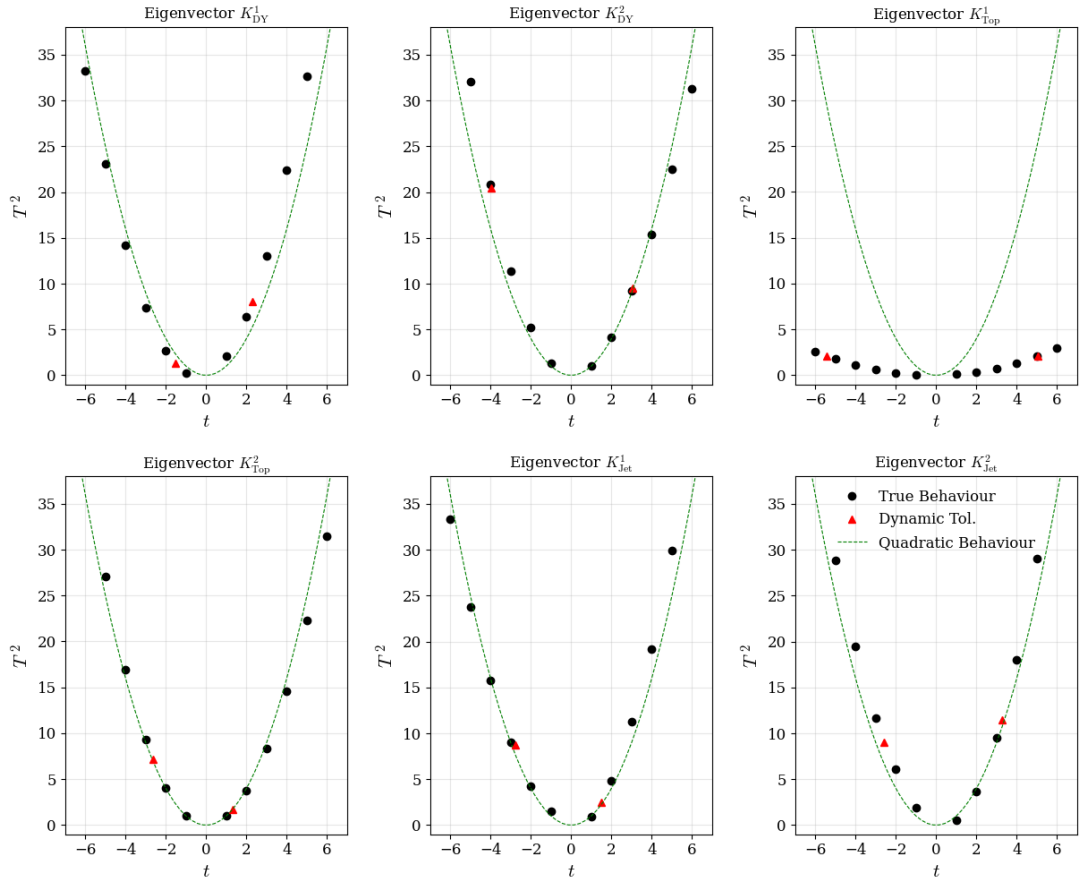

Figure E.1.: *(Continued)* Dynamic tolerances for each eigenvector direction in the case of complete decorrelation between the theory and PDF parameters, and the K-factor parameters included in the PDF fit.

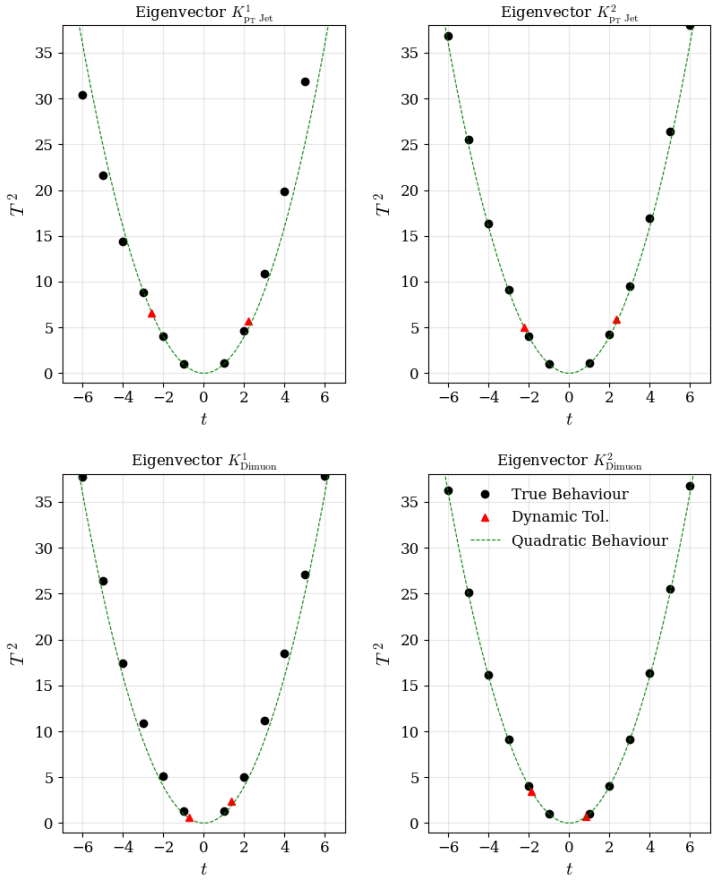

Figure E.1.: *(Continued)* Dynamic tolerances for each eigenvector direction in the case of complete decorrelation between the theory and PDF parameters, and the K-factor parameters included in the PDF fit.

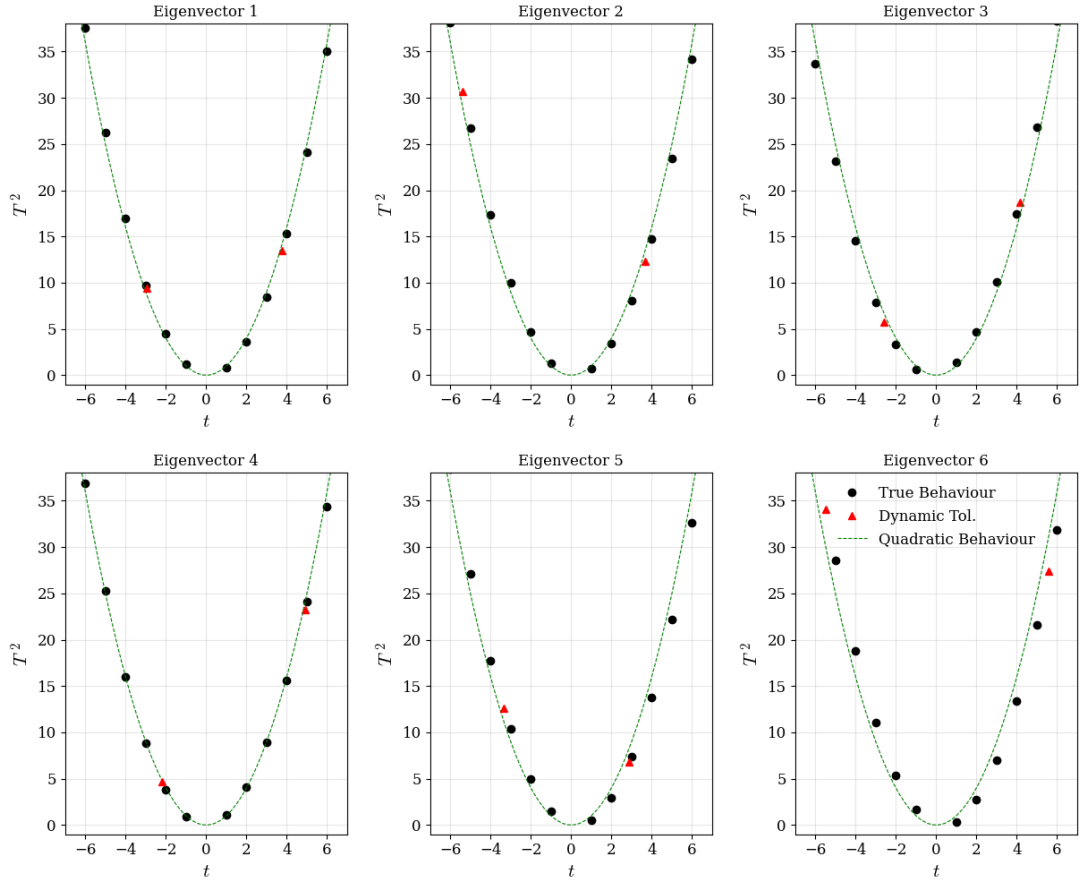

Figure E.2.: Dynamic tolerances for each eigenvector direction in the case of complete correlation between all theory, PDF and K-factor parameters included in the PDF fit.

E.2. Case 2: Correlated K-factor Parameters

Fig. E.2 displays the tolerance landscape for each eigenvector found from the correlated (H'_{ij}) Hessian described in Chapter 5. Across all 52 eigenvectors we show an overall general agreement with the quadratic assumption similar to that found at NNLO.

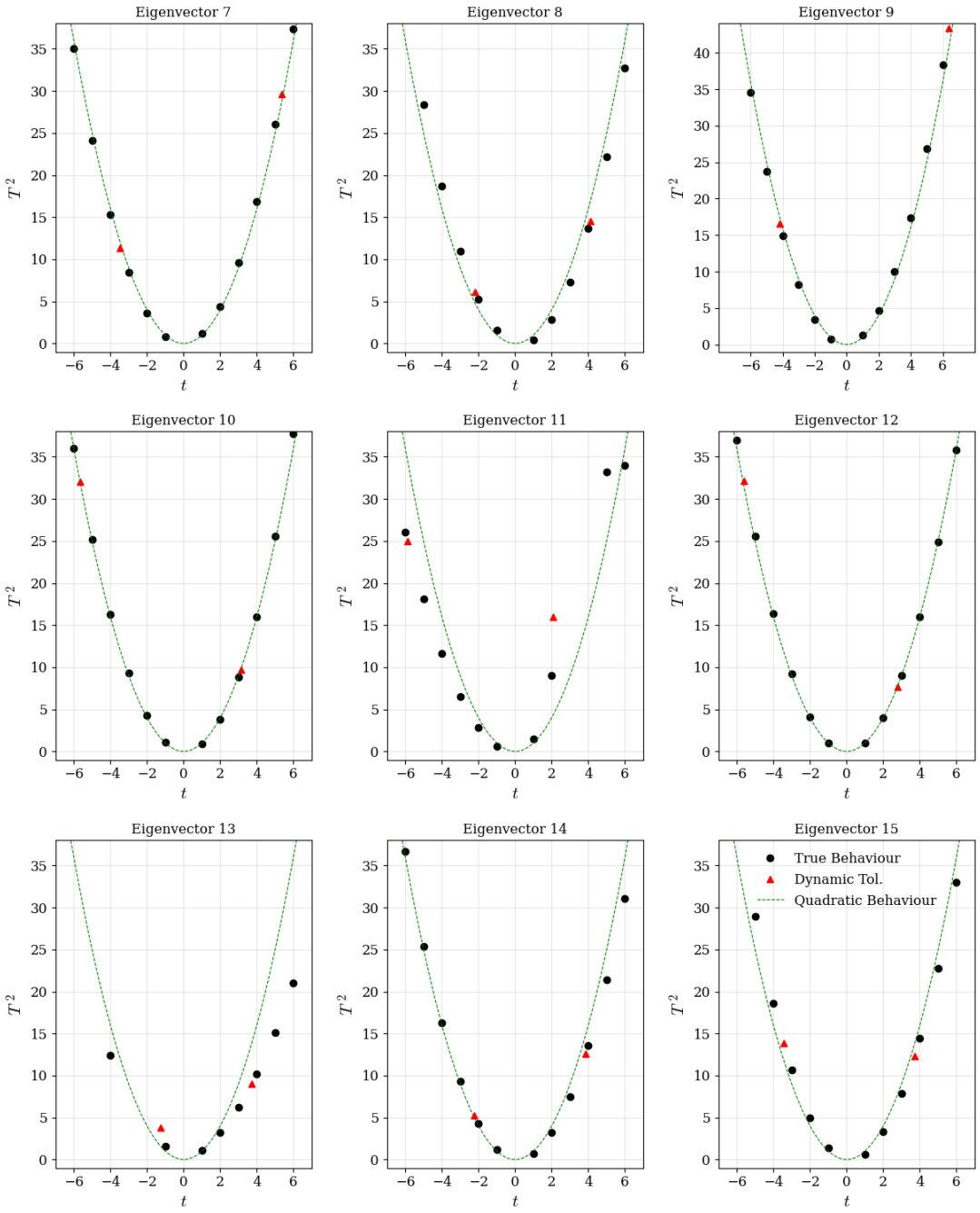

Figure E.2.: *(Continued)* Dynamic tolerances for each eigenvector direction in the case of complete correlation between all theory, PDF and K-factor parameters included in the PDF fit.

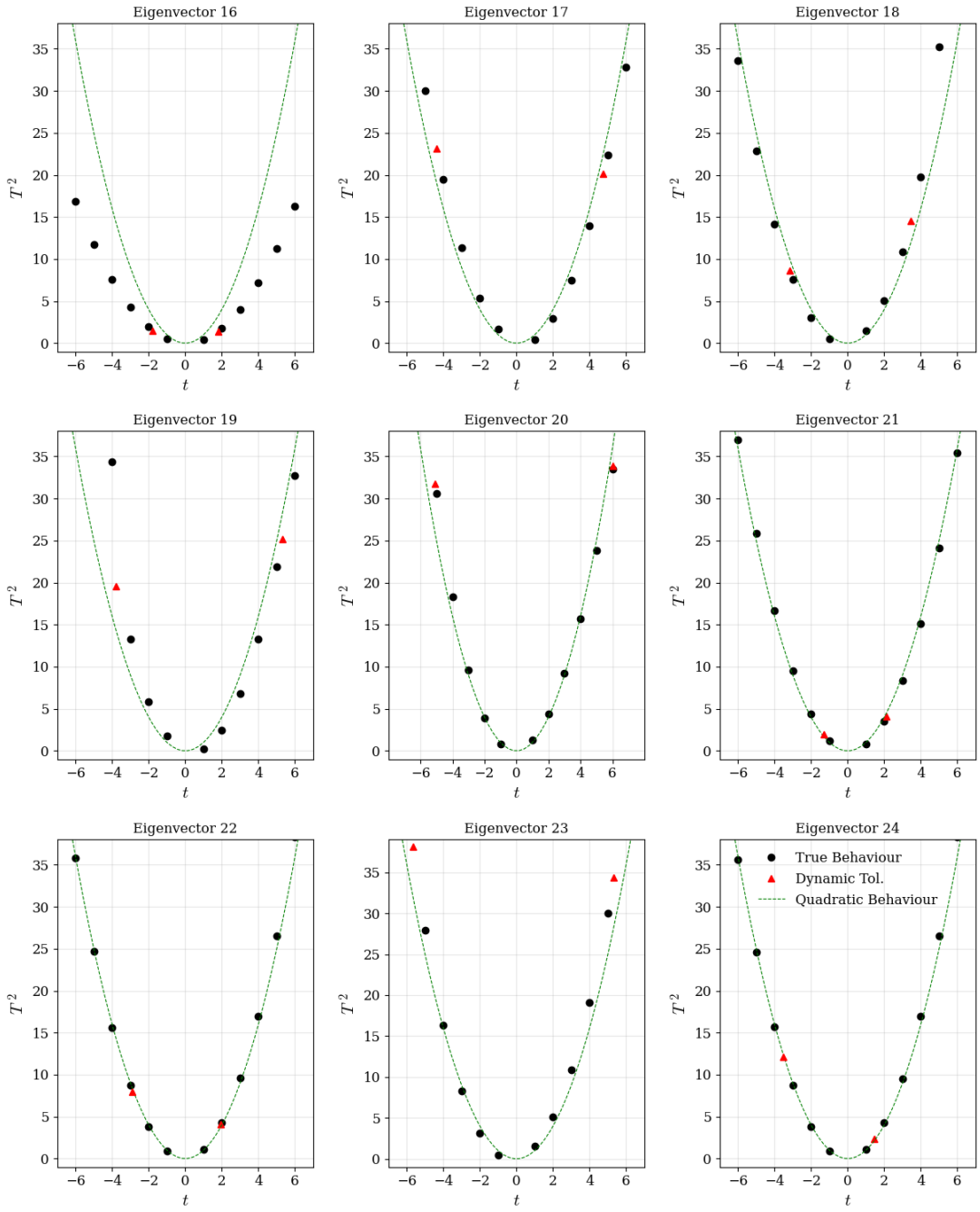

Figure E.2.: *(Continued)* Dynamic tolerances for each eigenvector direction in the case of complete correlation between all theory, PDF and K-factor parameters included in the PDF fit.

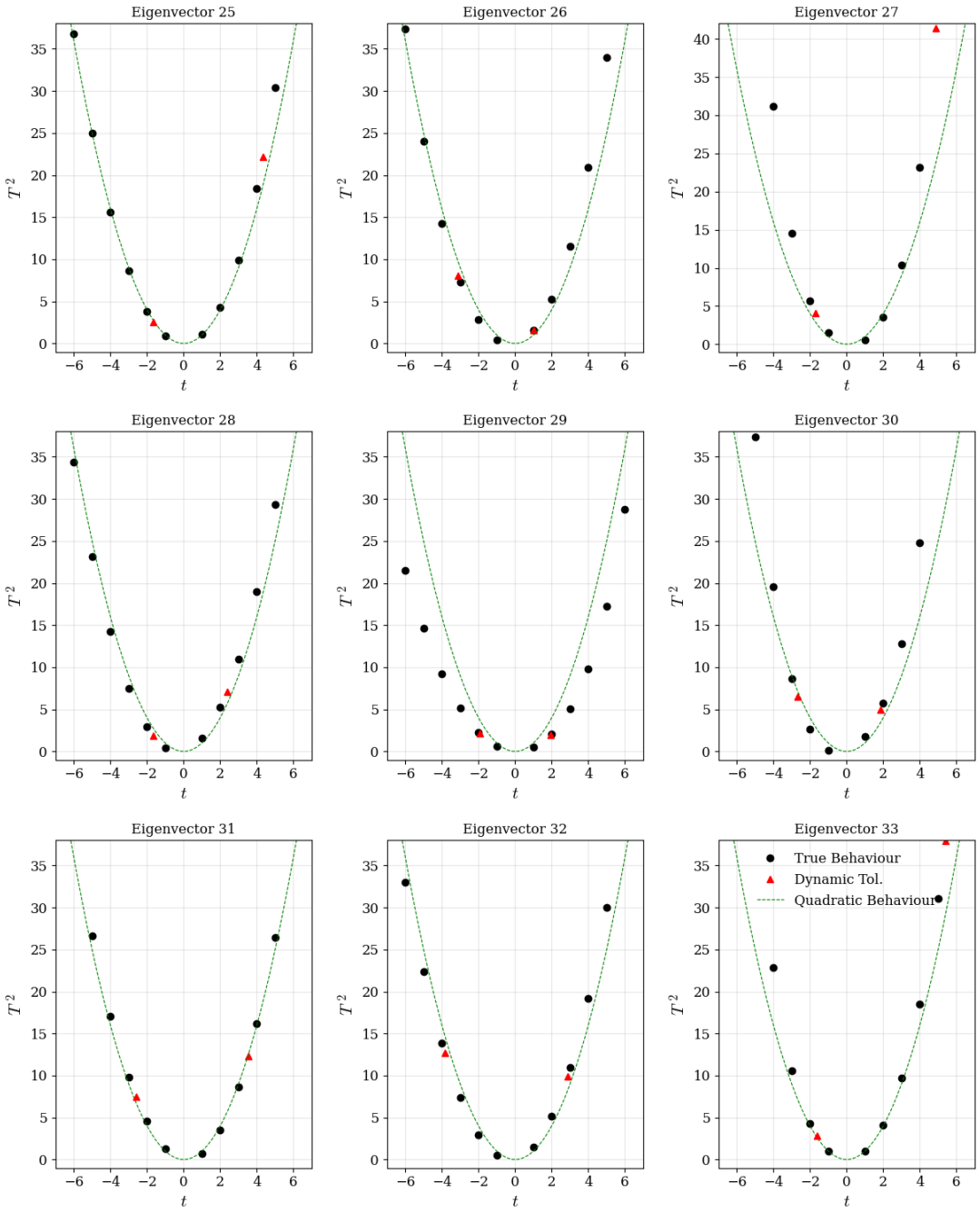

Figure E.2.: *(Continued)* Dynamic tolerances for each eigenvector direction in the case of complete correlation between all theory, PDF and K-factor parameters included in the PDF fit.

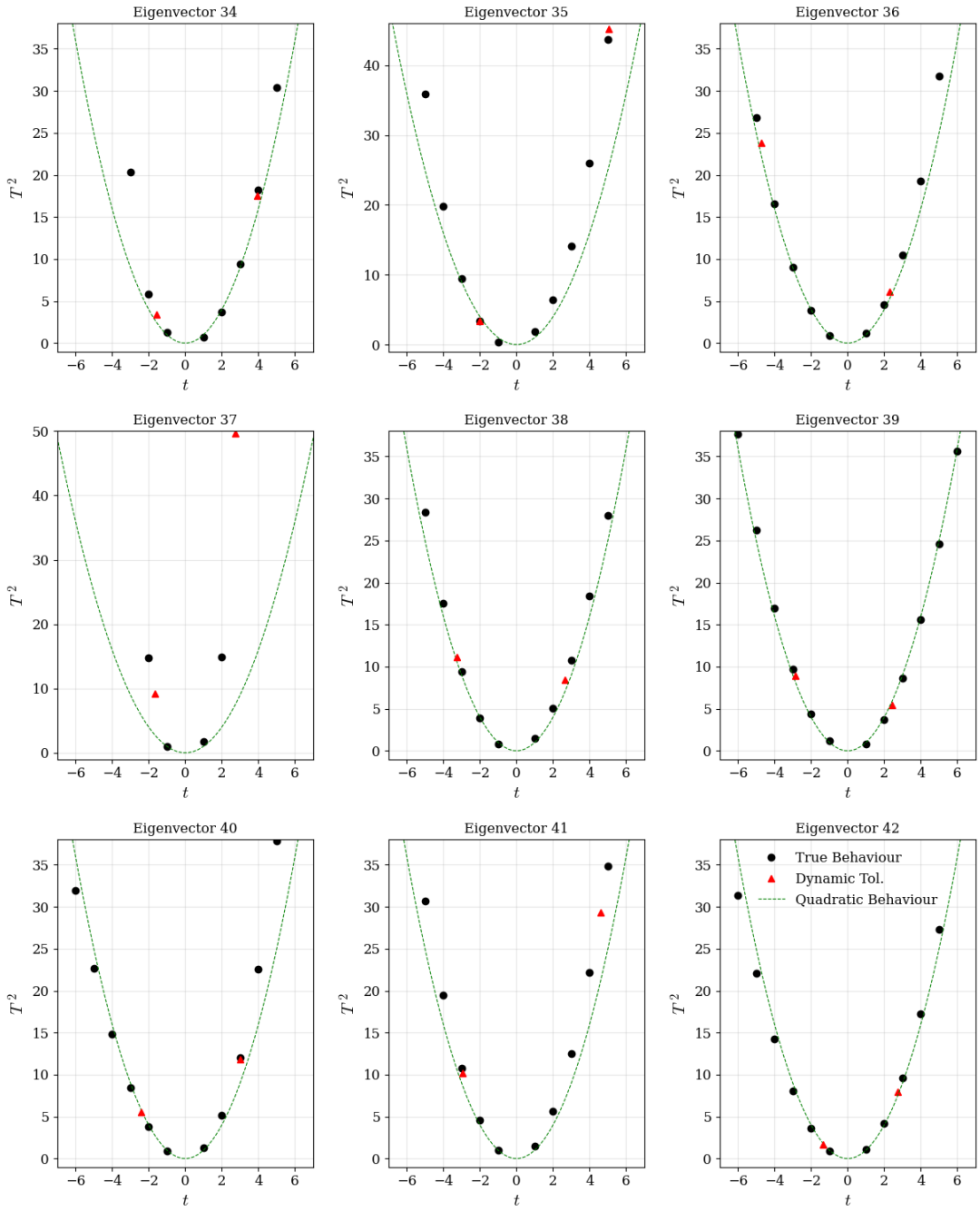

Figure E.2.: *(Continued)* Dynamic tolerances for each eigenvector direction in the case of complete correlation between all theory, PDF and K-factor parameters included in the PDF fit.

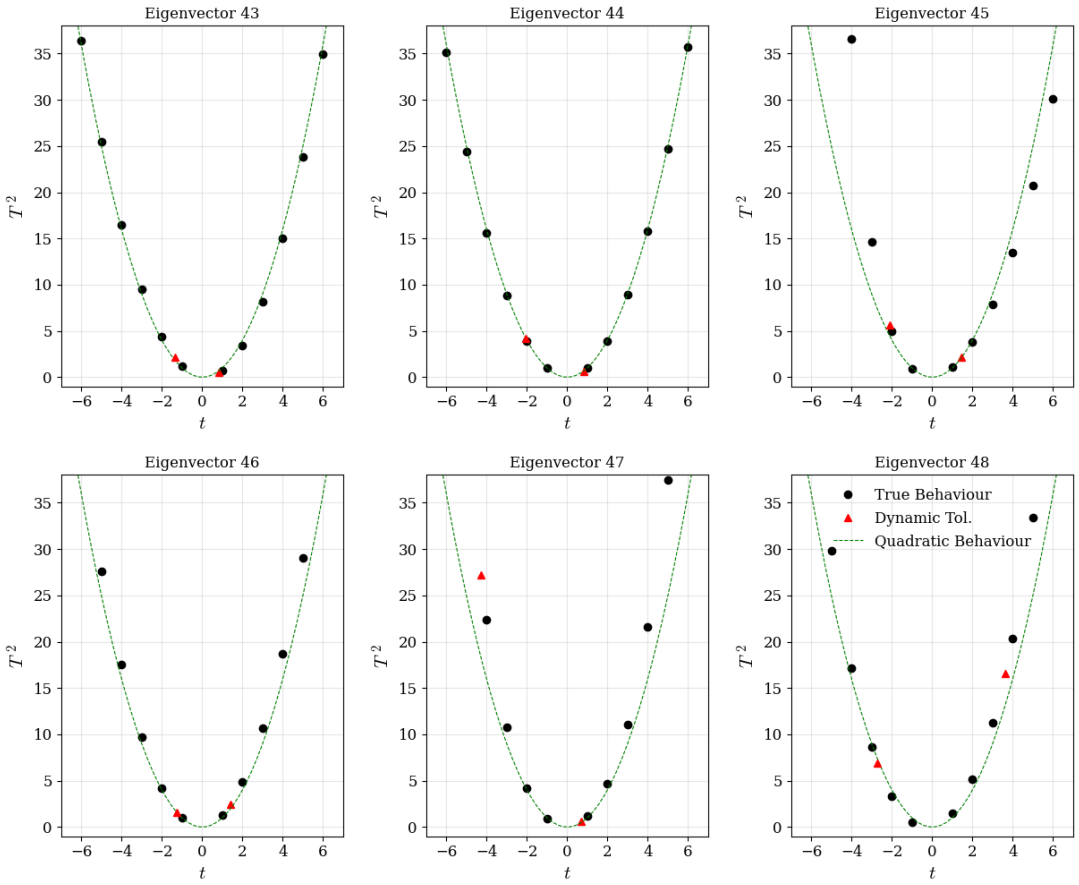

Figure E.2.: *(Continued)* Dynamic tolerances for each eigenvector direction in the case of complete correlation between all theory, PDF and K-factor parameters included in the PDF fit.

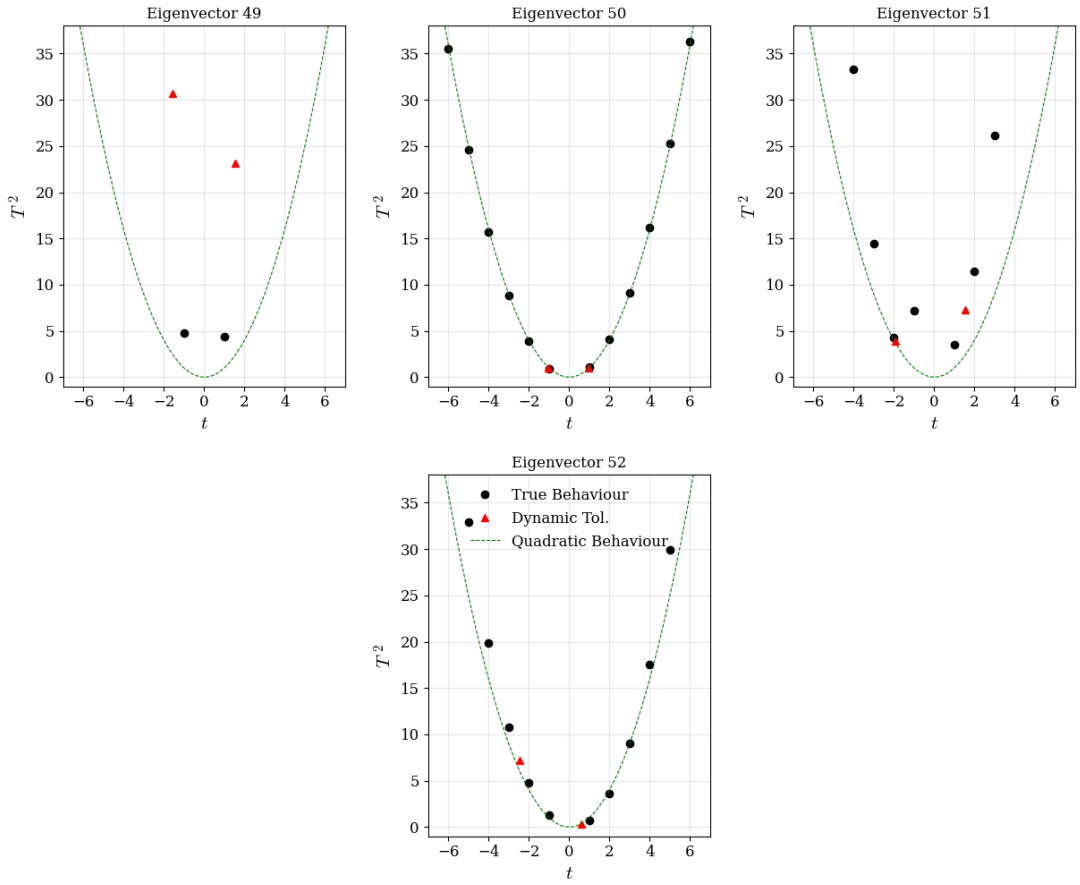

Figure E.2.: *(Continued)* Dynamic tolerances for each eigenvector direction in the case of complete correlation between all theory, PDF and K-factor parameters included in the PDF fit.

Appendix F.

Higgs Gluon Fusion $\mu = m_H$ Results

Provided in Table F.1 are the results analogous to those in Table 12.1 but with the central scale set to $\mu = \mu_f = \mu_r = m_H$. These results show a higher level of stability for aN^{3}LO PDFs with the chosen central scale. By the renormalisation group arguments, this scale dependence should disappear at all orders in perturbation theory. Therefore the results here suggest that the aN^{3}LO PDFs are following this trend.

σ order	PDF order	$\sigma + \Delta\sigma_+ - \Delta\sigma_-$ (pb)	σ (pb) $+ \Delta\sigma_+ - \Delta\sigma_-$ (%)
PDF uncertainties			
N^{3}LO	aN^{3}LO (no theory unc.)	42.709 + 1.282 - 1.342	42.709 + 2.81% - 3.14%
	aN^{3}LO	42.709 + 1.409 - 1.357	42.709 + 3.30% - 3.17%
	aN^{3}LO (K correlated)	42.709 + 1.448 - 1.317	42.709 + 3.39% - 3.08%
	NNLO	46.243 + 0.524 - 0.563	46.243 + 1.13% - 1.22%
NNLO	NNLO	42.129 + 0.472 - 0.510	42.129 + 1.12% - 1.21%
PDF + Scale uncertainties			
N^{3}LO	aN^{3}LO (no theory unc.)	42.709 + 2.000 - 2.750	42.709 + 4.68% - 6.44%
	aN^{3}LO	42.709 + 2.088 - 2.757	42.709 + 4.89% - 6.45%
	aN^{3}LO (K correlated)	42.709 + 2.114 - 2.738	42.709 + 4.95% - 6.41%
	NNLO	46.243 + 1.845 - 3.078	46.243 + 3.99% - 6.66%
NNLO	NNLO	42.129 + 4.989 - 5.106	42.129 + 11.84% - 12.12%

Table F.1.: Higgs production cross section results via gluon fusion using N^{3}LO and NNLO hard cross sections combined with NNLO and aN^{3}LO PDFs. All PDFs are at the standard choice $\alpha_s = 0.118$. These results are found with $\mu = m_H$ unless stated otherwise, with the values for $\mu = m_H/2$ supplied in Table 12.1.

Bibliography

[1] M. Mojaza, S. J. Brodsky, and X.-G. Wu, Phys. Rev. Lett. **1**10, 192001 (2013), 1212.0049.

[2] M. Czakon, D. Heymes, and A. Mitov, JHEP **0**4, 071 (2017), 1606.03350.

[3] S. Bailey, T. Cridge, L. A. Harland-Lang, A. D. Martin, and R. S. Thorne, Eur. Phys. J. C **8**1, 341 (2021), 2012.04684.

[4] T.-J. Hou *et al.*, Phys. Rev. D **1**03, 014013 (2021), 1912.10053.

[5] NNPDF, R. D. Ball *et al.*, Eur. Phys. J. C **7**7, 663 (2017), 1706.00428.

[6] NNPDF, R. D. Ball *et al.*, Eur. Phys. J. C **8**2, 428 (2022), 2109.02653.

[7] NNPDF, R. D. Ball *et al.*, Eur. Phys. J. C **8**1, 958 (2021), 2109.02671.

[8] PDF4LHC Working Group, R. D. Ball *et al.*, J. Phys. G **4**9, 080501 (2022), 2203.05506.

[9] NNPDF, R. Abdul Khalek *et al.*, Eur. Phys. J. C **7**9, 931 (2019), 1906.10698.

[10] L. A. Harland-Lang and R. S. Thorne, Eur. Phys. J. C **7**9, 225 (2019), 1811.08434.

[11] J. Gao, L. Harland-Lang, and J. Rojo, Phys. Rept. **7**42, 1 (2018), 1709.04922.

[12] R. D. Ball and R. L. Pearson, Eur. Phys. J. C **8**1, 830 (2021), 2105.05114.

[13] Z. Kassabov, M. Ubiali, and C. Voisey, (2022), 2207.07616.

[14] M. Bonvini, Eur. Phys. J. C **8**0, 989 (2020), 2006.16293.

[15] R. D. Ball *et al.*, Eur. Phys. J. C **7**8, 321 (2018), 1710.05935.

[16] xFitter Developers' Team, H. Abdolmaleki *et al.*, Eur. Phys. J. C **7**8, 621 (2018), 1802.00064.

[17] Tackmann, Frank, SCET 2019 Workshop (2019).

[18] F. J. Tackmann, DESY-19-021 .

[19] SeaQuest, J. Dove *et al.*, Nature **5**90, 561 (2021), 2103.04024, [Erratum: Nature 604, E26 (2022)].

[20] J. J. Thomson, Phil. Mag. Ser. 5 **4**4, 293 (1897).

[21] E. Rutherford, Phil. Mag. Ser. 6 **2**1, 669 (1911).

[22] N. Bohr, Phil. Mag. Ser. 6 **2**6, 1 (1913).

[23] D. J. Gross and F. Wilczek, Phys. Rev. Lett. **3**0, 1343 (1973).

[24] M. Peskin and D. Schroeder, *An Introduction To Quantum Field Theory*Frontiers in Physics (Avalon Publishing, 1995).

[25] P. W. Higgs, Phys. Rev. Lett. **1**3, 508 (1964).

[26] F. Englert and R. Brout, Phys. Rev. Lett. **1**3, 321 (1964).

[27] N. Cabibbo, Phys. Rev. Lett. **1**0, 531 (1963).

[28] M. Kobayashi and T. Maskawa, Prog. Theor. Phys. **4**9, 652 (1973).

[29] B. Pontecorvo, Zh. Eksp. Teor. Fiz. **3**4, 247 (1957).

[30] Z. Maki, M. Nakagawa, and S. Sakata, Prog. Theor. Phys. **2**8, 870 (1962).

[31] Particle Data Group, P. A. Zyla *et al.*, PTEP **2**020, 083C01 (2020).

[32] C. G. Callan Jr and D. J. Gross, Physical Review Letters **2**2, 156 (1969).

[33] J. C. Collins, D. E. Soper, and G. F. Sterman, Adv. Ser. Direct. High Energy Phys. **5**, 1 (1989), hep-ph/0409313.

[34] G. Altarelli and G. Parisi, Nucl. Phys. B **1**26, 298 (1977).

[35] Y. L. Dokshitzer, Sov. Phys. JETP **4**6, 641 (1977).

[36] V. N. Gribov and L. N. Lipatov, Sov. J. Nucl. Phys. **1**5, 438 (1972).

[37] M. Buza, Y. Matiounine, J. Smith, and W. L. van Neerven, Eur. Phys. J. C **1**, 301 (1998), hep-ph/9612398.

[38] M. Buza, Y. Matiounine, J. Smith, and W. L. van Neerven, Nucl. Phys. B **4**85, 420 (1997), hep-ph/9608342.

[39] J. D. Bjorken and E. A. Paschos, Phys. Rev. **1**85, 1975 (1969).

[40] M. Gluck, E. Hoffmann, and E. Reya, Z. Phys. C **1**3, 119 (1982).

[41] L. Baulieu and C. Kounnas, Nucl. Phys. B **1**55, 429 (1979).

[42] E. Eichten, I. Hinchliffe, K. D. Lane, and C. Quigg, Rev. Mod. Phys. **5**6, 579 (1984), [Addendum: Rev.Mod.Phys. 58, 1065–1073 (1986)].

[43] H. Abramowicz *et al.*, Z. Phys. C **17**, 283 (1983).

[44] J. G. Morfin and W.-K. Tung, Z. Phys. C **52**, 13 (1991).

[45] A. D. Martin, R. G. Roberts, and W. J. Stirling, Phys. Rev. D **37**, 1161 (1988).

[46] M. Diemoz, F. Ferroni, E. Longo, and G. Martinelli, Z. Phys. C **39**, 21 (1988).

[47] P. Aurenche, R. Baier, M. Fontannaz, J. F. Owens, and M. Werlen, Phys. Rev. D **39**, 3275 (1989).

[48] P. N. Harriman, A. D. Martin, W. J. Stirling, and R. G. Roberts, Phys. Rev. D **42**, 798 (1990).

[49] A. D. Martin, W. J. Stirling, and R. G. Roberts, Phys. Rev. D **50**, 6734 (1994), hep-ph/9406315.

[50] H. L. Lai *et al.*, Phys. Rev. D **51**, 4763 (1995), hep-ph/9410404.

[51] J. Huston *et al.*, Phys. Rev. Lett. **77**, 444 (1996), hep-ph/9511386.

[52] A. D. Martin, R. G. Roberts, W. J. Stirling, and R. S. Thorne, Eur. Phys. J. C **28**, 455 (2003), hep-ph/0211080.

[53] J. Pumplin *et al.*, JHEP **07**, 012 (2002), hep-ph/0201195.

[54] J. Pumplin *et al.*, Phys. Rev. D **65**, 014013 (2001), hep-ph/0101032.

[55] W. T. Giele, S. A. Keller, and D. A. Kosower, (2001), hep-ph/0104052.

[56] V. Barone, C. Pascaud, and F. Zomer, Eur. Phys. J. C **12**, 243 (2000), hep-ph/9907512.

[57] M. Botje, Eur. Phys. J. C **1**4, 285 (2000), hep-ph/9912439.

[58] S. Alekhin, Eur. Phys. J. C **1**0, 395 (1999), hep-ph/9611213.

[59] M. A. G. Aivazis, J. C. Collins, F. I. Olness, and W.-K. Tung, Phys. Rev. D **5**0, 3102 (1994), hep-ph/9312319.

[60] R. S. Thorne and R. G. Roberts, Phys. Rev. D **5**7, 6871 (1998), hep-ph/9709442.

[61] J. C. Collins, Phys. Rev. D **5**8, 094002 (1998), hep-ph/9806259.

[62] S. Moch, J. A. M. Vermaseren, and A. Vogt, Nucl. Phys. B **6**88, 101 (2004), hep-ph/0403192.

[63] A. Vogt, S. Moch, and J. A. M. Vermaseren, Nucl. Phys. B **6**91, 129 (2004), hep-ph/0404111.

[64] A. D. Martin, W. J. Stirling, R. S. Thorne, and G. Watt, Eur. Phys. J. C **6**3, 189 (2009), 0901.0002.

[65] J. Gao *et al.*, Phys. Rev. D **8**9, 033009 (2014), 1302.6246.

[66] S. Alekhin, J. Blumlein, S. Klein, and S. Moch, Phys. Rev. D **8**1, 014032 (2010), 0908.2766.

[67] S. Forte, L. Garrido, J. I. Latorre, and A. Piccione, JHEP **0**5, 062 (2002), hep-ph/0204232.

[68] L. A. Harland-Lang, A. D. Martin, P. Motylinski, and R. S. Thorne, Eur. Phys. J. C **7**5, 204 (2015), 1412.3989.

[69] R. D. Ball *et al.*, Nucl. Phys. B **8**67, 244 (2013), 1207.1303.

[70] S. Dulat *et al.*, Phys. Rev. D **9**3, 033006 (2016), 1506.07443.

[71] S. Alekhin, J. Blümlein, S. Moch, and R. Placakyte, Phys. Rev. D **9**6, 014011 (2017), 1701.05838.

[72] BCDMS, A. C. Benvenuti *et al.*, Phys. Lett. **B**223, 485 (1989).

[73] CDF, T. Aaltonen *et al.*, Phys. Rev. Lett. **1**02, 181801 (2009), 0901.2169.

[74] D0, V. M. Abazov *et al.*, Phys. Rev. Lett. **1**01, 211801 (2008), 0807.3367.

[75] NMC, M. Arneodo *et al.*, Nucl. Phys. **B**483, 3 (1997), hep-ph/9610231.

[76] D0, V. M. Abazov *et al.*, Phys. Rev. **D**85, 052006 (2012), 1110.3771.

[77] ATLAS, G. Aad *et al.*, Phys. Rev. D **8**5, 072004 (2012), 1109.5141.

[78] L. W. Whitlow, E. M. Riordan, S. Dasu, S. Rock, and A. Bodek, Phys. Lett. **B**282, 475 (1992).

[79] L. W. Whitlow, S. Rock, A. Bodek, E. M. Riordan, and S. Dasu, Phys. Lett. **B**250, 193 (1990).

[80] CMS, S. Chatrchyan *et al.*, Phys. Rev. Lett. **1**09, 111806 (2012), 1206.2598.

[81] CMS, S. Chatrchyan *et al.*, JHEP **0**4, 050 (2011), 1103.3470.

[82] E665, M. R. Adams *et al.*, Phys. Rev. **D**54, 3006 (1996).

[83] LHCb, R. Aaij *et al.*, JHEP **0**2, 106 (2013), 1212.4620.

[84] LHCb, R. Aaij *et al.*, JHEP **0**6, 058 (2012), 1204.1620.

[85] NuTeV, M. Tzanov *et al.*, Phys. Rev. **D**74, 012008 (2006), hep-ex/0509010.

[86] CMS, S. Chatrchyan *et al.*, Phys. Rev. **D**85, 032002 (2012), 1110.4973.

[87] ATLAS, G. Aad *et al.*, Phys. Lett. **B**725, 223 (2013), 1305.4192.

[88] NMC, M. Arneodo *et al.*, Nucl. Phys. **B**487, 3 (1997), hep-ex/9611022.

[89] CDF, D0, T. A. Aaltonen *et al.*, Phys. Rev. **D**89, 072001 (2014), 1309.7570.

[90] ATLAS, G. Aad *et al.*, Eur. Phys. J. **C**71, 1577 (2011), 1012.1792.

[91] ATLAS, G. Aad *et al.*, Phys. Lett. **B**707, 459 (2012), 1108.3699.

[92] ATLAS, G. Aad *et al.*, Phys. Lett. **B**711, 244 (2012), 1201.1889.

[93] ATLAS, G. Aad *et al.*, JHEP **0**5, 059 (2012), 1202.4892.

[94] ATLAS, G. Aad *et al.*, Phys. Lett. **B**717, 89 (2012), 1205.2067.

[95] ATLAS, G. Aad *et al.*, Eur. Phys. J. **C**73, 2328 (2013), 1211.7205.

[96] CMS, S. Chatrchyan *et al.*, Phys. Rev. D **8**5, 112007 (2012), 1203.6810.

[97] CMS, S. Chatrchyan *et al.*, JHEP **1**1, 067 (2012), 1208.2671.

[98] CMS, S. Chatrchyan *et al.*, Phys. Lett. B **7**20, 83 (2013), 1212.6682.

[99] CMS, S. Chatrchyan *et al.*, Eur. Phys. J. C **7**3, 2386 (2013), 1301.5755.

[100] CMS, S. Chatrchyan *et al.*, JHEP **0**5, 065 (2013), 1302.0508.

[101] CMS, S. Chatrchyan *et al.*, JHEP **0**2, 024 (2014), 1312.7582, [Erratum: JHEP 02, 102 (2014)].

[102] J. C. Webb, *Measurement of continuum dimuon production in 800-GeV/C proton*

nucleon collisions, PhD thesis, New Mexico State U., 2003, hep-ex/0301031.

[103] CMS, S. Chatrchyan *et al.*, JHEP **12**, 030 (2013), 1310.7291.

[104] NuSea, R. S. Towell *et al.*, Phys. Rev. **D**64, 052002 (2001), hep-ex/0103030.

[105] LHCb, R. Aaij *et al.*, JHEP **0**8, 039 (2015), 1505.07024.

[106] LHCb, R. Aaij *et al.*, JHEP **0**1, 155 (2016), 1511.08039.

[107] H1, ZEUS, H. Abramowicz *et al.*, Eur. Phys. J. C **7**3, 2311 (2013), 1211.1182.

[108] LHCb, R. Aaij *et al.*, JHEP **0**5, 109 (2015), 1503.00963.

[109] CMS, V. Khachatryan *et al.*, Eur. Phys. J. C **7**6, 469 (2016), 1603.01803.

[110] H1, F. D. Aaron *et al.*, Phys. Lett. **B**665, 139 (2008), 0805.2809.

[111] H1, F. D. Aaron *et al.*, Eur. Phys. J. **C**71, 1579 (2011), 1012.4355.

[112] ZEUS, S. Chekanov *et al.*, Phys. Lett. **B**682, 8 (2009), 0904.1092.

[113] ATLAS, G. Aad *et al.*, JHEP **0**2, 153 (2015), 1410.8857, [Erratum: JHEP 09, 141 (2015)].

[114] NuTeV, M. Goncharov *et al.*, Phys. Rev. **D**64, 112006 (2001), hep-ex/0102049.

[115] CMS, S. Chatrchyan *et al.*, JHEP **0**2, 013 (2014), 1310.1138.

[116] ATLAS, M. Aaboud *et al.*, Eur. Phys. J. C **7**7, 367 (2017), 1612.03016.

[117] CHORUS, G. Onengut *et al.*, Phys. Lett. **B**632, 65 (2006).

[118] CMS, S. Chatrchyan *et al.*, Phys. Rev. D **9**0, 072006 (2014), 1406.0324.

[119] D0, V. M. Abazov *et al.*, Phys. Rev. Lett. **1**12, 151803 (2014), 1312.2895, [Erratum: Phys.Rev.Lett. 114, 049901 (2015)].

[120] H1, ZEUS, F. Aaron *et al.*, JHEP **0**1, 109 (2010), 0911.0884.

[121] ATLAS, G. Aad *et al.*, Eur. Phys. J. C **7**6, 291 (2016), 1512.02192.

[122] CMS, V. Khachatryan *et al.*, JHEP **0**3, 156 (2017), 1609.05331.

[123] ATLAS, G. Aad *et al.*, Eur. Phys. J. C **7**6, 538 (2016), 1511.04716.

[124] ATLAS, M. Aaboud *et al.*, Phys. Rev. D **9**4, 092003 (2016), 1607.07281.

[125] ATLAS, G. Aad *et al.*, JHEP **0**8, 009 (2016), 1606.01736.

[126] ATLAS, M. Aaboud *et al.*, JHEP **0**5, 077 (2018), 1711.03296.

[127] CMS, A. M. Sirunyan *et al.*, Eur. Phys. J. C **7**7, 459 (2017), 1703.01630.

[128] CDF, A. Abulencia *et al.*, Phys. Rev. **D**75, 092006 (2007), hep-ex/0701051, [Erratum: Phys. Rev.D75,119901(2007)].

[129] ATLAS, G. Aad *et al.*, Eur. Phys. J. C **7**9, 760 (2019), 1904.05631.

[130] D0, V. M. Abazov *et al.*, Phys. Rev. **D**76, 012003 (2007), hep-ex/0702025.

[131] CMS, V. Khachatryan *et al.*, Eur. Phys. J. C **7**6, 265 (2016), 1512.06212.

[132] CDF, T. A. Aaltonen *et al.*, Phys. Lett. **B**692, 232 (2010), 0908.3914.

[133] CMS, V. Khachatryan *et al.*, Eur. Phys. J. C **7**5, 542 (2015), 1505.04480.

[134] D0, V. M. Abazov *et al.*, Phys. Rev. **D**88, 091102 (2013), 1309.2591.

[135] ATLAS, M. Aaboud *et al.*, JHEP **1**2, 059 (2017), 1710.05167.

[136] `http://lhapdf.hepforge.org`.

[137] J. Currie, E. W. N. Glover, and J. Pires, Phys. Rev. Lett. **1**18, 072002 (2017), 1611.01460.

[138] A. Gehrmann-De Ridder, T. Gehrmann, E. W. N. Glover, A. Huss, and T. A. Morgan, PoS **L**L2016, 056 (2016), 1607.01749.

[139] M. Czakon *et al.*, JHEP **1**0, 186 (2017), 1705.04105.

[140] R. S. Thorne, Phys. Rev. D **7**3, 054019 (2006), hep-ph/0601245.

[141] R. S. Thorne, Phys. Rev. D **8**6, 074017 (2012), 1201.6180.

[142] A. D. Martin, R. Roberts, W. Stirling, and R. S. Thorne, Eur. Phys. J. C **1**8, 117 (2000), hep-ph/0007099.

[143] T. Cridge, L. A. Harland-Lang, A. D. Martin, and R. S. Thorne, Eur. Phys. J. C **8**1, 744 (2021), 2106.10289.

[144] K. Levenberg, Quarterly of Applied Mathematics **2**, 164 (1944).

[145] D. W. Marquardt, Journal of the Society for Industrial and Applied Mathematics **1**1, 431 (1963).

[146] M. Guzzi, P. M. Nadolsky, H.-L. Lai, and C. P. Yuan, Phys. Rev. D **8**6, 053005 (2012), 1108.5112.

[147] R. A. Khalek *et al.*, The NNPDF Collaboration (2019), 1906.10698.

[148] NNPDF, R. D. Ball *et al.*, Eur. Phys. J. C **7**8, 408 (2018), 1802.03398.

[149] G. Watt and R. S. Thorne, JHEP **0**8, 052 (2012), 1205.4024.

[150] T.-J. Hou *et al.*, JHEP **0**3, 099 (2017), 1607.06066.

[151] J. Gao and P. Nadolsky, JHEP **0**7, 035 (2014), 1401.0013.

[152] S. Carrazza, S. Forte, Z. Kassabov, J. I. Latorre, and J. Rojo, Eur. Phys. J. C **7**5, 369 (2015), 1505.06736.

[153] S. Carrazza, S. Forte, Z. Kassabov, and J. Rojo, Eur. Phys. J. C **7**6, 205 (2016), 1602.00005.

[154] S. Carrazza, J. I. Latorre, J. Rojo, and G. Watt, Eur. Phys. J. C **7**5, 474 (2015), 1504.06469.

[155] A. Candido, S. Forte, and F. Hekhorn, JHEP **1**1, 129 (2020), 2006.07377.

[156] J. Collins, T. C. Rogers, and N. Sato, Phys. Rev. D **1**05, 076010 (2022), 2111.01170.

[157] G. B. Arfken and H. J. Weber, Mathematical methods for physicists, 1999.

[158] A. Jeffrey and D. Zwillinger, *Table of integrals, series, and products* (Elsevier, 2007).

[159] S. Moch, B. Ruijl, T. Ueda, J. A. M. Vermaseren, and A. Vogt, JHEP **1**0, 041 (2017), 1707.08315.

[160] E. G. Floratos, D. A. Ross, and C. T. Sachrajda, Nucl. Phys. B **1**52, 493 (1979).

[161] A. Gonzalez-Arroyo and C. Lopez, Nucl. Phys. B **1**66, 429 (1980).

[162] W. Furmanski and R. Petronzio, Phys. Lett. B **9**7, 437 (1980).

[163] E. G. Floratos, C. Kounnas, and R. Lacaze, Nucl. Phys. B **1**92, 417 (1981).

[164] S. Catani and F. Hautmann, Nucl. Phys. B **4**27, 475 (1994), hep-ph/9405388.

[165] L. N. Lipatov, Sov. J. Nucl. Phys. **2**3, 338 (1976).

[166] E. A. Kuraev, L. N. Lipatov, and V. S. Fadin, Sov. Phys. JETP **4**5, 199 (1977).

[167] I. I. Balitsky and L. N. Lipatov, Sov. J. Nucl. Phys. **2**8, 822 (1978).

[168] V. S. Fadin and L. N. Lipatov, Phys. Lett. B **4**29, 127 (1998), hep-ph/9802290.

[169] M. Ciafaloni and G. Camici, Phys. Lett. B **4**30, 349 (1998), hep-ph/9803389.

[170] M. Bonvini and S. Marzani, JHEP **0**6, 145 (2018), 1805.06460.

[171] A. Vogt *et al.*, PoS **L**L2018, 050 (2018), 1808.08981.

[172] S. Moch, B. Ruijl, T. Ueda, J. A. M. Vermaseren, and A. Vogt, Phys. Lett. B **8**25, 136853 (2022), 2111.15561.

[173] R. K. Ellis, W. J. Stirling, and B. R. Webber, *QCD and Collider Physics*, Cambridge monographs on particle physics, nuclear physics and cosmology Vol. 8 (Cambridge University Press, 2011).

[174] E. Laenen, S. Riemersma, J. Smith, and W. L. van Neerven, Nucl. Phys. B **3**92, 229 (1993).

[175] B. W. Harris and J. Smith, Nucl. Phys. B **4**52, 109 (1995), hep-ph/9503484.

[176] S. Catani, M. Ciafaloni, and F. Hautmann, Nucl. Phys. B **3**66, 135 (1991).

[177] E. Laenen and S.-O. Moch, Phys. Rev. D **5**9, 034027 (1999), hep-ph/9809550.

[178] H. Kawamura, N. A. Lo Presti, S. Moch, and A. Vogt, Nucl. Phys. B **8**64, 399

(2012), 1205.5727.

[179] I. Bierenbaum, J. Blumlein, and S. Klein, Nucl. Phys. B **8**20, 417 (2009), 0904.3563.

[180] J. Ablinger *et al.*, Nucl. Phys. B **8**86, 733 (2014), 1406.4654.

[181] J. Ablinger *et al.*, Nucl. Phys. B **8**90, 48 (2014), 1409.1135.

[182] J. Ablinger *et al.*, Nuclear Physics B **8**82, 263 (2014), 1402.0359.

[183] J. Blümlein *et al.*, PoS **Q**CDEV2017, 031 (2017), 1711.07957.

[184] M. A. G. Aivazis, F. I. Olness, and W.-K. Tung, Phys. Rev. D **5**0, 3085 (1994), hep-ph/9312318.

[185] J. A. M. Vermaseren, A. Vogt, and S. Moch, Nucl. Phys. B **7**24, 3 (2005), hep-ph/0504242.

[186] W. L. van Neerven and A. Vogt, Nucl. Phys. B **5**68, 263 (2000), hep-ph/9907472.

[187] W. L. van Neerven and A. Vogt, Nucl. Phys. B **5**88, 345 (2000), hep-ph/0006154.

[188] J. Blümlein, P. Marquard, C. Schneider, and K. Schönwald, Nucl. Phys. B **9**71, 115542 (2021), 2107.06267.

[189] J. Ablinger *et al.*, Nucl. Phys. B **8**85, 280 (2014), 1405.4259.

[190] J. Ablinger *et al.*, Nucl. Part. Phys. Proc. **2**58-259, 37 (2015), 1409.1435.

[191] C. Duhr, F. Dulat, and B. Mistlberger, Phys. Rev. Lett. **1**25, 172001 (2020), 2001.07717.

[192] X. Chen *et al.*, Phys. Rev. Lett. **1**28, 052001 (2022), 2107.09085.

[193] C. Duhr and B. Mistlberger, JHEP **0**3, 116 (2022), 2111.10379.

[194] N. Kidonakis, (2022), 2203.03698.

[195] R. D. Ball, M. Bonvini, S. Forte, S. Marzani, and G. Ridolfi, Nucl. Phys. B **8**74, 746 (2013), 1303.3590.

[196] M. Bonvini, R. D. Ball, S. Forte, S. Marzani, and G. Ridolfi, J. Phys. G **4**1, 095002 (2014), 1404.3204.

[197] M. Bonvini, S. Marzani, C. Muselli, and L. Rottoli, JHEP **0**8, 105 (2016), 1603.08000.

[198] T. Ahmed, M. C. Kumar, P. Mathews, N. Rana, and V. Ravindran, Eur. Phys. J. C **7**6, 355 (2016), 1510.02235.

[199] M. Bonvini and S. Marzani, Phys. Rev. Lett. **1**20, 202003 (2018), 1802.07758.

[200] M. Bonvini, Eur. Phys. J. C **7**8, 834 (2018), 1805.08785.

[201] M. Bonvini, EPJ Web Conf. **6**0, 12008 (2013), 1306.6633.

[202] C. Anastasiou *et al.*, JHEP **0**3, 091 (2015), 1411.3584.

[203] C. Anastasiou *et al.*, JHEP **0**5, 058 (2016), 1602.00695.

[204] B. Mistlberger, JHEP **0**5, 028 (2018), 1802.00833.

[205] L. A. Harland-Lang, A. D. Martin, and R. S. Thorne, Eur. Phys. J. C **7**8, 248 (2018), 1711.05757.

[206] ATLAS, M. Aaboud *et al.*, JHEP **0**9, 020 (2017), 1706.03192.

[207] R. Abdul Khalek *et al.*, Eur. Phys. J. C **8**0, 797 (2020), 2005.11327.

[208] N. Kidonakis and G. F. Sterman, Nucl. Phys. B **5**05, 321 (1997), hep-ph/9705234.

[209] N. Kidonakis, Phys. Rev. Lett. **1**02, 232003 (2009), 0903.2561.

[210] N. Kidonakis, Phys. Rev. D **8**2, 114030 (2010), 1009.4935.

[211] N. Kidonakis, (2021), 2109.14102.

[212] E. L. Berger, J. Gao, C. S. Li, Z. L. Liu, and H. X. Zhu, Phys. Rev. Lett. **1**16, 212002 (2016), 1601.05430.

[213] Particle Data Group, P. A. Zyla *et al.*, PTEP **2**020, 083C01 (2020).

[214] M. Cacciari, F. A. Dreyer, A. Karlberg, G. P. Salam, and G. Zanderighi, Phys. Rev. Lett. **1**15, 082002 (2015), 1506.02660, [Erratum: Phys.Rev.Lett. 120, 139901 (2018)].

[215] F. A. Dreyer and A. Karlberg, Phys. Rev. Lett. **1**17, 072001 (2016), 1606.00840.

[216] M. Bonvini, https://www.ge.infn.it/~bonvini/higgs/ .

[217] M. Cacciari, F. Dreyer, A. Karlberg, G. Salam, and G. Zanderighi, https://provbfh.hepforge.org/ .

[218] ATLAS, G. Aad *et al.*, JHEP **0**5, 059 (2014), 1312.3524.

[219] CMS, S. Chatrchyan *et al.*, Phys. Rev. D **8**7, 112002 (2013), 1212.6660, [Erratum: Phys.Rev.D 87, 119902 (2013)].

[220] CMS, A. M. Sirunyan *et al.*, Eur. Phys. J. C **7**7, 746 (2017), 1705.02628.

[221] A. Buckley *et al.,* Eur. Phys. J. C **75**, 132 (2015), 1412.7420.